

**Binding Biological Polyanions -
Understanding and Controlling
Binding Mode in order to
Achieve Controlled Nanoscale
Assembly**

Ching Wan Chan

PhD

University of York

Chemistry

March 2016

Abstract

This thesis explores polyanion binding and sensing using variety of different approaches and aims to understand and manipulate these interactions.

Amine-functionalised pyrene derivatives Py-G1 and Py-DAPMA can act as effective heparin sensors in competitive media using a ratiometric fluorescence sensing approach. The assembly of Py-G1 into pre-formed self-assembled multivalent (SAMul) nanostructures provides it with a significant (order of magnitude) advantage in terms of the dynamic range of sensory response over the non-SAMul Py-DAPMA in buffer. In the presence of serum, both ligands can still detect heparin ratiometrically, however, the SAMul sensing mechanism of Py-G1 is switched off.

Three series of SAMul dendrons based on L or D lysine and focal point hydrophobic groups, either pyrene or hydrocarbon chains, have been developed. Their ability to exhibit different chiral binding preferences towards chiral polyanions DNA and heparin have been studied. The way in which the ligands are displayed, which in turn depends on the nature of the hydrophobic component and the overall structural characteristics, are absolutely critical. Insertion of a simple linker allows expression of the chiral information at the nanoscale surface.

The interaction between heparin and Mallard Blue (Mal-B) or a series of SAMul heparin binders are explored by NMR spectroscopy. The choice of buffer has significant impact on Mal-B/heparin binding, but precipitation of the Mal-B:heparin complex limits the opportunity for NMR analysis. NMR provides some insight to the binding events at the nanoscale and appears particularly useful for uncovering the role of ligands and dynamics in mediating binding with the best binder appearing to have best resolved ligand NMR resonances.

The ability of C₂₂-G1 and Py-G1 to act as “nanoglue”, causing adhesion between polyanions and carbon nanotubes was studied. Both can self-assemble and bind to DNA and SWCNT respectively and C₂₂-G1 is a better DNA and SWCNT binder. Although

the attempt to quantitatively assay simultaneous DNA and SWCNT binding was unsuccessful, TEM imaging clearly allowed onto monitor the binding of DNA and CNT, and demonstrated that our synthetic nanoglue system causes them to co-assemble.

Table of Contents

Abstract	2
Table of Contents	4
List of Figures	9
List of Tables	22
List of Schemes	23
Acknowledgements	24
Declaration.....	25
Chapter 1 Introduction	26
1.0 Overview.....	26
1.1 Supramolecular chemistry.....	26
1.2 Self- Assembly	27
1.2.1 Inspiration From Nature.....	27
1.2.2 Self-Assembly in Synthetic Chemistry.....	30
1.3 Multivalent binding.....	37
1.4. Self-Assembled Multivalency (SAMul)	39
1.5 Project Aims	41
Chapter 2 Pyrene-based heparin sensors in highly competitive aqueous solution and serum	43
2.1 Introduction	43
2.1.1 Heparin	43
2.1.2 Heparin Sensors.....	47
2.1.3 Aim	58
2.2 Effect of SAMul in Heparin Sensing.....	59
2.2.1 Synthesis of Py-G1 and Py-DAPMA.....	59
2.2.2 Critical Aggregation Concentration (CAC)	67
2.2.3 Transmission Electron Microscopy (TEM)	69
2.2.4 Dynamic Light Scattering (DLS).....	70
2.2.5 Heparin sensing in 10 mM Tris HCl with 150 mM NaCl buffer	72
2.2.6 Heparin sensing in 12.5% serum with 20 mM Tris HCl	78
2.2.7 Heparin sensing in 100% serum	81
2.2.8 Heparin sensing in 10 mM Tris HCl with 150 mM NaCl buffer at	

elevated concentrations.	84
2.2.9 Heparin sensing in 12.5% serum with 20 mM Tris HCl at elevated concentrations	89
2.2.10 Heparin sensing in 100% serum at elevated concentrations	92
2.3 Conclusion and future work.....	95
Chapter 3 Effect of Chirality on Self-Assembled Multivalent (SAMul) Biological Polyanion Binder.....	97
3.1 Introduction	97
3.2 Heparin binder.....	97
3.3 DNA binder	100
3.4 Effect of chirality on DNA and heparin binding	105
3.5 Project aim	108
3.6 C ₁₆ -L-Lys and C ₁₆ -D-Lys	109
3.6.1 Synthesis of C ₁₆ -L-Lys and C ₁₆ -D-Lys	109
3.6.2 Circular Dichroism (CD).....	111
3.6.3 Critical Aggregation Concentration (CAC)	111
3.6.4 Transmission Electron Microscopy (TEM)	113
3.6.5 Dynamic Light Scattering (DLS).....	114
3.6.6 DNA assay (Ethidium bromide displacement assay)	115
3.6.7 Heparin assay (Mallard Blue (Mal-B) competition assay).....	116
3.6.8 Summary	117
3.7 C ₁₆ -Gly-L-Lys and C ₁₆ -Gly-D-Lys	118
3.7.1 Synthesis of C ₁₆ -Gly-L-Lys and C ₁₆ -Gly-D-Lys	118
3.7.2 Circular Dichroism (CD).....	121
3.7.3 Critical Aggregation Concentration (CAC)	121
3.7.4 Transmission Electron Microscopy (TEM)	123
3.7.5 Dynamic Light Scattering (DLS).....	124
3.7.6 DNA assay (Ethidium bromide displacement assay)	126
3.7.7 Heparin assay (Mallard Blue (Mal-B) competition assay).....	127
3.7.8 Summary	128
3.8 Chirality effect in heparin sensing.....	129
3.8.1 Synthesis of Py-L-Lys and Py-D-Lys	129

3.8.2 Critical Aggregation Concentration (CAC)	130
3.8.3 Transmission Electron Microscopy (TEM)	132
3.8.4 Dynamic Light Scattering (DLS)	133
3.8.5 Heparin sensing in 10 mM Tris HCl with 150 mM NaCl buffer	134
3.8.6 Heparin sensing in 12.5% serum with 20 mM Tris HCl	138
3.8.7 Heparin sensing in 100% serum	141
3.8.8 Heparin sensing in 10 mM Tris HCl with 150 mM NaCl buffer at elevated concentrations.	144
3.8.9 Heparin sensing in 12.5% serum with 20 mM Tris HCl at elevated concentrations	147
3.8.10 Heparin sensing in 100% serum at elevated concentrations	150
3.8.11 Conclusion and future work.....	153
Chapter 4 NMR investigation of Heparin binding with Mallard Blue (Mal-B) and Self-Assembled Multivalent (SAMul) Heparin Binders	156
4.1 Introduction	156
4.1.1 Heparin NMR.....	156
4.1.2 Mallard Blue.....	158
4.1.3 NMR study of heparin interaction.....	159
4.1.4 Project aim.....	161
4.2 NMR investigation of Heparin binding with Mallard Blue (Mal-B)	162
4.2.1 NMR spectra of heparin and Mal-B.....	162
4.2.2 2D NMR spectra	163
4.2.3 Low concentration Mal-B NMR study.....	166
4.2.4 Effect of buffer in Mal-B binding with heparin	171
4.2.5 Titration study of Mal-B with heparin in phosphate buffer.....	175
4.2.6 Conclusions	176
4.3 NMR investigation of Heparin binding with Self-Assembled Multivalent (SAMul) Heparin Binders.....	178
4.3.1 Self-Assembled Multivalent (SAMul) Heparin Binders	178
4.3.2 Result and discussion	179
4.3.3 Conclusion and future work.....	196
Chapter 5 Orthogonal Nanoscale adhesion of Nanotubes and DNA using SAMul	

System	198
5.0 Overview	198
5.1 Nanomaterial	198
5.1.1 Carbon nanotubes	198
5.1.2 Functionalising CNTs	199
5.1.3 Dendrons and carbon nanotubes	201
5.1.4 CNTs in biomedical applications	203
5.1.5 Cellular uptake of CNTs	204
5.1.6 CNTs as gene delivery vector	206
5.2 Project Aim	207
5.3 Compound Design	208
5.4 Result and Discussion	209
5.4.1 Synthesis of C ₂₂ -G1	209
5.4.2 Critical Aggregation Concentration (CAC) of C ₂₂ -G1 and Py-G1	211
5.4.3 DNA assay C ₂₂ -G1 and Py-G1	213
5.4.4 Carbon nanotube assay	216
5.4.5 CNTs and DNA binding assay of C ₂₂ -G1	219
5.4.6 Transmission Electron Microscopy (TEM)	221
5.5 Summary and future work	228
Chapter 6 Experimental	230
6.1 General Materials and Methods	230
6.2 Assay Methods	230
Appendices	262
Appendix one: NMR spectra of Py-G1	262
Appendix two: NMR spectra of Py-DAPMA	263
Appendix three: NMR spectra of C ₁₆ -L-Lys	264
Appendix four: NMR spectra of C ₁₆ -D-Lys	265
Appendix five: NMR spectra of C ₁₆ -Gly-L-Lys	266
Appendix six: NMR spectra of C ₁₆ -Gly-D-Lys	267
Appendix seven: NMR spectra of Py-L-LysG1	268
Appendix eight: NMR spectra of Py-D-Lys	269
Appendix nine: NMR spectra of C ₂₂ -G1	270

Abbreviations	271
References.....	273

List of Figures

Figure 1.1 Example of non-covalent intermolecular forces: Schematic representation of the interactions between polarizable non-polar groups involving flavonoids through dispersive van der Waals interactions (π -stacking) and the role of the surrounding hydrogen-bond network. ⁶	27
Figure 1.2: Complementary base pairing in DNA helical structure and base pairing in DNA (guanine and cytosine form triple hydrogen bonds; adenine and thymine form double hydrogen bonds). ¹³	28
Figure 1.3: The tobacco mosaic virus (TMV). a) Electron micrograph. b) schematic representation. The protein subunits are colored yellow. (Taken from ref. ¹⁴).....	29
Figure 1.4: Self-assembly of the tobacco mosaic virus at different stages. ¹⁰	30
Figure 1.5: Energy-minimized structures of the benzene dimer: a) T-shaped and b) π – π stacked. ²⁵	30
Figure 1.6: Structure of crown ether phthalocyanine ²⁷	31
Figure 1.7: Transmission electron micrographs (platinum shadowing) of crown ether phthalocyanine. (A) Left-handed coiled-coil aggregates in chloroform. (B) Schematic representation of the helices in (A). (C) Non-helical rods formed in chloroform in the presence of KCl. (D) Schematic representation of the rods in (C). ²⁷	32
Figure 1.8: Schematic representation of the formation and breakdown of the sandwich-type complexes between K^+ ions and crown ether phthalocyanine	32
Figure 1.9: Structure of supramolecular aggregates according to the packing factor of amphiphiles. ³⁴	34
Figure 1.10 Schematic representation of the organization of amphiphilic dendrimers with different alkyl chain lengths in the process of self-assembly (Q_1QPAMC_8 = Generations 1 PAMAM with 8 carbon alkyl chain; Q_1QPAMC_{16} = Generations 1 PAMAM with 16 carbon alkyl chain). ³⁵	35
Figure 1.11: Cryo-TEM images of the structures assembled of (a) (3,4,5)12G1-L-Ala-CH ₂ -(3,4,5)-3EO-G1-(OCH ₃) ₃ , 9cf ;	(b)
(3,5)12G1-CH ₂ -L-Ala-(3,4)-3EO-G1-(OCH ₃) ₂ , 10bd ;	(c)
(3,5)12G1-L-CH ₂ -Ala-(3,4,5)-3EO-G1-(OCH ₃) ₃ , 10bf ;	(d)

(3,4,5)12G1-L-Ala-CH ₂ -(3,4,5)-3EO-G1-(OCH ₃) ₃ , 10cf. ³⁶	36
Figure 1.12: Specific modes of multivalent binding. ³⁹	38
Figure 1.13: Self-assembled high affinity multivalent binding. ³⁸	39
Figure 1.14: Structure of sialic acid functionalised lipid used as a SAMul inhibitor of hemagglutinin. ⁴⁷	40
Figure 1.15: Self-assembling multivalent mannose-functionalised lectin-binding discotic molecules. ⁴⁸	41
Figure 2.1: An example heparin polysaccharide (top) along with the predominant disaccharide repeat unit (bottom left) and the specific pentasaccharide sequence required to confer anticoagulant activity (bottom right). ⁵¹	43
Figure 2.2: Schematic representation of the blood coagulation cascade. ⁵⁵	45
Figure 2.3: An example protamine structure with the prevalent arginine residues depicted as wedges, adapted from reference ⁴³	46
Figure 2.4: Computer model of protamine (blue) bound to the major disaccharide repeat unit of heparin (alternating purple and green units represent the two different saccharides). ⁵¹	47
Figure 2.5 : Schematic representation of heparin binding to Ma's quaternary amine functionalized membrane, adapted from reference ⁶⁸	48
Figure 2.6: Selection of dyes from the thionine family	49
Figure 2.7: Zhong's heparin sensors operating in an indicator displacement regime.	49
Figure 2.8: Structure of the tripodal ammonium and boronic acid functionalised heparin receptor. ⁷⁸	50
Figure 2.9 Structures of heparin chemosensors Heparin Orange and Heparin Blue. ⁷⁹ ..	51
Figure 2.10: Heparin Orange (10 μM, Top) and Heparin Blue (10 μM, Bottom) with indicated concentrations of UFH and LMWH in 10 μM, HEPES buffer (pH = 7.4) in a 96-well plate under 365 nm UV lamp light.	51
Figure 2.11: GO-AuNPs sensing system from Fu <i>et al.</i> , figured adapted from reference ⁸³	53
Figure 2.12: (Left) A polyfluorene heparin sensing derivative from Pu <i>et al.</i> ; (Right) photoluminescence (PL) spectra of polyfluorene heparin sensing derivative at 60μM in 2 mM PBS at pH 7.4 in the presence of heparin with concentrations ranging	

from 0 to 50 μM at intervals of 2 μM (excitation at 365 nm), figure adapted from reference ⁸⁴	54
Figure 2.13: (Left) A phosphorescent conjugated polyelectrolyte structure from Zhao, Liu and Huang. (Right) PL spectra in HEPES buffer with addition of heparin from 0 to 70 μM upon excitation at 380 nm. Inset: emission color changes of solution under hand-held UV-lamp excited at 365 nm. ⁸⁵	55
Figure 2.14: Chemical structures of bis-pyrene and conformational changes from stacked to unstacked conformations in aqueous solution under basic and acidic conditions by Zhang <i>et al.</i> , figure adapted from reference ⁸⁸	55
Figure 2.15: Structure of PQ	56
Figure 2.16: Structure of Py12.	57
Figure 2.17: Structure of C ₂₂ -G1 (top) and Py-G1 (bottom).....	60
Figure 2.18: Plausible mechanisms for the Cu(I) catalyzed reaction between azides and alkynes. ¹⁰⁹	63
Figure 2.19: ¹ H NMR spectra of Compound 11	64
Figure 2.20: ¹ H NMR spectra of Py-G1	65
Figure 2.21: ¹ H NMR spectra of Py-DAMPA	67
Figure 2.22: Fluorescence intensity at 495 nm of Py-G1 at increasing concentration in aqueous PBS Buffer (0.01 mM).	68
Figure 2.23: Fluorescence intensity of Py-DAPMA against wavelength (450 nm to 550 NM) as recorded for increasing concentrations of Py-DAPMA in PBS Buffer (0.01 mM).	69
Figure 2.24: TEM images of Py-DAPMA (left) and Py-G1 (right) in the absence (top) and presence of heparin (bottom).....	70
Figure 2.25: DLS data for Py-G1 measured at 1 mg/mL.....	71
Figure 2.26: DLS data for Py-DAPMA measured at 1 mg/mL.....	72
Figure 2.27: UV-Vis Absorption spectra of Py-G1 (0.5 mg/mL Tris Hcl with 150 mM NaCl)	73
Figure 2.28: Fluorescence spectra of Py-G1 on addition of heparin in buffer. The inset shows the photographs of a solution of Py-G1 without heparin (A) and with heparin (B).	74

Figure 2.29: Fluorescence intensities extracted at 383 nm and 495 nm for the titration of heparin into Py-G1 in buffer.....	74
Figure 2.30: Fluorescence spectra of Py-DAPMA on addition of heparin in buffer. The inset shows the photographs of a solution of Py-DAPMA without heparin (A) and with heparin (B).....	75
Figure 2.31: Fluorescence intensities extracted at 383 nm (Top) and 495 nm (Bottom) for the titration of heparin into Py-DAPMA in buffer.....	76
Figure 2.32: The changes of the fluorescence intensity ratio of Py-G1 and Py-DAPMA ($\log(I_{495}/I_{383})$) plotted against increasing heparin concentration in 10 mM Tris HCl buffer with 150mM NaCl buffer.	77
Figure 2.33: Fluorescence intensities extracted at 383 nm (Top) and 495 nm (Bottom) for the titration of heparin into Py-G1 in 12.5% serum with 20 mM Tris HCl.....	79
Figure 2.34: Fluorescence intensities extracted at 383 nm (Top) and 495 nm (Bottom) for the titration of heparin into Py-DAPMA in 12.5% serum with 20 mM Tris HCl.....	80
Figure 2.35: The changes of the fluorescence intensity ratio of Py-G1 and Py-DAPMA ($\log(I_{495}/I_{383})$) plotted against increasing heparin concentration in 12.5% serum with 20 mM Tris HCl.	81
Figure 2.36: Fluorescence intensities extracted at 383 nm (Top) and 495 nm (Bottom) for the titration of heparin into Py-G1 in 100% serum.	82
Figure 2.37: Fluorescence intensities extracted at 383 nm (Top) and 495 nm (Bottom) for the titration of heparin into Py-DAPMA in 100% serum.	83
Figure 2.38: The changes of the fluorescence intensity ratio of Py-G1 and Py-DAPMA ($\log(I_{495}/I_{383})$) plotted against increasing heparin concentration in 100% serum.....	84
Figure 2.39: Fluorescence spectra of Py-G1 (213 μ M) on addition of heparin. The inset shows the photographs of a solution of Py-G1 without heparin (A) and with heparin (B) in buffer.	85
Figure 2.40: Fluorescence intensities extracted at 383 nm and 495 nm for the titration of heparin into Py-G1 (213 μ M) in buffer.....	86
Figure 2.41: Fluorescence spectra of Py-DAPMA on addition of heparin. The inset shows the photographs of a solution of Py-DAPMA without heparin (A) and with heparin (B) in buffer.	87

Figure 2.42: Fluorescence intensities extracted at 383 nm (Top) and 495 nm (Bottom) for the titration of heparin into Py-DAPMA (426 μ M) in buffer.....	88
Figure 2.43: The changes of the fluorescence intensity ratio of Py-G1 and Py-DAPMA ($\log(I_{495}/I_{383})$) plotted against increasing heparin concentration in buffer.....	89
Figure 2.44: Fluorescence intensities extracted at 383 nm (Top) and 495 nm (Bottom) for the titration of heparin into Py-G1 in 12.5% serum with 20 mM Tris HCl.....	90
Figure 2.45: Fluorescence intensities extracted at 383 nm (Top) and 495 nm (Bottom) for the titration of heparin into Py-DAPMA (426 μ M) in 12.5% serum with 20 mM Tris HCl.	91
Figure 2.46: The changes of the fluorescence intensity ratio of Py-G1 (213 μ M) and Py-DAPMA (426 μ M) ($\log(I_{495}/I_{383})$) plotted against increasing heparin concentration in 12.5% serum with 20 mM Tris HCl.	92
Figure 2.47: Fluorescence intensities extracted at 383 nm (Top) and 495 nm (Bottom) for the titration of heparin into Py-G1 (213 μ M) in 100% serum.	93
Figure 2.48: Fluorescence intensities extracted at 383 nm (Top) and 495 nm (Bottom) for the titration of heparin into Py-DAPMA (426 μ M) in 100% serum.	94
Figure 2.49: The changes of the fluorescence intensity ratio of Py-G1 (213 μ M) and Py-DAPMA (426 μ M) ($\log(I_{495}/I_{383})$) plotted against increasing heparin concentration in 100% serum.....	95
Figure 3.1: Structure of polycationic calix[8]arenes (left) and space-filled species represents calix[8]arene, stick model represents heparin. Figure adapted from ¹²¹	98
Figure 3.2: Structure of lipophilic lysine and arginine functionalised dendrons. ¹²⁴	98
Figure 3.3: A self-assembling heparin-binding lipopeptide (top) and Schematic representation of heparin-nucleated nanofiber (bottom) from Rajangam <i>et al.</i> ¹²⁵	99
Figure 3.4: Structure of C ₂₂ -G1 (top), TEM images in absence (bottom left) and presence (bottom right) of heparin.	100
Figure 3.5: Some example of cationic polymers. ¹³⁰	101
Figure 3.6: Structure of cationic lipids DOTMA, DORIE and DMRIE.....	102
Figure 3.7: Structure of cationic lipids DOTAP, DOGS and DOSPA.....	103
Figure 3.8: Self-assembling dendritic systems which possess groups to bind DNA (polyamines) as well as groups which encourage the self-assembly of the system	

(hydrophobic alkyl tails). ³⁰	104
Figure 3.9: Structure of first and second generation Newkome dendrons with peripheral spermine ligands. ¹⁴⁷	105
Figure 3.10: Structure of cholesterol functionalised Newkome dendrons with peripheral spermine ligands. ¹⁴⁸	105
Figure 3.11: Structure of PNAs.....	106
Figure 3.12: Self-assembling chiral cationic ligands for binding polyanions by Bromfield and Smith. ¹⁶⁰	107
Figure 3.13: ¹ H NMR spectra of C ₁₆ -L-Lys.	110
Figure 3.14: ¹ H NMR spectra of C ₁₆ -D-Lys.	110
Figure 3.15 : Circular dichroism spectra of target molecules C ₁₆ -L-Lys and C ₁₆ -D-Lys (1 mg/mL in methanol) indicating opposing chirality.	111
Figure 3.16: Fluorescence intensity of Nile Red in the presence of increasing amounts of C ₁₆ -L-Lys.....	112
Figure 3.17: Fluorescence intensity of Nile Red in the presence of increasing amounts of C ₁₆ -D-Lys.....	112
Figure 3.18: TEM images of C ₁₆ -L-Lys (left) and C ₁₆ -D-Lys (right) in the absence (top) and presence of heparin (middle) and DNA (bottom).	113
Figure 3.19: DLS data for C ₁₆ -L-Lys measured at 1mg/ mL.....	114
Figure 3.20: DLS data for C ₁₆ -D-Lys measured at 1mg/ mL.....	115
Figure 3.21: Charge ratio vs. normalised fluorescence from the EthBr displacement assay used to determine CE ₅₀ values for C ₁₆ -L-Lys and C ₁₆ -D-Lys.....	116
Figure 3.22: Charge ratio vs. normalised fluorescence from the (MalB) competition assay used to determine CE ₅₀ values for C ₁₆ -L-Lys and C ₁₆ -D-Lys.....	117
Figure 3.23: Schematic representation of C ₁₆ -L-Lys and C ₁₆ -D-Lys with spacing group.	117
Figure 3.24: ¹ H NMR spectra of C ₁₆ -Gly-L-Lys.....	120
Figure 3.25: ¹ H NMR spectra of C ₁₆ -Gly-L-Lys.....	120
Figure 3.26: Circular dichroism spectra of target molecules C ₁₆ -Gly-L-Lys and C ₁₆ -Gly-D-Lys (1 mg/mL in methanol) indicating opposing chirality	121
Figure 3.27: Fluorescence intensity of Nile Red in the presence of increasing amounts	

of C ₁₆ -Dly-L-Lys	122
Figure 3.28: Fluorescence intensity of Nile Red in the presence of increasing amounts of C ₁₆ -Gly-D-Lys	122
Figure 3.29: TEM images of C ₁₆ -Gly-L-Lys (left) and C ₁₆ -Gly-D-Lys (right) in the absence (top) and presence of heparin (middle) and DNA (bottom).	124
Figure 3.31: DLS data for C ₁₆ -Gly-D-Lys measured at 1mg/ mL.	126
Figure 3.32: Charge ratio vs. normalised fluorescence from the EthBr displacement assay used to determine CE ₅₀ values for C ₁₆ -Gly-L-Lys and C ₁₆ -Gly-D-Lys.....	127
Figure 3.33: Charge ratio vs. normalised fluorescence from the (MalB) competition assay used to determine CE ₅₀ values for C ₁₆ -Gly-L-Lys and C ₁₆ -Gly-D-Lys.....	128
Figure 3.34: Fluorescence intensity at 495 nm of Py-L-Lys with increasing concentration in aqueous PBS Buffer (0.01 mM)	131
Figure 3.35: Fluorescence intensity at 495 nm of Py-D-Lys with increasing concentration in aqueous PBS Buffer (0.01 mM)	131
Figure 3.36: TEM images of Py-L-Lys (left) and Py-D-Lys (right) in the absence (top) and presence of heparin (bottom).....	132
Figure 3.37: DLS data for Py-L-Lys measured at 1mg/ mL.....	133
Figure 3.38: DLS data for Py-L-Lys measured at 1mg/ mL.....	134
Figure 3.39: Fluorescence intensities extracted at 383 nm (Top) and 495 nm (Bottom) for the titration of heparin into Py-L-Lys in buffer.....	135
Figure 3.40: Fluorescence spectra of Py-L-Lys on addition of heparin in buffer. The inset shows the photographs of a solution of Py-L-Lys without heparin (A) and with heparin (B).	135
Figure 3.41: Fluorescence intensities extracted at 383 nm (Top) and 495 nm (Bottom) for the titration of heparin into Py-D-Lys in buffer.....	136
Figure 3.42: Fluorescence spectra of Py-D-Lys on addition of heparin in buffer. The inset shows the photographs of a solution of Py-D-Lys without heparin (A) and with heparin (B).	137
Figure 3.43: The changes of the fluorescence intensity ratio of Py-L-Lys and Py-D-Lys ($\log(I_{495}/I_{383})$) plotted against increasing heparin concentration in in 10 mM Tris HCl buffer with 150mM NaCl buffer.	138

Figure 3.44: Fluorescence intensities extracted at 383 nm (Top) and 495 nm (Bottom) for the titration of heparin into Py-L-Lys in 12.5% serum with 20 mM Tris HCl.	139
Figure 3.45: Fluorescence intensities extracted at 383 nm (Top) and 495 nm (Bottom) for the titration of heparin into Py-D-Lys in 12.5% serum with 20 mM Tris HCl.....	140
Figure 3.46: The changes of the fluorescence intensity ratio of Py-L-Lys and Py-D-Lys ($\log(I_{495}/I_{383})$) plotted against increasing heparin concentration in 12.5% serum with 20 mM Tris HCl.	141
Figure 3.47: Fluorescence intensities extracted at 383 nm (Top) and 495 nm (Bottom) for the titration of heparin into Py-L-Lys in 100% serum.	142
Figure 3.48: Fluorescence intensities extracted at 383 nm (Top) and 495 nm (Bottom) for the titration of heparin into Py-D-Lys in 100% serum.	143
Figure 3.49: The changes of the fluorescence intensity ratio of Py-L-Lys and Py-D-Lys ($\log(I_{495}/I_{383})$) plotted against increasing heparin concentration in 100% serum.	144
Figure 3.50: Fluorescence intensities extracted at 383 nm and 495 nm for the titration of heparin into Py-L-Lys (426 μ M) in buffer.....	145
Figure 3.51: Fluorescence intensities extracted at 383 nm and 495 nm for the titration of heparin into Py-D-Lys (426 μ M) in buffer.....	146
Figure 3.52: The changes of the fluorescence intensity ratio of PyL-Lys and Py-D-Lys ($\log(I_{495}/I_{383})$) plotted against increasing heparin concentration in buffer.....	147
Figure 3.53: Fluorescence intensities extracted at 383 nm (Top) and 495 nm (Bottom) for the titration of heparin into Py-L-Lys in 12.5% serum with 20 mM Tris HCl.	148
Figure 3.54: Fluorescence intensities extracted at 383 nm (Top) and 495 nm (Bottom) for the titration of heparin into Py-D-Lys in 12.5% serum with 20 mM Tris HCl.....	149
Figure 3.55: The changes of the fluorescence intensity ratio of Py-L-Lys and Py-D-Lys (426 μ M) ($\log(I_{495}/I_{383})$) plotted against increasing heparin concentration in 12.5% serum with 20 mM Tris HCl.	150
Figure 3.56: Fluorescence intensities extracted at 383 nm (Top) and 495 nm (Bottom) for the titration of heparin into Py-L-Lys (426 μ M) in 100% serum.....	151
Figure 3.57: Fluorescence intensities extracted at 383 nm (Top) and 495 nm (Bottom) for the titration of heparin into Py-D-Lys (426 μ M) in 100% serum.	152
Figure 3.58: The changes of the fluorescence intensity ratio of Py-G1 (213 μ M) and	

Py-DAPMA (426 μ M) ($\log(I_{495}/I_{383})$) plotted against increasing heparin concentration in 100% serum.....	153
Figure 4.1: Synthetic scheme for Mal-B (MalB, 1) along with the UV-visible absorption band at 615 nm (25 μ M, photo) before (solid line) and after (dashed line) binding to heparin. ⁸⁰	52
Figure 4.2: (Top) ¹ H-NMR spectra acquired at 800 MHz and assignment of heparin: a, H1 GlcNS, GlcNS6S; b, H1 IdoA2S; c, H1 IdoA; d, H5 IdoA2S; e, H1 GlcA; f, H6 GlcNS6S; g, H2 IdoA2S; h, H6' GlcNS6S; i, H3 IdoA2S; j, H4 IdoA2S; k, H5 GlcNS6S; l, H6 GlcNS; m, H4 GlcNS6S; n, H3 GlcNS, GlcNS6S; o, H2 GlcA; p, H2 GlcNS6S; q, acetyl CH ₃ . ¹⁷³ (bottom) Structures of the common disaccharide pairs in the heparin chains and assignment. 157	157
Figure 4.3: Plot of the anomeric region (4.4 to 6.1 ppm proton (f2) and 90 to 110 carbon ppm (f1)) the 2D ¹ H- ¹³ C HSQC spectrum obtained on a 50 mg sample of sodiated heparin in 700 μ L of D ₂ O. ¹⁷⁴	158
Figure 4.4: Equilibrated MD snapshot of the Mal-B-heparin system. Mal-B, rosy brown sticks; heparin (D-glucosamine units), dark magenta spheres; and CPK (L-iduronic acid units), chartreuse spheres. Some Cl ⁻ and Na ⁺ ions are shown as large and small white spheres, respectively. Water omitted for clarity. ⁸⁰	159
Figure 4.5: (Top) Structure of G5 PAMAM dendrimer (Bottom) ¹ H NMR titration spectra of G5 dendrimer with heparin. The G5 dendrimer concentration in the samples is fixed at a concentration of 2 mg/mL. The molar ratios of heparin/G5 dendrimer in (1-8) are 0, 1, 2, 4, 8, 10, 15, and 20, respectively. ¹⁷⁹	160
Figure 4.6: ¹ H NMR spectrum of heparin in D ₂ O.....	162
Figure 4.7: ¹ H NMR spectrum of Mal-B in D ₂ O.	163
Figure 4.8: HSQC NMR spectrum of heparin in D ₂ O	164
Figure 4.9: Plot of aliphatic region (3.0 to 5.0 ppm proton (f2) and 50 to 90 ppm	164
Figure 4.10: Plot of anomeric region (4.0 to 6.0 ppm proton (f2) and 90 to 110 ppm carbon (f1)). Selected signals are labeled based on the assignments of Keire <i>et al.</i> ¹⁷²	165
Figure 4.11: HSQC NMR spectrum of Mal-B in D ₂ O	166
Figure 4.12: ¹ H NMR spectrum of low concentration of Mal-B in D ₂ O.....	167
Figure 4.13: Expansion of the 6.0-9.0 ppm region of the of low concentration of Mal-B in D ₂ O.	167

Figure 4.14: Expansion of the 6.0-9.0 ppm region of the of low concentration of Mal-B in D ₂ O at 50 °C overnight.	168
Figure 4.15: Expansion of the 6.0-9.0 ppm region of the of Mal-B with heparin in D ₂ O.	169
Figure 4.16: Expansion of the 6.0-9.5 ppm region of the of Mal-B (40 μM) in Tris HCl ,10 mM, pH 7, 150 nM NaCl, D ₂ O.....	170
Figure 4.17: Expansion of the 6.0-8.5 ppm region of the of Mal-B in phosphate,10 mM, pH 7, 150 nM NaCl, D ₂ O.	171
Figure 4.18: UV absorbance of Mal-B with increasing heparin concentration in Tris HCl ,10 mM, pH 7, 150 nM NaCl,	172
Figure 4.19: UV absorbance of Mal-B with increasing heparin concentration in phosphate ,10 mM, pH 7, 150 nM NaCl,.....	172
Figure 4.20: Normalised absorbance of Mal-B vs heparin concentration in different buffer systems at max absorbance 615 nm.	173
Figure 4.21: UV absorbance of Mal-B in different ratio of buffer (1:0 to 0:1 phosphate : Tris HCl)	174
Figure 4.22: UV absorbance of Mal-B with heparin in different ratio of buffer (1:0 to 0:1 phosphate : Tris HCl)	175
Figure 4.23: ¹ H NMR spectra of Mal-B (200 μM) with increasing heparin concentration (1:0 to 1:1).....	176
Figure 4.24: Photo of NMR tubes of Mal-B with increasing of heparin concentration	176
Figure 4.25: Structure of self-assembled multivalent (SAMul) heparin binders.	178
Figure 4.26: ¹ H NMR spectra of C ₁₆ -DAPMA with increase heparin concentration (1:0 to 1:1)	180
Figure 4.27: Photo of NMR tubes of C ₁₆ -DAPMA with increase of heparin concentration (1:0 to 1:1).....	181
Figure 4.28: ¹ H NMR spectra of C ₁₆ -DAPMA with increase of heparin concentration from 0 to 3.5 ppm.	182
Figure 4.29: ¹ H NMR spectra of heparin with increase of C ₁₆ -DAPMA concentration (1:0 to 1:1).....	183
Figure 4.30: ¹ H NMR spectra of heparin with increase of C ₁₆ -DAPMA concentration	

from 4.7 to 5.7 ppm	184
Figure 4.31: ^1H NMR spectra of heparin with increase of C_{16} -DAPMA concentration from 3.0 to 4.5 ppm	184
Figure 4.32: ^1H NMR spectra of C_{16} -Spermidine with increase of heparin concentration (1:0 to 1:1).....	186
Figure 4.33: ^1H NMR spectra of C_{16} -Spermidine with increase of heparin concentration (1:0 to 1:1) from 0 to 3.5 ppm.....	187
Figure 4.34: ^1H NMR spectra of heparin with increase of C_{16} -Spermidine concentration (1:0 to 1:1).....	188
Figure 4.35: ^1H NMR spectra of heparin with increase of C_{16} -SPERMIDINE concentration from 4.7 to 5.7 ppm.....	188
Figure 4.36: ^1H NMR spectra of heparin with increase of C_{16} -Spermidine concentration from 3.0 to 4.5 ppm	189
Figure 4.37: ^1H NMR spectra of C_{16} -Spermine with increase of heparin concentration (1:0 to 1:1).....	190
Figure 4.38: ^1H NMR spectra of C_{16} -Spermine with increase of heparin concentration (1:0 to 1:1) from 0 to 3.5 ppm.....	191
Figure 4.39: ^1H NMR spectra of heparin with increase of C_{16} -Spermine concentration (1:0 to 1:1).....	192
Figure 4.40: ^1H NMR spectra of heparin with increase of C_{16} -Spermine concentration from 4.7 to 5.7 ppm	193
Figure 4.41: ^1H NMR spectra of heparin with increase of C_{16} -Spermine concentration from 3.0 to 4.5 ppm	193
Figure 4.42: ^1H NMR spectra (700 MHz) of heparin with increase of C_{16} -DAPMA concentration (1:0 to 1:1)	195
Figure 4.43: ^1H NMR spectra (700 MHz) of heparin with increase of C_{16} -DAPMA concentration from 4.7 to 5.7 ppm.....	195
Figure 4.44: ^1H NMR spectra (700 Mhz) of heparin with increase of C_{16} -DAPMA concentration from 4.5 to 3.0 ppm.....	196
Figure 5.1: Single-wall carbon nanotube.	199
Figure 5.2: (A) CNT treated with acid to cut them and form carboxylic groups at the tips	

and the sidewalls. (B) CNT undergoing 1,3 dipolar cycloaddition by reacting an α -amino acid derivative with para-formalaldehyde. R = CH₃O(CH₂CH₂O)₂CH₂CH₂.¹⁹¹200

Figure 5.3: 1-Pyrenebutanoic acid, succinimidyl ester irreversibly adsorbing onto the sidewall of a SWCNT via π - π stacking.¹⁹²201

Figure 5.4: Non-covalent modification of MWCNT inducing water solubility.¹⁹³202

Figure 5.5: Schematic illustration of the interaction between a linear-dendritic hybrid polymer (second generation dendron) and a SWNT.¹⁹⁴202

Figure 5.6: Overview of functionalization of carbon nanotubes (CNTs) using different molecules and their biomedical applications. Figure adapted from Ref¹⁹⁵.204

Figure 5.7: Pathways for the penetration of CNTs into the cell. (a) Non-receptor mediated endocytosis: (1) membrane that surrounds the drug loaded functionalized CNTs, (2) internalization of drug loaded CNTs, and (3) release of drug; (b) receptor mediated endocytosis: (4) membrane surrounds the CNT-receptor conjugate by forming endosomes followed by internalization, (5) release of drug, and (6, 7, 8) regeneration of receptor; (c) endocytosis independent pathway: (9) direct penetration of drug loaded functionalized CNT and (10) release of the drug.¹⁹⁶205

Figure 5.8: Azomethineylides functionalized carbon nanotube.206

Figure 5.9: Schematic drawing of dendrons as a "nanoglue" that glue two different nanoscale building blocks together such as double helical DNA and a carbon nanotube.208

Figure 5.10: HMBC correlations observed for proton at 5.20 ppm in compound **10** in CDCl₃.....210

Figure 5.11: Fluorescence intensity of Nile Red in the presence of increasing amounts of C₂₂-G1 in SHE Buffer212

Figure 5.12: Fluorescence intensity at 495 nm of Py-G1 in the presence of increasing amounts of Py-G1 in SHE Buffer (0.01 M).213

Figure 5.13: Charge ratio vs. normalised fluorescence from the EthBr displacement assay used to determine CE₅₀ values for C₂₂-G1 and Py-G1.....214

Figure 5.14: Dendrons investigated by Barnard *et al.*²⁰⁷215

Figure 5.15: UV Absorbance at 400 nm vs time sonicated for SWCNT with/without C₂₂-G1 in H₂O.....216

Figure 5.16: Difference in Absorbance of SWCNT in H ₂ O before and after adding C ₂₂ -G1 vs [C ₂₂ -G1] at 2000 RPM.....	217
Figure 5.17: Difference in Absorbance of SWCNT in H ₂ O before and after adding C ₂₂ -G1 vs [C ₂₂ -G1] at 3000 RPM.....	218
Figure 5.18: Difference in Absorbance of SWCNT in H ₂ O before and after adding C ₂₂ -G1 vs [C ₂₂ -G1] at 4000 RPM.....	218
Figure 5.19: Difference in absorbance at 400 nm of SWCNT in SHE buffer before and after adding binder and centrifugation.....	219
Figure 5.20: TEM image of (left) C ₂₂ -G1 and (right) CNT (100nm).....	222
Figure 5.21: TEM of C ₂₂ -G1 with DNA (100 nm).....	222
Figure 5.22: TEM of C ₂₂ -G1 with heparin. ⁹²	222
Figure 5.23: Atomistic models of self-assembled C ₂₂ -G1 is shown as teal sticks, with heparin is in dark olive green (L-iduronic acid) and light green (D-glucosamine) spheres. Water molecules are omitted for clarity while some Na ⁺ and Cl ⁻ ions are shown as orange and grey spheres, respectively. ⁴³	223
Figure 5.24: TEM image of C ₂₂ -G1 with CNT (100nm)	224
Figure 5.25: TEM image of C ₂₂ -G1 + CNT + DNA (100 nm).....	224
Figure 5.26: TEM image of C ₂₂ -G1 with CNT after filtration (100nm).....	225
Figure 5.27: TEM image of C ₂₂ -G1 + CNT + DNA after filtration (100 nm).....	226
Figure 5.28: TEM image of Py-G1 with DNA (100 nm).....	227
Figure 5.29: TEM image of Py-G1 with CNT after filtration (100nm).....	227
Figure 5.30: TEM image of Py-G1 + CNT + DNA after filtration (100 nm).....	228

List of Tables

Table 2.1: DLS data for Py-G1 and Py-DAPMA.	71
Table 2.2: DLS data for Py-L-Lys and Py-D-Lys.	133
Table 3.1: DLS data for C ₁₆ -L-Lys and C ₁₆ -D-Lys.	114
Table 3.2: DLS data for C ₁₆ -Gly-L-Lys and C ₁₆ -Gly-D-Lys.	125
Table 3.3: List of SAMul polyanion binder.	154
Table 4.1 Summary of the binding parameters for heparin binding for SAMul heparin binder	179
Table 5.1: Fluorescence intensity recorded at 590 nm.	221

List of Schemes

Scheme 2.1: Structure of ratiometric fluorescence sensor and the schematic illustration of heparin detection developed by Dai <i>et al.</i> ⁹⁰	57
Scheme 2.2: Synthesis of alkyne-functionalised dendron, 7 , based on previously published method for C ₂₂ -G1. ⁹¹	61
Scheme 2.3: Synthesis route of azide-functionalised pyrene 10	62
Scheme 2.4: Synthesis route of 11	62
Scheme 2.5: Synthesis of Py-G1.	65
Scheme 2.6: Synthesis of Py-DAMPA	66
Scheme 3.1: Synthesis of Synthesis of C ₁₆ -L-Lys and C ₁₆ -D-Lys	109
Scheme 3.2: Synthesis of C ₁₆ -Gly-L-Lys and C ₁₆ -Gly-D-Lys	119
Scheme 3.3: Synthesis of Py-L-Lys and Py-D-Lys	130
Scheme 5.1: Synthesis of C ₂₂ -G1	209

Acknowledgements

My heartfelt gratitude goes to my supervisor Professor David Smith, who gave me the opportunity to work under his supervision and provided me with all the necessary guidance that I needed to complete this research.

I would like to thank past and present members of the DKS group with whom I have been performed research. In particular I must thank Dr Stephen Bromfield who mentored me when I started the research, guided me through the synthesis and shared ideas. Dr Babatunde Okesola who was not only a good friend and let me understand more about supramolecular gels.

I would also like to thank those who helped me with the technical aspects of my research: Heather Fish (NMR), Pedro Aguiar (NMR), Dr Karl Heaton (Mass spec), Dr Andrew Leach (CD), Meg Stark (SEM/TEM) and Loryn Fechner (SAMul Heparin binders).

Lastly I wish to thank my family for their endless support throughout the time that I have been in the United Kingdom.

Declaration

I declare that the work presented within this thesis is entirely my own, except where otherwise acknowledged. This work has not been submitted in part or fully for examination towards any other degrees or qualifications.

Chapter 1 Introduction

1.0 Overview

This thesis explores molecular recognitions processes at nanoscale surfaces and aims to understand them at a molecular level and then apply this understanding to achieve controlled adhesion between nanosystems. Each chapter has its own specific introduction, and as such, this general introduction aims to present area of the key over-arching concepts in outline form to inform more detailed discussion which comes later.

1.1 Supramolecular chemistry

Supramolecular chemistry was defined by Jean-Marie Lehn, who was awarded the Nobel Prize for his work in the area in 1987. He defined the field as the "chemistry of molecular assemblies and of the intermolecular bond"¹ and sometimes summarised as "chemistry beyond the molecule!"² In other words, supramolecular chemists aim to control and understand non-covalent interactions, and as a result, develop highly complex systems which are held together and organized by non-covalent intermolecular forces such as hydrogen bonds, π - π stacking interactions, electrostatic, van der Waals forces, metal-ligand bonds or hydrophobic effects (**Figure 1.1**).^{1, 3-5} The controllable nature of such interactions allows supramolecular chemists to manipulate molecules and the way they communicate with one another with a high degree of precision.

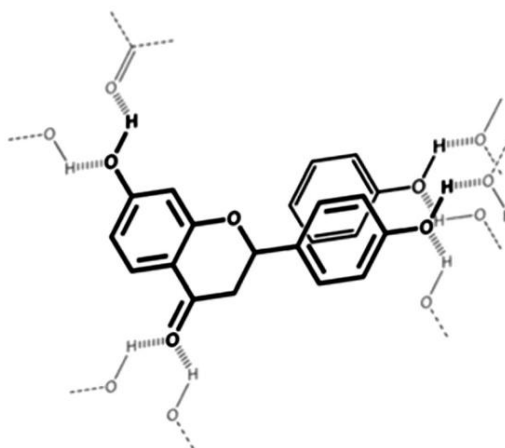


Figure 1.1 Example of non-covalent intermolecular forces: Schematic representation of the interactions between polarizable non-polar groups involving flavonoids through dispersive van der Waals interactions (π -stacking) and the role of the surrounding hydrogen-bond network.⁶

1.2 Self- Assembly

Self-assembly is the spontaneous association of molecules into well-defined structures held together by non-covalent interactions.⁷⁻⁹ While large molecules held together by covalent bonds normally need a number of synthetic steps, self-assembly often only requires smaller, simpler building blocks which can aggregate spontaneously to generate large nano-scale structures. This process is driven by directed non-covalent interactions between the molecules. As such, self-assembly provides a simple methodology by which molecular-scale building blocks can be used to assemble the nanoworld from “bottom-up” which opens a route to nanostructures that are currently inaccessible by the “top down” approach.^{10, 11}

1.2.1 Inspiration From Nature

DNA (Deoxyribonucleic acid), exists in double helical form,¹² and constitutes one of the best known self-assembling structures in biological systems. The two single strands are held together by hydrogen bonds between purine and pyrimidine bases. Guanine (G) forms triple hydrogen bonds with cytosine (C) and adenine (A) forms double hydrogen bonds with thymine (T). (**Figure 1.2**) The X-ray diffraction studies

revealed that the hydrogen bonds holding G-C and A-T complexes are about the same length ($2.9 \pm 0.1 \text{ \AA}$). The molecular-scale information programmed into the self-assembled double helix has the function of passing on hereditary information and the double helical structure plays a key role in helping protecting this vital information from damage by binding it within the interior of the nanostructure.

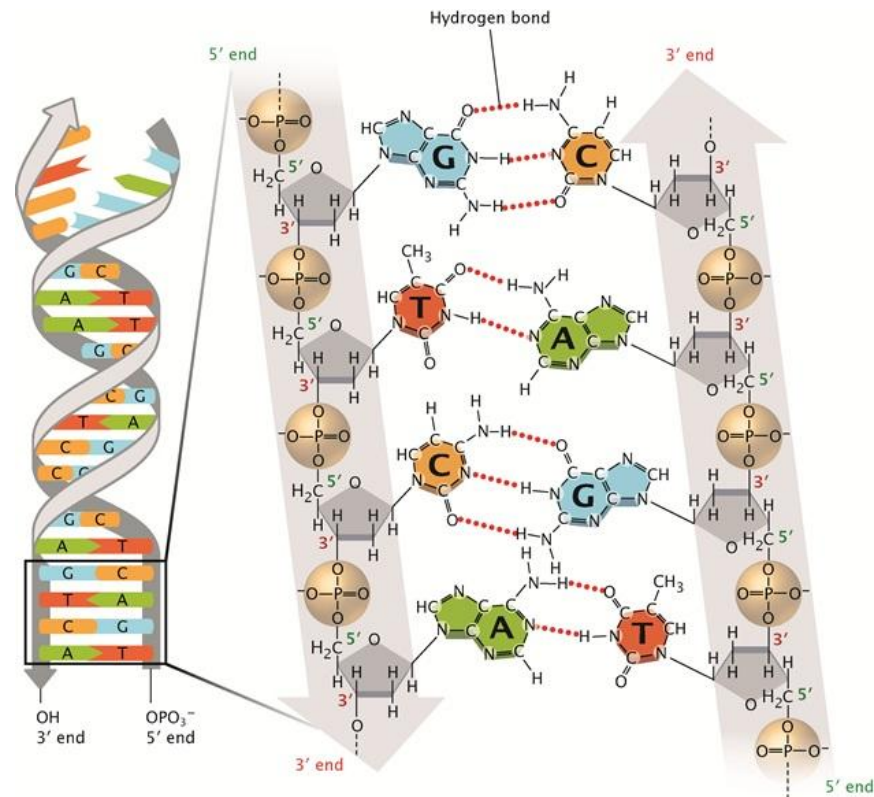


Figure 1.2: Complementary base pairing in DNA helical structure and base pairing in DNA (guanine and cytosine form triple hydrogen bonds; adenine and thymine form double hydrogen bonds).¹³

Another archetypal example of self-assembly is the tobacco mosaic virus (TMV) (**Figure 1.2**), the first virus discovered by Demetri Iwanowsky in 1892 and isolated by Wendell Stanley in 1935. The viral particle is composed of 2130 identical protein subunits, each comprising 158 amino acids, which form a helical sheath around a single strand of RNA with 6390 nucleotide bases in length which give a helical rod-shaped particle with dimensions of 300 nm in length and 18 nm in diameter.¹⁴

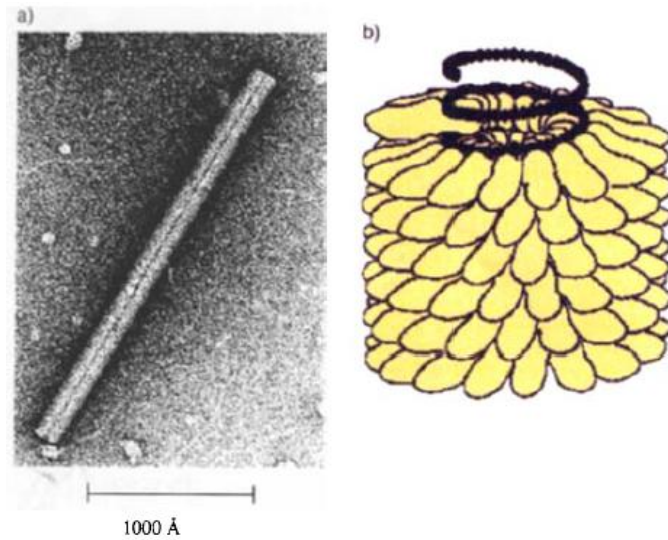


Figure 1.3: The tobacco mosaic virus (TMV). a) Electron micrograph. b) schematic representation. The protein subunits are colored yellow. (Taken from ref. ¹⁴)

As illustrated in **Figure 1.4**, the protein subunits form a stable doubly docked disk-shape sub-assembly (a), then a loop of RNA into the central hole of the protein disk opens up the base-paired stem as it does so (b) and is then transformed into a helical form (c). Additional protein disks, each corresponding to two turns of the final helix, associate with the growing viral particle (d) until assembly is complete. The formation of a doubly docked disk sub-assembly from protein subunits through noncovalent interactions is under thermodynamic control. This gives a low probability of generating a defect TMV structure by intrinsically error-checking and self-correcting.¹⁴ Remarkably, simply mixing together the individual compounds in solution leads to spontaneous self-assembly of the functional virus. This clearly demonstrates how self-assembly of non-functional compounds can give rise to overall assemblies with new emergent properties.¹⁵

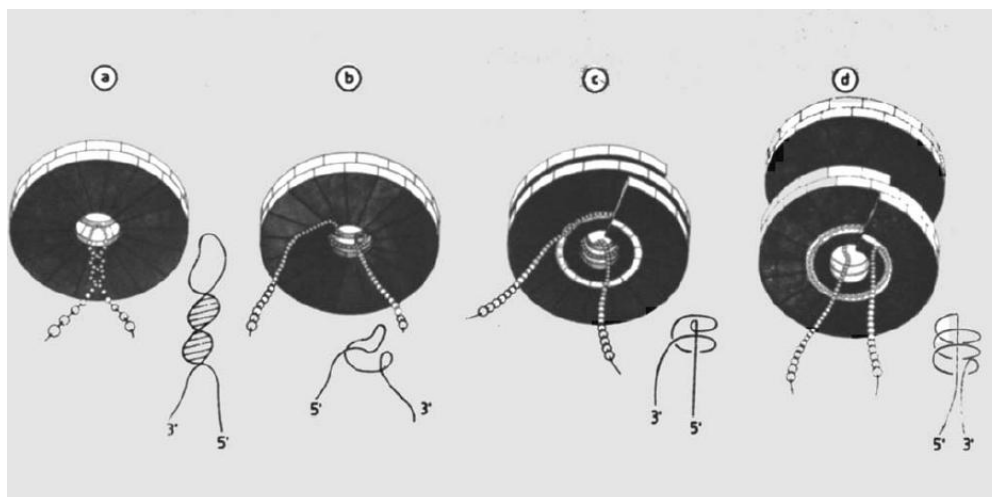


Figure 1.4: Self-assembly of the tobacco mosaic virus at different stages.¹⁰

1.2.2 Self-Assembly in Synthetic Chemistry

Inspired by nature, many examples of supramolecular assemblies have been reported involving hydrogen bonding,^{16, 17} π - π stacking,^{18, 19} charge transfer,^{20, 21} the hydrophobic effect,²² and chelation of metal cations.^{23, 24} This section will focus on describing selected recent advances in the area of self-assembly in supramolecular chemistry driven by π - π stacking and the hydrophobic effect which are important within the context of this thesis.

1.2.2.1 Self-Assembly by π - π stacking

π - π Stacking refers to non-covalent interactions between the π -orbitals of a unsaturated organic system (**Figure 1.5**).²⁵ The benzene dimer is the prototypical system for the study of π - π stacking, and is experimentally bound by 2–3 kcal/mol in the gas phase with a separation of 4.96 Å between the centers of mass for the T-shaped dimer. T-shaped (edge-to-face) is more stable than π - π stacking (face to face) due to high electrostatic repulsion of the electrons in the π orbitals.²⁶



Figure 1.5: Energy-minimized structures of the benzene dimer: a) T-shaped and b) π - π stacked.²⁵

As an example, crown ether phthalocyanine (**Figure 1.6**), contains a phthalocyanine ring with four benzo crown ether moieties attached. It can self-assemble into helix and superhelix forms based on the self-assembly of disk-shaped molecules driven by $\pi - \pi$ interactions. The helicity in these superstructures is controlled by chiral centers remote from the sites of interaction in the periplal chain and can be tuned by the addition of K^+ ions. The effects of this can be observed using transmission electron microscopy (TEM) (**Figure 1.7**).²⁷

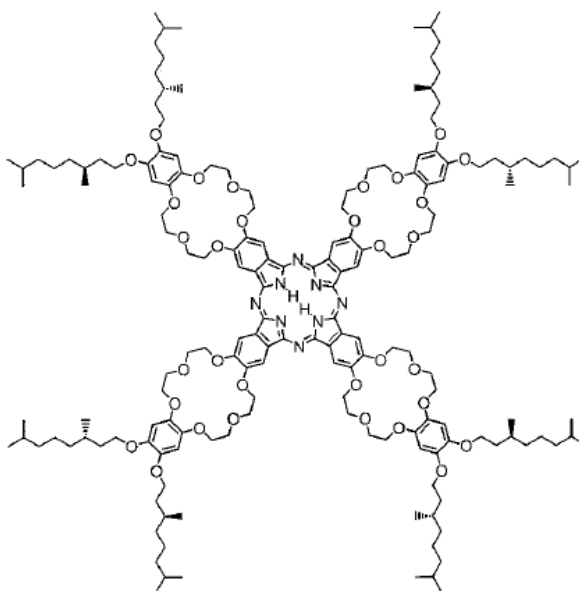


Figure 1.6: Structure of crown ether phthalocyanine²⁷

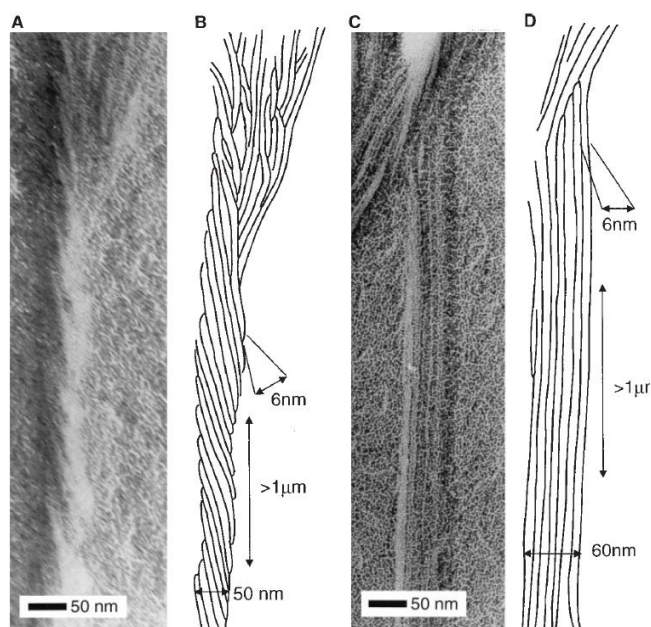


Figure 1.7: Transmission electron micrographs (platinum shadowing) of crown ether phthalocyanine. **(A)** Left-handed coiled-coil aggregates in chloroform. **(B)** Schematic representation of the helices in **(A)**. **(C)** Non-helical rods formed in chloroform in the presence of KCl. **(D)** Schematic representation of the rods in **(C)**.²⁷

Crown ethers can form stable complexes with alkali metal cations and a titration experiment of crown ether phthalocyanine with K^+ ions was performed. At low concentrations, K^+ ions are shared between two crown ether units of two different phthalocyanines. At higher concentration, the crown ethers start to take up one K^+ ion in each ring, which leads to separation of the sandwich-like complexes (Figure 1.8). In this way, complexation to the self-assembled nanostructures helps to control the evolution of the morphology.



Figure 1.8: Schematic representation of the formation and breakdown of the sandwich-type complexes between K^+ ions and crown ether phthalocyanine

1.2.2.2 Self-Assembly by hydrophobic effect

The hydrophobic effect is the phenomenon of non-polar substances to aggregate in aqueous solution and exclude water molecules.²⁸ The free energy to solvate small hydrophobic molecules scales linearly with solute volume, while that to solvate large hydrophobic species scales linearly with surface area. This process is driven by the entropic gain of releasing high energy water from hydrophobic sites. These water molecules can then also maximise their enthalpically favourable solvent-solvent hydrogen bond interactions.

A simple amphiphilic molecule will aggregate in aqueous solution, the driving force for which is the hydrophobic effect. The overall structure of the aggregates formed depends on a number of factors such as monomer concentration and morphology.²⁹ The hydrophobic group at the focal point controls the size of the nanoscale aggregate;³⁰ the ratio of sizes of hydrophobic and hydrophilic groups controls the resulting self-assembled morphology.³¹ Israelachvili *et al.* demonstrated how these relative sizes can affect surfactant self-assembly, and predicted the structure by using the so-called packing factor (p), $p = \frac{V}{a_0 l_c}$ where, V is the volume of the hydrophobic chain, a_0 is the mean cross sectional area of the head group in the aggregate and l_c is the length of the fully extended chain (**Figure 1.9**).^{32, 33} As the volume contribution of the hydrophobic region increases, the aggregate morphology in solution alters in order to provide greater internal volume and hence minimise unfavourable solvent interactions with the hydrophobic domain. These rules can be derived from simple geometric relationships, for example in spherical micelles the head groups cannot exceed the surface area of the sphere while the hydrophobic chains must fit within the volume of the sphere.

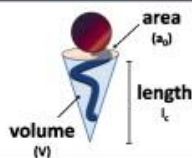


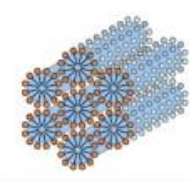



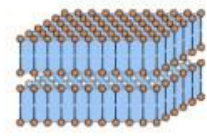


Aggregate type	Packing parameter	Surfactant geometry	Aggregate structure
Spherical Micelles	$\frac{V}{a_a l_c} < \frac{1}{3}$		
Cylindrical Micelles	$\frac{1}{3} < \frac{V}{a_a l_c} < \frac{1}{2}$		
Flexible Bilayers or Vesicles	$\frac{1}{2} < \frac{V}{a_a l_c} < 1$		
Planar Bilayers	$\frac{V}{a_a l_c} \sim 1$		
Inverted Micelles	$\frac{V}{a_a l_c} > 1$		

Figure 1.9: Structure of supramolecular aggregates according to the packing factor of amphiphiles.³⁴

Zhang *et al.*³⁵ have demonstrated the self-assembly behaviour of amphiphilic dendrimers dependent on both head-group and hydrophobic chain length. Short hydrophobic chains lead to irregular spherical micelles whereas long alkyl chains with a theoretical alkyl chain length/radius above 1 is conducive to forming regular vesicular structures (**Figure 1.10**).

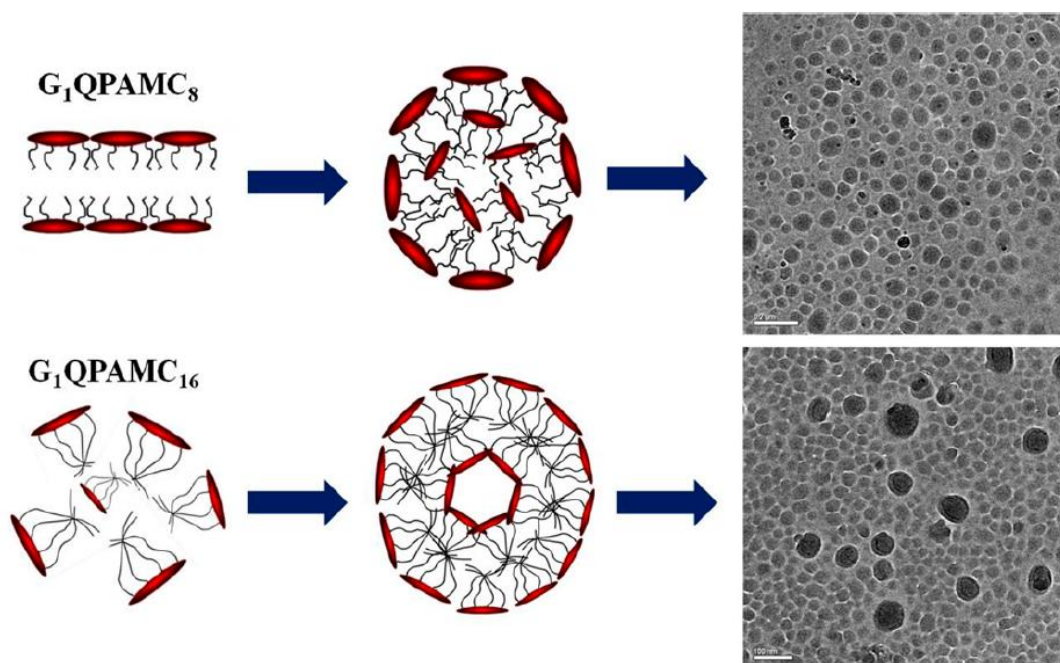


Figure 1.10 Schematic representation of the organization of amphiphilic dendrimers with different alkyl chain lengths in the process of self-assembly (Q_1QPAMC_8 = Generations 1 PAMAM with 8 carbon alkyl chain; Q_1QPAMC_{16} = Generations 1 PAMAM with 16 carbon alkyl chain).³⁵

Another example is from Percec's group with their self-assembly of the amphiphilic Janus dendrimers in 2014.³⁶ The group studied the effect of branching pattern in the hydrophilic part to the architectures assembled in water. They suggested that the (3,4,5)-hydrophilic pattern with three triethylene glycol monomethyl ether groups favors the formation of vesicles. When the hydrophilic part only had two triethylene glycol monomethyl ether groups in (3,4)- or (3,5)-hydrophilic patterns, the dendrimers did not self-assemble into vesicles apart from **10bd** (**Figure 1.11b**). If the hydrophilic part has the (3,4,5)-substitution pattern and the (3,4)-dodecyl substitution in their hydrophobic building block, the dendrimers self-assemble into vesicles (**Figure 1.11c**). The effect of the linking group between the two groups did not have effect on self-assembly. For example, both **9cf** (**Figure 1.11a**) and its constitutional isomers, **10cf**, form dendrimersomes (**Figure 1.11d**).

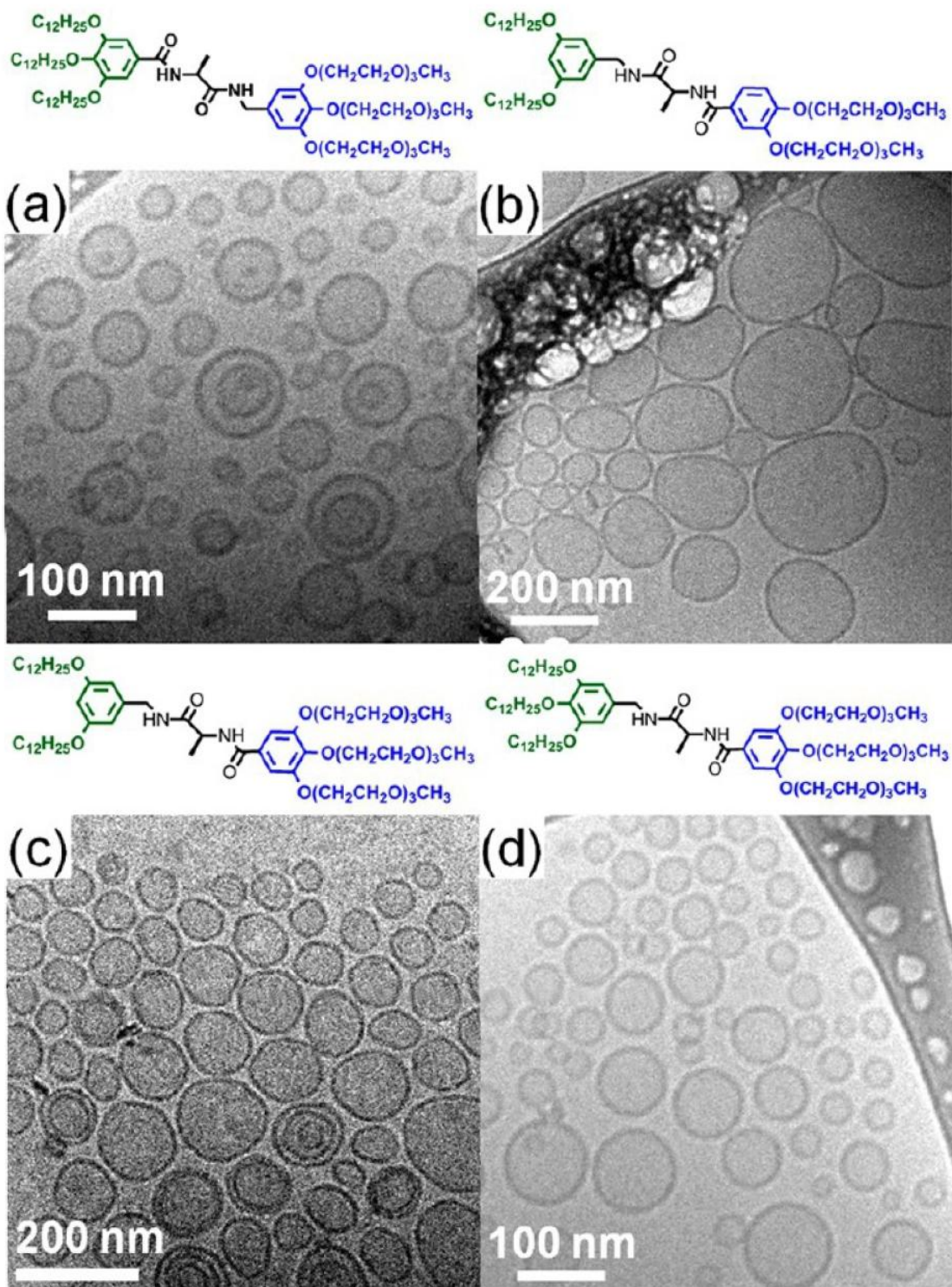


Figure 1.11: Cryo-TEM images of the structures assembled of (a) (3,4,5)12G1-L-Ala-CH₂-(3,4,5)-3EO-G1-(OCH₃)₃, **9cf**; (b) (3,5)12G1-CH₂-L-Ala-(3,4)-3EO-G1-(OCH₃)₂, **10bd**; (c) (3,5)12G1-L-CH₂-Ala-(3,4,5)-3EO-G1-(OCH₃)₃, **10bf**; (d) (3,4,5)12G1-L-Ala-CH₂-(3,4,5)-3EO-G1-(OCH₃)₃, **10cf**.³⁶

1.3 Multivalent binding

Multivalency is frequently used in biological systems to generate high affinity binding at nanoscale surfaces via simultaneous interaction of multiple binding groups on one molecule with the complementary receptors on another to achieve complexation in competitive media. This approach has been used extensively by supramolecular chemists, when binding to large biomolecules or attempting to achieve high affinity adhesion in solid surfaces.^{37, 38}

Multivalent ligand binding is related to the well-known "chelate effect" and can bring about high affinity binding through statistical rebinding, chelation, clustering, and subsite binding as depicted in **Figure 1.12**: (A) Statistical rebinding between a monomeric receptor and a tetravalent scaffolded ligand. High local concentration of ligand enables occupation of the receptor by another ligand upon dissociation. (B) Chelation achieved by bridging adjacent binding sites of a dimeric receptor with a divalent ligand. (C) Clustering of receptors via binding of a trivalent scaffolded ligand. (D) Subsite binding between a receptor with a secondary binding site and divalent molecule containing two discrete ligands.³⁹ In general thermodynamic terms multivalent binding is entropically preferred in comparison to monovalent ligands as a result of the pre-organisation of the ligand array and the enhanced local concentration.

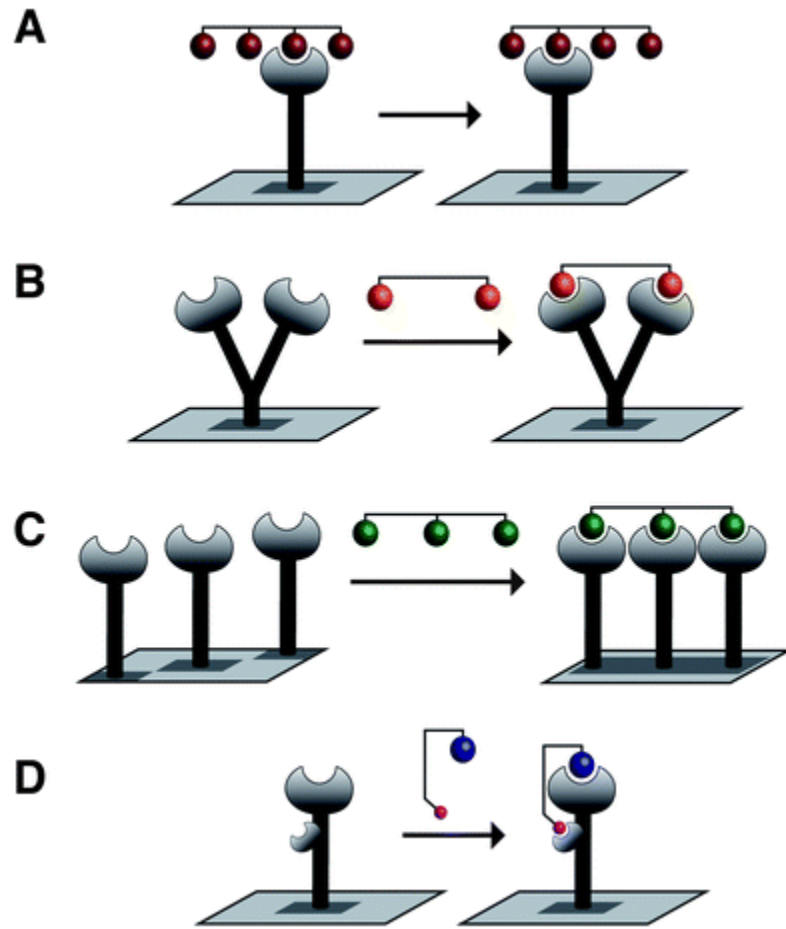


Figure 1.12: Specific modes of multivalent binding.³⁹

Rigid multivalent arrays benefit from the greatest pre-organisation with lower entropic cost upon binding. Conversely, flexible multivalent systems exhibit the ability to optimise each individual interaction in enthalpic term and screen themselves from the surrounding competitive medium.⁴⁰ As such, there are advantages and disadvantages of each approach. Whitesides *et al.* compared the free energy change of a multivalent interaction with a monovalent interaction in order to define a binding enhancement factor, α , described as the degree of cooperativity, Equation 1.1;⁴¹

$$\alpha = \frac{\Delta G_{\text{multi}}}{N\Delta G_{\text{mono}}} = \frac{\ln(K_{\text{multi}})}{\ln(K_{\text{mono}})^N} \quad \text{Equation 1.1}$$

where N is the number of ligand-receptor pairs, ΔG_{multi} is the free energy associated with the interaction between N receptors and N ligands, ΔG_{mono} is the free energy change from the corresponding monovalent interaction and K_{multi} and K_{mono} are the

affinities resulting from a multivalent and a monovalent binding event, respectively. This allowed multivalent systems to be categorized as cooperative (synergistic, $\alpha > 1$), non-cooperative (additive, $\alpha = 1$) or negatively cooperative (interfering, $\alpha < 1$).

It is worth noting that biological systems make use of multivalent binding interactions, particularly to enhance relatively weak binding interactions such as those formed by sugars. Glycoside clusters are extensively found on cell surfaces to mediate molecular recognition through multivalent binding interactions.⁴²

1.4. Self-Assembled Multivalency (SAMul)

The combined concept of self-assembly, the spontaneous association of molecules into well-defined structures held together by non-covalent interactions, and multivalency have been referred to as 'self-assembling multivalency' or 'SAMul' by Smith and co-workers.^{38, 43-45} The key advantages of this approach are spontaneous assembly, well-defined low-molecular-weight building blocks, easily tunable ligands, tunable nanostructure morphologies, ability to assemble different active components into a single nanostructure and simple or triggered disassembly/degradation (see **Figure 1.13**).³⁸ This approach is becoming a powerful and general tool for generating synthetic multivalent nanoscale binding arrays with biomolecular applications.⁴⁶

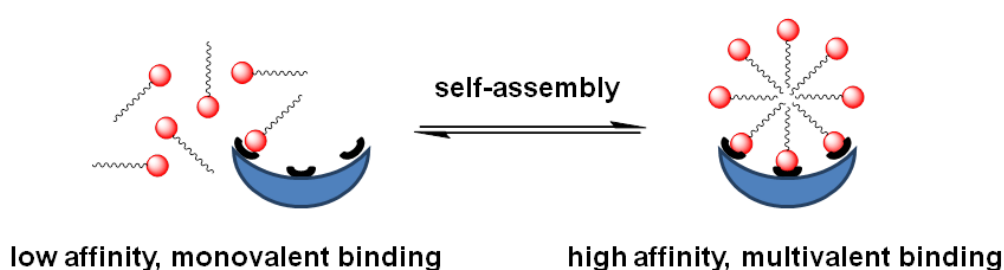


Figure 1.13: Self-assembled high affinity multivalent binding.³⁸

One of the first examples of SAMul was developed by Whitesides and co-workers, who attached a sialic acid (SA) group to a lipid chain and incorporated the resulting amphiphilic ligand into a phosphatidylcholine and cholesterol based liposome (**Figure**

1.14).⁴⁷ It was found that the self-assembled system was an extremely potent inhibitor of the protein hemagglutinin, with up to 100,000 times higher activity than the equivalent monovalent system.

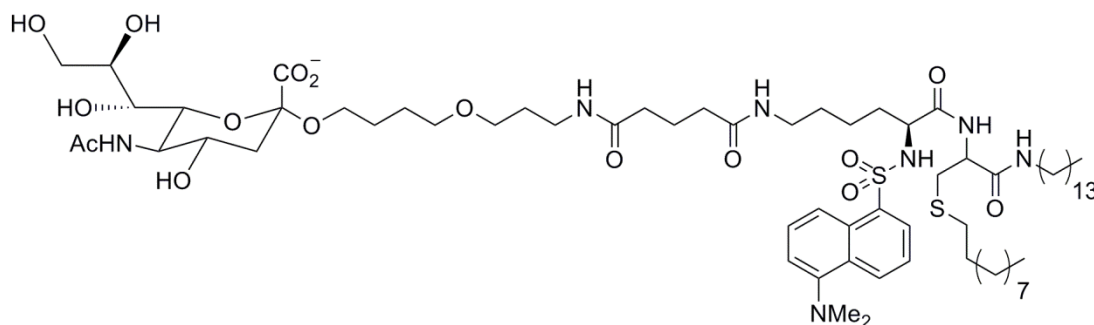


Figure 1.14: Structure of sialic acid functionalised lipid used as a SAMul inhibitor of hemagglutinin.⁴⁷

Brunsveld and co-workers used photo-active discotic molecules containing C_3 -symmetric aromatic cores consisting of three 2,2'-bipyridine-3,3'-diamine molecules connected to a central benzene-1,3,5-tricarbonyl unit which self-assembles into columnar stacks via $\pi - \pi$ stacking (**Figure 1.15**).⁴⁸ The surface ligands are tunable by controlling the ratio of mono-, di- and/or tri-functionalised discotics present within a 'mixed' columnar stack. With water-solubilizing glycol and mannose functionalization, the SAMul discotics become able to bind targets such as Con A with enhanced affinity over the non-assembled discotics. Additionally, Brunsveld and co-workers also studied the effect of mono- and tri-functionalisation of each monomer disk with mannose and discovered that the tri-functionalized derivative offered no valency-corrected binding enhancement over the mono-functionalized derivative. This suggested that "less is more", a feature observed in many multivalent binding events. Clearly optimizing ligand display plays an important role in mediating the SAMul binding effect.³¹

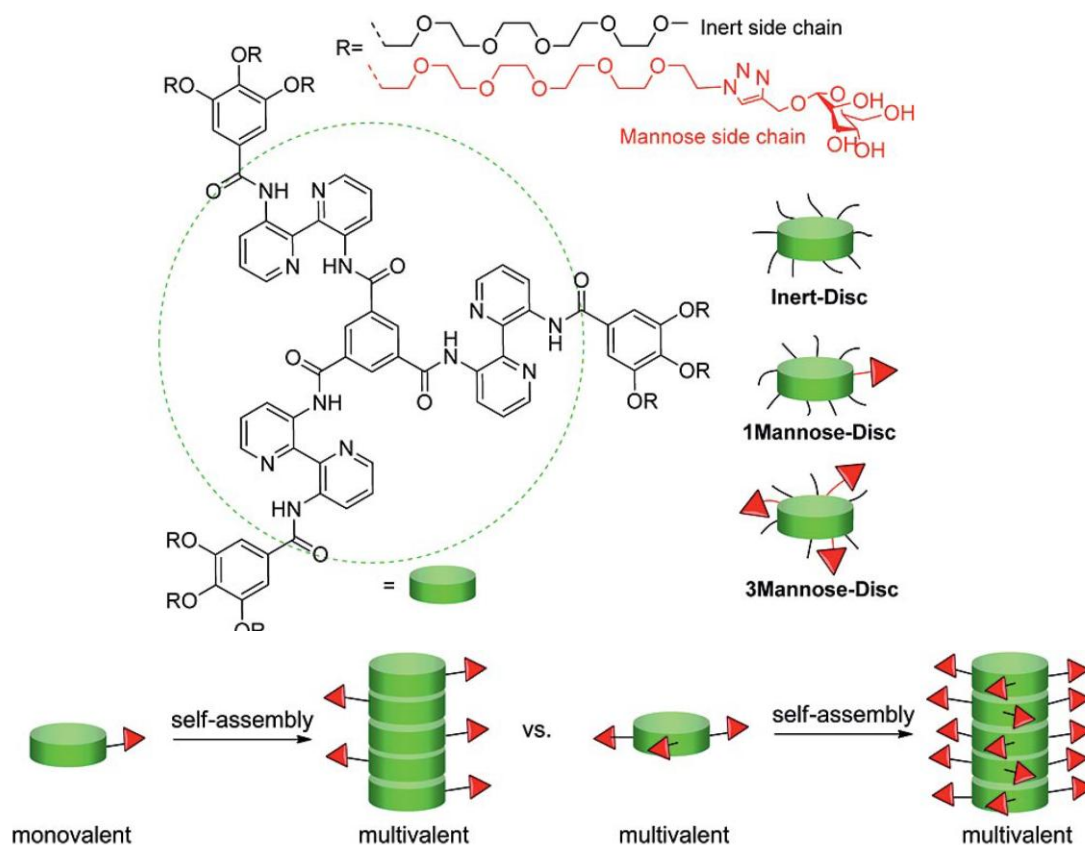


Figure 1.15: Self-assembling multivalent mannose-functionalised lectin-binding discotic molecules.⁴⁸

1.5 Project Aims

This thesis aims to use fundamental principles of supramolecular chemistry, such as those described in brief above, in order to understand and control the binding mode to different biological polyanions in order to achieve controlled nanoscale assembly. Polyanions make versatile targets for this study as a result of their potential biomedical and clinical applications, as described in more detail in the following chapters.

The initial goals of the research were to use simple binding of polyanions to develop innovative sensors while can self-assemble and bind in a multivalent manner to their targets. We aimed to explore and understand the way in which binding could be tuned and controlled using molecular-scale programming. For example, installing chiral information in the molecular-scale building blocks would allow us to explore how self-assembly displayed this information for polyanion binding. NMR methods would

enable us to gain a molecular scale insight into the binding interface. Bringing all this information together we then hoped to gain precise and controllable adhesion between different types of nanoscale surfaces.

Chapter 2 Pyrene-based heparin sensors in highly competitive aqueous solution and serum

Some of the results presented in this Chapter have been reported in C. W. Chan and D. K. Smith, *Chem. Commun.*, 2016, 52, 3785-3788.⁴⁹

2.1 Introduction

2.1.1 Heparin

Heparin is a highly sulfated polysaccharide, a member of the glycosaminoglycan (GAG) family and the most charge-dense polyanion present in biological systems, widely used as an anti-coagulant drug during surgical processes or administration in low doses to bed-bound patients to prevent thrombosis.⁵⁰ Structurally, heparin consists primarily of 1–4 linked L-iduronic acid and β -D-glucosamine subunits (**Figure 2.1**, bottom left), and the varying degrees of sulfation along these sugar components makes heparin the most complex member of the GAG family (**Figure 2.1**, Top).

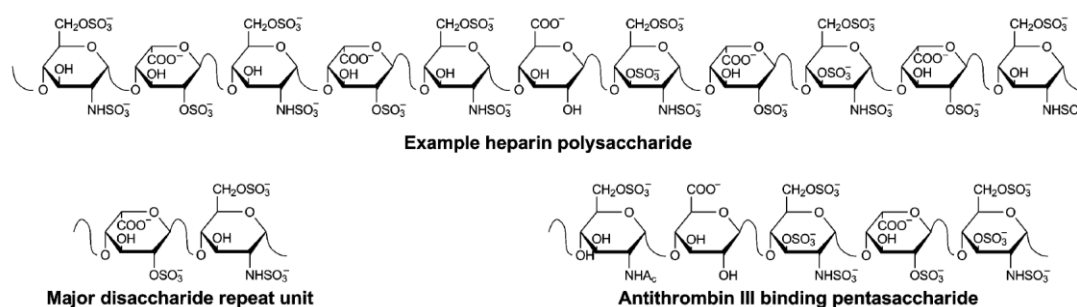


Figure 2.1: An example heparin polysaccharide (top) along with the predominant disaccharide repeat unit (bottom left) and the specific pentasaccharide sequence required to confer anticoagulant activity (bottom right).⁵¹

The anticoagulant activity of heparin is dependent on the presence of a specific pentasaccharide sequence (**Figure 2.1**, bottom right),⁵² which forms a ternary complex with thrombin and the naturally occurring thrombin inhibitor, antithrombin III (ATIII). In general, only approximately one third of the polysaccharide content in heparin displays anticoagulant activity.⁵³ As such, the concentration of heparin is not defined by mass

(based on the average reptile unit) in clinical use but rather in the measurement of “international units” (IU). The current international heparin standard (IHS) is calibrated by using all major assay methods to determine the amount of heparin required to cause one millilitre of sheep plasma to half-clot when held for one hour at 37°C.⁵⁴ Heparin is sold in terms of activity (IU) rather than mass, such as 100 kIU of heparin with a designated activity of 185 IU mg⁻¹.

The blood coagulation cascade *in vivo* starts with two distinct pathways (**Figure 2.2**).⁵⁵ The ‘intrinsic’ pathway originates from a surface contact trauma event while the ‘extrinsic’ pathway originates from tissue damage. Both pathways involve a plethora of clotting factors, distinguished by roman numerals, becoming activated or deactivated through interaction or reaction with each other, before converging and sharing the final few steps of the cascade to ultimately generate a fibrin-reinforced clot.⁵⁶ At the convergence of this ‘common’ pathway sits Factor-Xa, which plays a key role catalysing the production of thrombin, the species responsible for catalysing the production of the insoluble fibrin fibre and hence the final clot. It is the ability of heparin to directly inhibit the catalytic activity of thrombin, thereby retarding the production of fibrin, which primarily confers the anti-coagulant activity.⁵⁷

The three pathways that make up the classical blood coagulation pathway

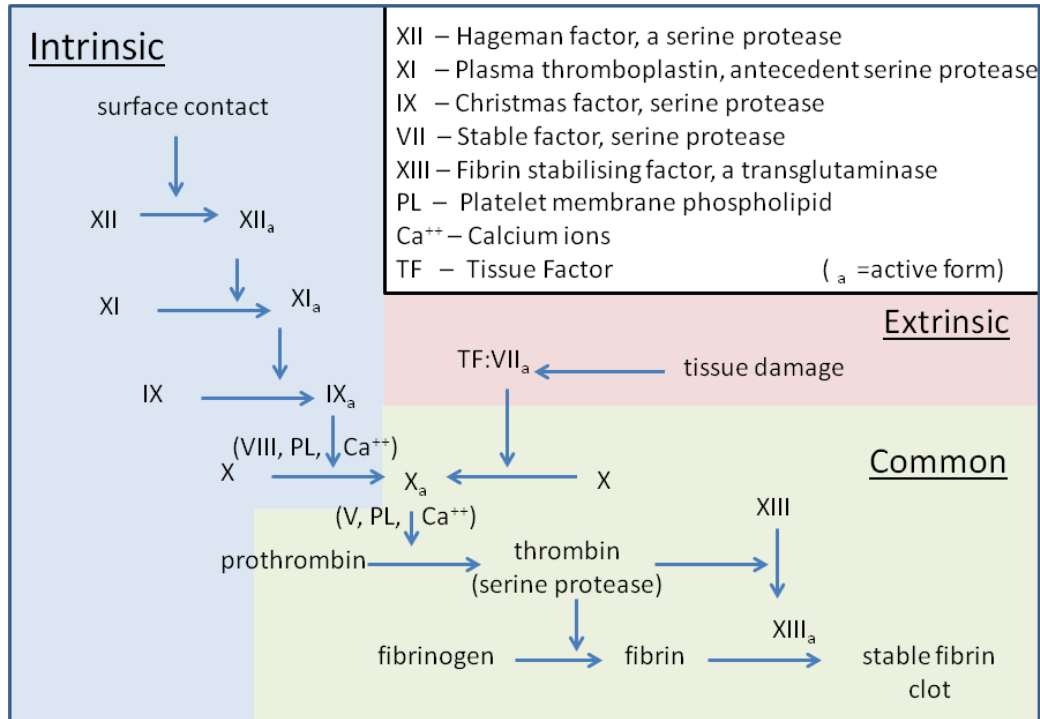


Figure 2.2: Schematic representation of the blood coagulation cascade.⁵⁵

Following the administration of heparin as an anticoagulant drug during surgery, there is a need to reverse its effects in order to allow the blood to regain its natural clotting ability. This is important to prevent patients from internal bleeding after surgical operations. Currently the only heparin reversal agent licensed for clinical use is protamine sulphate, which is constituted by a diverse family of small arginine-rich proteins, synthesised in the spermatids of many animals and plants (**Figure 2.3**). The primary role of naturally occurring protamines is to bind with polyanionic DNA.⁵⁸ However, the large number of arginine residues present in the primary structure of protamines in high density makes them highly cationic⁵⁹ and thus able to also bind electrostatically to negatively charged heparin in order to reverse its anticoagulant activity.⁶⁰



Figure 2.3: An example protamine structure with the prevalent arginine residues depicted as wedges, adapted from reference⁴³.

On the other hand, protamines are known to have adverse effect in patients which vary from urticaria and rash to systemic hypotension, bronchospasm, pulmonary hypertension, cardiovascular collapse, and death.^{61, 62} Overdose of protamine sulfate may cause bleeding as protamine has a weak anticoagulant effect of its own due to an interaction with platelets, and with many proteins including fibrinogen. Hence, it is important to have effective knowledge of heparin levels *in vivo*.

Heparin determination is also of crucial importance during surgery itself due to the risk of adverse effects such as hemorrhages and heparin-induced thrombocytopenia (HIT) resulting from heparin overdoses.^{63, 64} Various assays have been established to monitor heparin concentration, including the most commonly used activated partial thromboplastin time (aPTT), anti-Xa and activated clotting time (ACT) assays.⁶⁵ All of these assays determine the amount of heparin present in terms of its activity as they directly monitor its impact on the coagulation cascade. However, the aPTT assay is poorly standardized and is affected by numerous factors, anti-Xa is not widely available⁶⁶ and the ACT test is non-specific such that many variables can alter its results.⁶⁷ Furthermore, all of these tests require blood samples to be sent to the laboratory for “off-line” testing. Therefore, it is of great interest to monitor heparin binding spectroscopically and develop sensors with potential for development of “in-line” sensing and monitoring during major surgery.

2.1.2 Heparin Sensors

2.1.2.1 Electrochemical Sensors

The binding mode of protamine with heparin is mainly by electrostatic interaction (**Figure 2.4**). As such, protamine will not select between the regions of the heparin polysaccharide chain which are active or inactive in terms of their anti-coagulant behaviour. It would therefore be interesting to develop sensors which bind in the same way and can hence effectively predict the optimal protamine dose.

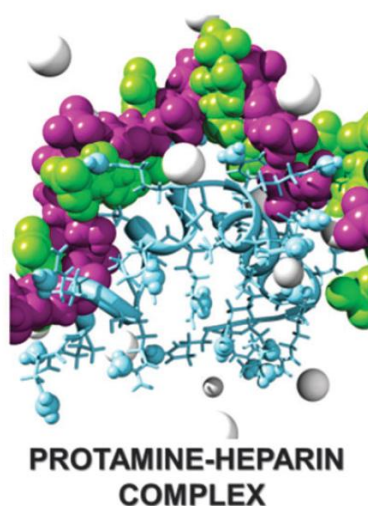


Figure 2.4: Computer model of protamine (blue) bound to the major disaccharide repeat unit of heparin (alternating purple and green units represent the two different saccharides).⁵¹

In 1993, Ma *et al.* developed a potentiometric sensor for heparin. Their system incorporating cationic units into PVC membranes and films which were able to obtain a quantitative heparin binding response even when using relatively non-functional quaternary ammonium groups as the cationic species within the membrane (**Figure 2.5**).⁶⁸ On the other hand, this methodology has a limitation of the irreversibility of heparin binding to the membranes and required a rinsing step between each heparin assay. Various groups have reported electrochemical and voltammetric techniques based on this general approach and in some case the detection limits were as low as 0.005 IU mL⁻¹.⁶⁹⁻⁷¹

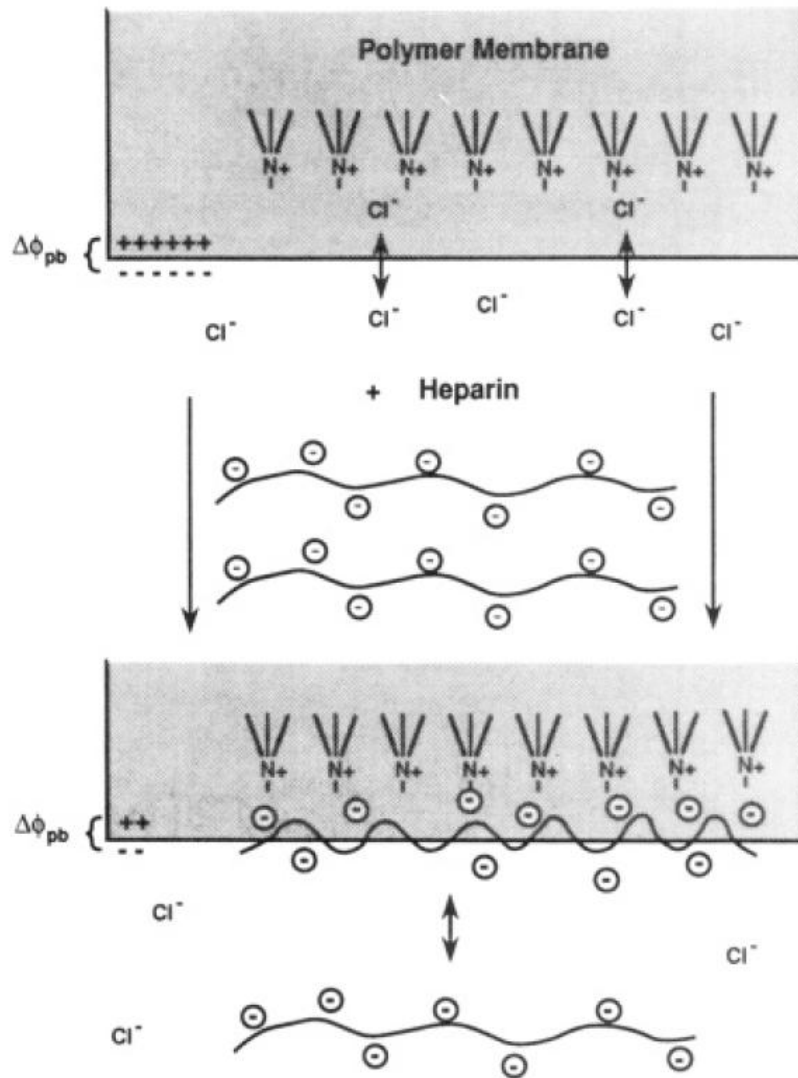


Figure 2.5 : Schematic representation of heparin binding to Ma's quaternary amine functionalized membrane, adapted from reference⁶⁸.

2.1.2.2 Fluorescent Sensors

Spectrophotometric or fluorescent heparin sensors are of particular interest as these methods can give simple read-out of heparin levels as well as potentially being optimized to respond to heparin only, rather than other competitor anionic species. Thionine dyes (**Figure 2.6**) were amongst the first to be investigated and have been used commercially as dyes during the twentieth century. Their unreliable purity⁷² meant that they require purification before using them.⁷³ Thionine dyes have previously been investigated in systems to bind biological polyanions such as DNA.⁷⁴

Azure A was reported to be able to monitor heparin levels in plasma.⁷⁵ However, it was also known to be acutely sensitive to many of the electrolytes present in biological samples as a consequence of the relatively low charge of the dye and it is unable to compete against media of high ionic strength for heparin binding.⁷⁶ As such, it does not work in biologically or medically relevant conditions.

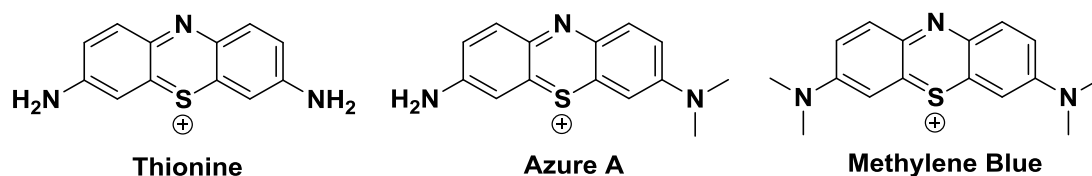


Figure 2.6: Selection of dyes from the thionine family

The unreliability of commercially available thionine-derived dyes led to interest in the design and development of synthetic systems for heparin sensing. In 2002, Zhong *et al.* produced a tris-boronic acid species able to indicate heparin indirectly through displacement of a more weakly-bond pyrocatechol violet indicator dye (**Figure 2.7**).⁷⁷ The system binds heparin as a result of electrostatic interaction and binding between the boronic acid units and diols on the heparin backbone. The system shows good affinity and selectivity for heparin over similar polysaccharides possessing lower anionic charge density and the authors suggested disaccharidic units are the likely sites for binding to the receptor.

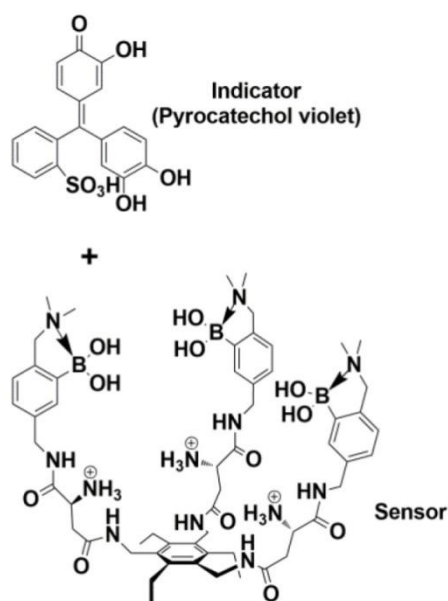


Figure 2.7: Zhong's heparin sensors operating in an indicator displacement regime.

However, the binding affinity of Zhong's heparin sensors was insufficient to allow quantification of heparin in serum at physiologically-relevant concentrations. Moreover, although the indicator-displacement assay gave a dramatic yellow to purple color change in response to heparin, it was found that the indicator also bound non-specifically with proteins in crude serum which undermined the quantitative results. To solve these problems, in 2005, the same group reported a related receptor with a fluorescent core scaffold functionalised with 1,3,5- triphenylethynylbenzene, modified with positively charged ammonium groups for electrostatic heparin binding and boronic acids which have high affinity for sugar moieties.⁷⁸ This did not require any indicator for sensing as a result of its built-in fluorescence (See **Figure 2.8**). Upon addition of heparin to the receptor the fluorescence emission was quenched, an effect which was then fully reversed by the addition of protamine. Importantly, this detection method was found to work in both human and equine serum making this system potentially applicable as a diagnostic tool for monitoring heparin concentrations in the clinic.

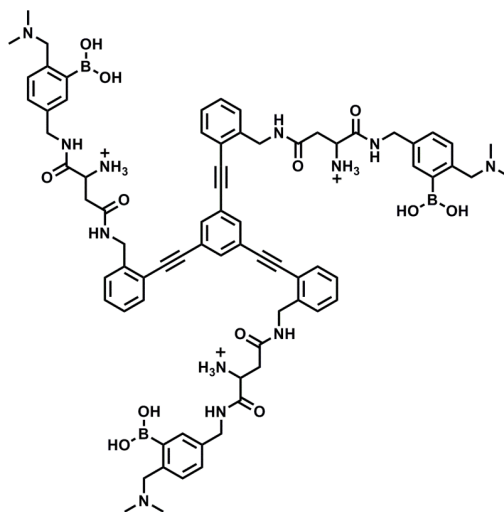


Figure 2.8: Structure of the tripodal ammonium and boronic acid functionalised heparin receptor.⁷⁸

In 2007, Wang and Chang discovered two benzimidazolium dyes (Heparin Orange and Heparin Blue, See **Figure 2.9**) using a diversity oriented fluorescence library approach.⁷⁹ Unlike the thionine dye family or Anslyn's heparin sensors which are

switch-off sensors, Heparin Orange and Heparin Blue are switch-on sensors (**Figure 2.10**). Compared with switch-off sensors, the spectroscopic signal increases from zero upon heparin binding. As such, switch-on sensors carry the advantage of even easier detection.

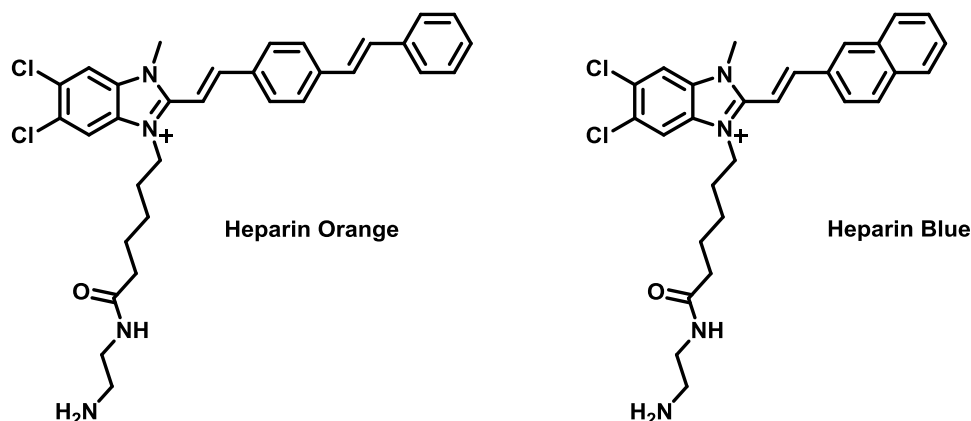


Figure 2.9 Structures of heparin chemosensors Heparin Orange and Heparin Blue.⁷⁹

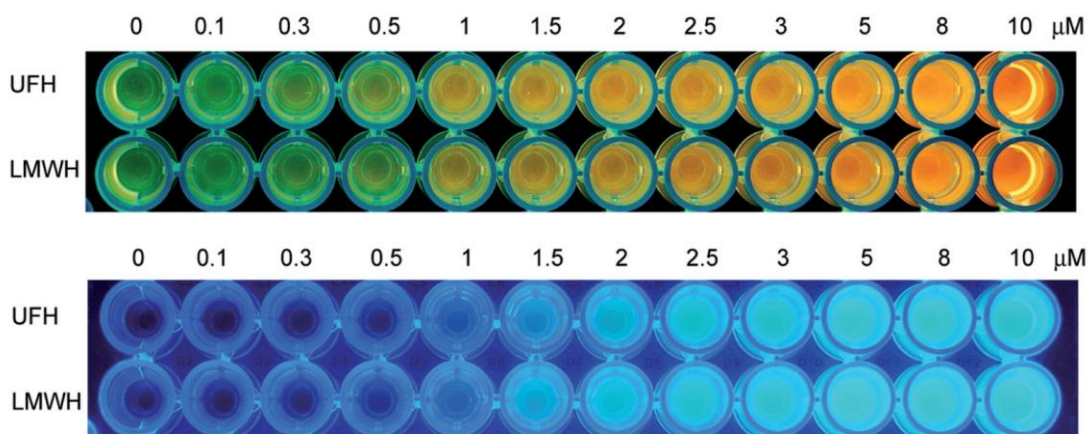
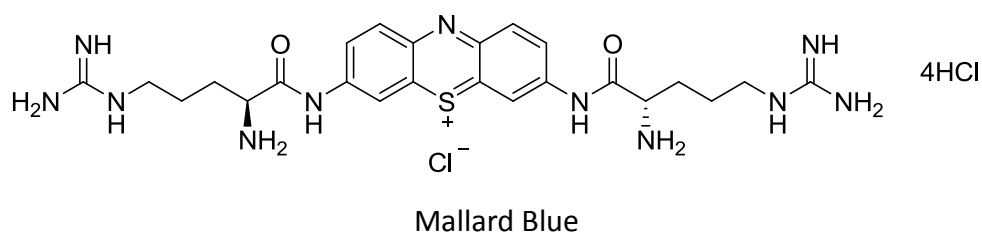


Figure 2.10: Heparin Orange (10 μM, Top) and Heparin Blue (10 μM, Bottom) with indicated concentrations of UFH and LMWH in 10 μM, HEPES buffer (pH = 7.4) in a 96-well plate under 365 nm UV lamp light.

Both fluorescent dyes were tested in various conditions (biological anionic analytes, proteins, pH differences) and high selectivity for heparin were confirmed with a detection range in HEPES buffer from 0.1 to 10 μM. Both dyes were able to respond to clinically relevant concentrations of heparin in the presence of 20% human plasma.

In 2013, Bromfield *et al.* reported the use of Mallard Blue (Mal-B), which is a

high-affinity selective heparin sensor that operates in highly competitive media.⁸⁰



Unlike most heparin sensors, Mal-B only required two synthetic steps from commercial starting materials with 29% overall yield (see **Figure 4.1**). The Mal-B - heparin interaction was reported to be highly tolerant of both electrolyte and buffer, as well as operating in human serum and horse serum. Moreover, it was reported that Mal-B can selectively bind with heparin over chondroitin sulfate and hyaluronic acid, which are potential glycosaminoglycan competitors for binding.

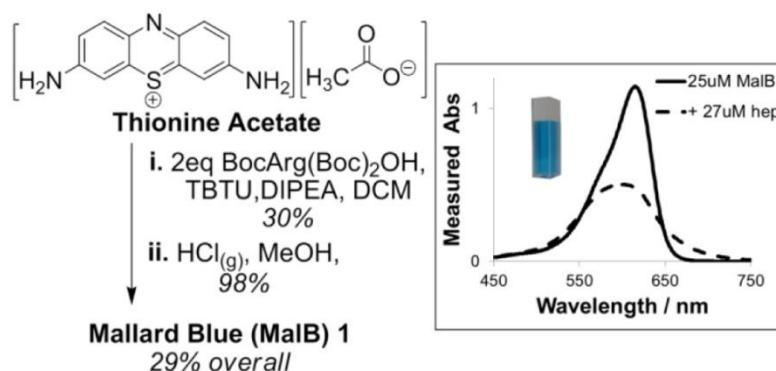


Figure 4.1: Synthetic scheme for Mal-B (MalB, 1) along with the UV-visible absorption band at 615 nm (25 μ M, photo) before (solid line) and after (dashed line) binding to heparin.⁸⁰

2.1.2.2 Nanoparticle Sensors

There is growing interest in using nanoparticle approaches, particularly gold nanoparticles (AuNPs), to heparin sensing. Li and Cao functionalized AuNPs with cationic cysteamine groups and were able to observe an absorbance change at 670 nm as the AuNPs aggregated along the heparin chain with a detection limit of 0.1 μ g mL⁻¹ in the presence of 1% human serum.⁸¹ Vasimalai and John reported a folic acid capped

gold nanoparticles (FA-AuNPs) as fluorophore for determination of protamine and heparin.⁸² The FA-AuNPs exhibit an emission maximum at 780 nm when excited at 510 nm. The emission intensity decreased at 780 nm upon the addition of protamine via electrostatic interaction and then increased upon the addition of heparin due to binding with heparin thus freeing up the FA-AuNPs. The lowest detection limits were found to be 4.8 ng mL⁻¹ for protamine and 12.6 ng mL⁻¹ for heparin in the presence of 1000-fold concentration of major interferences such as Na⁺, K⁺, Ca²⁺, etc. This system was tested with human blood serum and a good agreement was obtained between spiked and measured protamine and heparin samples. In other work, Fu *et al.* monitored the change in surface plasmon resonance signals as citrate-capped AuNPs aggregated on a graphene oxide (GO) surface, with protamine as a bridge between the GO and the AuNPs (**Figure 2.11**).⁸³ A blue-to-red' colour shift was observed upon the addition of heparin as protamine found preferential electrostatic interactions with it, which lead to AuNPs being deaggregated away from the GO surface. This system could detect heparin in fetal bovine serum samples at 1.7 ng mL⁻¹ with a linear range of 0–0.8 μg mL⁻¹.

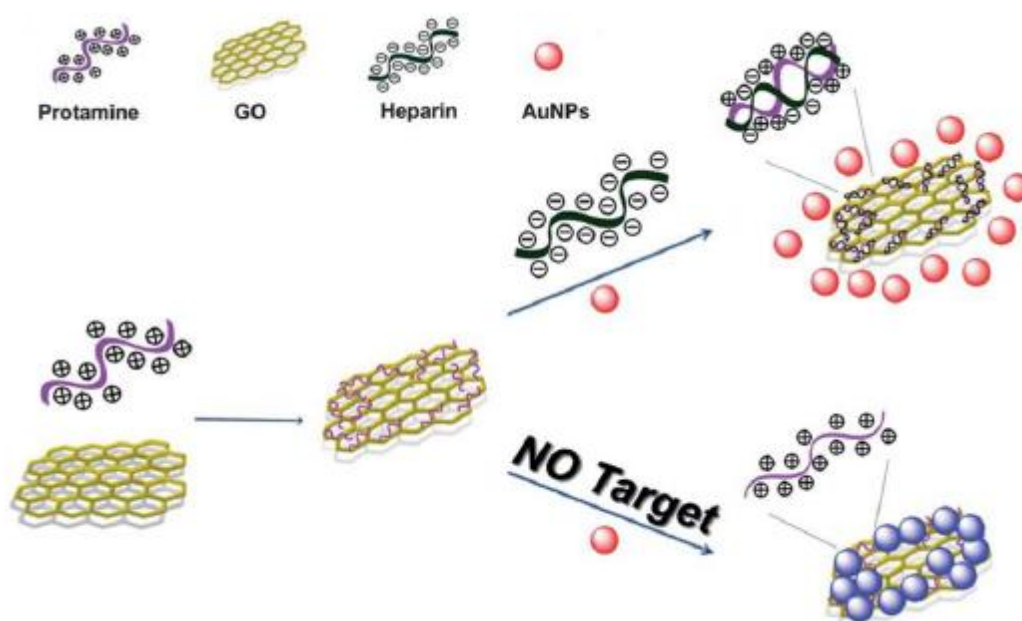


Figure 2.11: GO-AuNPs sensing system from Fu *et al.*, figured adapted from reference⁸³.

2.1.2.3 Ratiometric Sensors

Ratiometric sensing involves monitoring spectroscopic changes at two wavelengths to provide internal calibration of the system: a key advantage over a single wavelength approach which requires external calibration. A ratiometric outcome can either be achieved using a single component or multi component methodology. Pu *et al.* developed a range of versatile conjugated polyelectrolyte structures appended onto a polyfluorene backbone, able to respond to heparin either in a switch-on, direct colorimetric or ratiometric fashion as a result of aggregation. Furthermore, the colour change upon heparin binding in 2 mM PBS was so vivid that it could be observed by the naked eye (Figure 2.12).⁸⁴

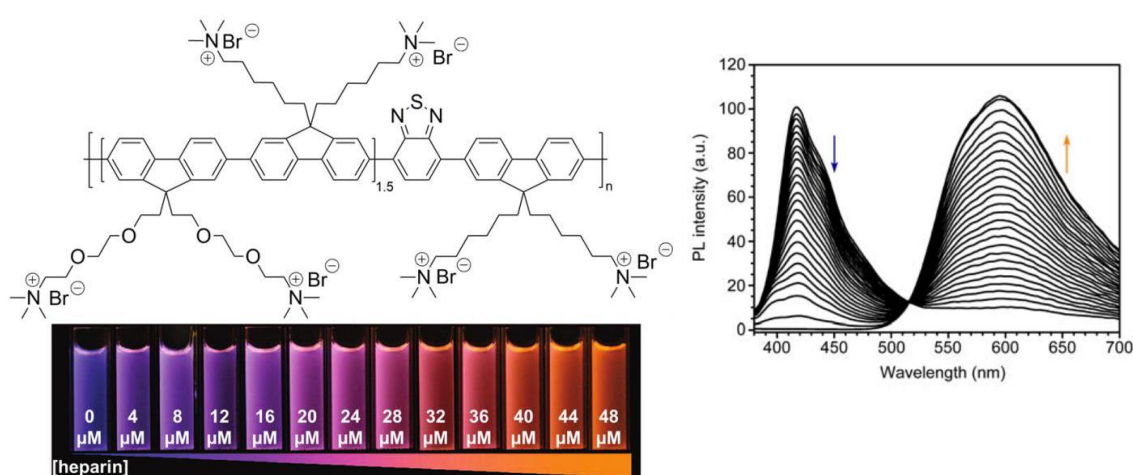


Figure 2.12: (Left) A polyfluorene heparin sensing derivative from Pu *et al.*; (Right) photoluminescence (PL) spectra of polyfluorene heparin sensing derivative at 60 μM in 2 mM PBS at pH 7.4 in the presence of heparin with concentrations ranging from 0 to 50 μM at intervals of 2 μM (excitation at 365 nm), figure adapted from reference⁸⁴.

Shi *et al.* reported a phosphorescent conjugated polyelectrolyte (PCPE) containing an Ir(III) complex which was able to selectively respond to heparin in a ratiometric manner both in aqueous solution and in the presence of serum with quantification ranges of 0–70 μM and 0–5 μM, respectively.⁸⁵ PCPEs had blue fluorescence in aqueous solutions, and on adding heparin, the electrostatic interaction between them improved the energy transfer between the polyfluorene units and the Ir(III) complex

and the result also lights up the red signal for effective naked-eye sensing.

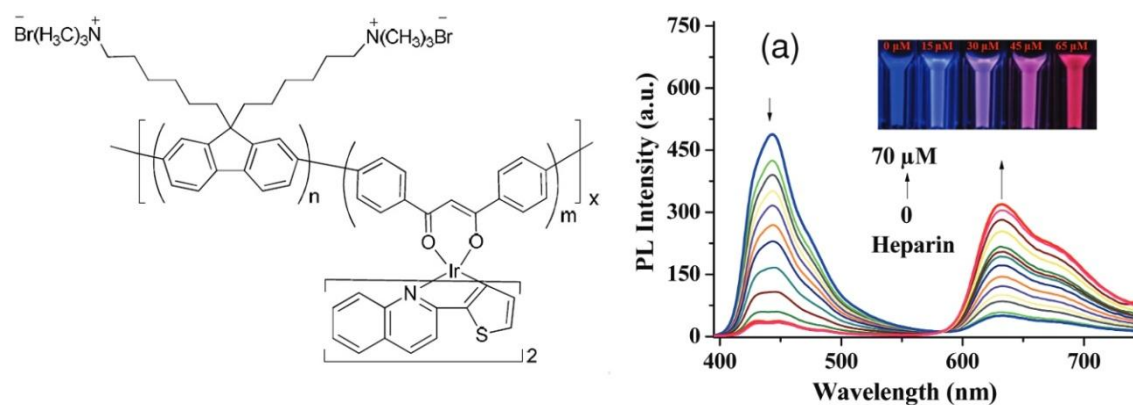


Figure 2.13: (Left) A phosphorescent conjugated polyelectrolyte structure from Zhao, Liu and Huang. (Right) PL spectra in HEPES buffer with addition of heparin from 0 to 70 μ M upon excitation at 380 nm. Inset: emission color changes of solution under hand-held UV-lamp excited at 365 nm.⁸⁵

2.1.2.4 Pyrene-derived Heparin Sensor

Pyrene is a useful fluorophore for ratiometric sensors, as it can form an excimer when excited-state and ground-state molecules are brought into close proximity.^{86, 87} To exemplify this, Zhang *et al.* reported a bis-pyrene-based pH-dependent conformationally responsive compound. It exists in an unstacked conformation under acidic conditions (low pH) due to the electrostatic repulsion of protonated nitrogen atoms with purple-blue monomer fluorescence at 370–420 nm when excited at 363 nm. Under basic conditions (high pH), however, it self-assembled in a stacked conformation owing to π - π interactions in aqueous solution with a new broad excimer emission in blue-green at 460–540 nm (**Figure 2.14**).⁸⁸

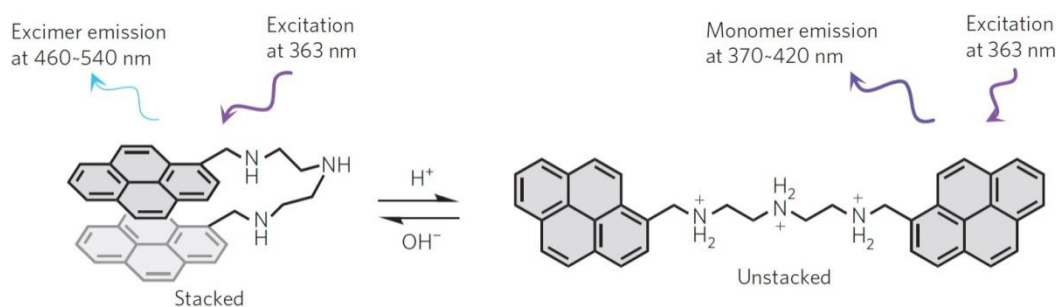


Figure 2.14: Chemical structures of bis-pyrene and conformational changes from stacked to unstacked conformations in aqueous solution under basic and acidic

conditions by Zhang *et al.*, figure adapted from reference⁸⁸.

The first pyrene-based heparin sensor **PQ** (**Figure 2.15**) was reported by Zeng *et al.*⁸⁹ This was a quinine derivative bearing a pyrenyl group as a fluorophore which mainly shows monomer-like emission at 376 nm in buffer. Upon addition of heparin, excimer emission at 489 nm developed while the monomer emission at 376 nm decreased concomitantly. The sensor exhibited good selectivity and sensitivity for heparin over other biological anions, even with highly charged ones. The sensor was also tested in the presence of diluted bovine serum albumin (BSA) with heparin and overcame the background fluorescence of blood. However, the assay required addition of a co-solvent ethanol to perform in both buffer and serum. This is probably a result of the relatively low charge of the sensor limiting the binding ability.

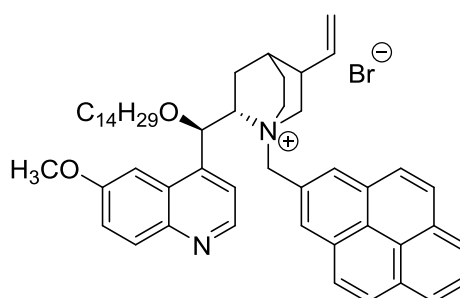
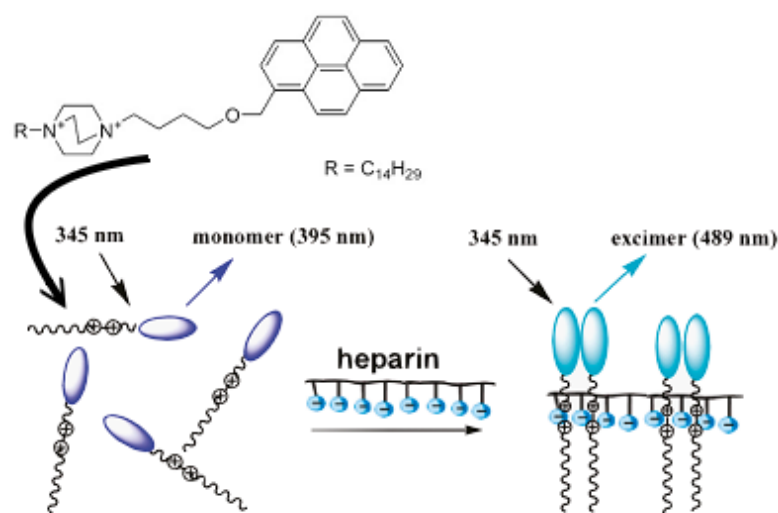


Figure 2.15: Structure of **PQ**

In 2011, Dai *et al.* reported a ratiometric fluorescence sensor based on a dual quaternary ammonium 1,4-diazobicyclo(2,2,2)octane (DABCO) derivative with a pyrene group attached.⁹⁰ They proposed that the dual positively charged DABCO unit can effectively form electrostatic interactions with the negatively charged heparin and bring two molecules of sensor close to one saccharide ring. It was argued that the long hydrophobic chain may help allow the directional alignment of the sensor, resulting in the formation of a dimer to give excimer emission (**Scheme 2.1**). Again, the assay required addition of co-solvent (ethanol) to perform in both buffer and serum, suggesting relatively weak binding interactions.



Scheme 2.1: Structure of ratiometric fluorescence sensor and the schematic illustration of heparin detection developed by Dai *et al.*⁹⁰

Very recently, while this work was in progress, Kim *et al.* reported a peptidyl fluorescent chemosensor Py12 (**Figure 2.16**).⁹¹ Py12 showed a sensitive ratiometric response to heparin over a wide pH range ($1.5 \leq \text{pH} \leq 11.5$) and exhibited very high selectivity for heparin compared to other biological competitors, such as hyaluronic acid and chondroitin sulphate, with a detection limit of ca. 30 pM in aqueous buffer solutions containing 5% human plasma for heparin. Clearly this sensor is highly effective but is also quite structurally complex and will have relatively high cost.

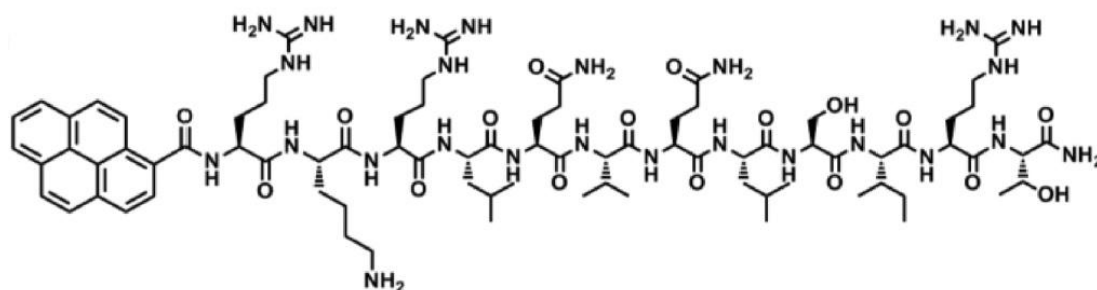


Figure 2.16: Structure of Py12.

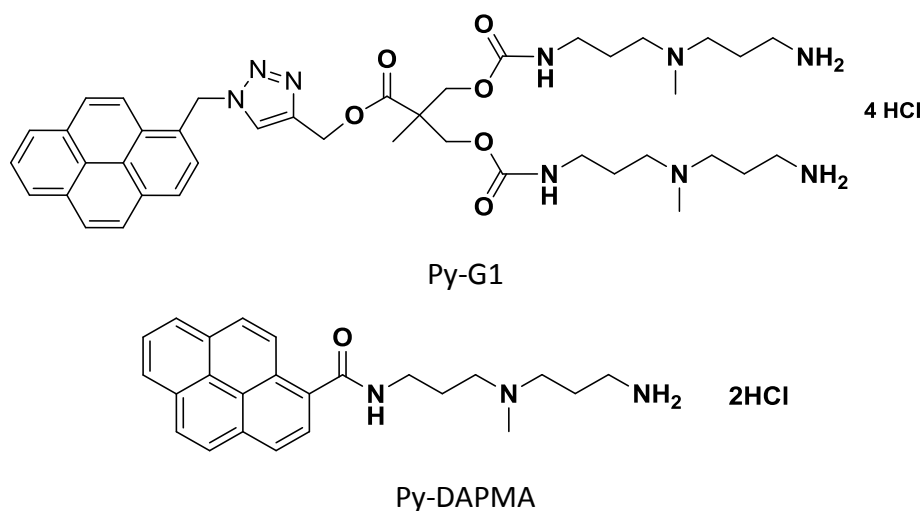
2.1.3 Aim

It is worth noting that a number of sensors which report binding 'in serum' actually achieve this by adding a small amount of heparinised serum to the sensor in buffer – in the assay itself, levels of serum are relatively low (<10%). Alternatively they employ co- solvent in order to reduce competition and strengthen relatively low affinity binding events. The development of robust, ratiometric dual-wavelength heparin sensors which operate in highly-competitive media therefore remains a desirable goal.

Self-assembled multivalency (SAMul), in which self-assembly (via non-covalent interactions) is used to organise the multiple binding sites, which then show high-affinity binding to the target was described in Chapter 1. Pyrene can act as a fluorescent unit capable of detecting heparin in a ratiometric manner, and it was realised that it can also provide a driving force for self-assembly of the system. As such, the pyrene sensing unit may mediate assembly of the ligand into a nanostructure capable of very high-affinity multivalent binding and sensing. It was reasoned that it would be of interest to study this two-in-one approach to high-affinity binding and ratiometric sensing in highly competitive media.

The aim of this chapter is to develop heparin sensors and explore the role of self-assembled multivalency (SAMul).

With this goal in mind we targeted the synthesis of SAMul pyrene derivatives Py-G1 and non-SAMul pyrene derivatives Py-DAPMA. Both of these compounds contain a pyrene unit and equivalent ligands but predicted that only Py-G1 would self-assemble into multivalent arrays prior to heparin binding. This was reasoned because of the lower flexibility of the Py-DAPMA and also its smaller hydrophilic unit compared with Py-G1 which will change the hydrophilic-lipophilic balance (HLB) and modify the assembly preference.⁹² As such we reasoned that we could probe the differential effects of self-assembly on heparin binding and sensing.



2.2 Effect of SAMul in Heparin Sensing

2.2.1 Synthesis of Py-G1 and Py-DAPMA

Py-G1 is an analogue of C₂₂-G1, which was first reported by Rodrigo *et al.* as a self-assembling dendron for heparin binding (**Figure 2.17**).⁹³ C₂₂-G1 contains peripheral amines that are protonated at physiological pH, allowing highly effective electrostatic binding to polyanionic heparin. These amines are supported on the degradable, biocompatible scaffold first introduced by Hult, Fréchet, and co-workers.⁹⁴⁻⁹⁸ The straight-chain alkane located at the focal point of the structure act as hydrophobic unit driving the self-assembly of the ligands into a larger nanoscale architecture in aqueous media as a consequence of the hydrophobic effect. C₂₂-G1 was reported to be a significantly more effective heparin binder than protamine in the presence of electrolyte.⁹³ However, it was reported later that the performance in serum was more disrupted than protamine due to partial disassembly of the multivalent array.⁴³

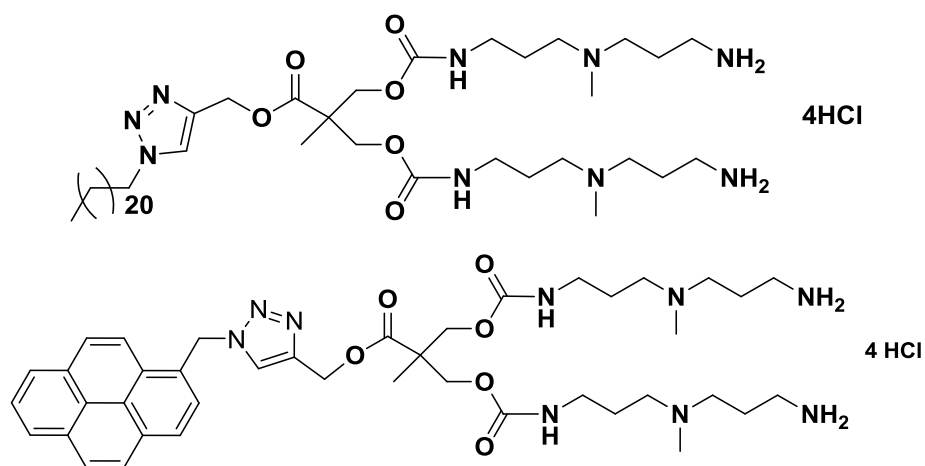
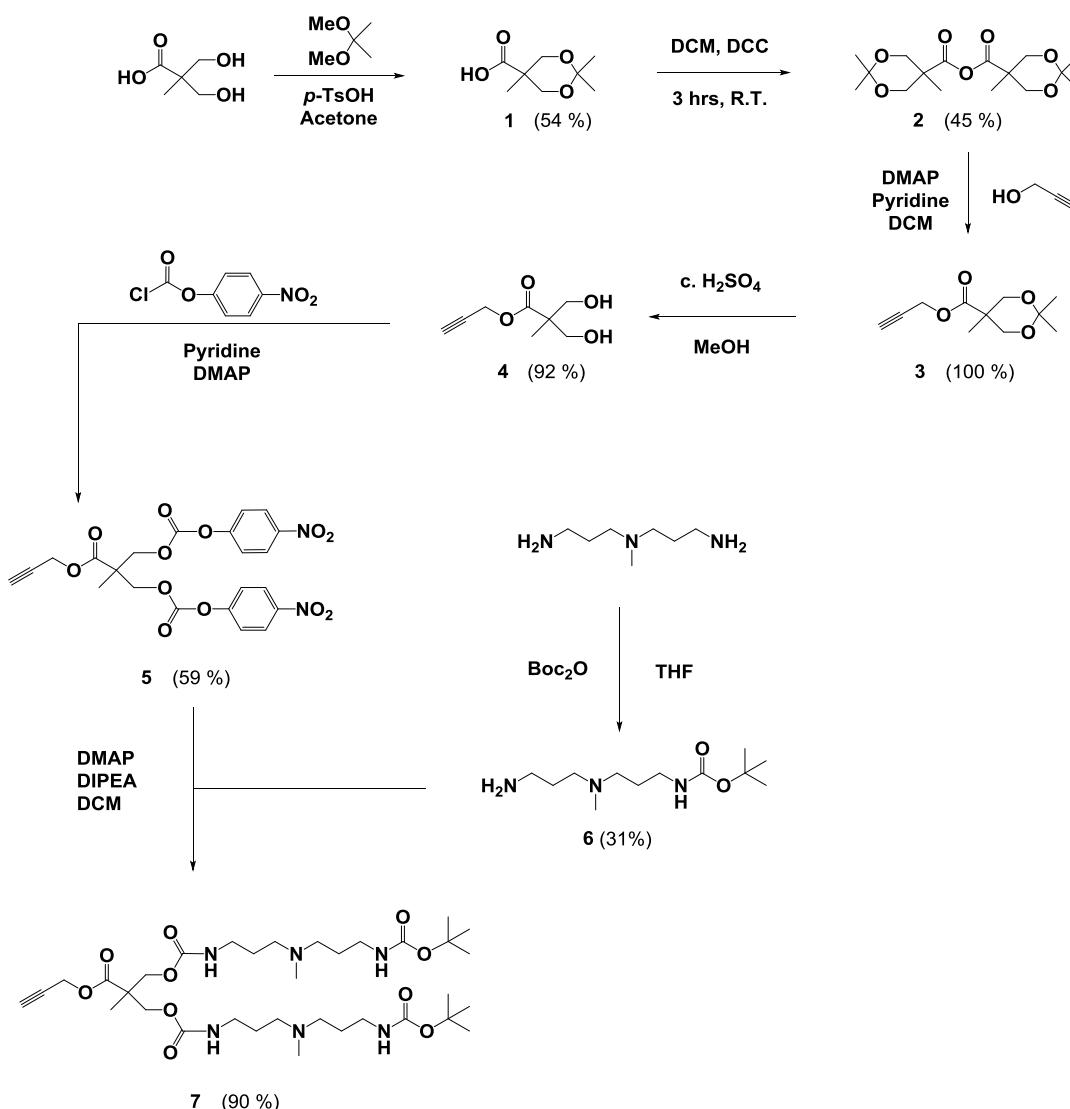


Figure 2.17: Structure of C₂₂-G1 (top) and Py-G1 (bottom).

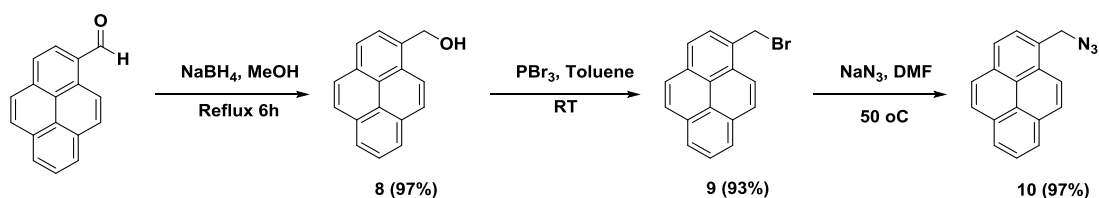
Py-G1 was designed in this project, replacing the alkyl chain with a pyrene unit. We hoped this would introduce inherent sensing ability at the focal point. At the same time, we reasoned that the π - π interactions of the pyrene units may allow self-assembly and also help to further stabilise the self-assembled structure in highly competitive media such as serum.

Compound Py-G1 required a new synthetic approach in order to attach the focal point unit. The Fréchet dendron scaffold was synthesized using the previously described methodology.⁹⁷ The 1,3 diol moiety of bis-MPA was protected to afford acetonide group **1** by reaction of bis-MPA with 2,2-dimethoxypropane and a catalytic amount of *p*-toluenesulfonic acid (TsOH) in acetone.⁹⁵ The product was then self-coupled to itself in dichloromethane using *N,N'*-dicyclohexylcarbodiimide (DCC). The resulting product **2** was reacted with propargyl alcohol, leading to the incorporation of an alkyne group appropriate for click chemistry, this reaction gave an excellent yield of **3**.⁹⁹ Compound **3** was then deprotected with conc. H₂SO₄ in MeOH to remove the acetonide group and result in the diol, giving **4**. Compound **4** was then reacted using *p*-nitrophenyl-chloroformate methodology to yield activated compound **5**. The *N,N*-di-(3-aminopropyl)-*N*-methylamine (DAPMA) surface ligands, with *N*-tert-butoxycarbonyl (Boc) protecting groups **6** produced by mono-boc protection of DAPMA, were then coupled to the activated surface groups to yield compound **7**.



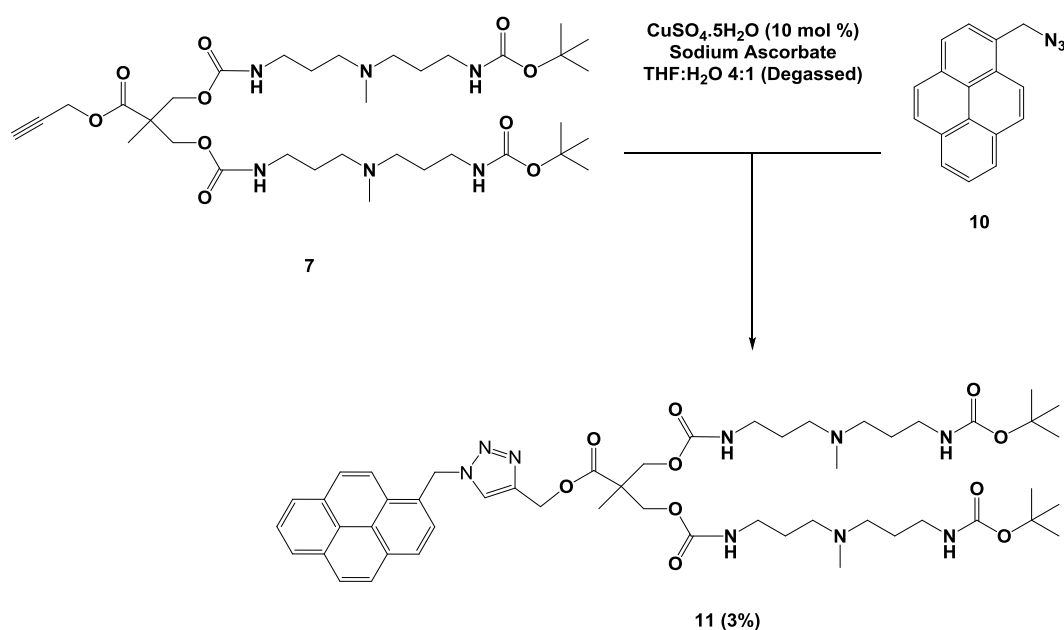
Scheme 2.2: Synthesis of alkyne-functionalised dendron, **7**, based on previously published method for C_{22} -G1.⁹¹

The procedure reported by Saha *et al.*¹⁰⁰ to synthesise an azide-functionalized pyrene suitable for click chemistry was then followed (**Scheme 2.3**). 1-Pyrenecarboxaldehyde was reduced to alcohol **8** using sodium borohydride. PBr_3 -mediated bromination replaced the alcohol with a bromine to give **9**. Finally, a nucleophilic substitution with azide in DMF gave target compound **10** in an excellent overall yield of 87%.



Scheme 2.3: Synthesis route of azide-functionalised pyrene **10**

Azide **10** was then attached via click chemistry methodology to alkyne-functionalised dendron, **7**, using the same method reported for the Rodrigo synthesis of C₂₂-G1 (**Scheme 2.4**). The ‘click’ chemistry reaction is a copper (I) catalysed modification of the Huisgen 1,3-dipolar cycloaddition¹⁰¹ developed by Meldal *et al.* in 2002.¹⁰² The reaction is generally high yielding and tolerant of a wide range of substrates and reaction conditions.¹⁰³⁻¹⁰⁵ Since its initial report, the methodology has been applied to the synthesis of many dendritic systems.¹⁰⁶⁻¹⁰⁸



Scheme 2.4: Synthesis route of **11**.

Unfortunately, in this case, only a 3% yield of compound **11** was obtained. This is possibly a result of interaction between the amine group of compound **7** and the copper catalyst. Also, since the compound will decompose in water as a result of the ester linkage between the head group and the azide linker and the procedure for the

"click" chemistry used water as medium, we reasoned that alternative "click" chemistry reaction conditions may improved yield. Meldal and Tornøe discussed the possibilities for coordination and delivery of azide to alkyne during the transition state of the Cu-Catalyzed azide-alkyne cycloaddition reaction ("click chemistry") as shown in **Figure 2.18**.¹⁰⁹ From the Figure, we can see at the intermediate **4** the pyrene (as R₂) may also become a steric hindrance increasing the activation energy and slowing the reaction rate.

Based on the review by Meldal and Tornøe,¹⁰⁹ DMF can be used as solvent for click chemistry¹¹⁰ which may overcome the problem that the compound will decompose in water and allow the reaction mixture to be left longer and overcome the steric hindrance.

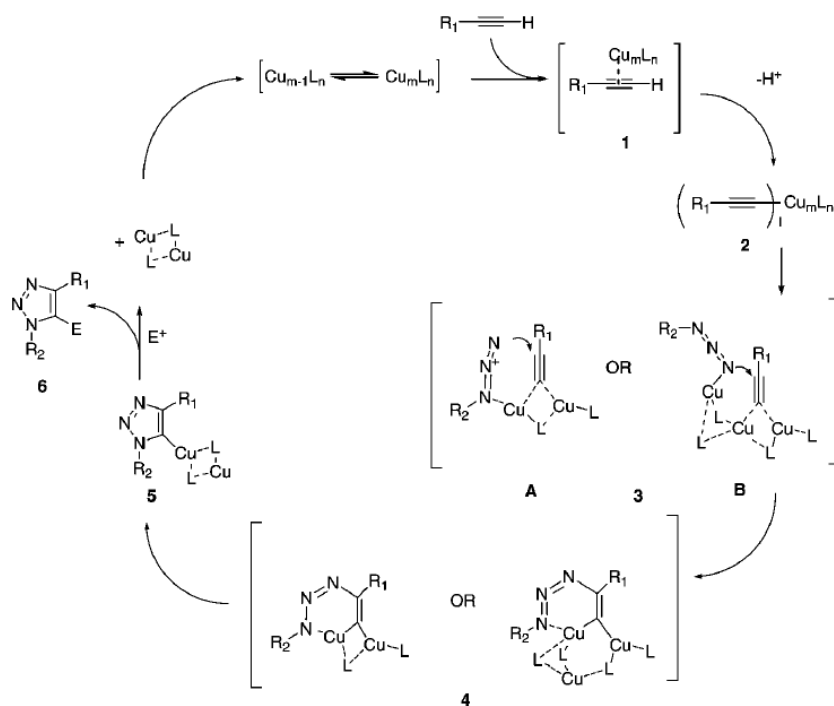


Figure 2.18: Plausible mechanisms for the Cu(I) catalyzed reaction between azides and alkynes.¹⁰⁹

Compound **11** was obtained with a much-improved 72 % yield (compared with 3%) by changing the solvent from degassed THF/H₂O to degassed DMF stirring under N₂ for 72 hours. Comparing the ¹H NMR spectra of compound **11** (**Figure 2.19**) with that of its synthetic precursor, **7**, the spectrum for compound **11** has a new peak observed at 7.45

ppm corresponding to the CH of the triazole. Moreover, the CH₂ adjacent to the propyne group for compound **7** at 4.68 ppm now moves to 5.11 ppm for compound **11** corresponding to the CH adjacent to the triazole in the hydrophilic part of the dendron, due to the alkyne functionality of **7** being converted to an aromatic ring in the formation of the triazole of **11**.

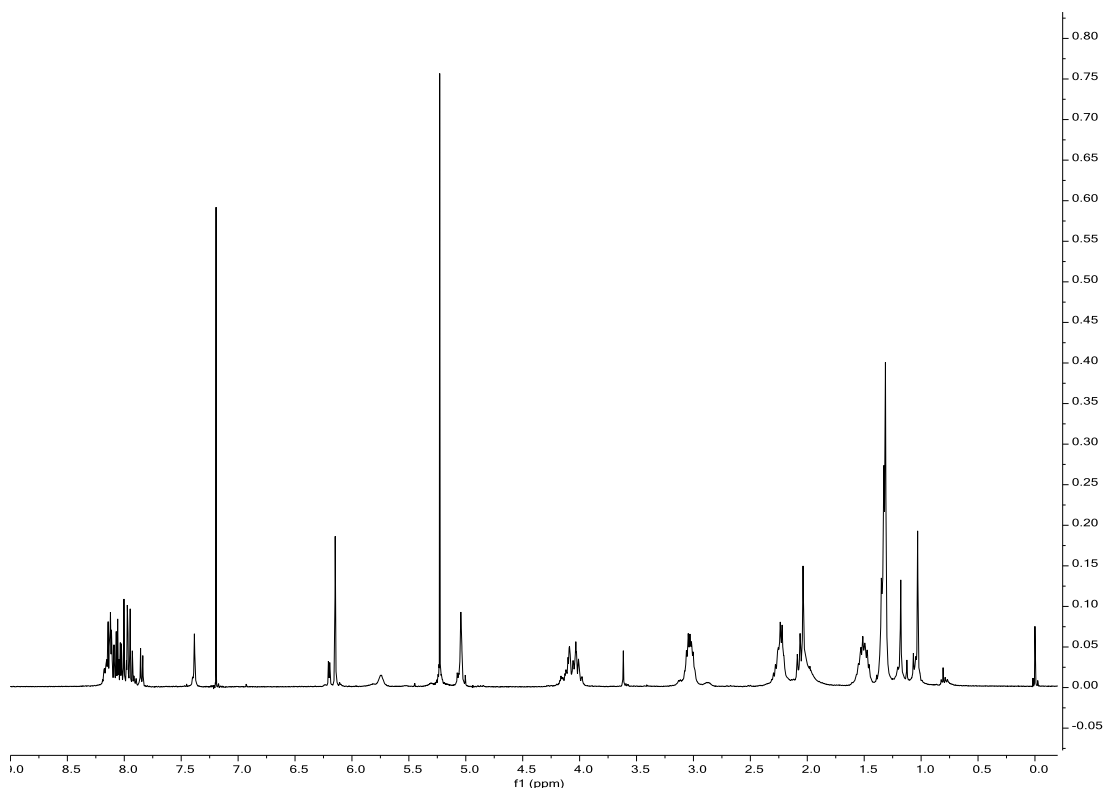
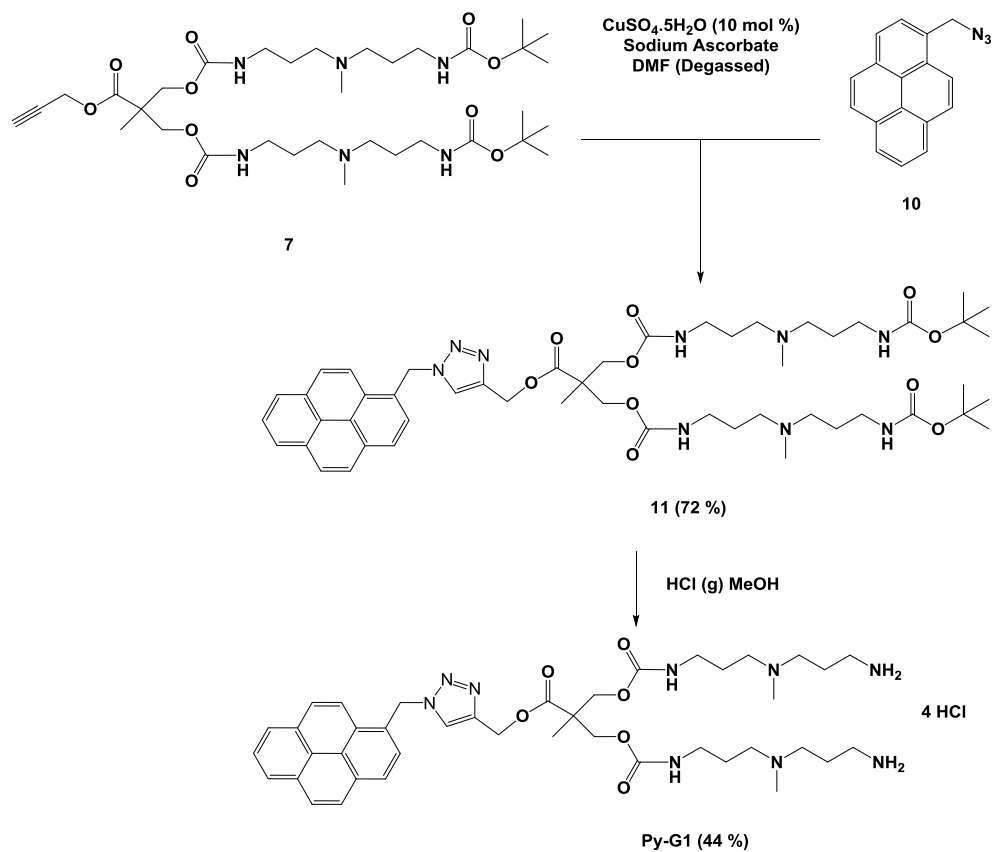


Figure 2.19: ¹H NMR spectra of Compound **11**.

Compound Py-G1 was then obtained by Boc-deprotection using HCl gas bubbled through MeOH (**Scheme 2.5**). The peak corresponding to the Boc group protons was no longer observed in the ¹H NMR spectrum for compounds Py-G1 (Figure 2.20), indicating that a successful Boc deprotection took place. Additional product confirmation was acquired by mass spectrometry and all other analytical methods (see Experimental section).



Scheme 2.5: Synthesis of Py-G1.

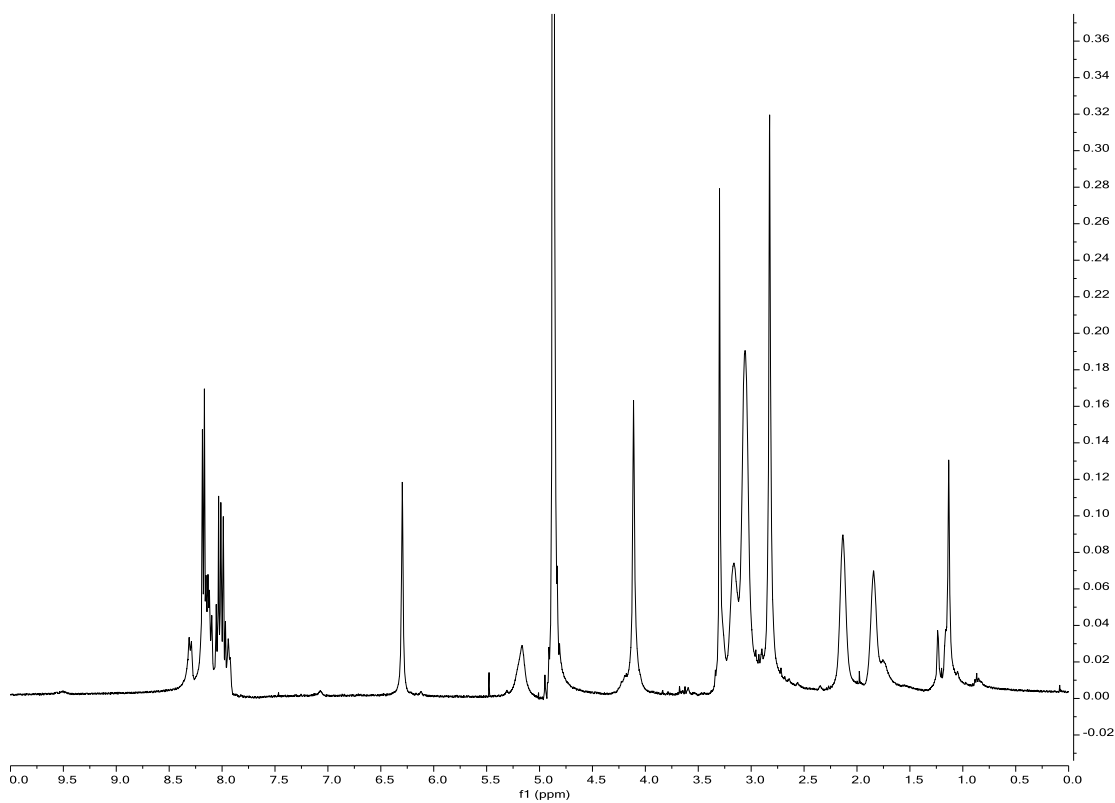
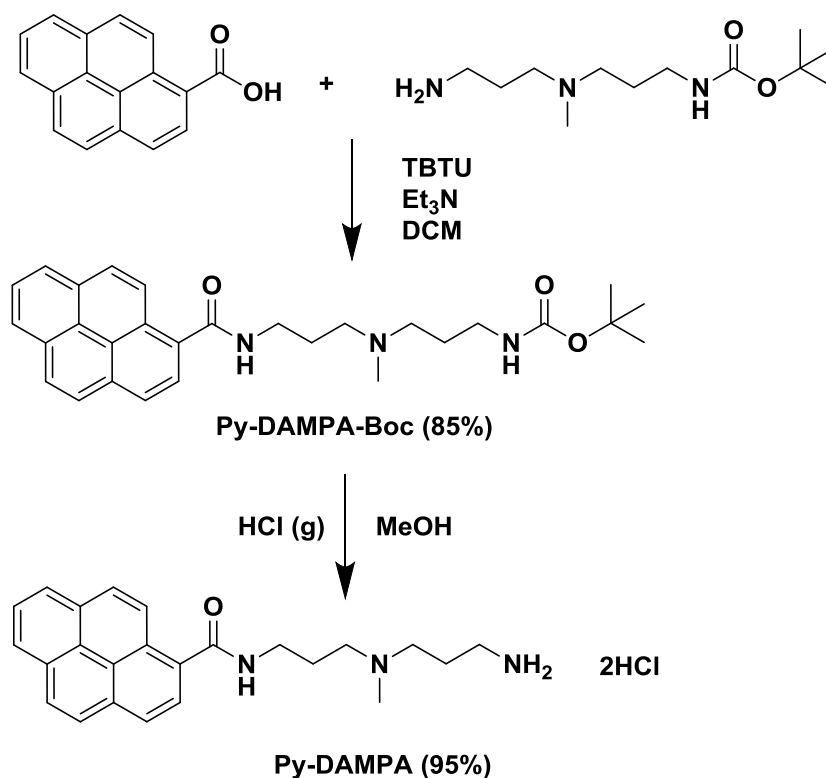


Figure 2.20: ^1H NMR spectra of Py-G1

To synthesise Py-DAPMA compound, **6** was coupled with 1-pyrenecarboxylic acid using TBTU and excess Et₃N in DCM and then the Boc protecting groups were removed using HCl gas bubbled through MeOH (**Scheme 2.6**). The peak corresponding to the Boc group protons was not observed in the ¹H NMR spectrum for compound Py-DAMPA (Figure 2.21), indicating that successful Boc deprotection took place. Additional product confirmation was acquired by mass spectrometry and all other analytical methods. This synthesis worked in good yield and gave the desired target compound quickly and simply.



Scheme 2.6: Synthesis of Py-DAMPA

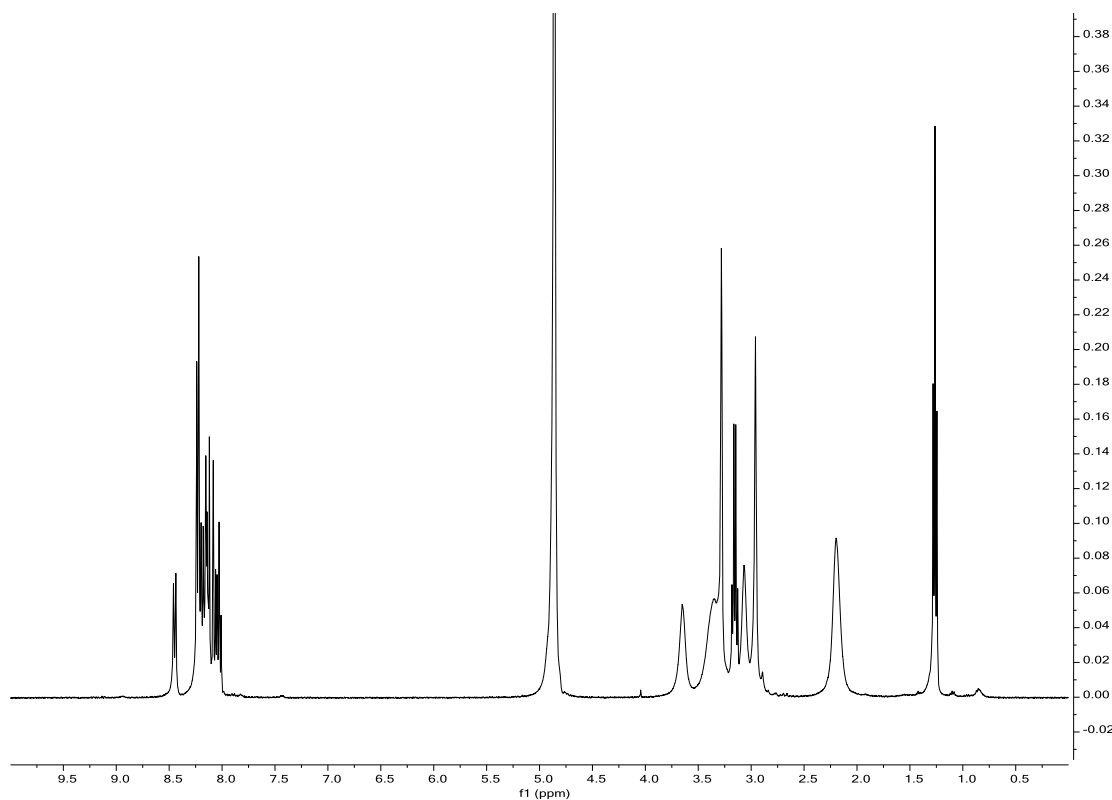


Figure 2.21: ^1H NMR spectra of Py-DAMPA

2.2.2 Critical Aggregation Concentration (CAC)

To probe the self-assembly of Py-G1, a Nile Red assay was performed, in which the solubilization of the hydrophobic dye, as monitored by fluorescence spectroscopy, acts as a probe for the minimum concentration at which self-assembly can take place.¹¹¹ Before the target compound self-assembly takes place, the dye is free in the solution and hence has a quenched fluorescence. When self-assembly takes place, a hydrophobic core is generated into which the dye can diffuse and therefore, as a result, there is no longer quenching of the fluorescence. However, studying Py-G1 using the Nile Red assay did not yield a result like C₂₂-G1.⁹³ We suggest that this may be due to the pyrene ring quenching the fluorescence of the encapsulated Nile Red when Py-G1 self-assembled.

We therefore developed an alternative approach to determine the CAC value. This assay method used the unique optical properties of the pyrene unit, which can report directly on its aggregation state, as if it is aggregated, when pyrene is excited at 363 nm,

it exhibits an excimer emission between 460 -540 nm.⁸⁸ It was found that when Py-G1 was excited at 363 nm, a emission band with max emission at 495 nm was observed and this band could therefore be monitored to determine the CAC. This band is concentration dependent because excimer formation is only favoured in the interior of the micelle when pyrene groups are close together in a self-assembled environment. We assumed that the discontinuity in the excimer emission bond plot represents the concentration at which self-assembly is initiated i.e. CAC. The CAC of Py-G1 was found to be $18.6 \pm 1.3 \mu\text{M}$ in 0.01M PBS buffer (**Figure 2.22**).

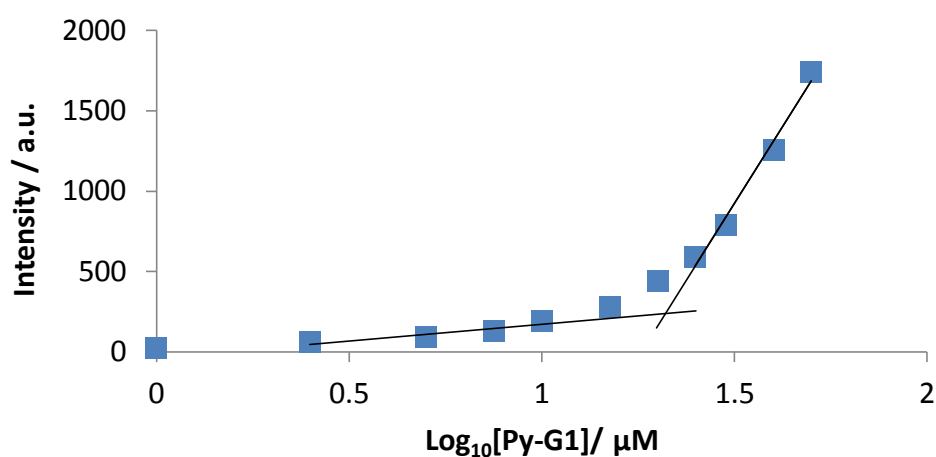


Figure 2.22: Fluorescence intensity at 495 nm of Py-G1 at increasing concentration in aqueous PBS Buffer (0.01 mM).

The same method was then applied to Py-DAPMA to discover the CAC, however, in this case, there was no emission band at 495 nm when this compound was excited at 363 nm (**Figure 2.23**). This suggested that Py-DAPMA did not self-assemble at concentrations below 200 μM. Having two potential sensors, one of which self-assembles at concentration above ca. 20 μM while the other one does not - of great interest for further study.

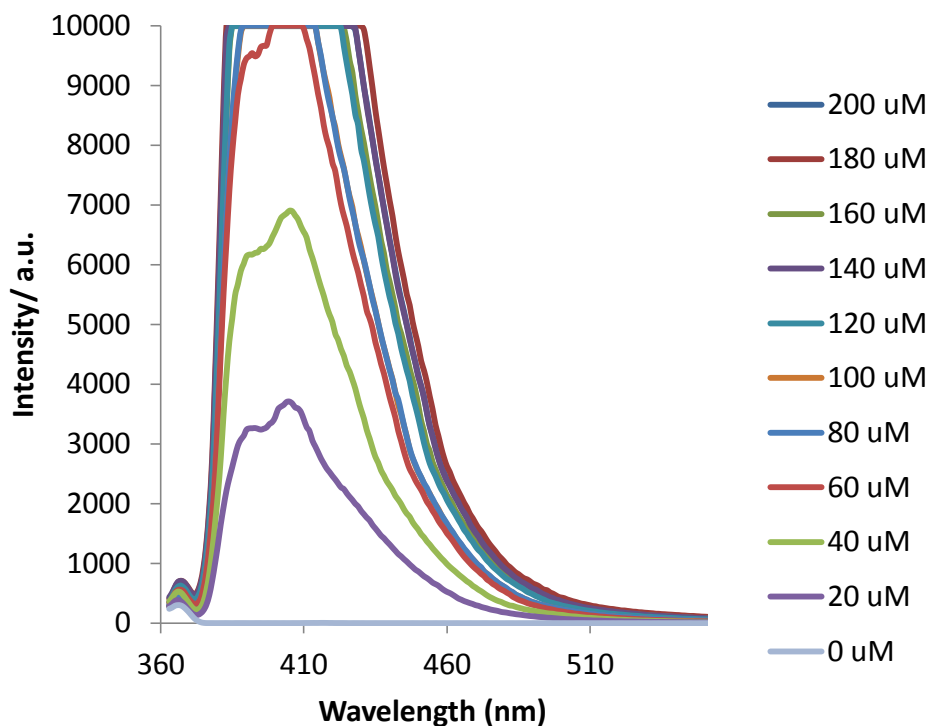


Figure 2.23: Fluorescence intensity of Py-DAPMA against wavelength (450 nm to 550 nm) as recorded for increasing concentrations of Py-DAPMA in PBS Buffer (0.01 mM).

2.2.3 Transmission Electron Microscopy (TEM)

The self-assembled nanostructures formed by these compounds were visualised using transmission electron microscopy (TEM). The samples were first prepared in clean water at concentrations of 1 mg/mL and then deposited as solution-phase aliquots onto a formvar grid, staining with uranyl acetate and drying in air. Py-G1 appeared to form relatively polydisperse spherical assemblies with approximate diameters ranging from ca. 10 to 40 nm (**Figure 2.24**) – given the (much smaller) molecular size (2-3 nm), it is suggested that these could be vesicular objects or clusters of micellar assemblies which aggregate on drying. Under these conditions, Py-DAPMA also appeared to form relatively polydisperse spherical assemblies with approximate diameters ranging from ca. 2 to 40 nm when visualised by TEM (**Figure 2.24**). Py-DAPMA was found not to self-assemble in the previous section when attempting to determine the CAC value. However, TEM images are determined at millimolar

concentrations (1 mg/mL) which are much higher than micromolar concentrations tested for the CAC value using fluorescence spectroscopy. It is these latter micromolar conditions which are relevant for the binding assays described in detail below. Hence we suggest that Py-DAPMA may self-assemble at high concentrations and clearly has some potential for self-assembly but not in the micromolar regime.

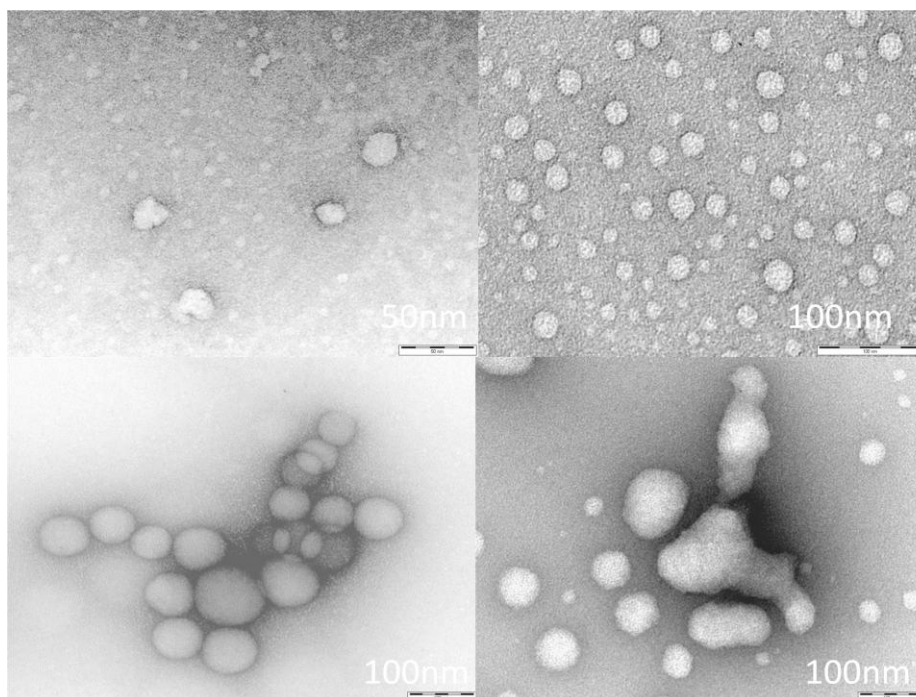


Figure 2.24: TEM images of Py-DAPMA (left) and Py-G1 (right) in the absence (top) and presence of heparin (bottom).

2.2.4 Dynamic Light Scattering (DLS)

Dynamic light scattering (DLS) investigates self-assembled objects in solution rather than, like TEM, deposited on a surface in the solid like phase. The DLS data for Py-G1 and Py-DAPMA are summarised in **Table 2.1**. Py-G1 supported the formation of relatively polydisperse assembled nanostructures, albeit with somewhat larger diameters (18.5 ± 21.9 nm) (volume distribution). The large error associated was due to the DLS software counting a second peak into single peak (**Figure 2.25**) and can be considered to be somewhat of an artefact. Inspection of the volume distribution data actually suggests a diameter of ca. 9 nm. For Py-DAPMA, again self-assembled nanostructures was observed with diameters of 15.4 ± 4.5 nm (**Figure 2.26**). In cases where the quality report is flagged, this is a result of sample polydispersity making

cumulant fit error high – this means that the ‘averaged’ results for the whole trace presented in red should be disregarded – the results listed for the individual peaks are still valid. Similarly to the TEM imaging, we propose that under these millimolar condition self-assembly of both Py-G1 and Py-DAPMA is able to occur. The zeta potentials for both Py-G1 and Py-DAPMA were positive ($+27.9 \pm 1.4$ mV for Py-G1, $+15.6 \pm 2.2$ mV for Py-DAPMA). This is a result of protonation of the DAPMA ligands at physiological pH. As such, these self-assembled cationic nanostructures would be expected to show high affinity towards polyanionic heparin. The higher zeta potential of Py-G1 may due to the fact that it has two DAPMA ligands rather than just one.

Sample in 10 mM Tris HCl, NaCl (150 mM)	Size (d.nm)	Zeta Potential (mV)	PDI
Py-G1	14.2 ± 28.2	27.9 ± 1.4	0.51
Py-DAPMA	12.3 ± 3.7	15.6 ± 2.2	0.57

Table 2.1: DLS data for Py-G1 and Py-DAPMA.

	Size (d.nm):	% Volume:	St Dev (d.nm):
Z-Average (d.nm): 74.84	Peak 1: 14.21	100.0	28.20
PdI: 0.504	Peak 2: 0.000	0.0	0.000
Intercept: 0.688	Peak 3: 0.000	0.0	0.000
Result quality : Good			

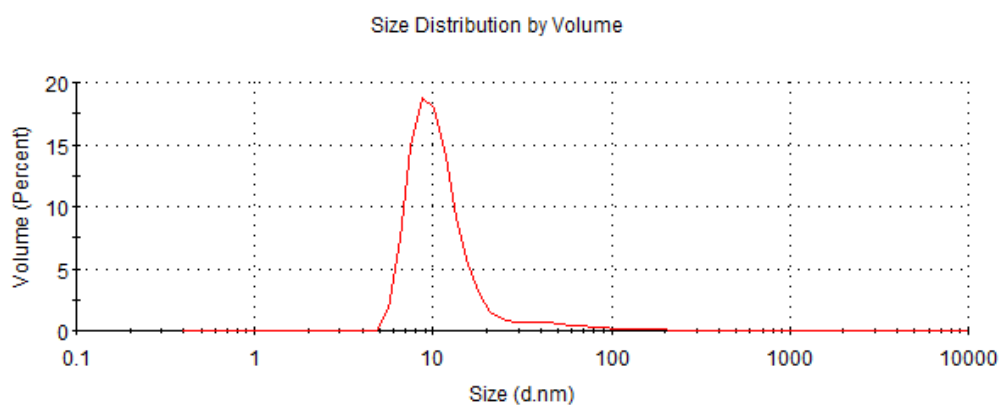


Figure 2.25: DLS data for Py-G1 measured at 1 mg/mL.

	Size (d.nm):	% Volume:	St Dev (d.nm):
Z-Average (d.nm): 67.31	Peak 1: 101.7	2.2	52.04
Pdl: 0.553	Peak 2: 12.25	97.8	3.709
Intercept: 0.765	Peak 3: 0.000	0.0	0.000

Result quality : Refer to quality report

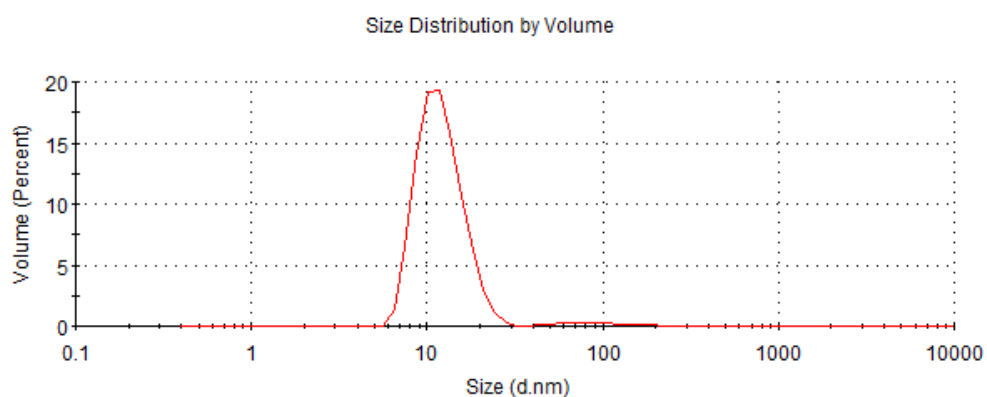


Figure 2.26: DLS data for Py-DAPMA measured at 1 mg/mL

2.2.5 Heparin sensing in 10 mM Tris HCl with 150 mM NaCl buffer

Having established the self-assembly characteristics of Py-G1 (micromolar) and Py-DAPMA (millmolar), we went on to assay their ability to bind to heparin. Hence, we were interested to determine whether there was any difference between them in terms of sensing ability induced by the enhanced ability of Py-G1 to self-assemble in aqueous solution. Both Py-G1 and Py-DAPMA were investigated. The interaction of both binders with heparin was investigated by titrating heparin (in buffer) into a buffered solution of the binder

Since the therapeutic dosing level of heparin is 2 – 8 U mL⁻¹ (17 to 67 μM) in cardiovascular surgery and 0.2 – 1.2 U mL⁻¹ (1.7 to 10 μM) for postoperative and long-term therapy,¹¹² the heparin assay range was set from 0 to 40 μM. The concentration of Py-G1 was set to be 30 μM, above the CAC to ensure self-assembly and Py-DAPMA was set to be 60 μM, for identical comparison with Py-G1 in terms of charge ratio (Py-G1 = 4 +ve, Py-DAPMA = 2 +ve). Experiments were preformed in triplicate.

Initially the UV-Vis spectrum was measured to characterise the system () prior to using fluorescence spectroscopy to monitor binding.

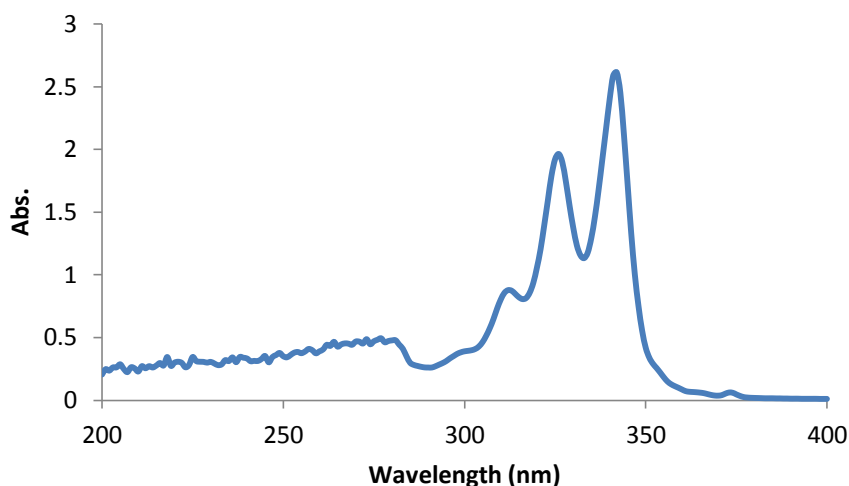


Figure 2.27: UV-Vis Absorption spectra of Py-G1 (0.5 mg/mL Tris Hcl with 150 mM NaCl)

In the absence of heparin, self-assembling Py-G1 shows characteristic monomer emission with peaks at 383 and 400 nm with small, but observable, excimer emission at 495 nm. Upon addition of heparin, the fluorescence emission intensity at 383 nm decreased while the emission band centred at 495 nm increased significantly until it became the dominant feature of the spectrum (**Figure 2.29**). The emission band at 495 nm shows a large enhancement with increasing concentration of heparin and can be attributed to the enhanced formation of pyrene excimers induced by heparin binding. **Figure 2.28** (inset) shows a photograph of Py-G1 when heparin is absent (A) or present (B). Clearly, the strong “switch-on” excimer emission can even be seen using the naked eye when the sample is under UV irradiation, as the fluorescence changes colour (and intensity) to be somewhat more ‘green’. **Figure 2.29** shows the emission intensity data extracted at λ 383 nm (monomer) and 495 nm (excimer). This clearly demonstrates the way in which excimer emission becomes dominant, once heparin has bound, and provides the basis of the sensing event. We define this as a self-assembled multivalency (SAMul) sensing mechanism.

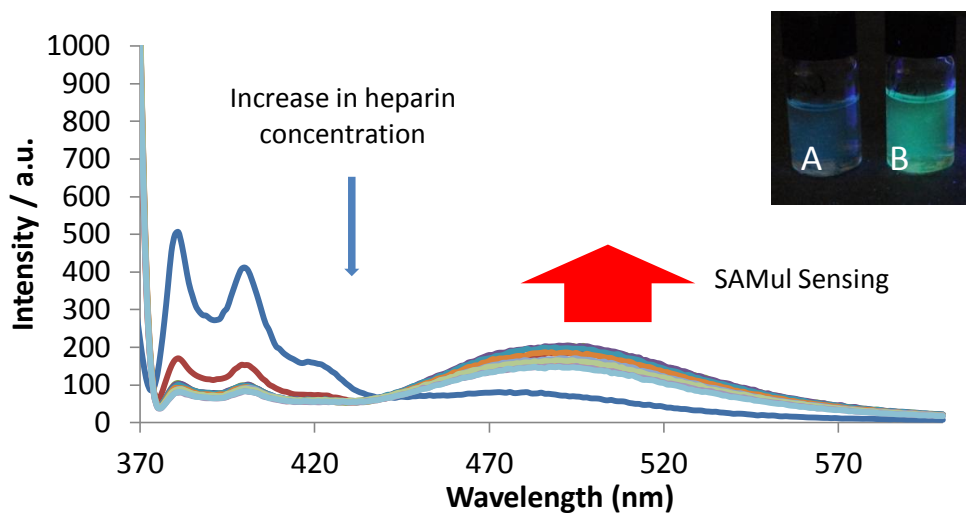


Figure 2.28: Fluorescence spectra of Py-G1 on addition of heparin in buffer. The inset shows the photographs of a solution of Py-G1 without heparin (A) and with heparin (B).

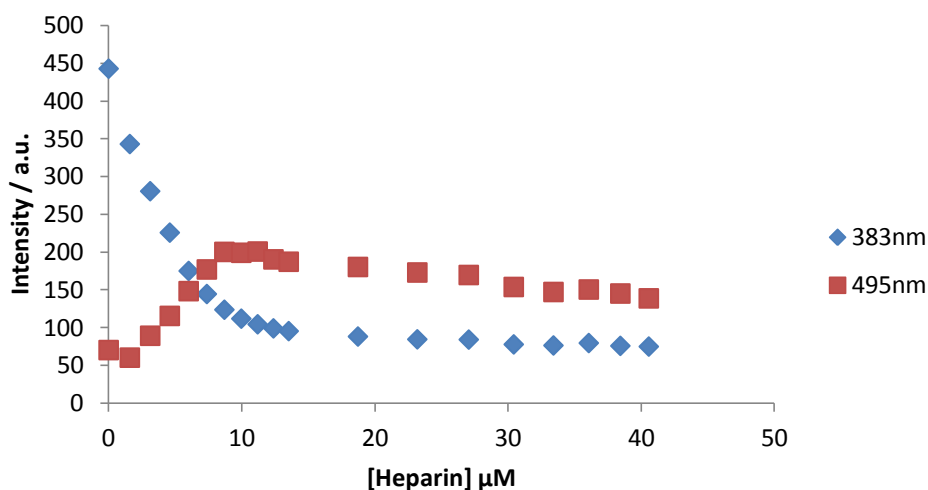


Figure 2.29: Fluorescence intensities extracted at 383 nm and 495 nm for the titration of heparin into Py-G1 in buffer.

On titrating Py-DAPMA with heparin under the same conditions as Py-G1, the fluorescence emission at 395 nm decreased in intensity but the band at 495 nm was effectively unchanged (**Figure 2.31**). There was also no ‘naked eye’ change in the fluorescence emission (**Figure 2.30**). This suggests that the large increase in excimer emission intensity observed for Py-G1 is associated with its self-assembly, and its subsequent reinforcement as a result of multivalent binding to the heparin. The

non-self-assembling system Py-DAPMA can sense heparin as a result of loss of intensity at 395 nm, but the system is unable to switch on an excimer-type response under these conditions. As such, the fluorescence sensing mechanism is clearly significantly different to that of the SAMul system (Py-G1).

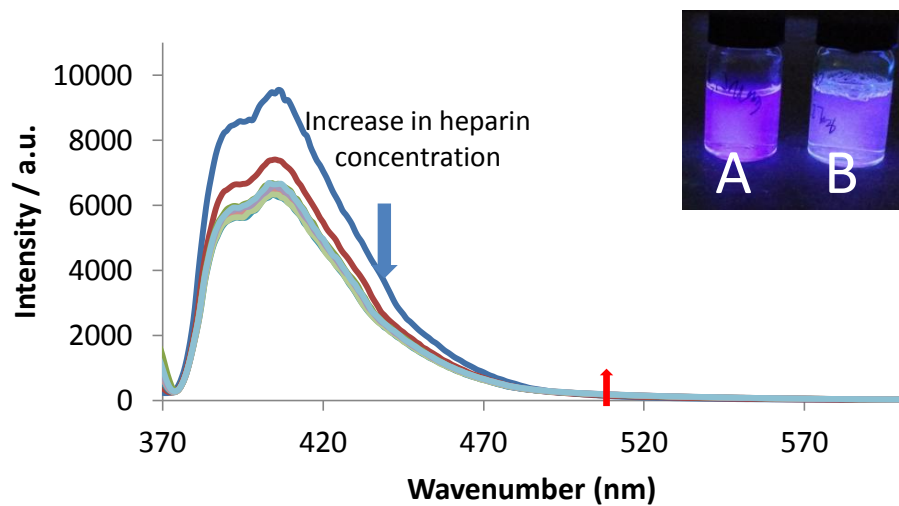


Figure 2.30: Fluorescence spectra of Py-DAPMA on addition of heparin in buffer. The inset shows the photographs of a solution of Py-DAPMA without heparin (A) and with heparin (B).

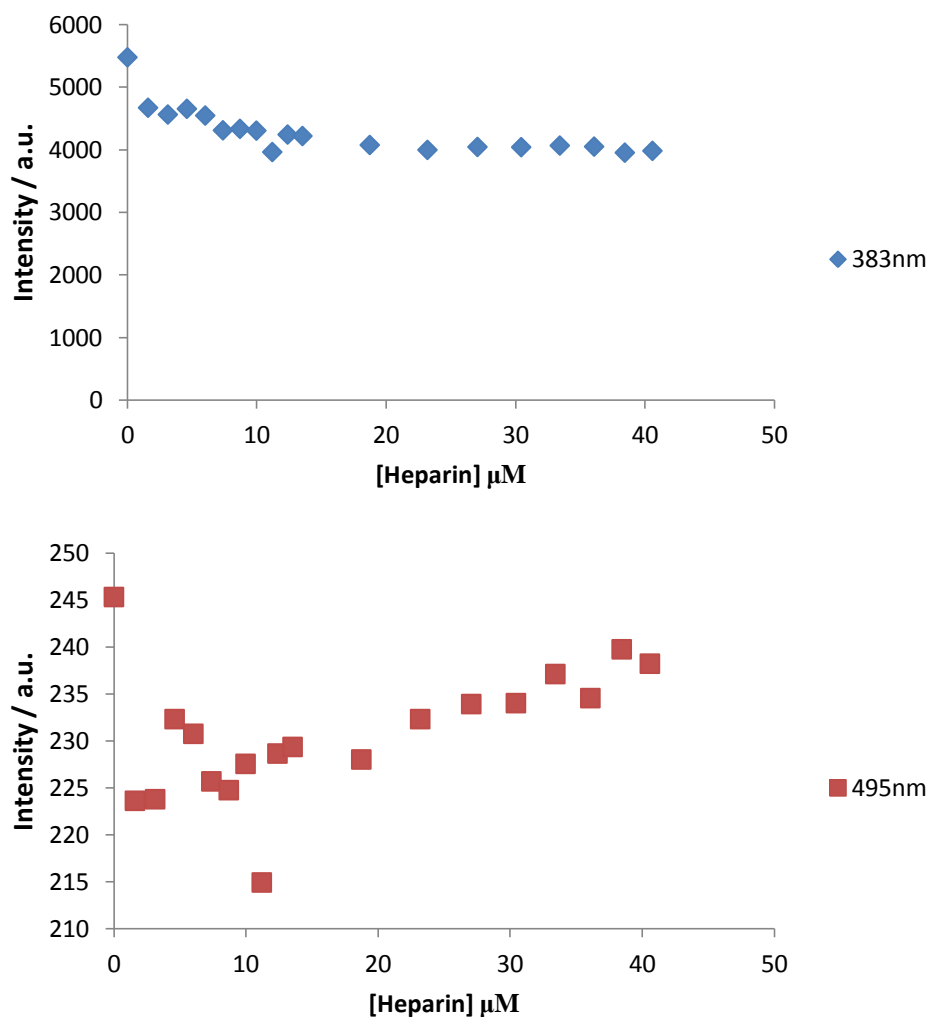


Figure 2.31: Fluorescence intensities extracted at 383 nm (Top) and 495 nm (Bottom) for the titration of heparin into Py-DAPMA in buffer.

By treating the data extracted at 383 nm and 495 nm, these compounds can be demonstrated to sense heparin in buffer solution through a ratiometric (dual-wavelength) approach. The emission intensity ratio, I_{495}/I_{383} , increases as the concentration of heparin increases. In order to obtain a linear plot, $\log(I_{495}/I_{383})$ was plotted against heparin concentration (**Figure 2.32**). Comparing the ratiometric response for Py-G1 and Py-DAPMA, it is evident that Py-G1 shows the much larger response. This is a result of the switching on of excimer emission by self-assembled multivalent binding leading to a much larger increase in I_{495} and hence giving an order of magnitude difference in the ratio $\log(I_{495}/I_{383})$ for Py-G1. We suggest that this SAMul mode of sensing is novel and has not been previously reported – it may be of general

use for quite a wide range of potential analytes beyond the scope of this heparin binding project. The difference between SAMul and non-SAMul sensing is clear under these conditions. It is evident that the SAMul system (Py-G1) shows better sensing of heparin than the non-SAMul system (Py-DAPMA). In particular there is an effective high sensory response to heparin across the clinically important concentration (1 to 10 μM). In summary, Py-G1 shows a significant advantage in terms of the dynamic range of sensory response due to the pre-formed SAMul nanostructures.

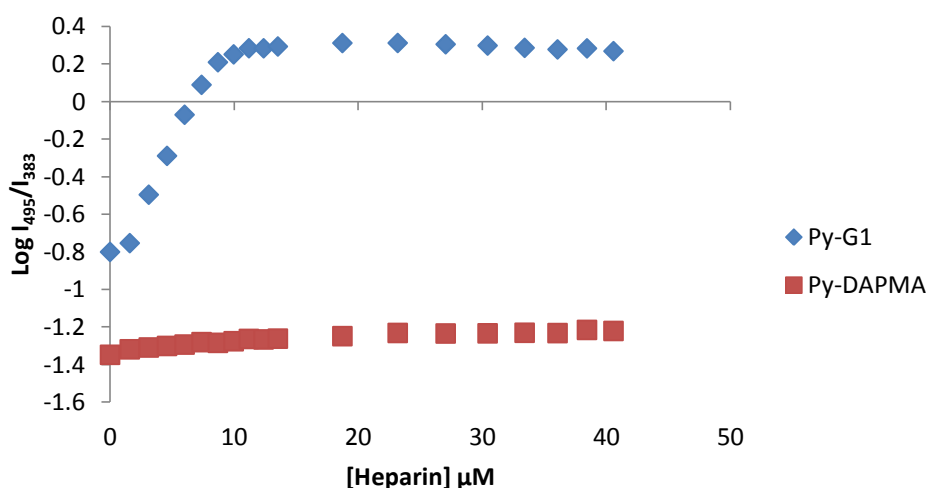


Figure 2.32: The changes of the fluorescence intensity ratio of Py-G1 and Py-DAPMA ($\log(I_{495}/I_{383})$) plotted against increasing heparin concentration in 10 mM Tris HCl buffer with 150mM NaCl buffer.

Binding constants were not determined for these binding events. Heparin is a disperse polyanion which has different binding sites along the polymer chain. As such, as binding processes and the heparin serves were fully saturated the effective binding constant will change for two reasons:

- (i) Different regions of heparin have different binding affinities.
- (ii) as heparin neutralization processes the binding constant will decrease.

As such modelling the data to a single binding constant is challenging and potentially misleading and it is preferred to consider instead the amounts of binder required to patially or fully saturated the of heparin chain as the best indicator of

binding affinity. This also avoids potential problems which may arise from different or poorly defined binding stoichiometries.

It is reasoned that these data are as surrogate for binding constants with greater applicability and without the assumption of a specific, potentially incorrect binding model.

2.2.6 Heparin sensing in 12.5% serum with 20 mM Tris HCl

In order to monitor the effectiveness of these sensors in more clinically relevant conditions we performed a titration study in 12.5% serum with 20 mM Tris HCl. This is typical of a sample of patient blood which has had its red blood cells removed by ultrafiltration and is then added into a sample of the sensor in buffered solution. Clearly 12.5% serum is more competitive than the buffered conditions described above and we wanted to determine the impact of this on the heparin sensing capacity. Both Py-G1 and Py-DAPMA were therefore tested for binding to heparin under these conditions. The interaction of both were investigated by titrating heparin in 12.5% serum with 20 mM Tris HCl into a solution of the binder in 12.5% serum with 20 mM Tris HCl.

In the absence of heparin, self-assembling Py-G1 shows a characteristic monomer emission with peaks at 383 and 400 nm with a small, but observable, excimer emission at 495 nm. Upon addition of heparin, the fluorescence emission intensity at 395 nm decreased while the emission band centred at 495 nm increased (**Figure 2.33**). However the increase in excimer band was significantly less than that observed in buffer alone (i.e. in absence of serum). Indeed the excimer band, which in buffer, never became the dominant feature of the emission spectrum in 12.5% serum. This would therefore suggest that serum disrupts the full self-assembled multivalency of Py-G1 as previously observed for some related systems.^{43, 93} C₂₂-G1 was reported to be a significantly more effective heparin binder than protamine in the presence of electrolyte, but in serum was not as good as protamine.⁴³ We suggest that the presence in serum of albumin proteins, which are well-known to bind to hydrophobic

fragments, can disrupt the self-assembly event and hence act in a competitive way to counteract the SAMul sensing mechanism observed in buffer.

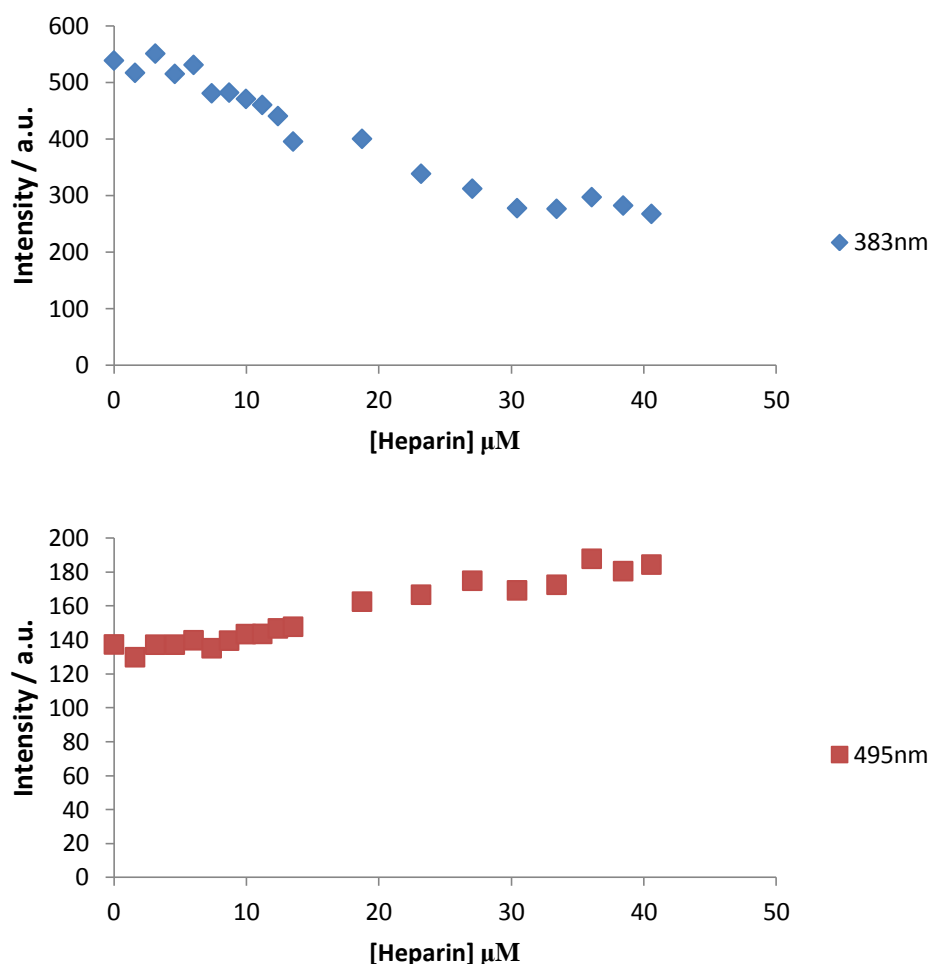


Figure 2.33: Fluorescence intensities extracted at 383 nm (Top) and 495 nm (Bottom) for the titration of heparin into Py-G1 in 12.5% serum with 20 mM Tris HCl.

In 12.5% serum, in the absence of heparin, like in buffer, self-assembling Py-DAPMA shows a characteristic monomer emission with peaks at 383 and 400 nm without significant excimer emission at 495 nm. Upon addition of heparin, the fluorescence emission intensity at 395 nm decreased while the emission band centred at 495 nm increased slightly (**Figure 2.34**). Clearly there is more of a response in 12.5% serum for this compound than there was in buffer. This may surprisingly suggest that the pyrene is somewhat better able to detect the presence of heparin under these conditions.

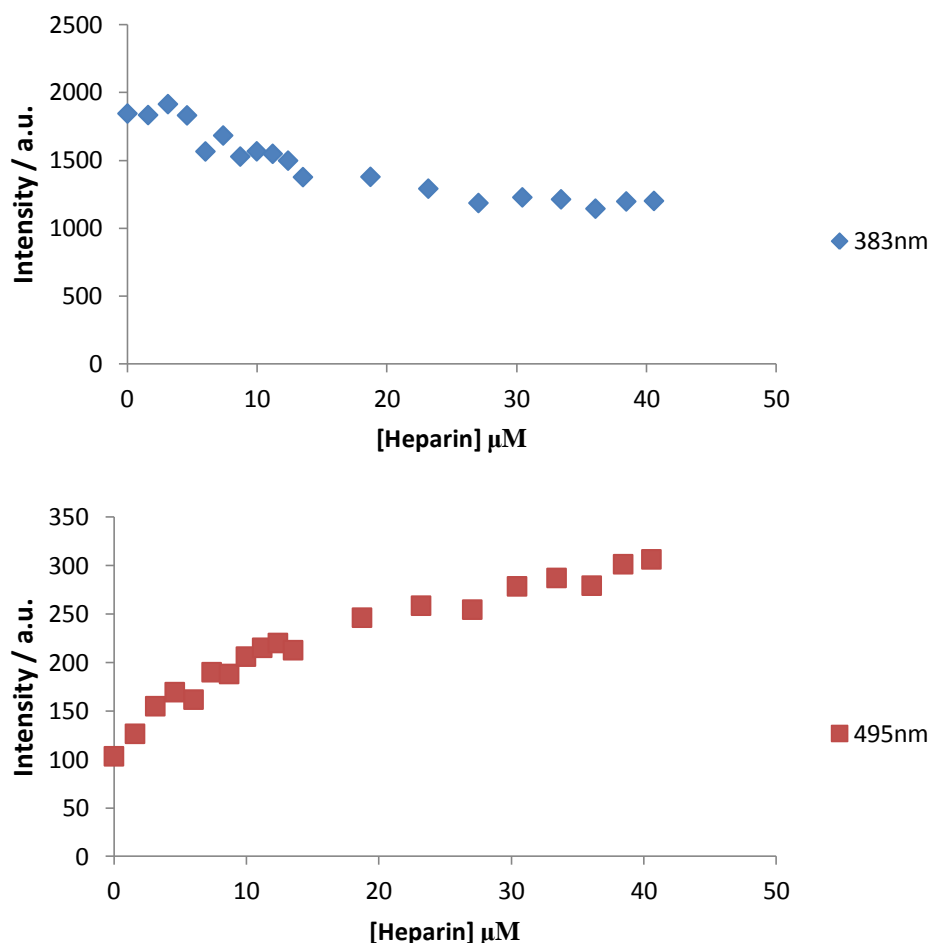


Figure 2.34: Fluorescence intensities extracted at 383 nm (Top) and 495 nm (Bottom) for the titration of heparin into Py-DAPMA in 12.5% serum with 20 mM Tris HCl.

Since serum disrupts the full self-assembled multivalency of Py-G1, this compound no longer shows a significant advantage for sensing heparin over Py-DAPMA. Indeed Both Py-G1 and Py-DAPMA showed similar responses (**Figure 2.35**), with a modest increase in the intensity at 495 nm for both Py-G1 (**Figure 2.33**) and Py-DAPMA (**Figure 2.34**). This can be explained by a model in which these non-assembled sensors bind to heparin, subsequently bringing pyrene units into closer proximity and encouraging a degree of formation of an excimer band. This reflects some less-ordered self-assembly induced on the heparin backbone, rather than full self-assembled multivalency prior to, and reinforced by, heparin binding of the heparin sensors. However, both Py-G1 and Py-DAPMA were effective sensors across the clinically relevant concentration range of 1 to 10 μM in serum.

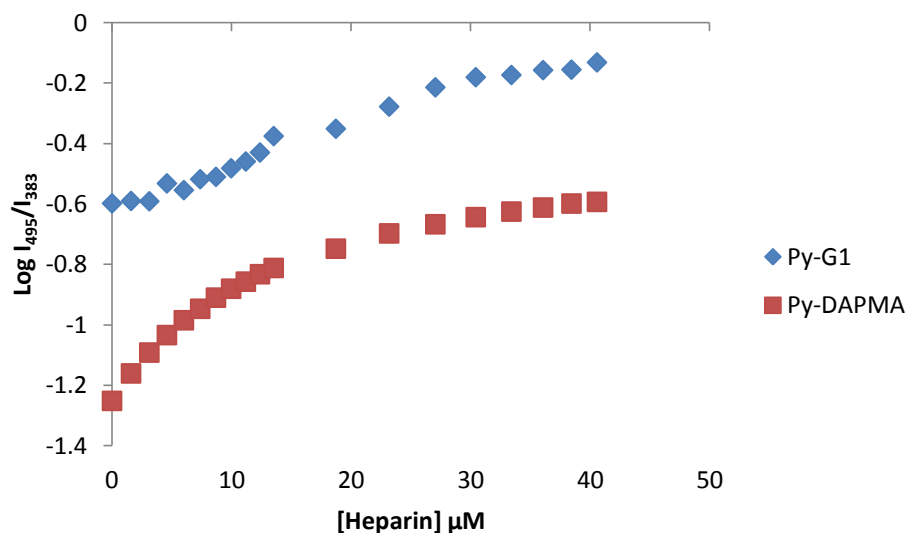


Figure 2.35: The changes of the fluorescence intensity ratio of Py-G1 and Py-DAPMA ($\log(I_{495}/I_{383})$) plotted against increasing heparin concentration in 12.5% serum with 20 mM Tris HCl.

2.2.7 Heparin sensing in 100% serum

After testing Py-G1 and Py-DAPMA in 12.5% serum, the ability of these sensors to detect heparin in 100% serum was then examined. Unlike in most studies of heparin sensing with pyrene derivatives,^{89-91, 113, 114} all components were dissolved in 100% serum. This was to simulate the condition of an in-line sensor which must detect heparin with only very limited sample treatment (i.e. with ultrafiltration to remove red blood cells but no dilution steps). In 100% serum, for Py-G1, both monomer emission with peaks at 383 and 400 nm and excimer emission with a peak at 495 nm did not change with increasing concentrations of heparin (**Figure 2.36**). This same was also observed for Py-DAPMA (**Figure 2.37**).

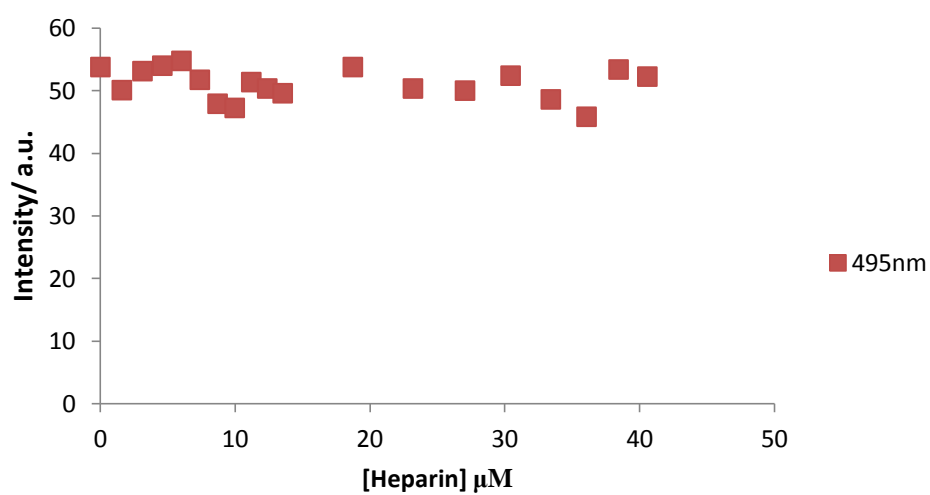
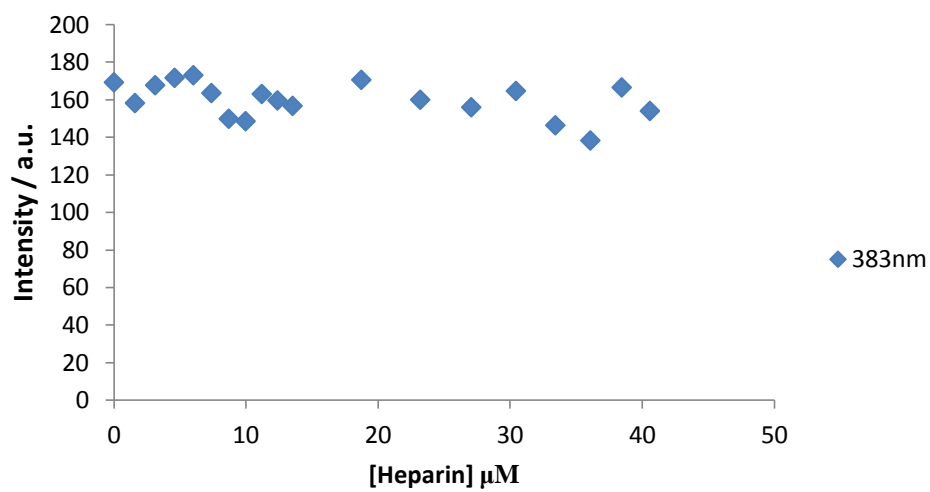


Figure 2.36: Fluorescence intensities extracted at 383 nm (Top) and 495 nm (Bottom) for the titration of heparin into Py-G1 in 100% serum.

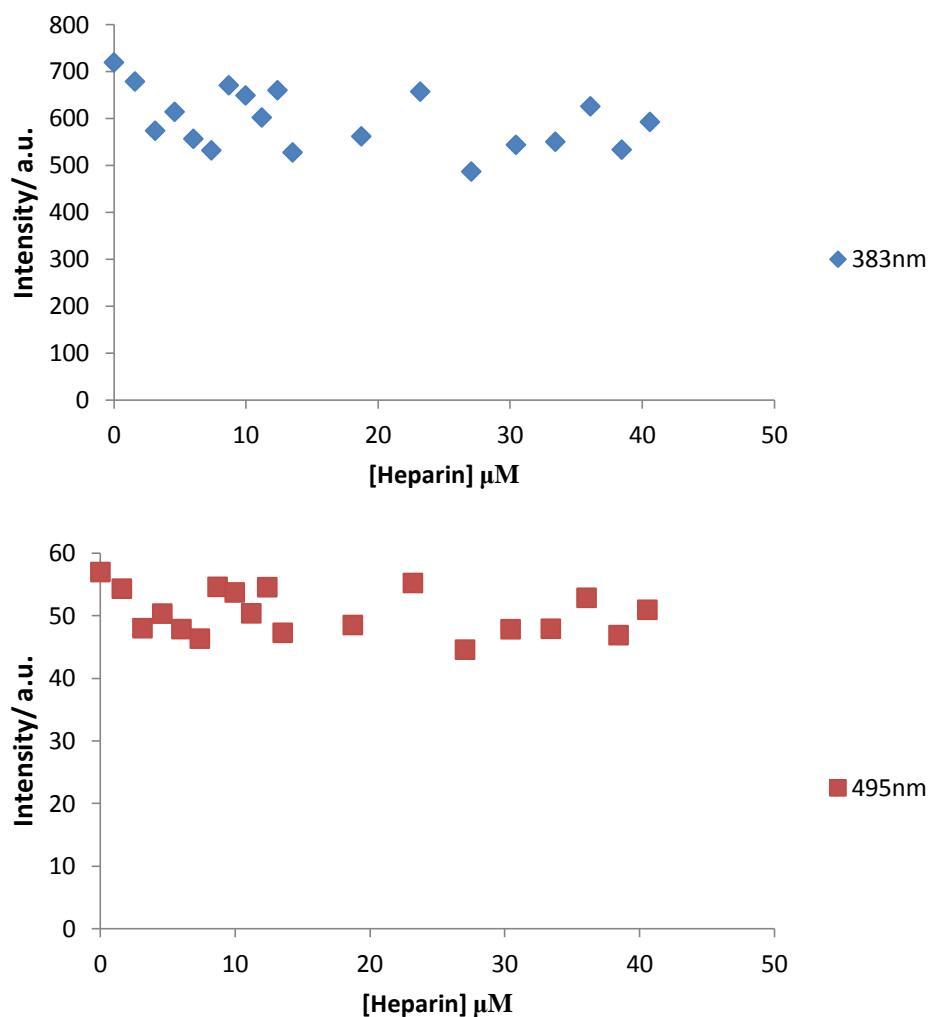


Figure 2.37: Fluorescence intensities extracted at 383 nm (Top) and 495 nm (Bottom) for the titration of heparin into Py-DAPMA in 100% serum.

From **Figure 2.38**, we can see there were no observable changes in the $\log(I_{495}/I_{383})$ plot in either compound. At this point, it could be either the background competition by albumin proteins (etc.) binding too strongly to all of the hydrophobic parts and hence preventing any excimer from being established and limiting heparin binding or the fluorescence scattering from serum itself meaning we can't detect anything. Therefore, we performed the test with elevated concentrations of both the sensors and heparin in order to determine the impact of concentration on the sensing array in these highly competitive conditions.

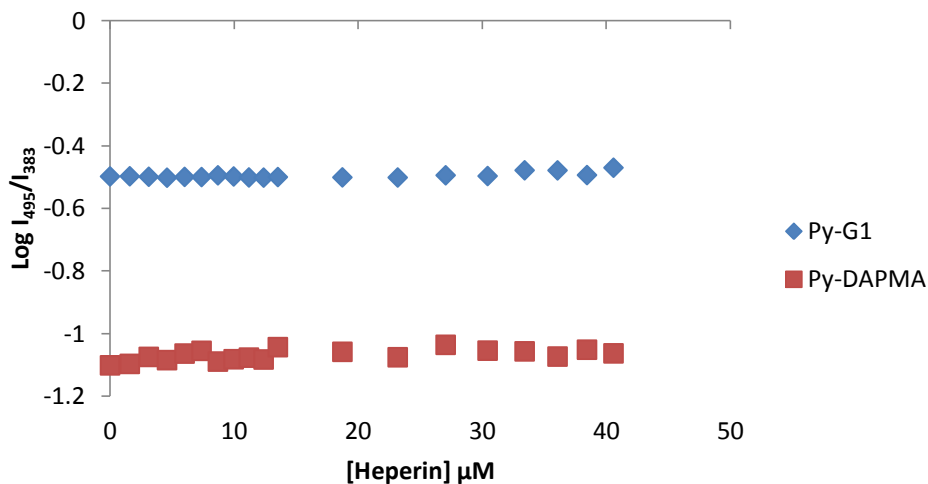


Figure 2.38: The changes of the fluorescence intensity ratio of Py-G1 and Py-DAPMA ($\log(I_{495}/I_{383})$) plotted against increasing heparin concentration in 100% serum.

2.2.8 Heparin sensing in 10 mM Tris HCl with 150 mM NaCl buffer at elevated concentrations.

Since in 100% serum, no response to heparin was observed, we decided to probe these sensors at ca. seven times elevated concentrations (Py-G1 213 μM , Py-DAPMA 426 μM). This may also provide the answer whether it was background competition by albumin proteins or fluorescence scattering by serum itself that limited detection. Once again, we performed the assay in buffer, 12.5% serum and 100% serum.

Under these elevated concentration conditions in buffer, Py-G1 showed a characteristic monomer emission with peaks at 383 and 400 nm with a small, but observable, excimer emission at 495 nm. Upon addition of heparin, the fluorescence emission intensity at 395 nm decreased while the emission band centred at 495 nm increased significantly (**Figure 2.39**). This was attributed to the formation of pyrene excimers induced by heparin binding. Strong “switch-on” excimer emission could be seen using the naked eye when the sample was under UV irradiation.

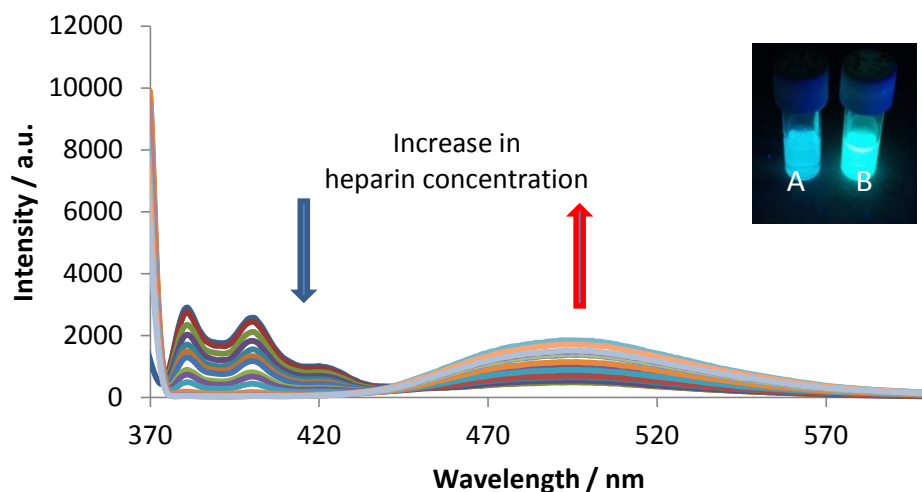


Figure 2.39: Fluorescence spectra of Py-G1 (213 μ M) on addition of heparin. The inset shows the photographs of a solution of Py-G1 without heparin (A) and with heparin (B) in buffer.

When looking much more closely at the change of intensity at 495 nm during the titration, it was clear that it initially decreased first and then increased back again. The initial drop in intensity may suggest that the self-assembled system was disrupted when a small amount of heparin was added. However, when more heparin was added into the system, this gave rise to additional aggregation which caused a large increase in intensity (SAMul sensing).

Overall, however, these observations are in-line with those in 100% buffer at lower concentrations.

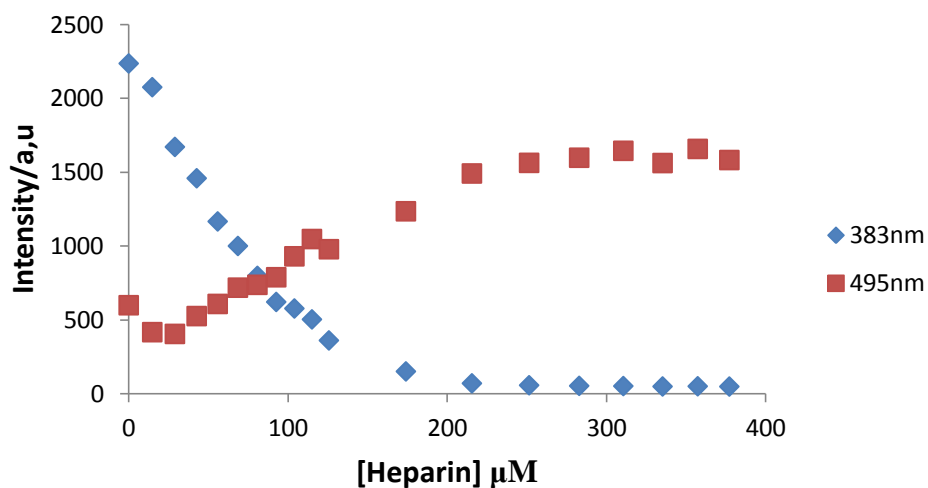


Figure 2.40: Fluorescence intensities extracted at 383 nm and 495 nm for the titration of heparin into Py-G1 (213 μM) in buffer.

On titrating Py-DAPMA (426 μM) with heparin under the same conditions, although the fluorescence emission at 395 nm decreased in intensity, the band at 495 nm was relatively unaffected (**Figure 2.42**) This is the same as what was observed for Py-DAPMA at low concentrations in buffer. Clearly, on binding the pyrene groups are still not brought into close proximity and no excimer is formed under these conditions. However, there was a ‘naked eye’ change in the fluorescence emission when the sample is under UV irradiation, as the fluorescence changed colour from somewhat more ‘purple’ to ‘green’ primarily due to the loss of the intense monomer emission band (**Figure 2.41**). It is clear therefore that even at elevated concentrations, Py-DAPMA remains unable to exhibit a true SAMul response in buffer – while Py-G1 is a useful sensor with a clear SAMul sensing mechanism.

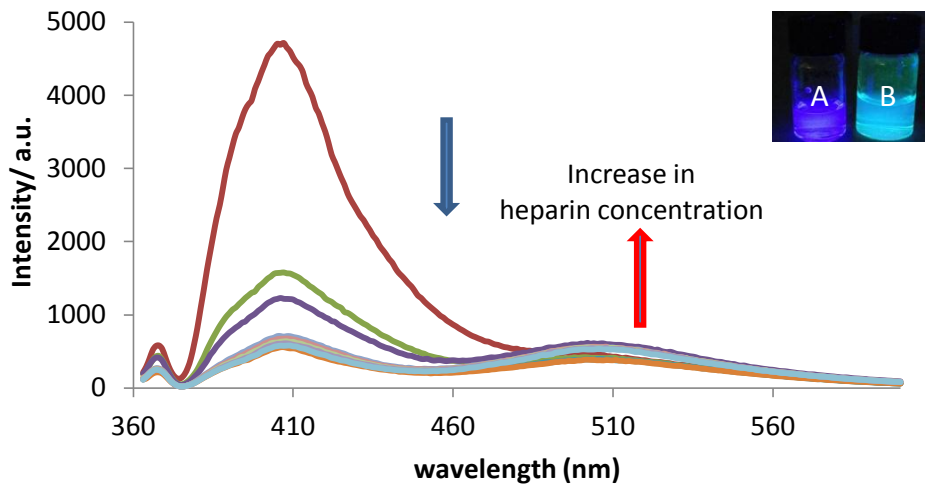
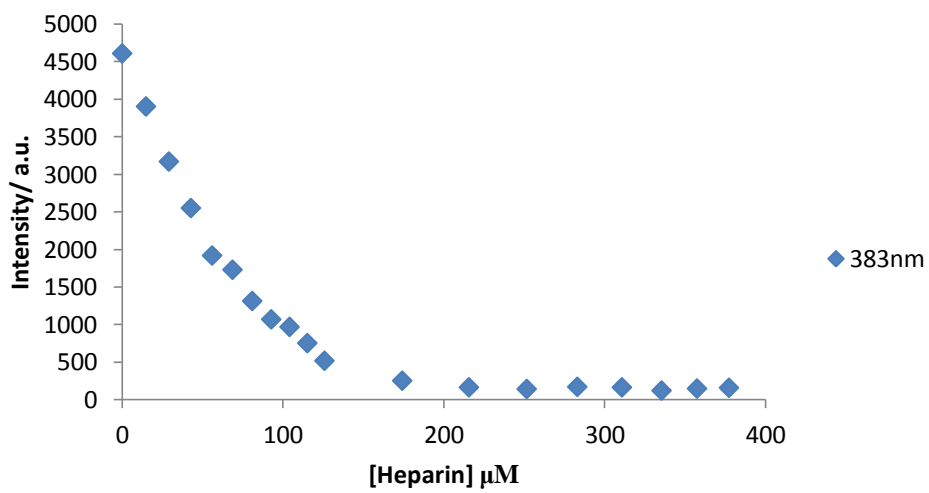


Figure 2.41: Fluorescence spectra of Py-DAPMA on addition of heparin. The inset shows the photographs of a solution of Py-DAPMA without heparin (A) and with heparin (B) in buffer.



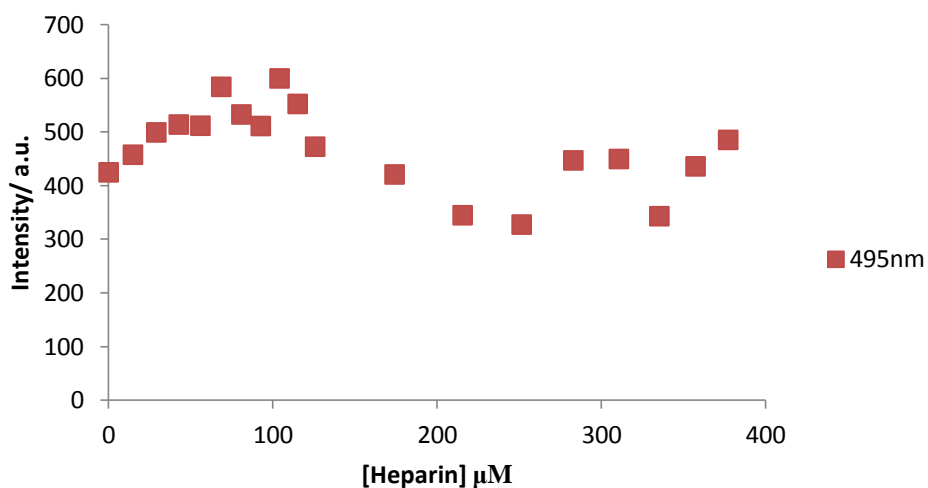


Figure 2.42: Fluorescence intensities extracted at 383 nm (Top) and 495 nm (Bottom) for the titration of heparin into Py-DAPMA (426 μM) in buffer.

Comparing the ratiometric response for Py-G1 and Py-DAPMA (**Figure 2.43**), it is evident that Py-G1 shows the larger response. This is a result of the very significant switching on of excimer emission induced by self-assembled multivalent binding of Py-G1 to heparin leading to a much larger increase in I_{495} and hence giving an order of magnitude difference in the ratio $\log(I_{495}/I_{383})$. The difference between SAMul and non-SAMul sensing is clear even under these elevated concentration conditions. Both sensors showed a linear response to heparin under these assay conditions in concentrations from 10-150 μM (Py-DAPMA) and 10-200 μM (Py-G1). Given that overall the concentration of DAPMA ligand was the same in each case, the fact that Py-G1 has a larger concentration range response than Py-DAPMA would suggest that more of the DAPMA ligands can be bound by heparin for Py-G1 than is the case for Py-DAPMA. This would suggest that the SAMul approach is a more effective way of displaying ligands to ensure they can more effectively interact with heparin polyanions.

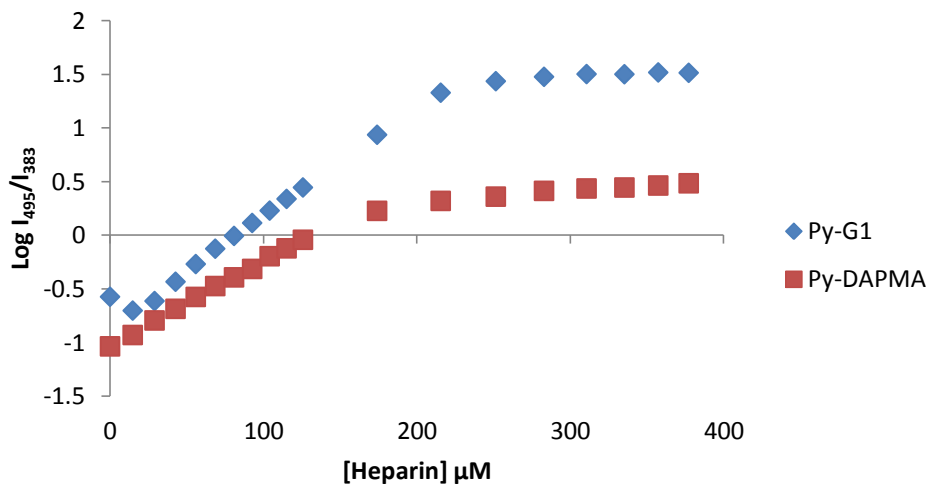


Figure 2.43: The changes of the fluorescence intensity ratio of Py-G1 and Py-DAPMA ($\log(I_{495}/I_{383})$) plotted against increasing heparin concentration in buffer.

2.2.9 Heparin sensing in 12.5% serum with 20 mM Tris HCl at elevated concentrations

We then performed this these elevated concentration assay in 12.5 % serum with 20 mM Tris HCl. This assay conditions were the same as those employed in the lower concentration regime.

In the absence of heparin, self-assembling Py-G1 shows a characteristic monomer emission, with peaks at 383 and 400 nm with a small, but observable, excimer emission at 495 nm. Upon addition of heparin, the fluorescence emission intensity at 395 nm decreased while the emission band centred at 495 nm increased slightly (**Figure 2.44**). This would suggest that serum disrupts the full self-assembled multivalency of Py-G1. However, unlike when the assay was performed at lower concentrations, in this case $I_{495} > I_{383}$ once heparin is bound which indicated that increasing the concentration has significantly improved the ability of the system to self-assemble and yield excimer emission in these more competitive conditions, once heparin binding has taken place.

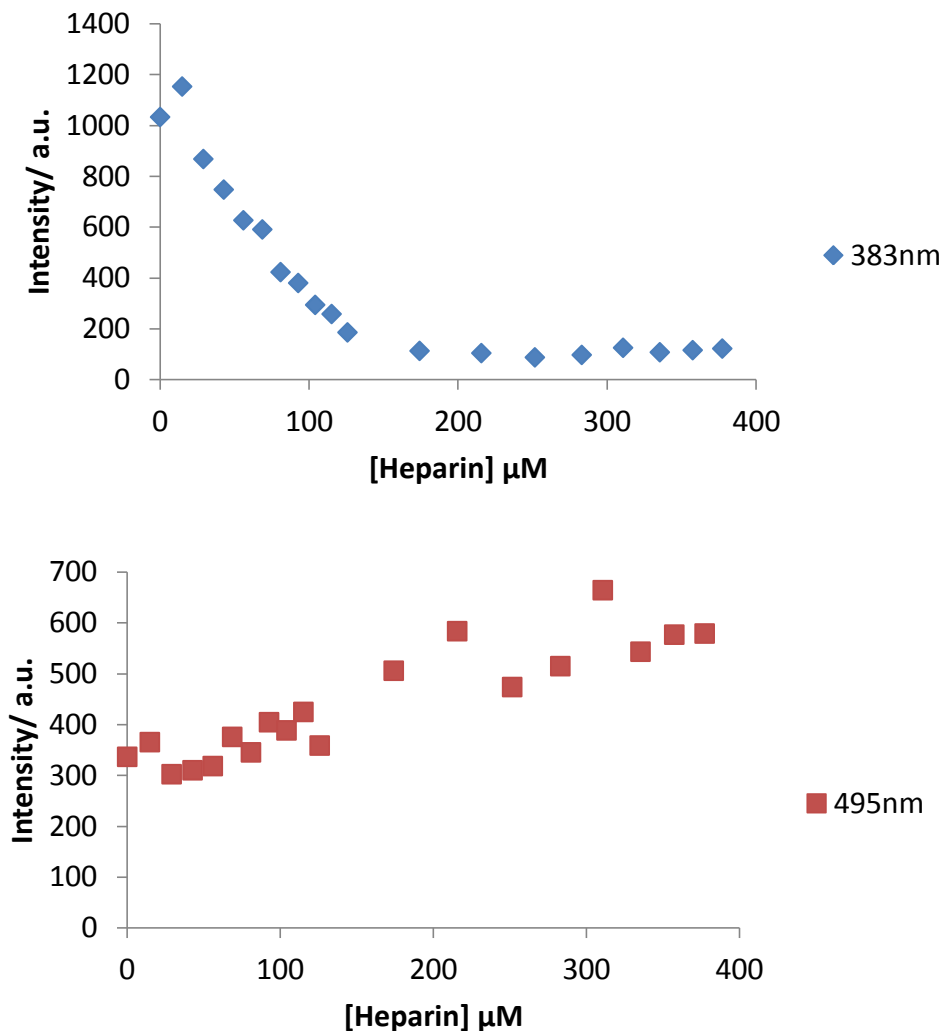


Figure 2.44: Fluorescence intensities extracted at 383 nm (Top) and 495 nm (Bottom) for the titration of heparin into Py-G1 in 12.5% serum with 20 mM Tris HCl.

In the absence of heparin, self-assembling Py-DAPMA shows a characteristic monomer emission with peaks at 383 and 400 nm. There is also some small amount of excimer emission at 495 nm, possibly encouraged by the significantly larger concentration supporting some self-assembly. On addition of heparin, the fluorescence emission intensity at 395 nm decreased while the emission band centred at 495 nm increased (**Figure 2.45**). We suggest that the increase in intensity at 495 nm was due to excimer emission of Py-DAPMA once bound to heparin. As for Py-G1, on binding to heparin the excimer peak became larger than the monomer.

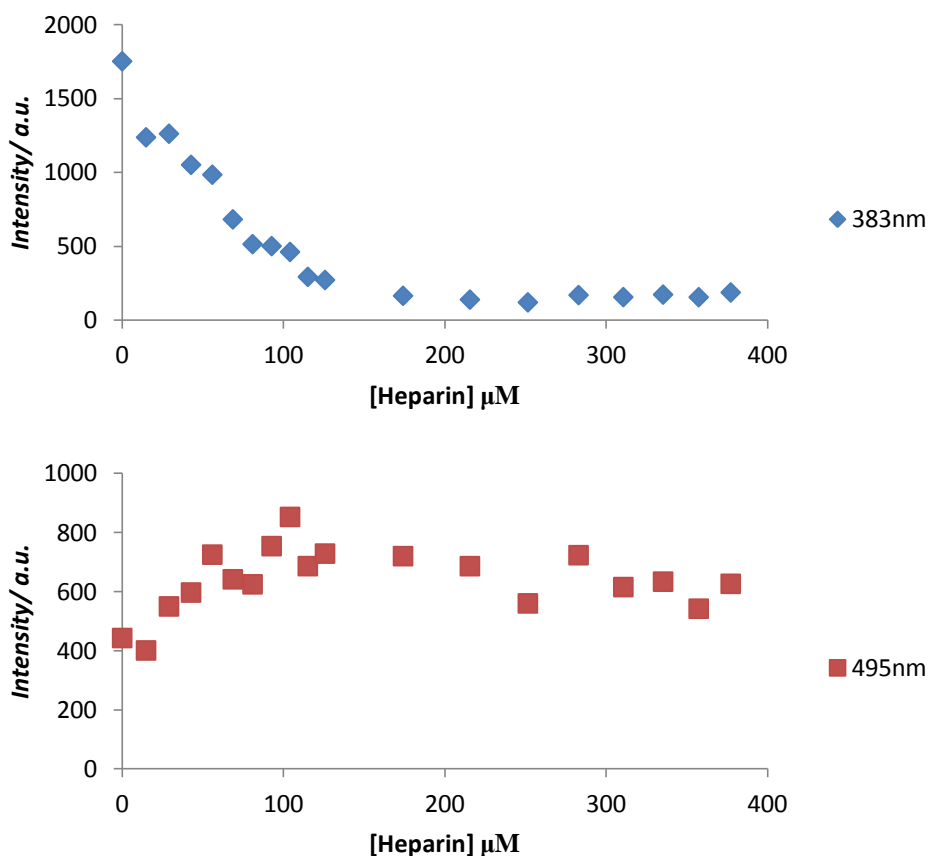


Figure 2.45: Fluorescence intensities extracted at 383 nm (Top) and 495 nm (Bottom) for the titration of heparin into Py-DAPMA (426 μM) in 12.5% serum with 20 mM Tris HCl.

Interestingly, both Py-G1 and Py-DAPMA showed similar ratiometric responses (Figure 2.46), which would support the view that the presence of serum to some extent limits the SAMul sensing response observed for Py-G1 under buffered conditions. Nevertheless, for both sensors, $\log(I_{495}/I_{383}) > 0$ in the presence of heparin which suggests that after binding to heparin, excimer emission dominates and some self-assembly was in operation. This is in contrast to the lower concentration studies in which $\log(I_{495}/I_{383})$ remained < 0 , indicating that the extent of sensor self-assembly was relatively limited. We therefore suggest that at higher concentration, self-assembly is now better able to compete against disruptive agents such as albumin proteins.

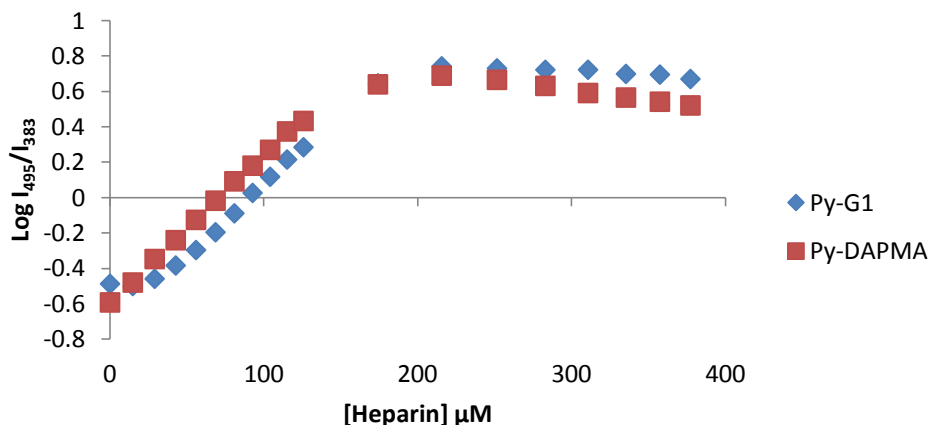


Figure 2.46: The changes of the fluorescence intensity ratio of Py-G1 (213 μM) and Py-DAPMA (426 μM) ($\log(I_{495}/I_{383})$) plotted against increasing heparin concentration in 12.5% serum with 20 mM Tris HCl.

2.2.10 Heparin sensing in 100% serum at elevated concentrations

We then studied these sensors in the most challenging conditions of 100% serum, at elevated concentrations. In 100% serum, monomer emission of Py-G1 with peaks at 383 and 400 nm decrease and the excimer emission with peak at 495 nm increased slightly on addition of heparin (**Figure 2.47**). This clearly suggested that Py-G1 was able to sense heparin in 100% serum, unlike in the low concentration regime. However, it is also clear that there is less evidence of SAMul sensing in 100% serum than there was in 12.5% serum or simple buffered conditions.

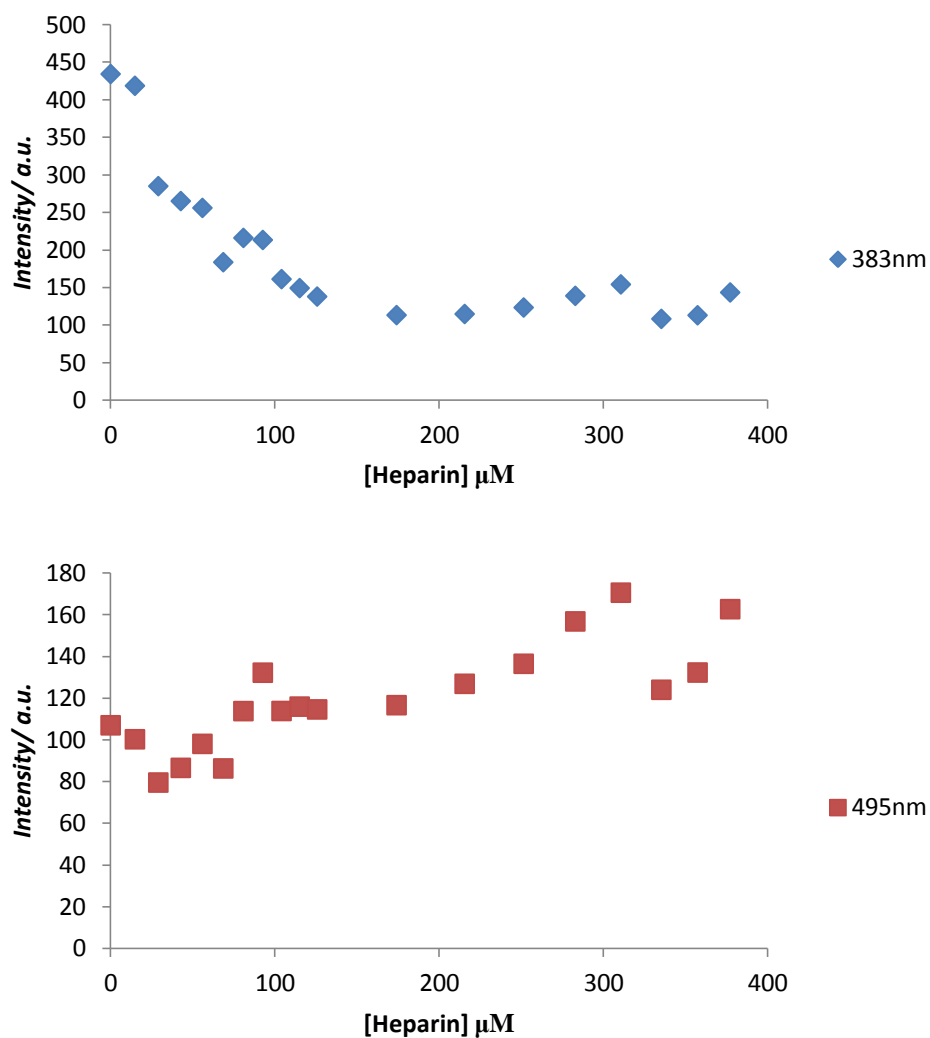


Figure 2.47: Fluorescence intensities extracted at 383 nm (Top) and 495 nm (Bottom) for the titration of heparin into Py-G1 (213 μM) in 100% serum.

In 100% serum, monomer emission of Py-DAPMA with peaks at 383 and 400 nm decreased and excimer emission with a peak at 495 nm increased slightly in addition of heparin (**Figure 2.47**). The behaviour, was similar to that observed for Py-G1 in 100% serum. This would suggest that full SAMul sensing is not occurring, but at elevated concentrations both Py-G1 and Py-DAPMA can undergo some self-assembly on binding to heparin allowing detection of this polyanion via fluorescent output.

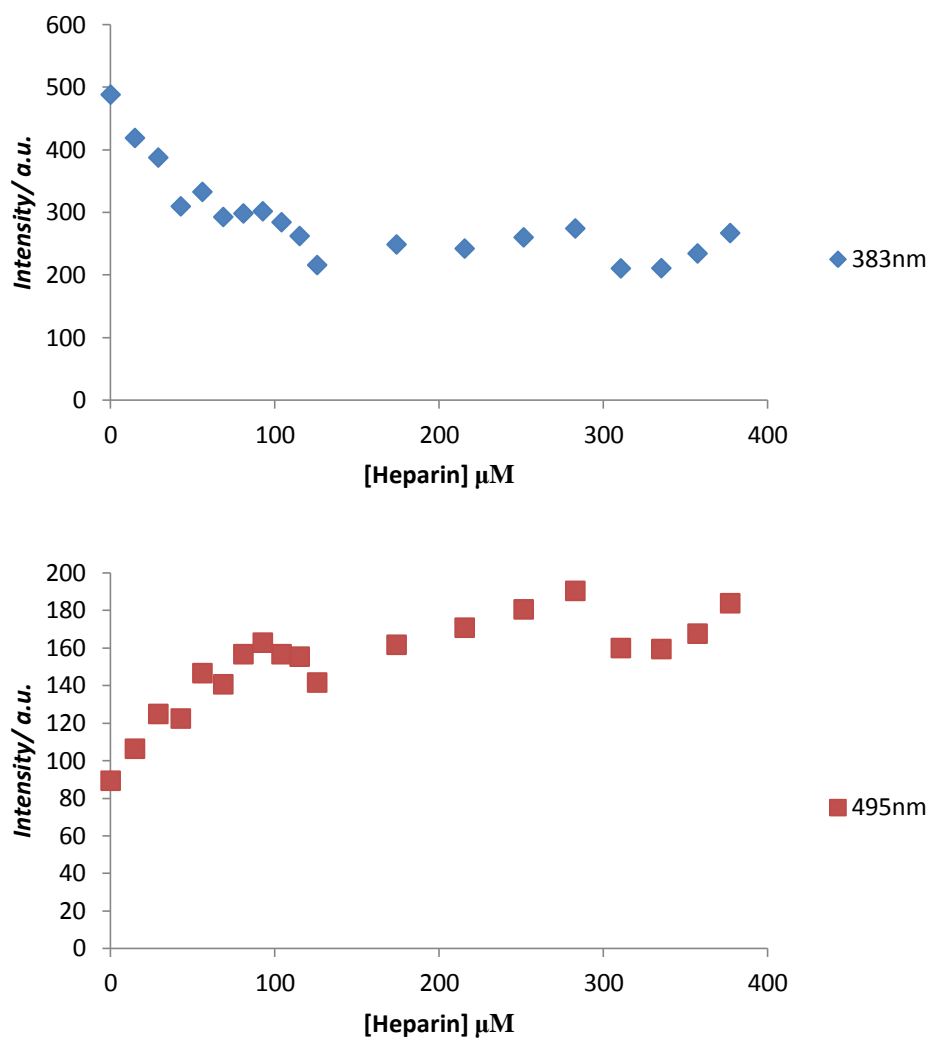


Figure 2.48: Fluorescence intensities extracted at 383 nm (Top) and 495 nm (Bottom) for the titration of heparin into Py-DAPMA (426μM) in 100% serum.

Once again, considering the ratiometric response, a linear response is observed (in this case better for Py-G1 than Py-DAPMA) (**Figure 2.49**). The dynamic range is less than observed in buffer for these compounds, presumably due to competition from other binding and fluorescence events in serum. However, it is clear from this assay that Py-G1 in spite of losing its large switch-on excimer response in serum, could still act as an effective heparin sensor under these elevated concentration conditions. In contrast to binding in 12.5% serum, $\log(I_{495}/I_{383})$ only just exceeded 0 for Py-G1 – this would suggest that, as expected, there is less self-assembly of the pyrene sensors in 100% serum than that was in 12.5% serum. However, it suggests that excimers are still

favoured for Py-G1 bound to heparin.

The study also indicates the, perhaps surprising, ability of even a very simple sensor (Py-DAPMA) to respond to heparin. Synthetically simple sensors have significant advantages for potential clinical application. Overall, it is remarkable that a simple dication (Py-DAPMA) and tetracation (Py-G1) can respond to heparin polyanions in such highly competitive media. It should however be noted that unlike Py-G1, for Py-DAPMA $\log(I_{495}/I_{383})$ did not exceed 0 in the presence of heparin, Nevertheless, we propose that the amphiphilic ligand design, and the ability of pyrene to assemble *after* binding to heparin, plays a significant role in assisting heparin sensing in 100% serum.

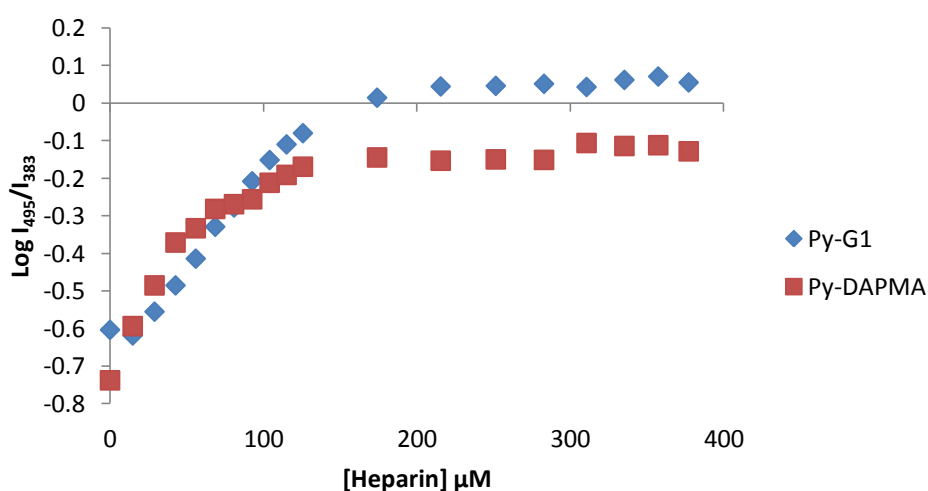


Figure 2.49: The changes of the fluorescence intensity ratio of Py-G1 (213 μM) and Py-DAPMA (426 μM) ($\log(I_{495}/I_{383})$) plotted against increasing heparin concentration in 100% serum

2.3 Conclusion and future work

Both Py-DAPMA and Py-G1 can act as effective heparin sensors in competitive media using a ratiometric fluorescence sensing approach, which is desirable for a clinical setting in terms of detecting this biologically important polyanion.

In buffered aqueous solution, self-assembled multivalency (SAMul) of Py-G1 into

pre-formed nanostructures provides it with a significant advantage in terms of the dynamic range of sensory response and its ability to give a naked eye response to polyanionic heparin (in comparison to non-assembling Py-DAPMA). We believe this is a new mechanism of sensing which may be broadly applicable for a wide range of SAMul ligands binding to a wide variety of target analytes in buffer.

In the presence of serum, both ligands can detect heparin ratiometrically with similar responses. In each case, a degree of aggregation appears to take place after these cations have bound to heparin, which helps mediate the sensing response. These sensors, particularly synthetically simple Py-DAPMA, may also have roles to play in heparin detection technologies. However, full SAMul sensing is not observed in the presence of serum, primarily due to competitive disassembly caused by the presence of albumin proteins. This conclusion is supported by the ability of the sensors to be effectively detect heparin in 100% serum at elevated concentrations. If the self-assembly event could be further reinforced at lower concentrations, this should give rise to SAMul sensors which are capable of operating at clinically-relevant concentrations in highly competitive conditions – including human serum.

For future work, binding different polyanions such as chondroitin sulfate, hyaluronic acid, siRNA, DNA, etc. and test the selectivity of the SAMul sensors towards them. Also, enhancing the stability of the self-assemblies formed in the presence of serum and thus enhance the SAMul sensing.

Chapter 3 Effect of Chirality on Self-Assembled Multivalent (SAMul) Biological Polyanion Binder

3.1 Introduction

In Chapter 2, the primary focus was on developing heparin sensors. However, there is also an acute need for heparin binders which do not necessarily directly report on the heparin binding event. Such systems are potential replacements for the clinical agent protamine which has a number of side effects. Furthermore, understanding the way in which such systems bind to biologically important polyanionic targets is of fundamental importance in terms of molecular recognition of complex biological targets.

3.2 Heparin binder

Many groups have attempted to synthesise alternative heparin rescue agent including low molecular weight protamine,⁶⁰ small molecules such as surfen¹¹⁵ and foldamers,¹¹⁶ peptides,^{117, 118} antibodies¹¹⁹ and lactoferrins.¹²⁰

Cunsolo *et al.* reported two polycationic calix[8]arenes (**Figure 3.1**, left) which are capable of binding to heparin in blood.^{121, 122} A dye displacement assay in conjunction with NMR titration data indicated that both compounds were able to bind to heparin as effectively, in some cases more effectively, than protamine in solution. It was proposed that the flexibility of the scaffold maximized heparin binding as the cationic groups had some freedom to optimize their individual interactions with the biopolymer (**Figure 3.1**, right) and an 'octopus-like' chelate effect was observed computationally. Blood clotting assays revealed some interesting differences between the calix[8]arenes; when unfractionated heparin was used, the lysine based system, **1**, performed most effectively whereas, in the case of low molecular weight heparin the amine derivative, **2**, with a lower overall positive charge, outperformed both the lysine calix[8]arene and protamine.¹²¹ The same group then successfully grafted the calix[8]arene **1** onto a polymer matrix. The system was still able to effectively reverse the effects of heparin in blood making it a potential blood filter for the extracorporeal removal of heparin.¹²²

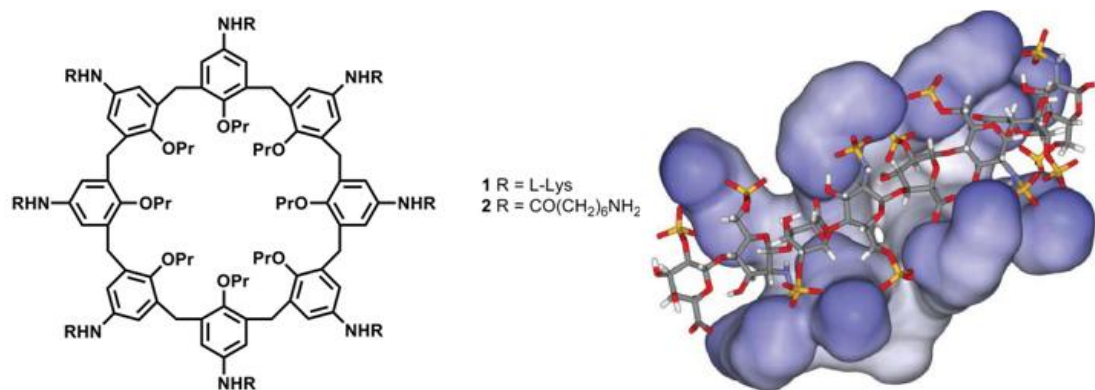


Figure 3.1: Structure of polycationic calix[8]arenes (left) and space-filled species represents calix[8]arene, stick model represents heparin. Figure adapted from¹²¹

With a different application in mind, Toth *et al.* employed dendrons, (which are branched, well-defined, wedge-like structures)¹²³ with a lipophilic core as potential heparin binding and delivery agents (**Figure 3.2**).¹²⁴ They found that the lysine derivative was much more effective at increasing the activity of heparin, indicated by an increased anti-factor Xa activity in rats, whereas the arginine dendron had an inhibitory effect. They proposed that the lysine dendron was much more effective at releasing its heparin cargo once adsorbed while the arginine derivative acts as a relatively effective heparin reversal agent.¹²⁴

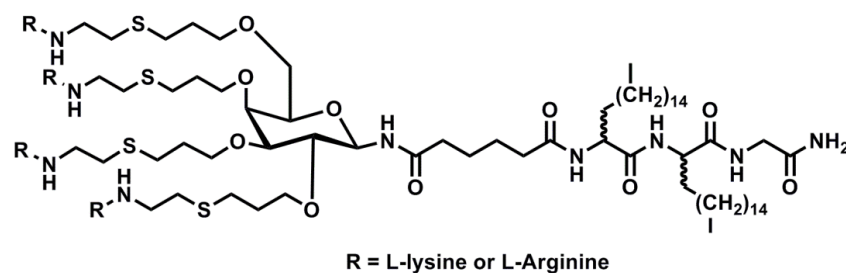


Figure 3.2: Structure of lipophilic lysine and arginine functionalised dendrons.¹²⁴

In 2006, Rajangam *et al.* reported a complex lipopeptide (**Figure 3.3**) capable of self-assembling into heparin binding cylindrical micellar nanostructures.¹²⁵ Structurally, it consisted of three lysine and one arginine group as the cationic hydrophilic region of the self-assembling lipopeptide, while an n-alkyl chain acted as the hydrophobic region and therefore the molecule is amphiphilic and has self-assembly potential. *In vivo*, the nanostructures stimulated the formation of new blood vessels (angiogenesis).

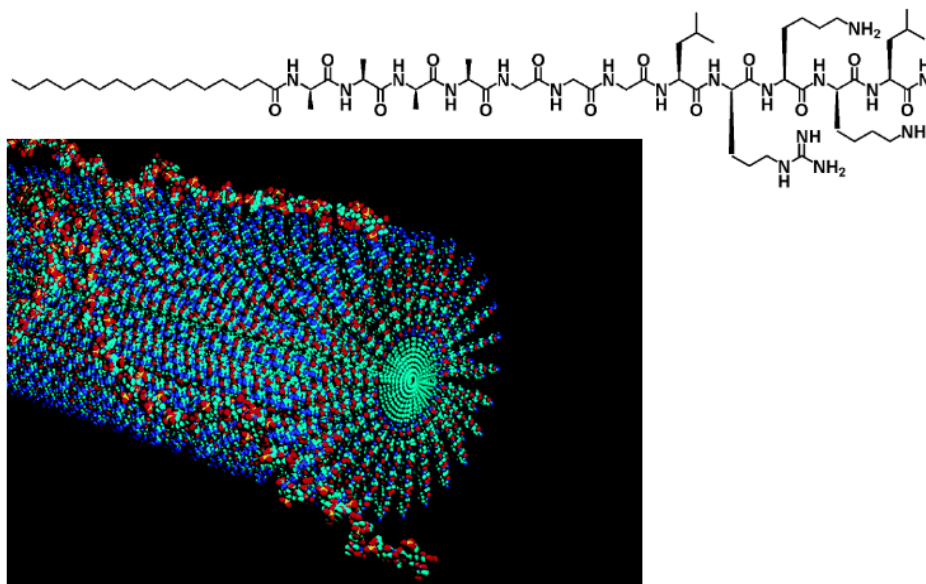


Figure 3.3: A self-assembling heparin-binding lipopeptide (top) and Schematic representation of heparin-nucleated nanofiber (bottom) from Rajangam *et al.*¹²⁵

In 2011, Rodrigo *et al.* reported C₂₂-G1 (**Figure 3.4**, top) as a self-assembling dendron for heparin binding.⁹³ C₂₂-G1 contains peripheral amines that are protonated at physiological pH, allowing electrostatic binding to polyanionic heparin. These amines are supported on the degradable, biocompatible scaffold first introduced by Hult, Fréchet, and co-workers.⁹⁴⁻⁹⁸ Straight-chain alkanes act as hydrophobic units located at the focal point of the structure, driving the self-assembly of the ligands into a larger nanoscale architecture in aqueous media as a consequence of the hydrophobic effect. C₂₂-G1 was able to self-assemble in aqueous conditions at concentrations above ca. 4 μM. TEM Images of dried samples of C₂₂-G1 showed micellar assemblies sized at approximately 8.5 (± 1.5) nm in diameter (**Figure 3.4**, bottom left). TEM also appeared to show micelles aligned in an ordered fashion across the polysaccharide surface of heparin (**Figure 3.4**, bottom right). C₂₂-G1 was reported to be a significantly more effective heparin binder than protamine in the presence of electrolyte.⁹³ However, it was reported later that the performance in serum was not as good as protamine, presumably due to disruption of the self-assembly event.⁴³

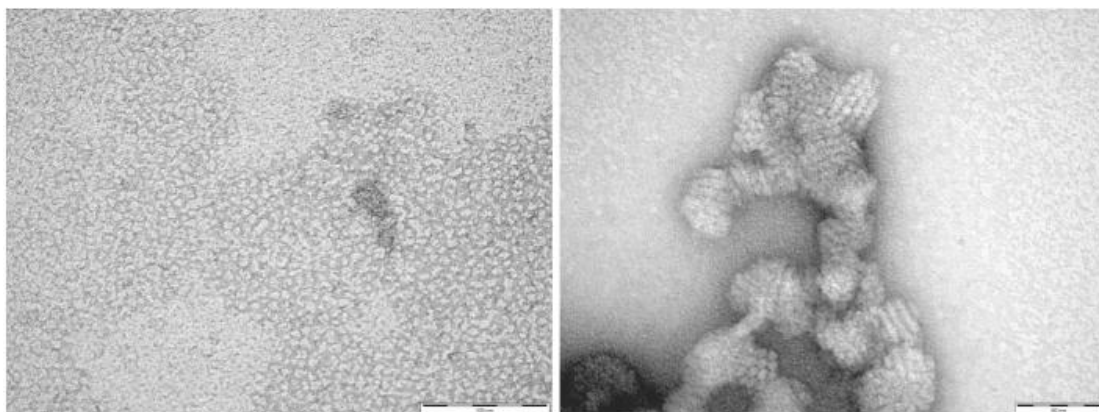
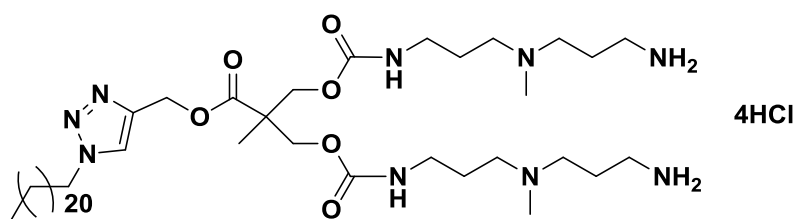


Figure 3.4: Structure of C₂₂-G1 (top), TEM images in absence (bottom left) and presence (bottom right) of heparin.

3.3 DNA binder

In terms of understanding the fundamentals of polyanion binding, it is of some interest and importance to compare the binding of heparin to that of other polyanionic targets such as DNA (Deoxyribonucleic acid). DNA, exists in double helical form,¹² one of the best known self-assembling structures in biological systems. The interest in synthetic DNA binders has been driven by research into gene therapy. The treatment of disease by the transfer of genetic material into a patient's cells, was conceptualized in 1972 by Friedmann and Roblin.^{126, 127} This started from the development of virus-based methods for transforming mammalian cells in the 1960s and the advent of recombinant DNA technology in the 1970s which offered the prospect of genetic medicines that could compensate for errors in an individual's DNA sequence associated with disease. Even through virus-based methods are effective, *in vivo* side effects such as development of leukaemia,¹²⁸ severe immune response and even patient death¹²⁹ have been observed. As a result non-virus-based methods have been gaining attention with potential safety advantages and a greater degree of control over toxicity. This section provides a brief insight into a few key systems.

Cationic polymers bind DNA through multiple electrostatic interactions (**Figure 3.5**).¹³⁰ For example, Poly(L-lysine) (PLL) has been used as a gene delivery vehicle for more than 20 years due to the fact that it is relatively biocompatible and can be easily degraded by cells.¹³¹ Polyethyleneimine (PEI), binds DNA among its cationic cage, and in linear and branched forms, still possesses unprotonated amines in its complexes with DNA at physiological pH which ensure endosomal escape within cells and hence help mediate gene delivery.¹³² Poly(amidoamine) (PAMAM) dendrimer are protonated at physiological pH and thus are able to bind polyanionic DNA electrostatically with partial degradation and increased flexibility of the fractured systems allowing for more compact complexation with DNA and more efficient gene delivery.^{133, 134} However, overall polymer chains > 3000 Da are required to effectively condense DNA¹³⁵ and high molecular-weight compounds exhibit relatively high cytotoxicity.¹³⁶

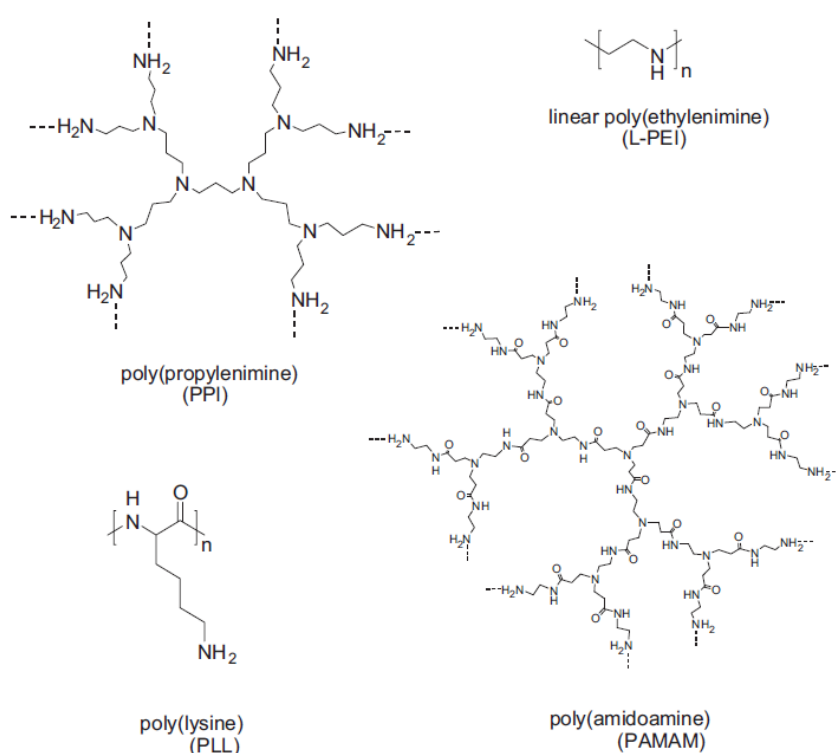


Figure 3.5: Some example of cationic polymers.¹³⁰

Cationic lipids self-assemble into higher order architectures with high-affinity for DNA.¹³⁷ They were pioneered by Felgner *et al.* who developed the lipid

N-[1(2,3-dioleyloxy)propyl]-*N,N,N*-trimethylammonium chloride (DOTMA).¹³⁸⁻¹⁴⁰ The same group then performed a more detailed structure-activity relationship study, including 1,2-dioleyloxypropyl-3-dimethyl-hydroxyethyl ammonium bromide (DORIE) and 1,2-dimyristyloxy-propyl-3-dimethyl-hydroxyethyl ammonium bromide (DMRIE), in order to further improve the performance of their vectors. (Figure 3.6).^{137, 141}

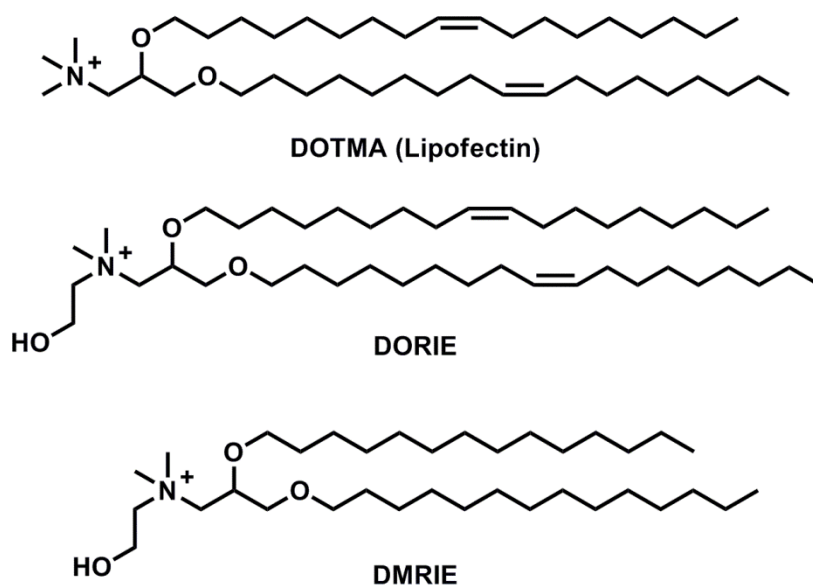


Figure 3.6: Structure of cationic lipids DOTMA, DORIE and DMRIE.

These studies yielded several commercially available vectors including DOTMA, sold under the name LipofectinTM,¹³⁸ 2,3-dioleyloxy-*N*-[2(sperminecarboxamido)ethyl]-*N,N*-dimethyl-1-propanaminiumtrifluoroacetate (DOSPA), known as LipofectamineTM,¹⁴² 1,2-dioleoyl-3-trimethyl-ammoniumpropane (DOTAP)¹⁴³ and dioctadecylamido- glycyispermene (DOGS) or Transfectam[®] (Figure 3.7).¹⁴⁴

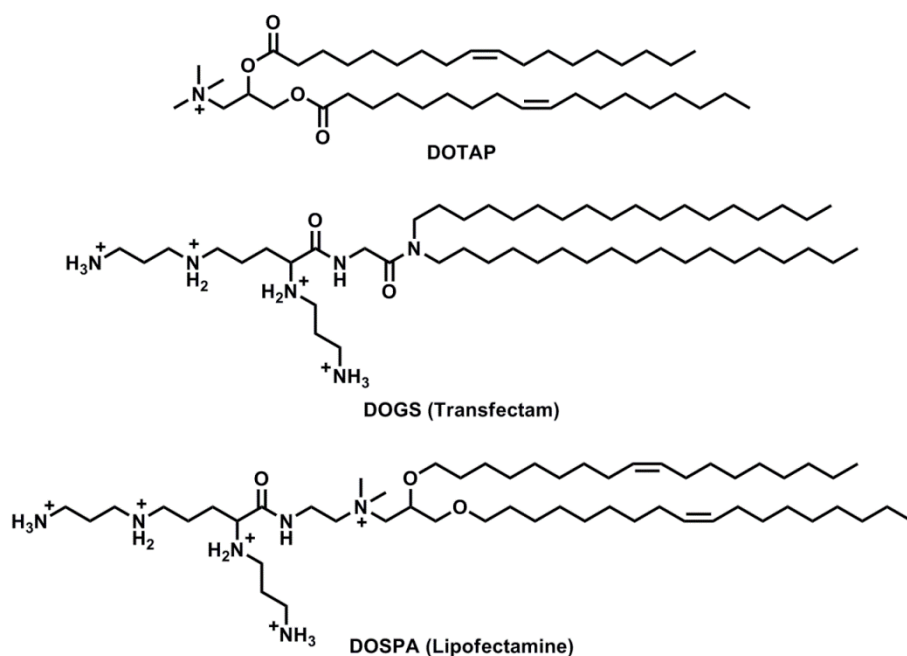


Figure 3.7: Structure of cationic lipids DOTAP, DOGS and DOSPA.

Self-assembling approaches have also been applied to DNA binding. In such systems, self-assembly of the hydrophobic chain(s) enables the formation of nanostructures which can then achieve high adhesion for DNA binding. Furthermore, the lipids chain can play an active role in disrupting cell membranes and hence mediating transfection via a “flip-flops” mechanism.¹⁴⁵

In 2003, Joester *et al.* reported a novel self-assembling vector for DNA binding and gene delivery which used a polyamine-surfaced dendron attached via a phenylacetylene rigid rod segment to a branched unit with long aliphatic dodecyl chain surface groups (**Figure 3.8**).¹⁴⁶ This systems could be designed and optimised to exhibit enhanced self-assembly with DNA for gene transfection applications with the balance between hydrophobic and cationic parts being of key importance for optimisation.³⁰

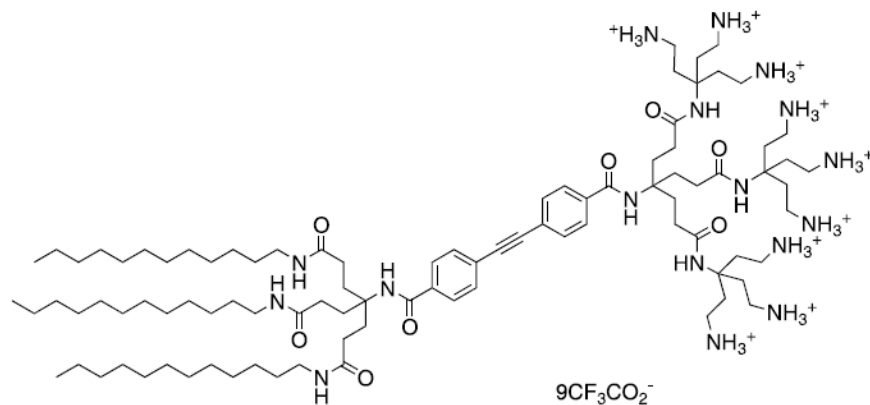


Figure 3.8: Self-assembling dendritic systems which possess groups to bind DNA (polyamines) as well as groups which encourage the self-assembly of the system (hydrophobic alkyl tails).³⁰

In 2005, Kostianen *et al.* reported the use of first and second generation Newkome branched dendrons for DNA binding (**Figure 3.9**).¹⁴⁷ Both vectors were able to effectively condense DNA while spermine alone showed very weak binding. However, in the presence of NaCl, the DNA binding of the G1 dendron was significantly reduced whereas the G2 dendron bound in a salt independent manner clearly demonstrating the strength of the multivalency. A further study of this with molecular modelling suggested that G2 dendron possess more surface ligands, and allows some spermine groups to sacrifice their binding energy for DNA in favour of screening the complex from increasing levels of NaCl. This demonstrates the importance of flexibility in this multivalent system.⁴⁰ In later work from the same group, hydrophobic cholesterol groups were grafted onto the focal point of the Newkome scaffold (**Figure 3.10**).¹⁴⁸ to introduce self-assembling capability to these molecules. Interestingly, Chol-G1 showed even more effective DNA binding than the equivalent generation two compound which had less capability to self-assemble. This was clear and quantifiable example of SAMul binding. Multiscale modelling provided some explanation as to the observed differences between the cholesterol dendrons. Chol-G1 was found to assemble more efficiently than Chol-G2 in terms of surface ligand packing, resulting in an aggregate with a much higher charge density which, in turn, leads to greater DNA binding affinity.¹⁴⁹

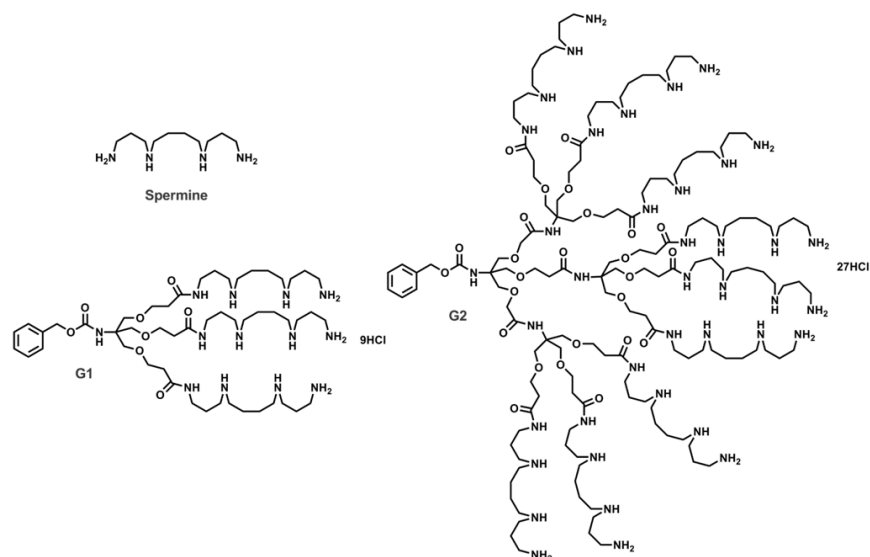


Figure 3.9: Structure of first and second generation Newkome dendrons with peripheral spermine ligands.¹⁴⁷

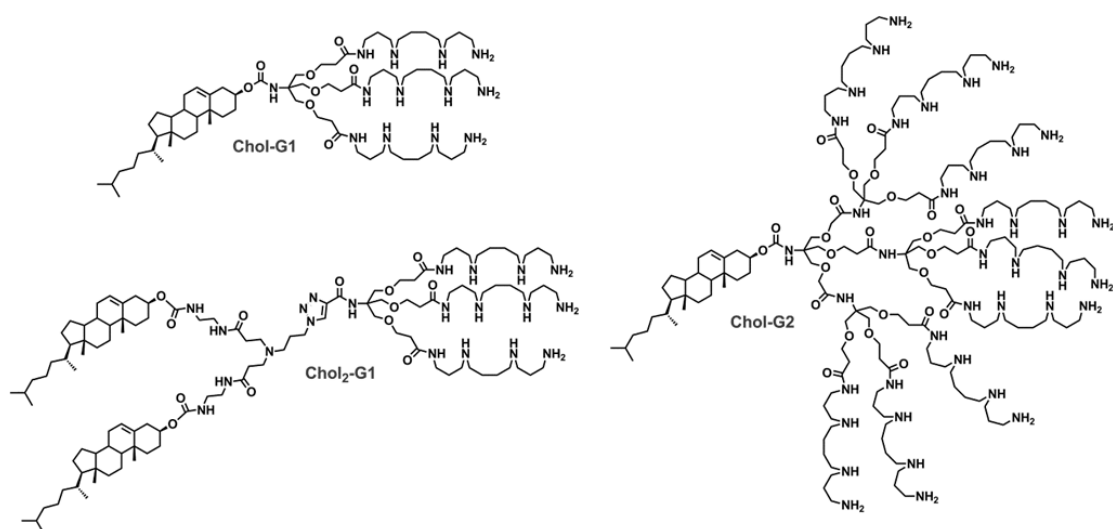
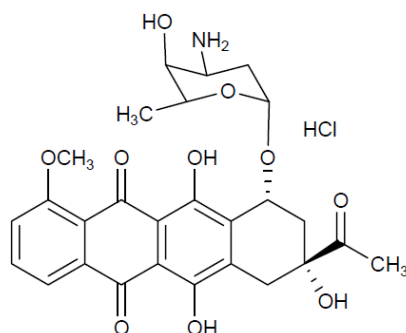


Figure 3.10: Structure of cholesterol functionalised Newkome dendrons with peripheral spermine ligands.¹⁴⁸

3.4 Effect of chirality on DNA and heparin binding

As mentioned in Chapter 1, DNA exists in double helical form,¹² which not surprisingly has led to some interest in the investigation of chirality effects with DNA. The impact of chirality on DNA binding was demonstrated by Qu *et al.* in 2000.¹⁵⁰ (-)-Daunorubicin (WP900), a synthesized enantiomer of the anticancer drug (+)-daunorubicin, binds selectively to a left-handed (Z-DNA) form of a synthetic DNA

polynucleotide whereas the (+)-daunorubicin binds selectively to a right-handed “normal” DNA. It was suggested that such work could lead to applications in areas such as enantiomeric purification¹⁵¹ and asymmetric catalysis.¹⁵²



(-)-daunorubicin (WP900)

Another example is provided by peptide nucleic acids (PNAs), which are oligonucleotide analogues in which the sugar-phosphate backbone has been replaced by a pseudopeptide skeleton (**Figure 3.11**). They bind DNA and RNA with high specificity and selectivity.¹⁵³ PNAs containing monomers derived from D-amino acids (D-PNAs) were found to bind to right-handed DNA with higher affinity than L-PNAs.^{154,}

155

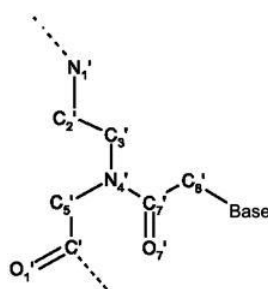


Figure 3.11: Structure of PNAs

In Chapter 2, we mentioned the heparin polysaccharide is composed primarily of an α -1,4-linked D-glucosamine–L-iduronic acid disaccharide repeat unit which of course means that heparin is also a chiral polyanion. Heparin has been used as a chiral additive in capillary electrophoresis via combination of ionic, hydrogen bonding and hydrophobic interactions to enantiomerically separate underivatized drugs such as anti-malarials and anti-histamines.¹⁵⁶⁻¹⁵⁸ However, Wang and Rabenstein reported that

a sequence of exclusively D amino acids interacted with heparin in exactly the same manner as the corresponding sequence of L amino acids (i.e., no chiral recognition) and suggested that the specific spatial arrangement of lysine and arginine residues in this peptide sequence promoted heparin interaction, rather than the presence of an enantiomerically complementary structure to heparin.¹⁵⁹

Very recently, however, while this work was in progress, Bromfield and Smith reported simple cationic self-assembling multivalent (SAMul) dendrons which demonstrated chiral preferences in polyanion binding (**Figure 3.12**).¹⁶⁰ Firstly it was reported that non-assembling **1** and **2** did not show any binding towards heparin and DNA, which suggested that self-assembly was required for multivalent binding. It was then stated that the first generation dendrons **1L** and **1D**, formed identical nanoscale assemblies in terms of dimensions and charge densities but exhibited different chiral binding preferences towards heparin and DNA compound. **1L** was preferentially bound by DNA whereas **1D** was preferentially bound by heparin. Conversely, higher generation dendrons (**2L** and **2D**) with larger hydrophilic head groups were bound identically by these polyanions, irrespective of chirality and it was suggested that the ligands were displayed less effectively on the large dendron surface and charge density effects became dominant.

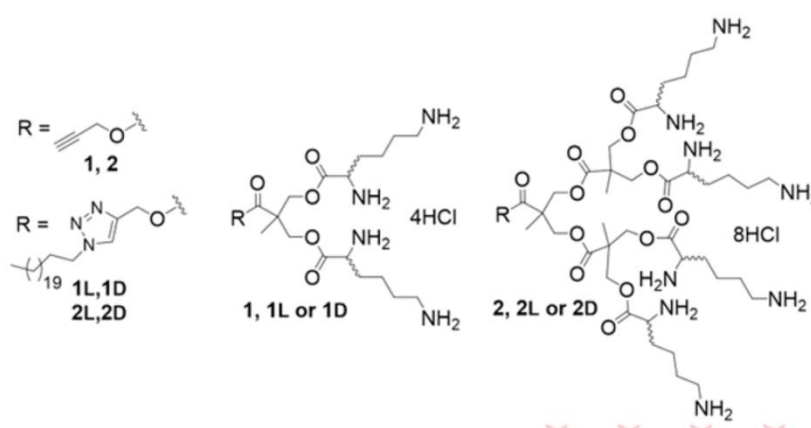
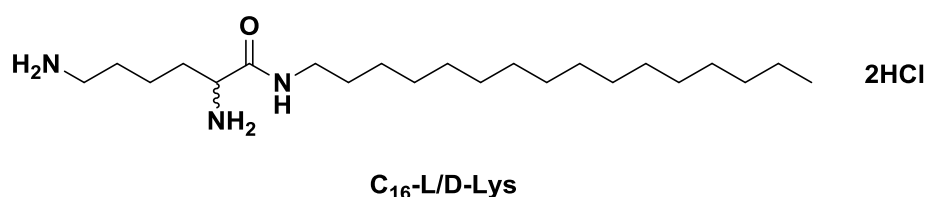


Figure 3.12: Self-assembling chiral cationic ligands for binding polyanions by Bromfield and Smith.¹⁶⁰

3.5 Project aim

While Bromfield and Smith reported that simple cationic chiral self-assembling multivalent (SAMul) dendrons showed chiral preferences in polyanion binding for the first generation dendrons.¹⁶⁰ It required multi-step synthesis to yield the desired compounds. Furthermore, in order to gain greater insight into polyanion binding processes we considered that there were minimal systems which might be capable of should both self-assembly and chiral discrimination characteristics that could be simply synthesised. As such we reasoned they could help provide insight into these kinds of binding processes, and potentially enable us to control nanoscale binding interfaces.

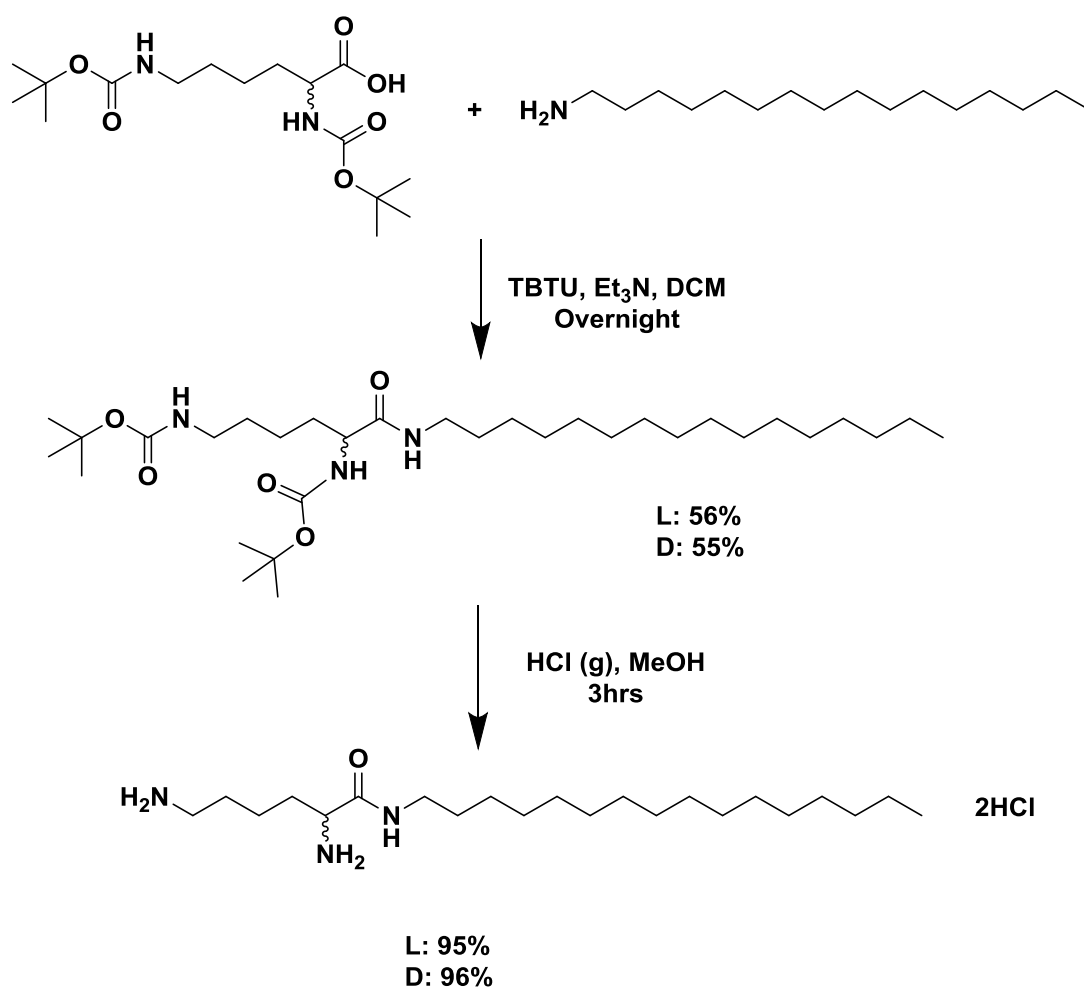
As such, we targeted the design and synthesis of 'simple' SAMul biological polyanion binders: C₁₆-L-Lys and C₁₆-D-Lys to explore the role of chirality in heparin and DNA binding. They contain lysine head group that are protonated at physiological pH, allowing highly effective electrostatic binding to polyanionic. The straight-chain alkane located at the focal point of the structure act as hydrophobic unit driving the self-assembly of the ligands into a larger nanoscale architecture in aqueous media as a consequence of the hydrophobic effect. We also aimed to explore the impact of modifying the pyrene sensor system described in Chapter 2 with the optimised chiral ligand groups.



3.6 C₁₆-L-Lys and C₁₆-D-Lys

3.6.1 Synthesis of C₁₆-L-Lys and C₁₆-D-Lys

Self assembling lysine derivatives with appropriate chirality were targeted to probe the head group effect on binding. Protected L/D-Lysine was coupled with 1-hexadecylamine using TBTU and excess Et₃N in DCM. Then the target C₁₆-L-Lys and C₁₆-D-Lys were obtained by removing the protecting groups using HCl gas bubbled through MeOH. The synthesis worked in good yields and gave the desired target compounds C₁₆-L-Lys and C₁₆-D-Lys (**Scheme 3.1**). The peak corresponding to the Boc group protons was not observed in the ¹H NMR spectrum for compounds C₁₆-L-Lys (**Figure 3.13**) and C₁₆-D-Lys (**Figure 3.14**), indicating that a successful Boc deprotection took place. Additional product confirmation was acquired by mass spectrometry and all other analytical methods (see Experimental section).



Scheme 3.1: Synthesis of C₁₆-L-Lys and C₁₆-D-Lys

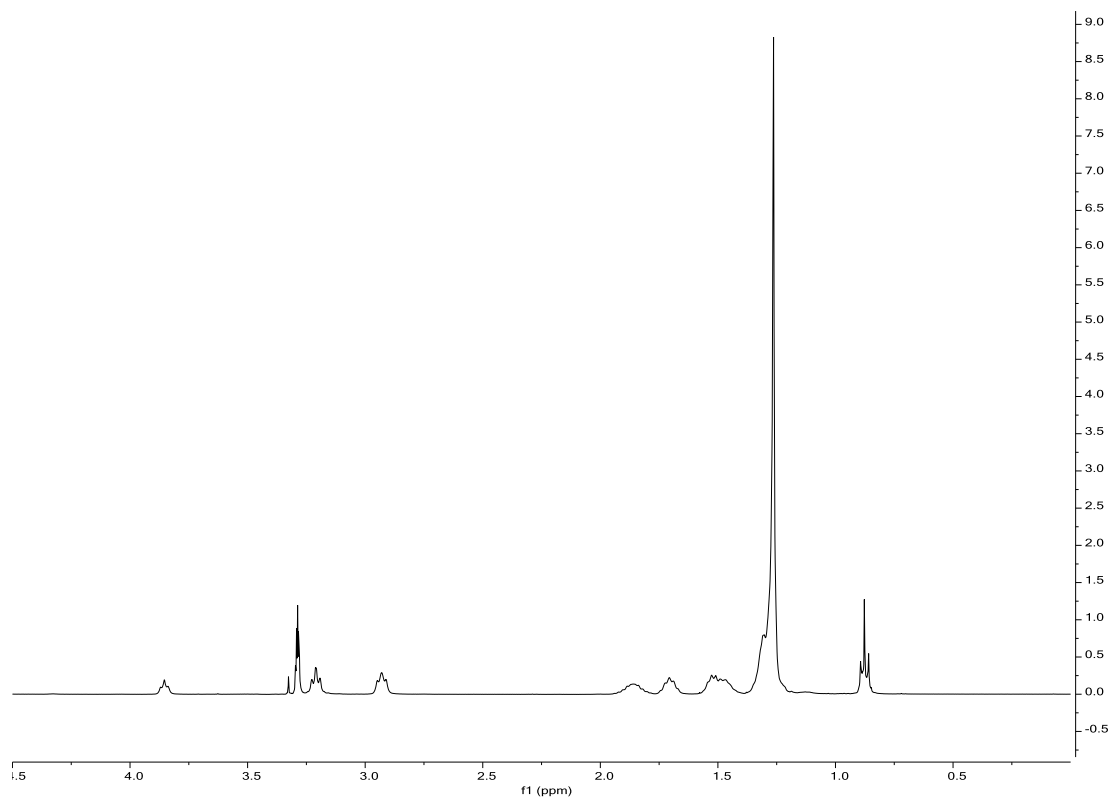


Figure 3.13: ^1H NMR spectra of C_{16} -L-Lys.

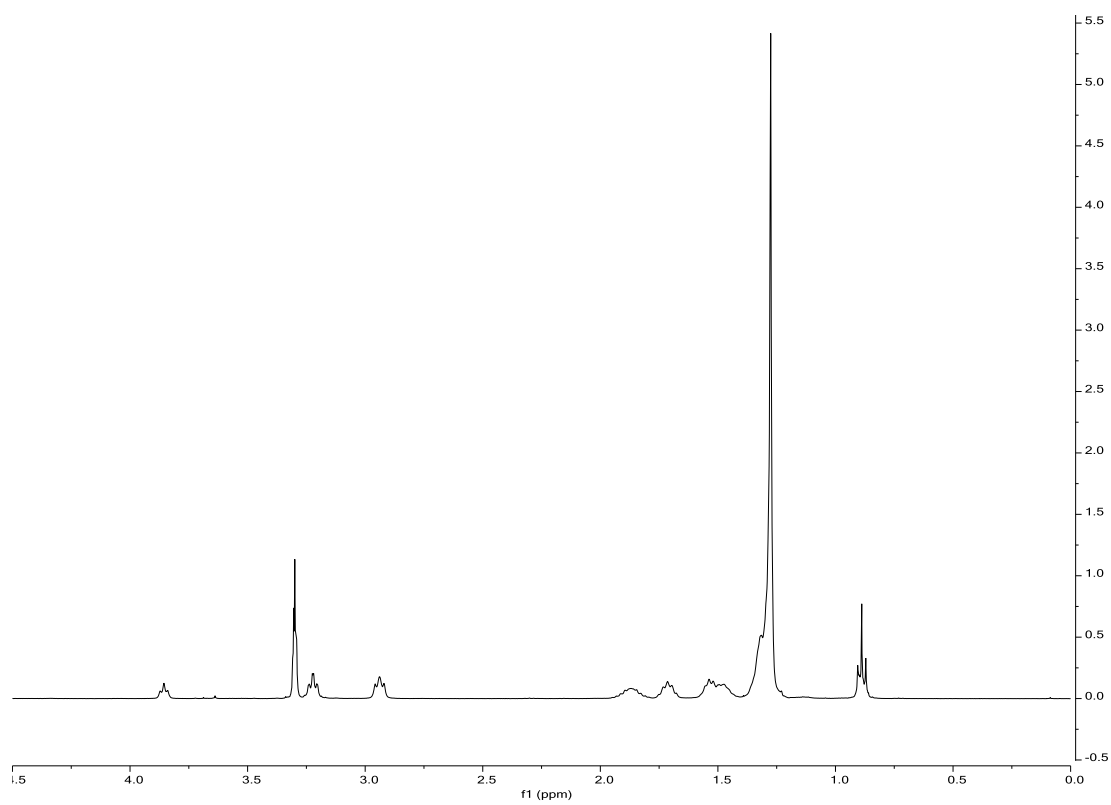


Figure 3.14: ^1H NMR spectra of C_{16} -D-Lys.

3.6.2 Circular Dichroism (CD)

Circular dichroism spectroscopy was used to probe the chirality of the final products to ensure amino acid chirality had been successfully preserved throughout the synthesis. As shown **Figure 3.15**, the molar ellipticity for the two systems is effectively equal and opposite, indicating that the two target molecules are of approximately equal enantiopurity, and crucially that chirality has not been scrambled lost during synthesis. As such, comparison of the performance to these two systems should provide insights into the impacts of chirality on polyanion binding.

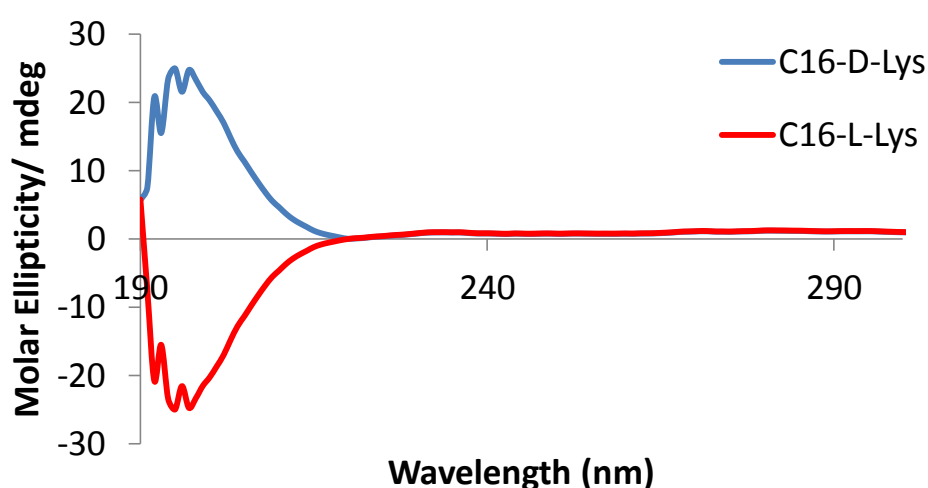


Figure 3.15 : Circular dichroism spectra of target molecules C₁₆-L-Lys and C₁₆-D-Lys (1 mg/mL in methanol) indicating opposing chirality.

3.6.3 Critical Aggregation Concentration (CAC)

Although C₁₆-L-Lys and C₁₆-D-Lys both dissolve in distilled water. They do not dissolve in PBS buffer at room temperature. PBS is the buffer of choice for the Nile Red assay, in which the solubilization of the hydrophobic dye monitored by fluorescence spectroscopy, acts as a probe for the minimum concentration at which self-assembly can take place.¹⁶¹ However, it was found that both C₁₆-L-Lys and C₁₆-D-Lys dissolved in PBS buffer at 45 °C in a water bath. Therefore cuvettes with the desired concentration of both compounds with Nile red (1 μL) were placed in the 45 °C water bath for 10 min prior to being monitored by the fluorimeter.

The CAC of C₁₆-L-Lys was found to be $33 \pm 3 \mu\text{M}$ (Figure 3.16) whereas the CAC of C₁₆-D-Lys was found as $29 \pm 4 \mu\text{M}$ (Figure 3.17). Both compounds therefore have similar CAC values (within error). Since the only difference between them are the L or D configuration, this equivalence in CAC was expected, as the only difference between the self-assemblies is their head group and hence their overall nanoscale chirality. Enantiomeric nanoscale object will be effectively identical unless or until they interact with other chiral objects.

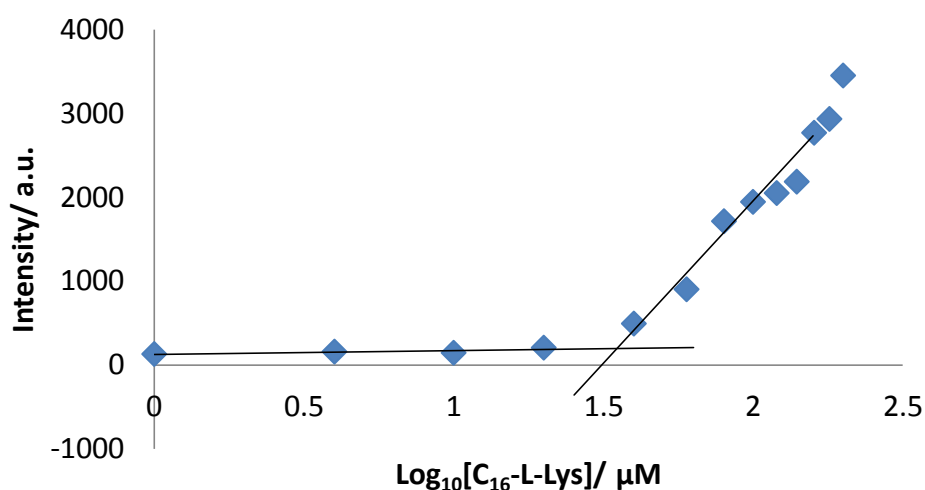


Figure 3.16: Fluorescence intensity of Nile Red in the presence of increasing amounts of C₁₆-L-Lys

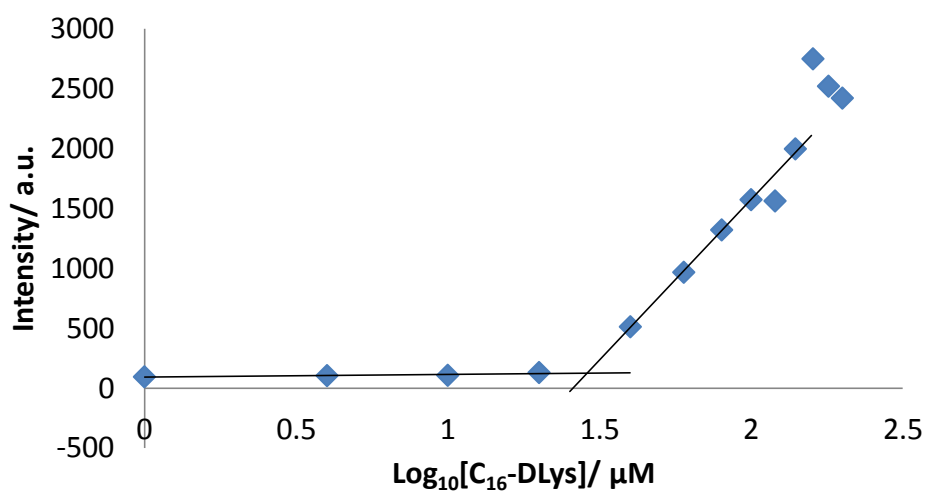


Figure 3.17: Fluorescence intensity of Nile Red in the presence of increasing amounts of C₁₆-D-Lys

3.6.4 Transmission Electron Microscopy (TEM)

Transmission Electron Microscopy (TEM) was used in order to observe the self-assembled morphologies of C_{16} -L-Lys and C_{16} -D-Lys (**Figure 3.18**). Both monomers appear to aggregate into micellar assemblies, with approximate diameters of ca. 8 nm. The binder assemblies were also imaged in the presence of DNA and heparin. In both cases, the micellar objects appeared to remain intact and co-assemble with the polyanionic components. The presence of 'un-bound' micelles in the background of the TEM images in the presence of heparin/DNA is thought to arise from a disproportionate amount of C_{16} -L-Lys and C_{16} -D-Lys being present in the samples. This clearly demonstrated that micellar stability is high and that the self-assembly event is not adversely affected by the presence of highly interactive polyanions. This is of considerable interest as in some cases it is predicted that simple cationic surfactant assemblies are disrupted by binding to polyanions.

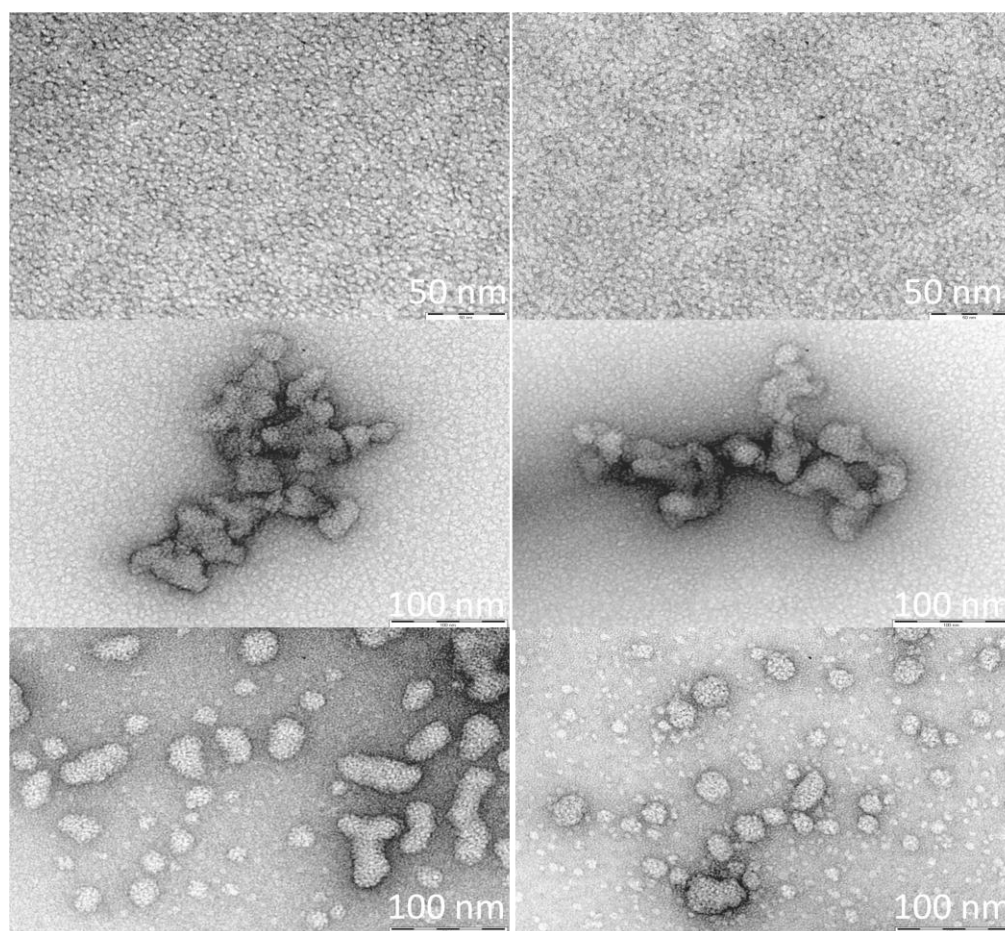


Figure 3.18: TEM images of C_{16} -L-Lys (left) and C_{16} -D-Lys (right) in the absence (top) and presence of heparin (middle) and DNA (bottom).

3.6.5 Dynamic Light Scattering (DLS)

DLS investigates self-assembled objects in solution. The DLS data for C₁₆-L-Lys and C₁₆-D-Lys are summarised in **Table 3.1**. Both C₁₆-L-Lys and C₁₆-D-Lys formed aggregates ca. 6.3 nm in diameter, in good agreement with TEM. The zeta potentials for both C₁₆-L-Lys and C₁₆-D-Lys were positive (45.2 ± 1.6 mV for C₁₆-L-Lys, +39.2 ± 1.55 mV for C₁₆-D-Lys). This is a result of protonation of the Lysine ligands at physiological pH. As such, these self-assembled cationic nanostructures would be expected to show high affinity towards polyanionic heparin and DNA. As expected, the assemblies formed by C₁₆-L-Lys and C₁₆-D-Lys are effectively equivalent, given that they are enantiomeric nanoscale objects.

Sample in 10 mM Tris HCl, NaCl (150 mM)	Size (d.nm)	Zeta Potential (mV)	PDI
C ₁₆ -L-Lys	6.2 ± 1.7	45.2 ± 1.6	0.6
C ₁₆ -D-Lys	6.3 ± 1.7	39.2 ± 1.55	0.5

Table 3.1: DLS data for C₁₆-L-Lys and C₁₆-D-Lys.

Z-Average (d.nm): 15.38
Pdl: 0.616
Intercept: 0.897

Peak 1: 6.167
Peak 2: 115.0
Peak 3: 0.000

Size (d.nm):
% Volume:
St Dev (d.nm):

100.0
0.0
0.0

1.716
47.63
0.000

Result quality : Refer to quality report

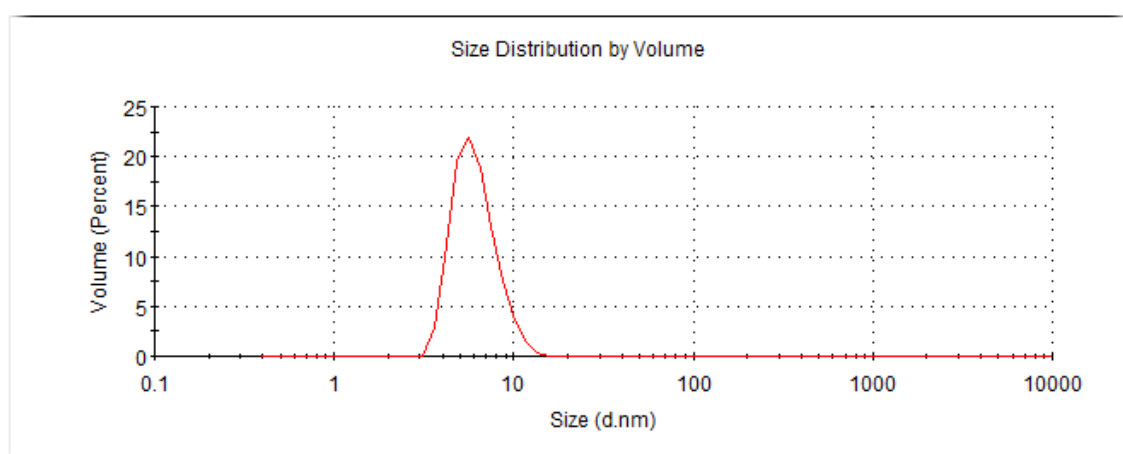


Figure 3.19: DLS data for C₁₆-L-Lys measured at 1mg/ mL.

	Size (d.nm):	% Volume:	St Dev (d.nm):
Z-Average (d.nm): 65.02	Peak 1: 6.270	100.0	1.697
Pdl: 0.181	Peak 2: 124.0	0.0	43.52
Intercept: 0.887	Peak 3: 0.000	0.0	0.000

Result quality : Refer to quality report

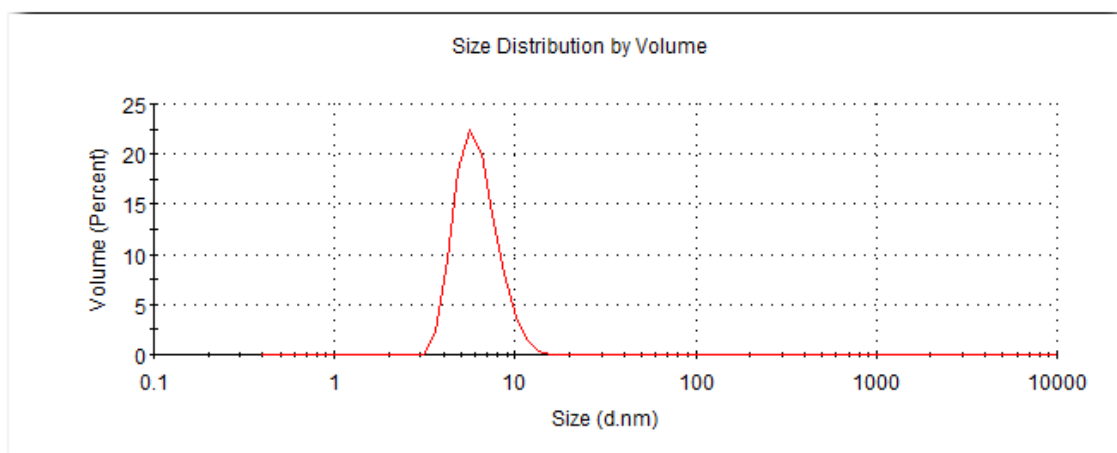


Figure 3.20: DLS data for C₁₆-D-Lys measured at 1mg/ mL.

3.6.6 DNA assay (Ethidium bromide displacement assay)

The DNA binding ability of C₁₆-L-Lys and C₁₆-D-Lys was initially measured via the displacement of the intercalating agent ethidium bromide (EthBr) from DNA as monitored by fluorescence spectroscopy in SHE buffer. This is a simple and quantifiable way to determining DNA binding affinity and has been widely employed by several groups.^{38, 162, 163} The CE₅₀ value is the charge excess required for the 50% displacement of ethidium bromide in the fluorescence displacement assay and the EC₅₀ value is the concentration required for the 50% displacement of ethidium bromide in the fluorescence displacement assay. C₁₆-L-Lys was found to have CE₅₀ = 1.6 ± 0.2 and EC₅₀ = 3.2 ± 0.1 μM whereas C₁₆-D-Lys was found CE₅₀ = 1.7 ± 0.1 and EC₅₀ = 3.2 ± 0.1 μM (**Figure 3.21**). The data therefore suggested C₁₆-L-Lys and C₁₆-D-Lys bind DNA similarly and under these conditions and the nanoscale chirality has no significant impact.

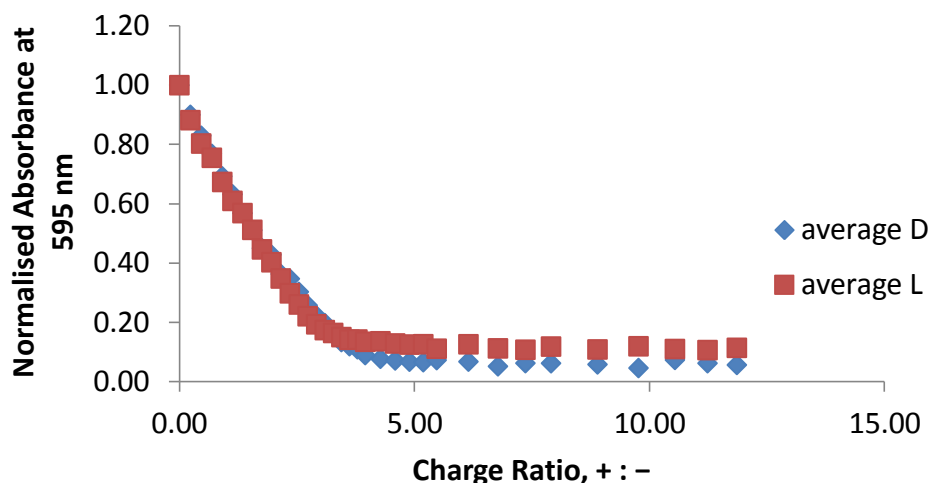


Figure 3.21: Charge ratio vs. normalised fluorescence from the EthBr displacement assay used to determine CE_{50} values for C_{16} -L-Lys and C_{16} -D-Lys.

3.6.7 Heparin assay (Mallard Blue (Mal-B) competition assay)

In order to quantify their relative heparin binding abilities, C_{16} -L-Lys and C_{16} -D-Lys were tested using a Mallard Blue (Mal-B) competition assay, in which the extent of MalB displacement from heparin, as monitored by the associated UV-Vis abs. change, indicates the extent of binding.^{80, 164} The CE_{50} value is the charge excess required for the 50% displacement of MalB in the fluorescence competition assay and the EC_{50} value is the concentration required for the 50% displacement of MalB in the fluorescence competition assay. C_{16} -L-Lys was found to have a $CE_{50} = 0.9 \pm 0.1$ and an $EC_{50} = 100 \pm 3 \mu\text{M}$ whereas C_{16} -D-Lys was found $CE_{50} = 0.9 \pm 0.1$ and $EC_{50} = 99.9 \pm 0.2 \mu\text{M}$ (**Figure 3.22**). The data suggested that, as for DNA binding, C_{16} -L-Lys and C_{16} -D-Lys also bind heparin similarly with absolutely no impact of chirality on the binding event. As such these result are similar to the previous report of Wang and Rabenstein,¹⁵⁹ and for the 2nd generation system reported by Bromfield and Smith.¹⁶⁰

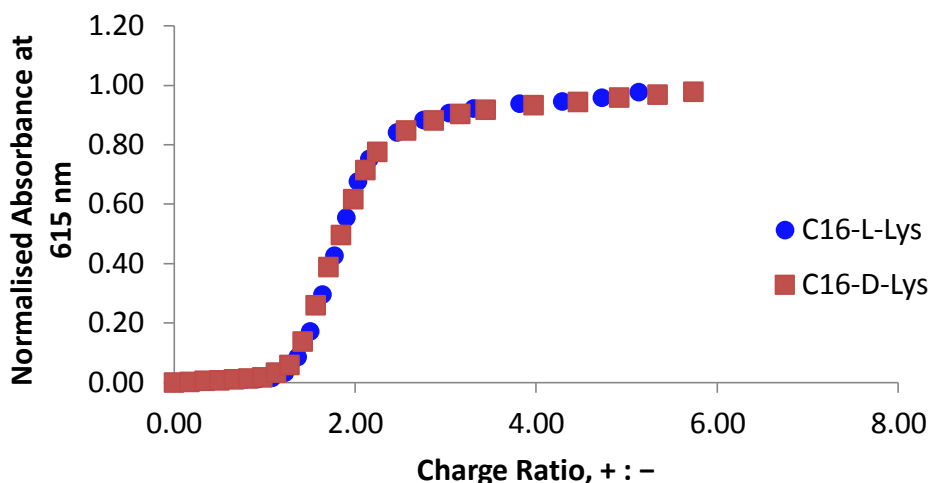


Figure 3.22: Charge ratio vs. normalised fluorescence from the (MalB) competition assay used to determine CE_{50} values for C_{16} -L-Lys and C_{16} -D-Lys.

3.6.8 Summary

Both C_{16} -L-Lys and C_{16} -D-Lys self assemble and bind to DNA and heparin. However, there were no chiral binding preferences to DNA or heparin for this system. It was reasoned that this may be due to the proximity of the molecular chiral information to the aliphatic tail of the monomer unit and suggested this may restrict the chiral expression at the surface of the chiral nanostructure with a densely packed nano-surface which simply binds to the targets or a result of charge density. Therefore, we decided to introduce a spacing group between the molecular-scale chiral information and the aliphatic tail (Figure 3.23). In the hope that this would allow the chirality to be less embedded in the self-assembled core of the nanostructure and hence have a potentially greater impact on the binding event at the nanoscale binding interface.

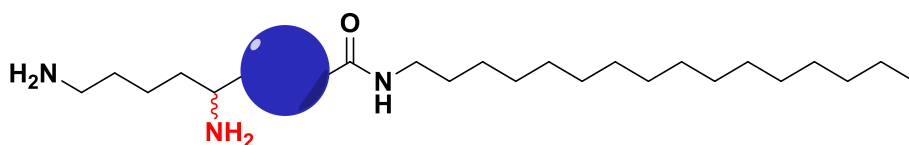
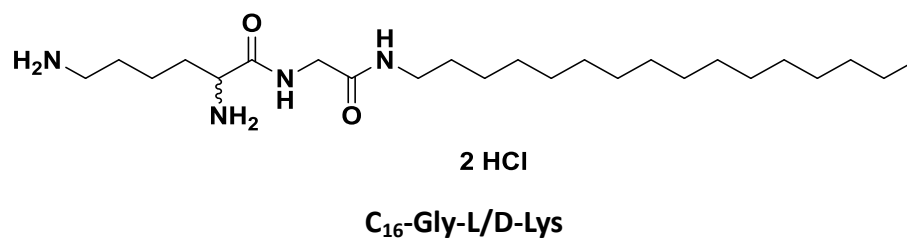


Figure 3.23: Schematic representation of C_{16} -L-Lys and C_{16} -D-Lys with spacing group.

To maintain the simple synthetic strategy, we chose glycine as a spacing group.

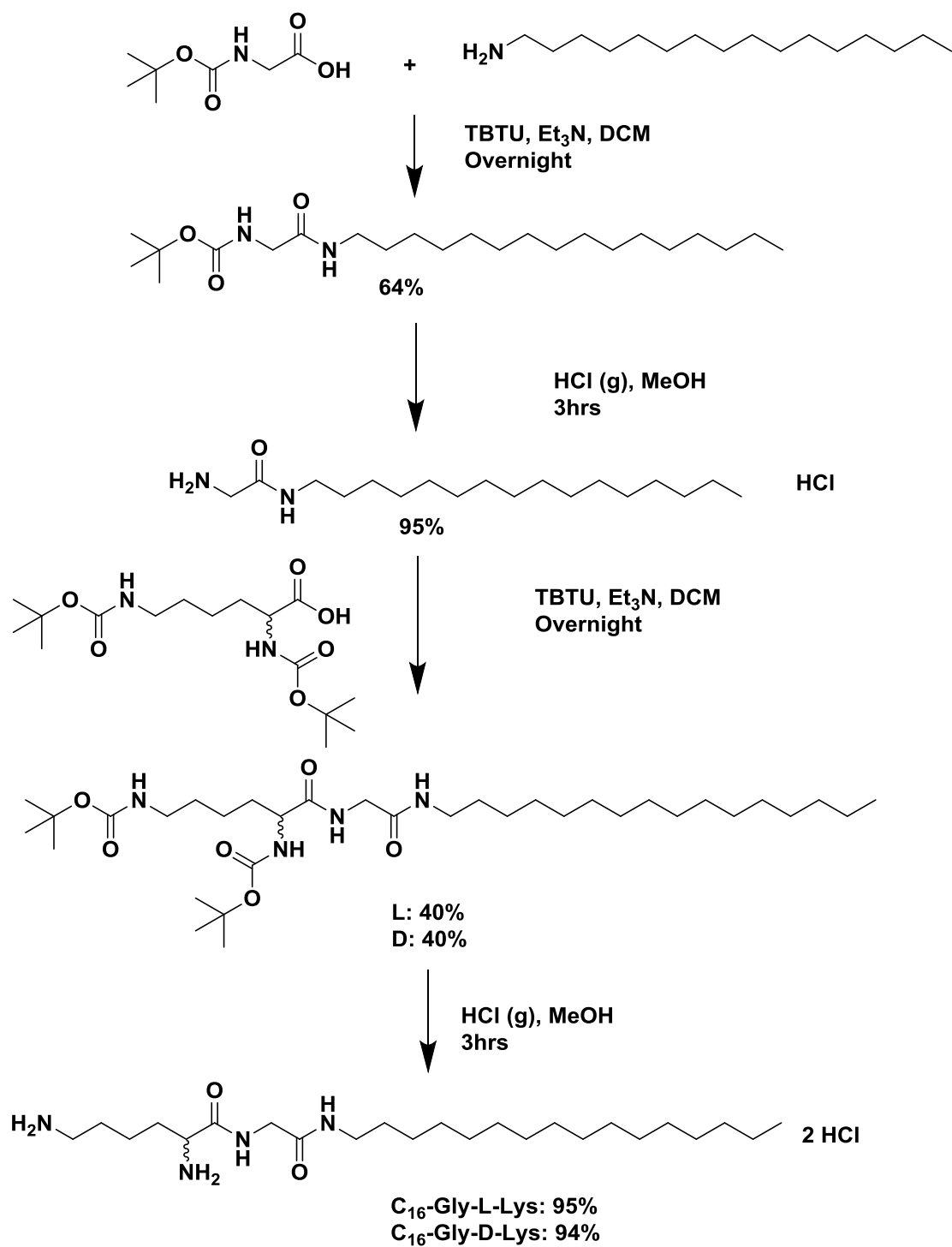
This is straight-forward to do, biologically relevant and does not introduce any other chiral information or significant binding sites.



3.7 C₁₆-Gly-L-Lys and C₁₆-Gly-D-Lys

3.7.1 Synthesis of C₁₆-Gly-L-Lys and C₁₆-Gly-D-Lys

Protected glycine was coupled with 1-hexadecylamine using TBTU and excess Et₃N in DCM, then the Boc protecting group was removed using HCl gas in methanol. The resulting compound was then coupled with protected L/D-Lysine using TBTU and excess Et₃N in DCM. The target compounds, C₁₆-Gly-L-Lys and C₁₆-Gly-D-Lys, were obtained by removing the Boc protecting groups using HCl gas in methanol. The synthesis worked in good yields and gave the desired target compounds C₁₆-Gly-L-Lys and C₁₆-Gly-D-Lys (**Scheme 3.2**). The peak corresponding to the Boc group protons was not observed in the ¹H NMR spectrum for compounds C₁₆-Gly-L-Lys (**Figure 3.24**) and C₁₆-Gly-D-Lys (**Figure 3.25**), indicating that a successful Boc deprotection took place. Additional product confirmation was acquired by mass spectrometry and all other analytical methods (see Experimental section).



Scheme 3.2: Synthesis of C₁₆-Gly-L-Lys and C₁₆-Gly-D-Lys

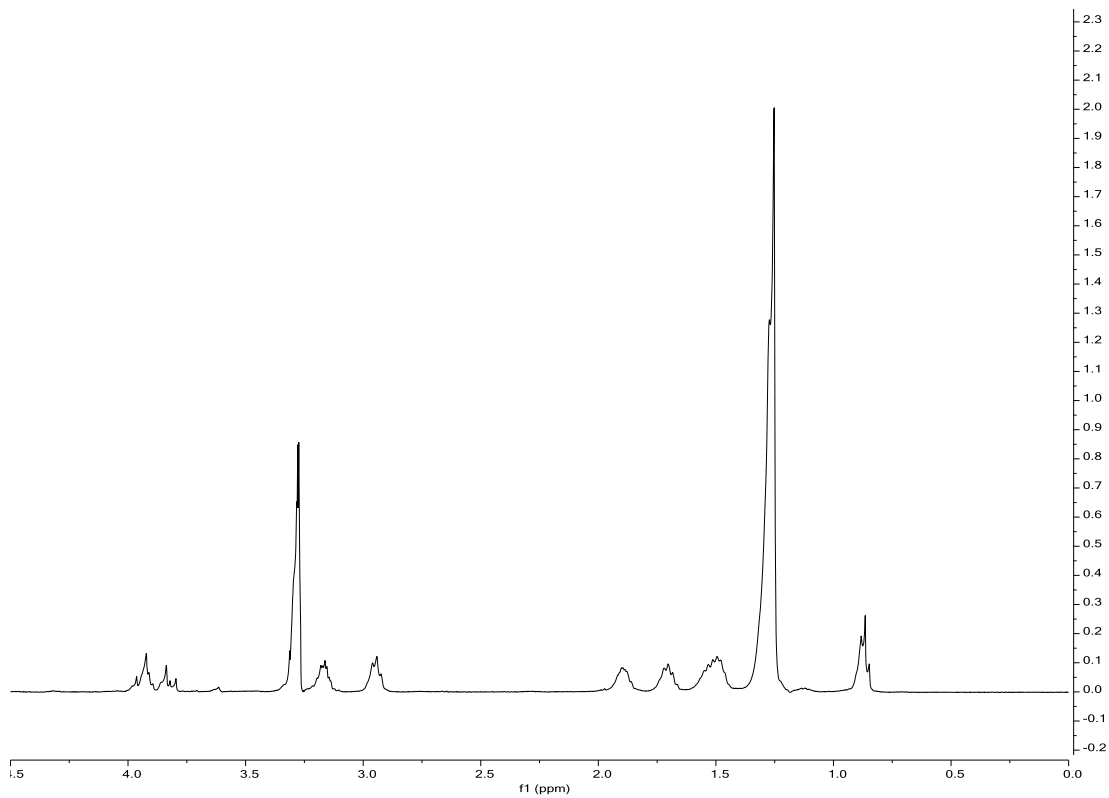


Figure 3.24: ^1H NMR spectra of $\text{C}_{16}\text{-Gly-L-Lys}$.

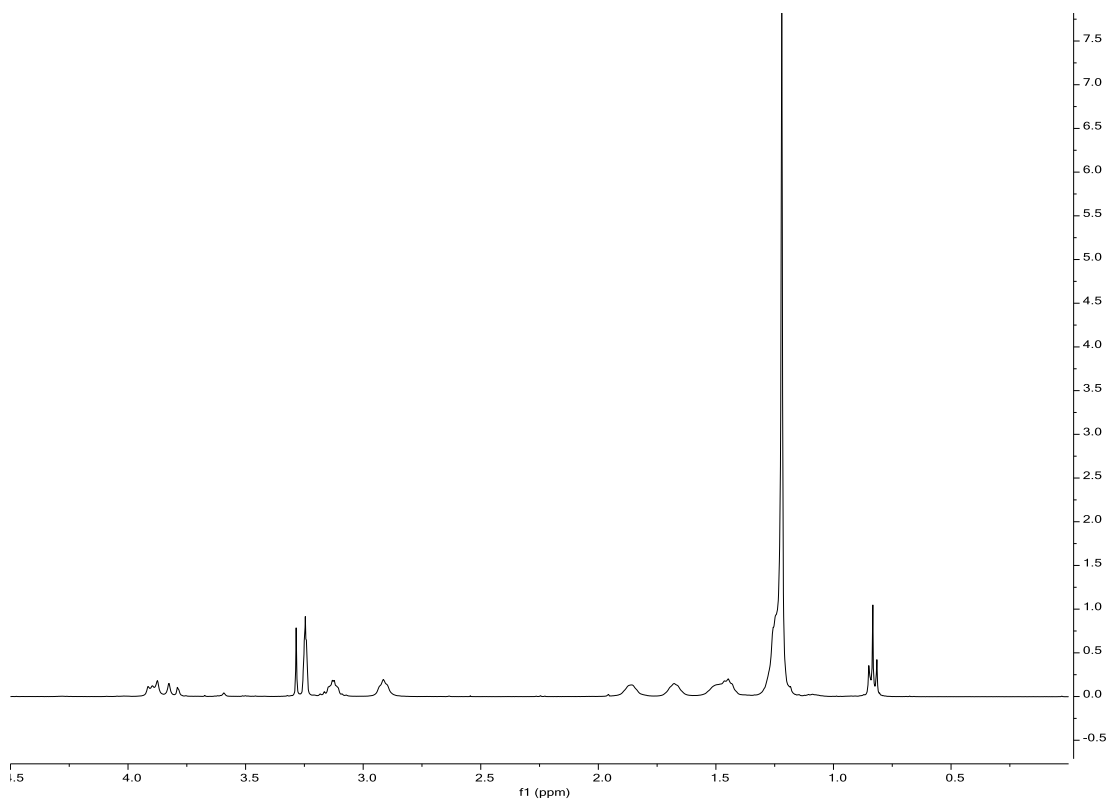


Figure 3.25: ^1H NMR spectra of $\text{C}_{16}\text{-Gly-L-Lys}$.

3.7.2 Circular Dichroism (CD)

Circular dichroism spectroscopy was used to probe the chiral character of the final products to ensure amino acid chirality had been successfully preserved throughout the synthesis. As shown in **Figure 3.26**, the molar ellipticity for the two systems is effectively equal and opposite. This indicates that the two target molecules are of equal enantiopurity, and crucially that chirality has not been scrambled or lost during synthesis. As such, any differences in binding between the systems will be the result of the chiral information programmed into the head group.

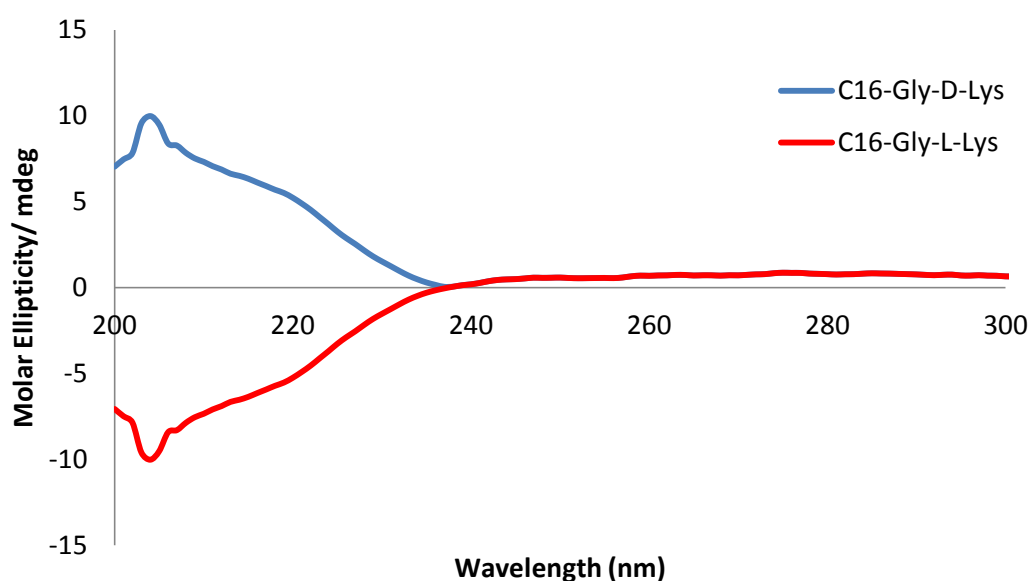


Figure 3.26: Circular dichroism spectra of target molecules C_{16} -Gly-L-Lys and C_{16} -Gly-D-Lys (1 mg/mL in methanol) indicating opposing chirality

3.7.3 Critical Aggregation Concentration (CAC)

Although C_{16} -Gly-L-Lys and C_{16} -Gly-D-Lys both dissolve in distilled water, again they do not dissolve in PBS buffer at room temperature. However, it was found that both C_{16} -Gly-L-Lys and C_{16} -Gly-D-Lys dissolved in PBS buffer at 45 °C in a water bath. Therefore cuvettes with the desired concentration of both compounds with Nile red (1 μ L) were placed in the 45 °C water bath for 10 min prior to being monitored by the fluorimeter.

The CAC of C₁₆-Gly-L-Lys was found to be $31 \pm 3 \mu\text{M}$ (Figure 3.27) whereas the CAC of C₁₆-Gly-D-Lys was found with $28 \pm 3 \mu\text{M}$ (Figure 3.28). Both compounds therefore have similar CAC values (within error). Since the only difference between them are the L or D configuration, this equivalence in CAC was expected as the self-assemblies are enantiomeric in nature and should be identical unless exposed to chiral influences .

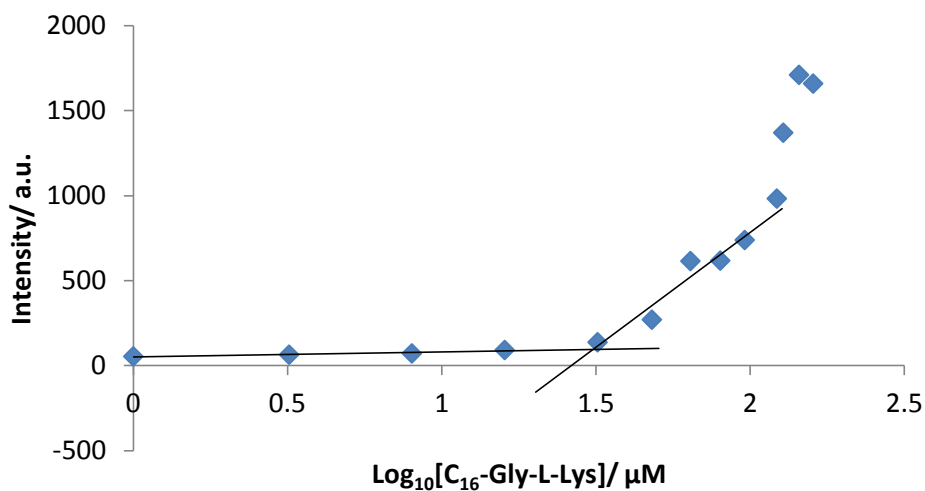


Figure 3.27: Fluorescence intensity of Nile Red in the presence of increasing amounts of C₁₆-Dly-L-Lys

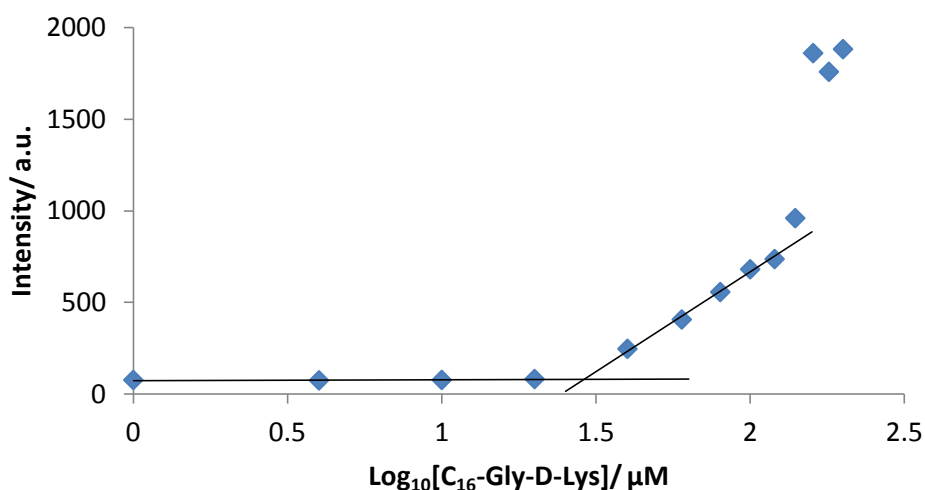


Figure 3.28: Fluorescence intensity of Nile Red in the presence of increasing amounts of C₁₆-Gly-D-Lys

3.7.4 Transmission Electron Microscopy (TEM)

Transmission Electron Microscopy (TEM) was used in order to observe the self-assembled morphologies of C₁₆-Gly-L-Lys and C₁₆-Gly-D-Lys (**Figure 3.29**). Both monomers appeared to aggregate into micellar assemblies, with approximate diameters of ca. 8 nm. The binder assemblies were also imaged in the presence of DNA and heparin. In both cases, the micellar objects appeared to remain intact and co-assemble with the polyanionic components. The presence of 'un-bound' micelles in the background of the TEM images in the presence of heparin/DNA is thought to arise from a disproportionate amount of C₁₆-Gly-L-Lys and C₁₆-Gly-D-Lys being present in the samples. Once again this indicates excellent stability of these self assemblies and no evidence that they rearrange in the presence of polyanions other than by being hierarchical organised into a nanoscale superstructure.

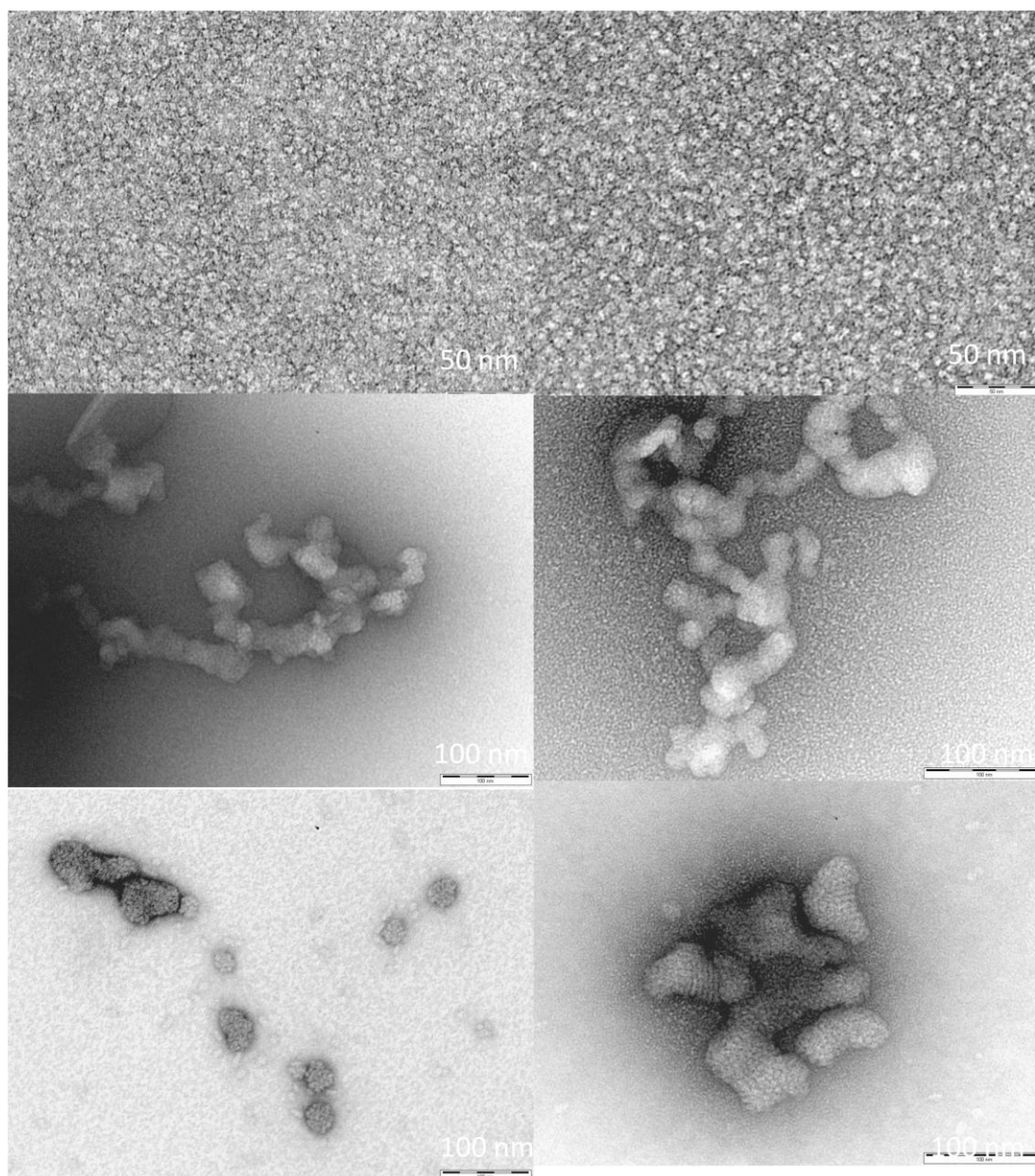


Figure 3.29: TEM images of C₁₆-Gly-L-Lys (left) and C₁₆-Gly-D-Lys (right) in the absence (top) and presence of heparin (middle) and DNA (bottom).

3.7.5 Dynamic Light Scattering (DLS)

The DLS data for C₁₆-Gly-L-Lys and C₁₆-Gly-D-Lys are summarised in Table 3.2. C₁₆-Gly-L-Lys formed aggregates ca. 120 nm in diameter and C₁₆-Gly-D-Lys formed aggregates ca. 83 nm in diameter, which were not in good agreement with TEM. DLS measures the molecules in the solution phase, this may suggest that they are not micellar assemblies but vesicular assemblies. It is known from Israelachvili's rule that

increasing the hydrophobic domain which we have done here by inserting the Gly spacer can drive a transition from spherical micelles to cylindrical or vesicular assemblies.^{32, 82} However, the large distribution of sizes is noted. It is also noted that DLS is performed at significantly elevated concentrations. The zeta potentials for both C₁₆-Gly-L-Lys and C₁₆-Gly-D-Lys were positive (40.1 ± 2.2 mV for C₁₆-Gly-L-Lys, +47.1 ± 1.4 mV for C₁₆-Gly-D-Lys). This is a result of protonation of the Lysine ligands at physiological pH. As such, these self-assembled cationic nanostructures would be expected to show high affinity towards polyanionic heparin and DNA. Importantly, the enantiomeric assemblies had size and charge characterisations which were roughly within error range of each other, as would be expected.

Sample in 10 mM Tris HCl, NaCl (150 mM)	Size (d.nm)	Zeta Potential (mV)	PDI
C ₁₆ -Gly-L-Lys	120.0 ± 56.6	40.1 ± 2.2	0.5
C ₁₆ -Gly-D-Lys	82.5 ± 50.0	47.1 ± 1.4	0.3

Table 3.2: DLS data for C₁₆-Gly-L-Lys and C₁₆-Gly-D-Lys.

	Size (d.nm):	% Volume:	St Dev (d.nm):
Z-Average (d.nm): 117.8	Peak 1: 119.7	100.0	57.59
Pdl: 0.203	Peak 2: 0.000	0.0	0.000
Intercept: 0.945	Peak 3: 0.000	0.0	0.000
Result quality : Good			

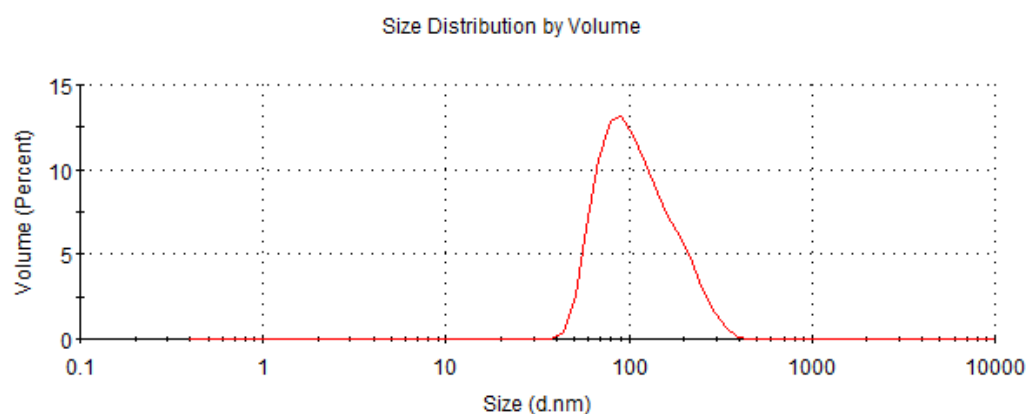


Figure 3.30: DLS data for C₁₆-Gly-L-Lys measured at 1mg/ mL.

	Size (d.nm):	% Volume:	St Dev (d.nm):
Z-Average (d.nm): 89.39	Peak 1: 82.46	98.6	50.06
Pdl: 0.303	Peak 2: 5000	1.4	879.4
Intercept: 0.888	Peak 3: 0.000	0.0	0.000

Result quality : Refer to quality report

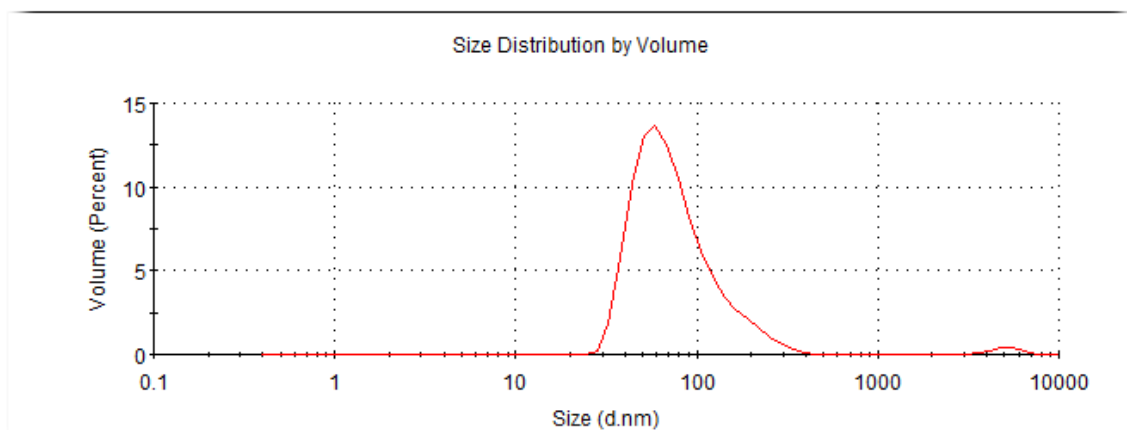


Figure 3.31: DLS data for C₁₆-Gly-D-Lys measured at 1mg/ mL.

3.7.6 DNA assay (Ethidium bromide displacement assay)

The DNA binding ability of C₁₆-Gly-L-Lys and C₁₆-Gly-D-Lys was measured via the displacement of the intercalating agent ethidium bromide (EthBr) from DNA as monitored by fluorescence spectroscopy in SHE buffer. C₁₆-Gly-L-Lys was found to have CE₅₀ = 3.8 ± 0.7 and EC₅₀ = 7.6 ± 1.3 μM whereas C₁₆-D-Lys was found to have CE₅₀ = 1.5 ± 0.1 and EC₅₀ = 3.1 ± 0.2 μM (**Figure 3.32**). As such there is now a very significant difference indeed between enantiomeric assemblies. The data therefore suggested C₁₆-Gly-D-Lys binds DNA much better than C₁₆-Gly-L-Lys (the lower the CE₅₀ value the better the binding).

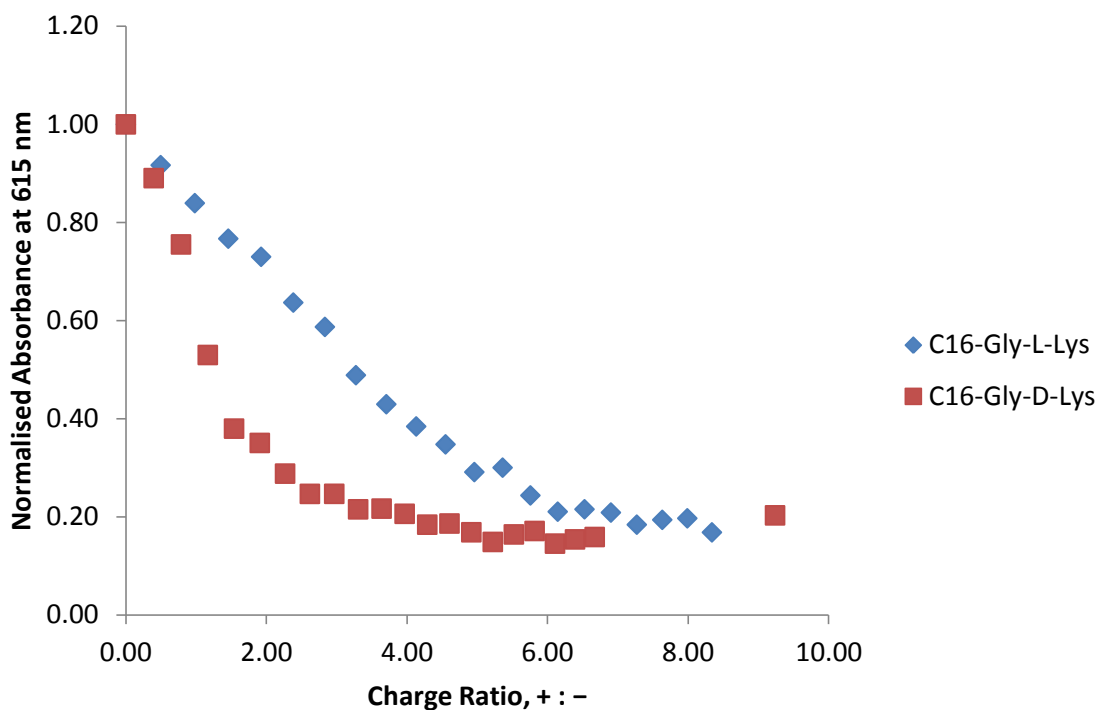


Figure 3.32: Charge ratio vs. normalised fluorescence from the EthBr displacement assay used to determine CE_{50} values for C₁₆-Gly-L-Lys and C₁₆-Gly-D-Lys.

3.7.7 Heparin assay (Mallard Blue (Mal-B) competition assay)

In order to quantify their relative heparin binding abilities, C₁₆-Gly-L-Lys and C₁₆-Gly-D-Lys were also tested using Mallard Blue (Mal-B) competition assay. C₁₆-Gly-L-Lys was found to have $CE_{50} = 1.7 \pm 0.2$ and $EC_{50} = 180 \pm 16 \mu\text{M}$ whereas C₁₆-Gly-D-Lys was found to have $CE_{50} = 1.1 \pm 0.1$ and $EC_{50} = 122 \pm 2 \mu\text{M}$ (**Figure 3.33**). The data therefore suggested that C₁₆-Gly-D-Lys also binds significantly heparin better than enantiomeric C₁₆-Gly-L-Lys.

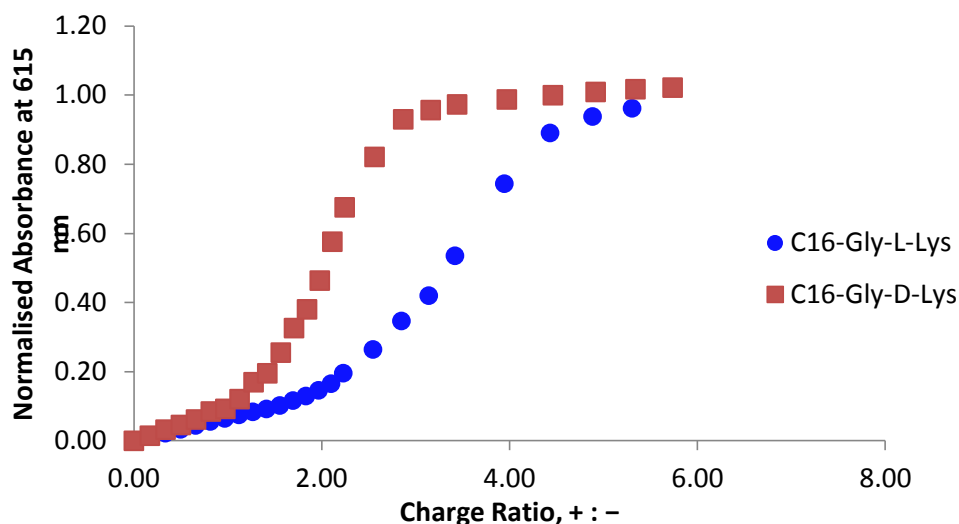


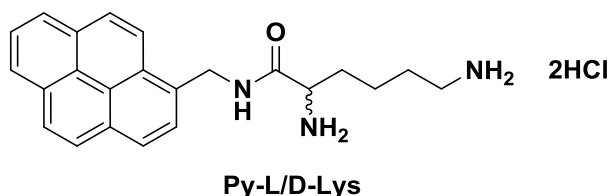
Figure 3.33: Charge ratio vs. normalised fluorescence from the (MalB) competition assay used to determine CE_{50} values for C_{16} -Gly-L-Lys and C_{16} -Gly-D-Lys.

3.7.8 Summary

Both C_{16} -Gly-L-Lys and C_{16} -Gly-D-Lys self assemble and bind to heparin and DNA. DNA and heparin both show a very significant preference towards binding C_{16} -Gly-D-Lys rather than the enantiomeric C_{16} -Gly-L-Lys. The introduction of a Gly spacer somewhat lower the apparent ability to bind but very importantly introduces a large discrimination ability between the enantiomeric assemblies. We suggest that the surface ligands are much more effectively displayed on a more “open” surface once the glycine group is present and that although this lowers the binding strength, it allows enough space for enantio-discrimination at the nanoscale binding interface. This is the first report in which a simple molecular-scale modification is able to switch on or off enantio-discrimination in the binding of biologically important polyanionic targets.

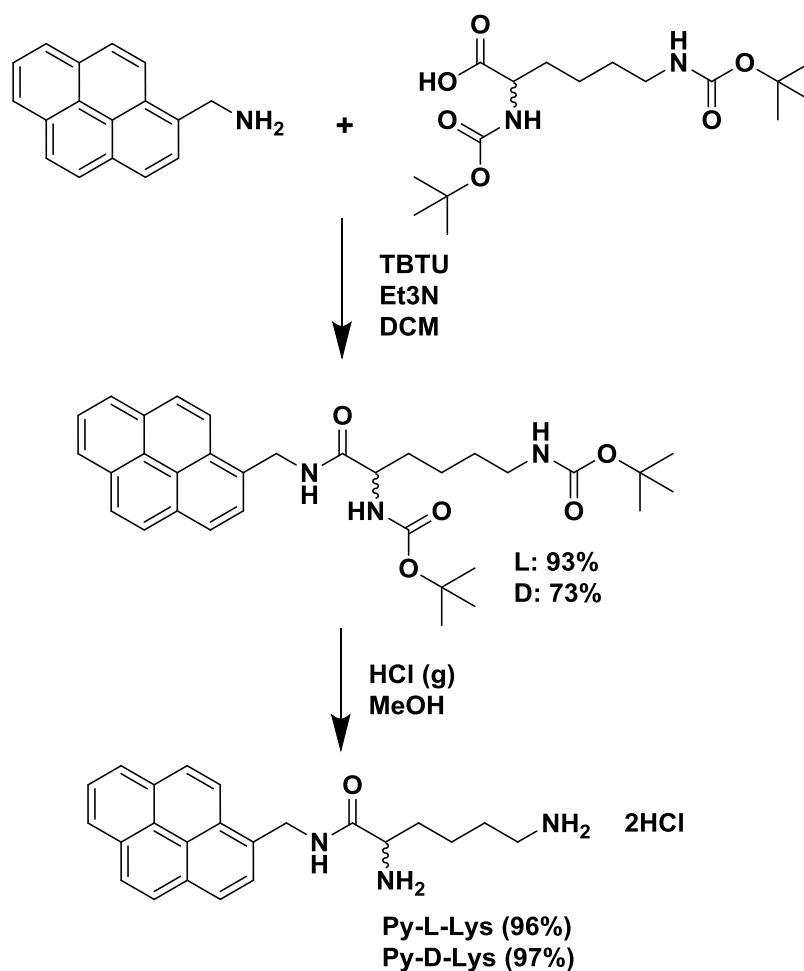
3.8 Chirality effect in heparin sensing

Having gained this unique insight into self-assembled chiral heparin binders, we reasoned that we could employ methods from Chapter 2 in order to give these systems interesting reporting and sensing characteristics. As such we designed systems in which the hydrophobic C₁₆ groups were replaced with a pyrene unit. In this section, we designed and synthesised synthetically simple Py-L-Lys and Py-D-Lys in order to determine the impact of chirality on some simple sensors.



3.8.1 Synthesis of Py-L-Lys and Py-D-Lys

To synthesise Py-L-Lys and Py-D-Lys, Boc-protected L-Lysine and D-Lysine were coupled with 1-pyrenemethylamine using TBTU and excess Et₃N in DCM and then protecting groups were removed using HCl gas bubbled through MeOH (**Scheme 3.3**). The peak corresponding to the Boc group protons at 1.4 ppm was not observed in the ¹H NMR spectrum for compounds Py-L/D-Lys, indicating that a successful Boc deprotection took place. Additional product confirmation was acquired by mass spectrometry. In analogy with the systems described in previous sections, we assumed the chirality was maintained during this procedure. This synthesis worked in good yield and gave the desired target compounds.



Scheme 3.3: Synthesis of Py-L-Lys and Py-D-Lys

3.8.2 Critical Aggregation Concentration (CAC)

The CAC value was determined using the same method described in section 2.2.2. In the previous chapter, Py-DAPMA was found to not self-assemble at these concentrations. Interestingly, however, when Py-L-Lys and Py-D-Lys were excited at 363 nm, an emission band with max emission at 495 nm was observed. This band was concentration dependent because excimer formation is favoured in the interior of the micelle when pyrene groups are close together. As such, this experiment clearly suggests that both Py-L-Lys and Py-D-Lys were able to self-assemble and therefore have potential to act as SAMul sensors. The CAC of Py-L-Lys was found to be $70 \pm 13 \mu\text{M}$ in 0.01M PBS buffer (**Figure 3.34**) and the CAC of Py-D-Lys was found to be $58 \pm 14 \mu\text{M}$ in 0.01M PBS buffer (**Figure 3.35**). Observably these values are within error of one another as the enantiomeric compounds should form identical, but mirror-image,

assemblies. It is interesting to consider why Py-Lys assembles but Py-DAPMA does not. The difference between Py-DAPMA and Py-Lys was a extra flexible spacing group in between the pyrene unit and the carbonyl group. We suggest that this flexible CH_2 may play a role in the self-assembly event by allowing the pyrene groups to organise themselves on the interior of the self-assembled nanostructures.

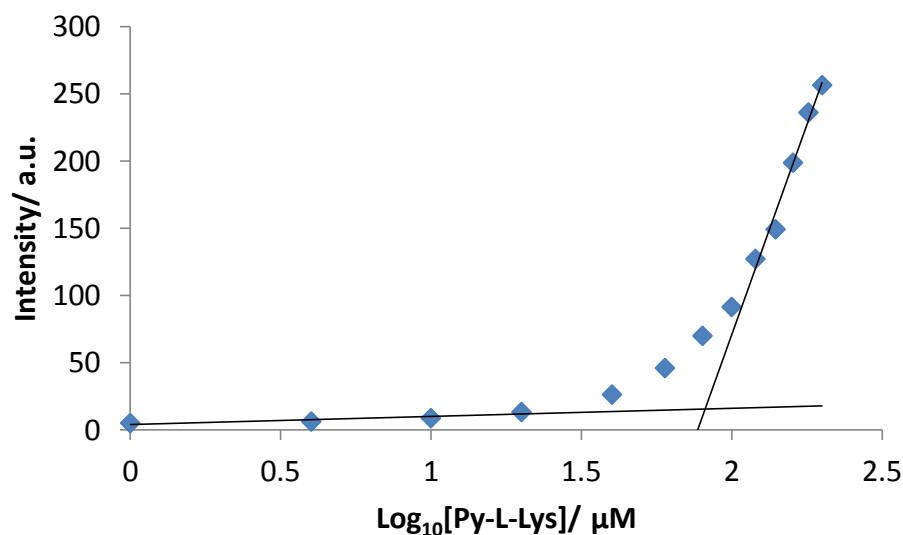


Figure 3.34: Fluorescence intensity at 495 nm of Py-L-Lys with increasing concentration in aqueous PBS Buffer (0.01 mM)

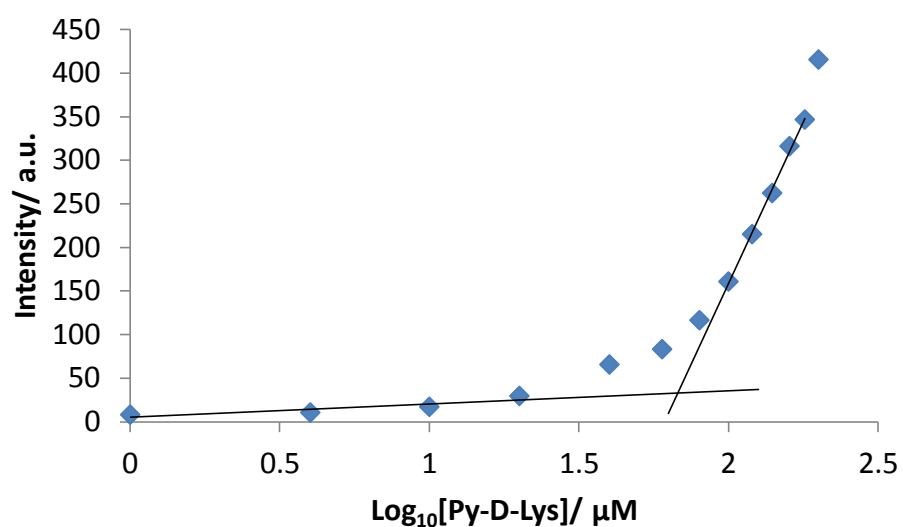


Figure 3.35: Fluorescence intensity at 495 nm of Py-D-Lys with increasing concentration in aqueous PBS Buffer (0.01 mM)

3.8.3 Transmission Electron Microscopy (TEM)

The self-assembled nanostructures being formed were visualised using transmission electron microscopy (TEM). The samples were first prepared in clean water at concentrations of 1 mg/mL and then deposited as solution-phase aliquots onto a formvar grid, stained with uranyl acetate and dried in air. Both Py-L-Lys and Py-D-Lys appeared to form relatively polydisperse spherical assemblies with approximate diameters ranging from ca. 10 to 40 nm (**Figure 3.36**) – given the (much smaller) molecular size (2-3 nm), it is suggested that these could be vesicular objects or clusters of micellar assemblies which aggregate on drying. Clearly, whatever self-assembly process is occurring is not as well-defined as for C₁₆-Lys. This may reflect the more bulky hindered nature of pyrene making it hard to organise the nanostructures.

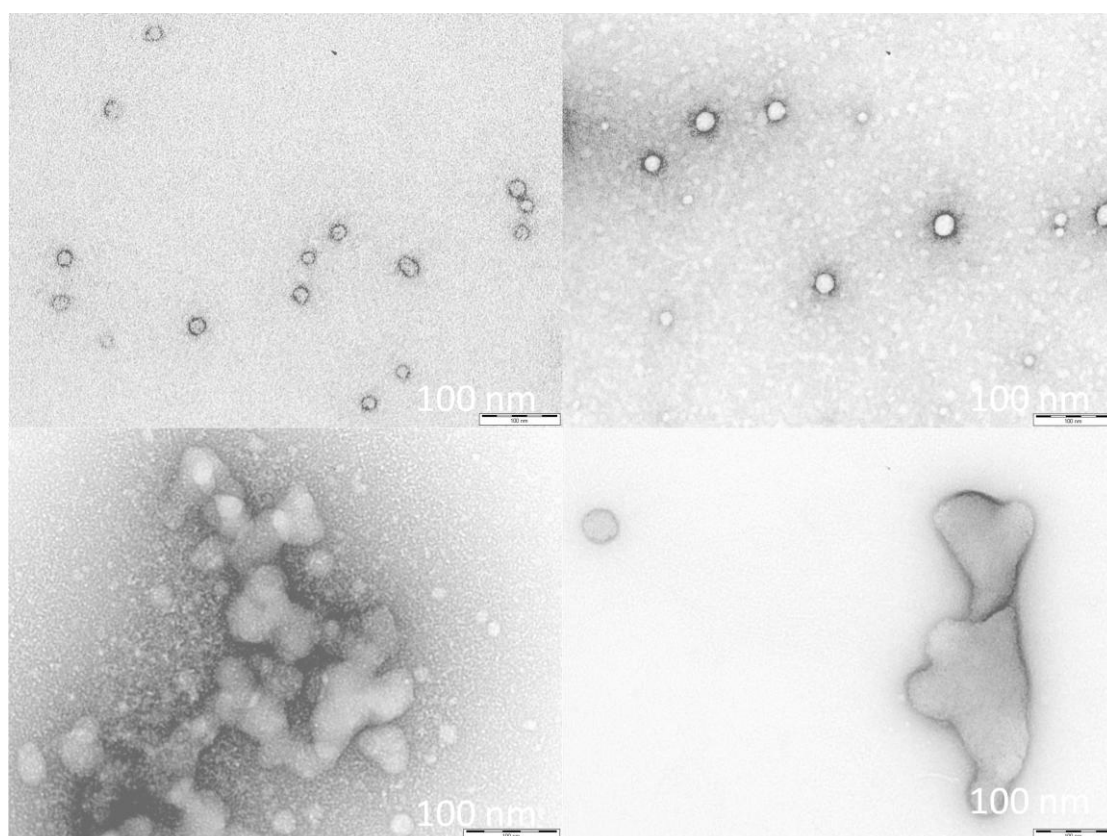


Figure 3.36: TEM images of Py-L-Lys (left) and Py-D-Lys (right) in the absence (top) and presence of heparin (bottom).

3.8.4 Dynamic Light Scattering (DLS)

The DLS data for enantiomeric assemblies are summarised in Table 2.2. Py-L-Lys supported the formation of relatively polydisperse self-assembled nanostructures with diameters 11.7 ± 3.8 nm (volume distribution). For Py-D-Lys, self-assembled nanostructures with diameters of 18.2 ± 8.1 nm similar to the TEM imaging. It should be noted that DLS also reflects a relatively polydisperse assembly process – diameters of the enantiomeric self-assembled nanostructures are within range of one another. The zeta potentials for both enantiomeric assemblies were positive ($+18.3 \pm 8.4$ mV for Py-L-Lys, $+34.1 \pm 1.5$ mV for Py-D-Lys). This is a result of protonation of the lysine ligands at physiological pH. As such, these self-assembled cationic nanostructures would be expected to show high affinity towards polyanionic heparin.

Sample in 10 mM Tris HCl, NaCl (150 mM)	Size (d.nm)	Zeta Potential (mV)	PDI
Py-L-Lys	11.7 ± 3.8	18.3 ± 8.4	0.58
Py-D-Lys	18.2 ± 8.1	34.1 ± 1.5	0.32

Table 2.2: DLS data for Py-L-Lys and Py-D-Lys.

Z-Average (d.nm): 25.28	Peak 1: 11.66	% Volume: 99.8	St Dev (d.nm): 3.827
Pdi: 0.629	Peak 2: 138.6	0.2	66.01
Intercept: 0.869	Peak 3: 5389	0.0	672.3
Result quality : Good			

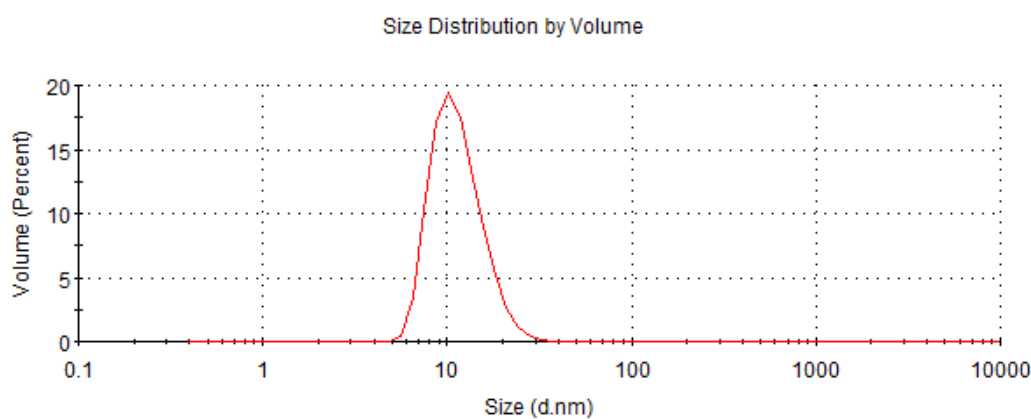


Figure 3.37: DLS data for Py-L-Lys measured at 1mg/ mL.

	Size (d.nm):	% Volume:	St Dev (d.nm):
Z-Average (d.nm): 30.10	Peak 1: 18.15	99.9	8.148
Pdl: 0.275	Peak 2: 379.1	0.1	192.1
Intercept: 0.909	Peak 3: 0.000	0.0	0.000
Result quality : Good			

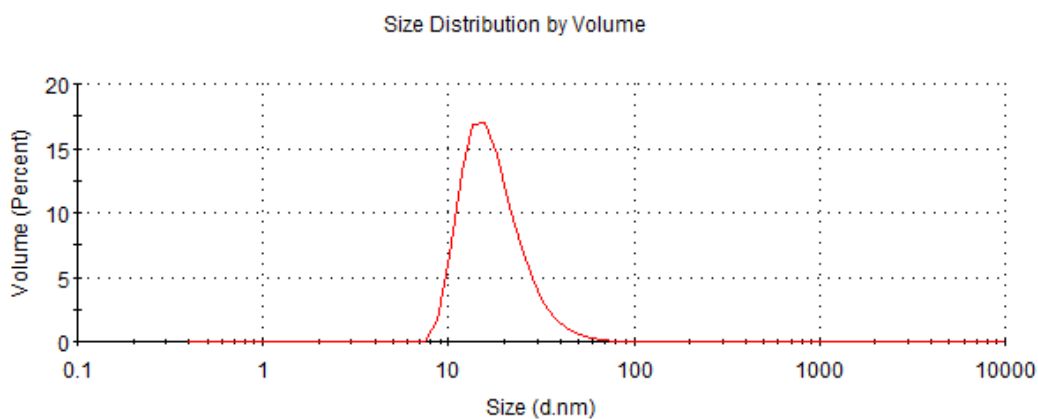


Figure 3.38: DLS data for Py-L-Lys measured at 1mg/ mL.

3.8.5 Heparin sensing in 10 mM Tris HCl with 150 mM NaCl buffer

On titrating Py-L-Lys (60 μ M) with heparin under the same conditions as Py-G1 in Section 2.2.5, the monomer fluorescence emission at 395 nm decreased in intensity but the excimer band at 495 nm was effectively unchanged (**Figure 3.39**). Titrating Py-D-Lys (60 μ M) with heparin had similar results as Py-L-Lys (**Figure 3.41**). Since the concentration of both sensors were only just at the CAC value (Section 3.8.2), this may limit the self-assembly, in any case, the SAMul sensing mechanism observed for Py-G1 was not seen and we instead observe similar behaviour as for Py-DAPMA. **Figure 3.40** (inset) shows a photograph of Py-L-Lys when heparin is absent (A) or present (B). Clearly, some “switch-on” emission can be seen using the naked eye when the sample is under UV irradiation, as the fluorescence changes colour (and intensity) to be somewhat more ‘green’. However, for Py-D-Lys (**Figure 3.42**), there was also no ‘naked eye’ change in the fluorescence emission. This is discussed in more detail below.

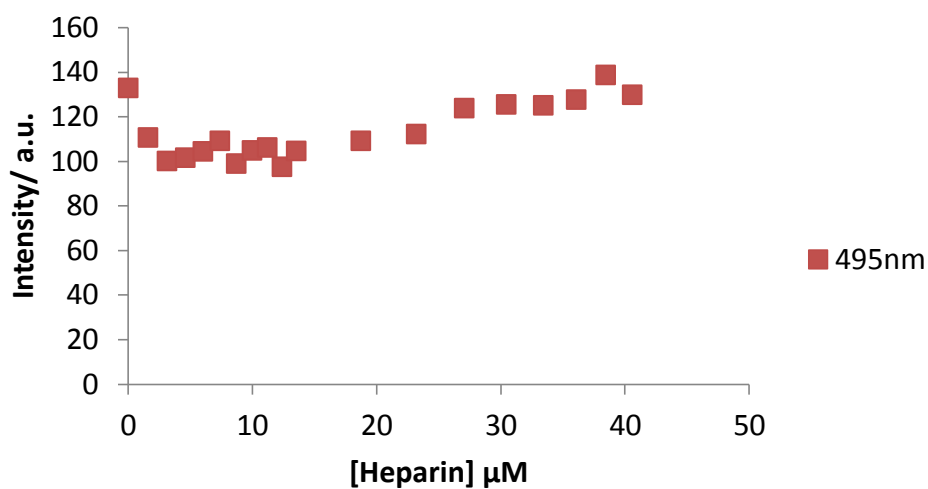
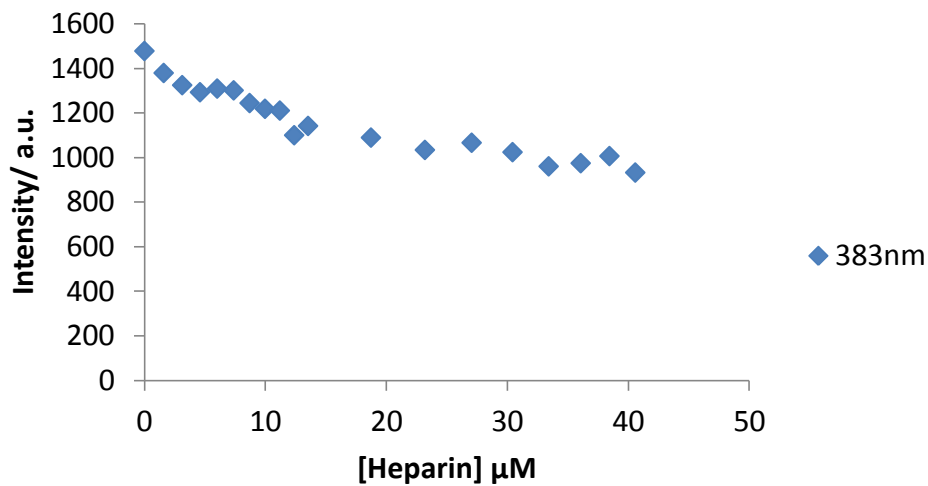


Figure 3.39: Fluorescence intensities extracted at 383 nm (Top) and 495 nm (Bottom) for the titration of heparin into Py-L-Lys in buffer.

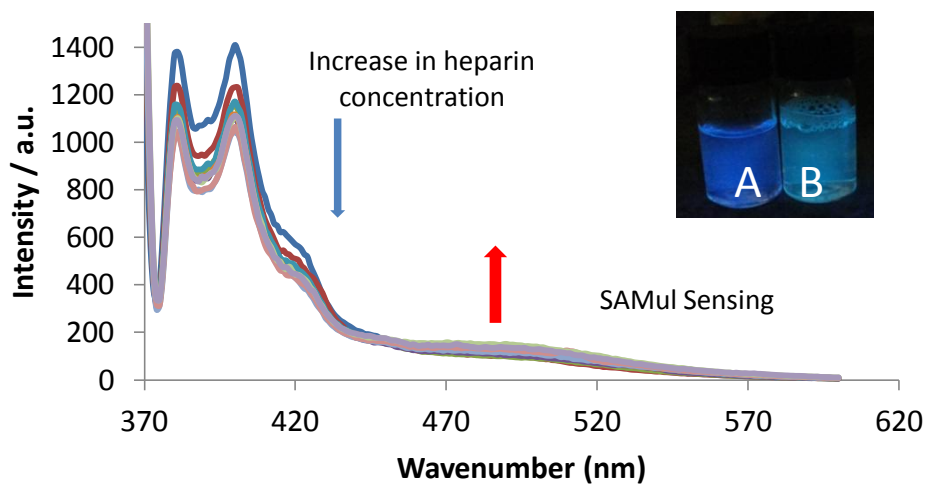


Figure 3.40: Fluorescence spectra of Py-L-Lys on addition of heparin in buffer. The inset

shows the photographs of a solution of Py-L-Lys without heparin (A) and with heparin (B).

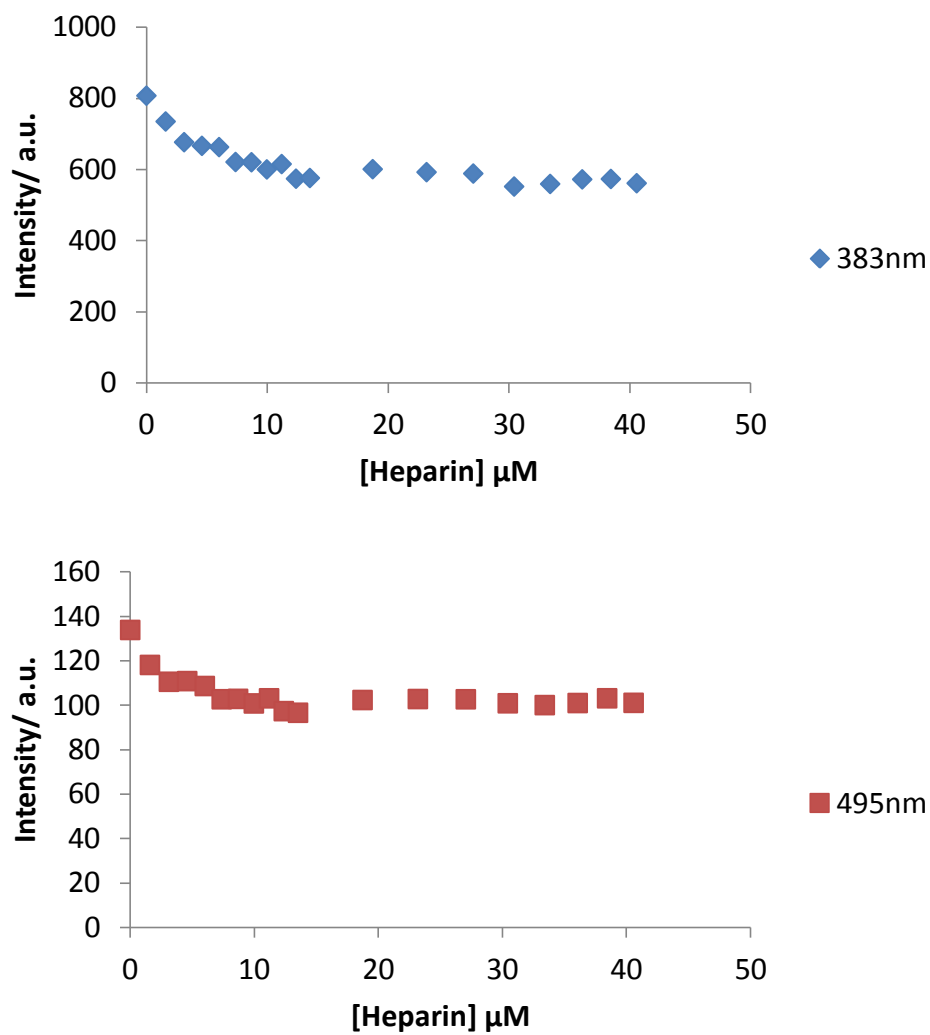


Figure 3.41: Fluorescence intensities extracted at 383 nm (Top) and 495 nm (Bottom) for the titration of heparin into Py-D-Lys in buffer.

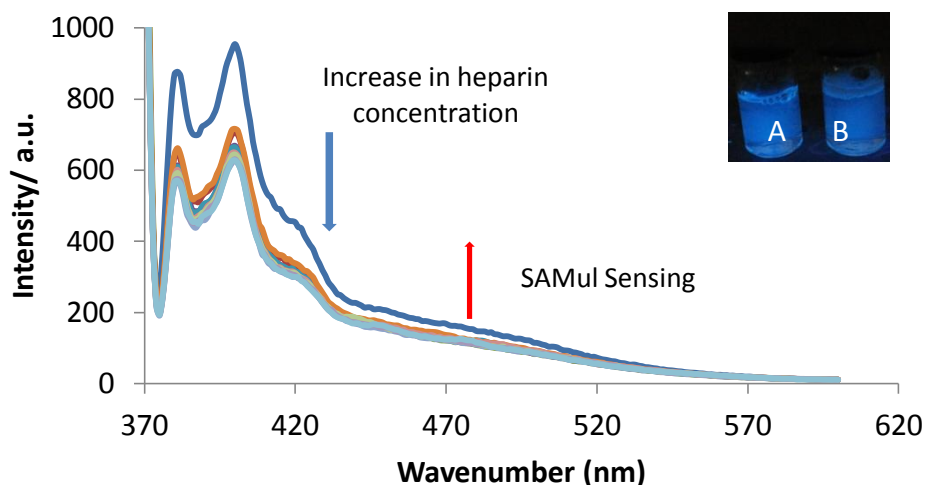


Figure 3.42: Fluorescence spectra of Py-D-Lys on addition of heparin in buffer. The inset shows the photographs of a solution of Py-D-Lys without heparin (A) and with heparin (B).

Comparing the ratiometric response for Py-L-Lys and Py-D-Lys, it is evident that Py-L-Lys shows the larger response in agreement with the naked eye observations. It was clear that Py-L-Lys shows better sensing of heparin than the Py-D-Lys (**Figure 3.43**). While this work was in progress, Bromfield *et al.* reported SAMul nanosystems exhibiting a chiral preference in polyanion binding. In particular, they reported that the D-conformation of lysine displayed on the surface of their nanostructures was more favoured for binding to heparin.¹⁶⁰ This is different to our observations here. In our study the sensor directly binds to heparin, whereas Bromfield was using a competition assay with a heparin sensor Mallard Blue (Mal-B), a high-affinity selective heparin sensor that operates in highly competitive media and is itself, also chiral.⁸⁰ However, it must also be noted that different hydrophobic units might be expected to self-assemble and display their chiral ligands in different ways and this may lie at the origin of the differences.

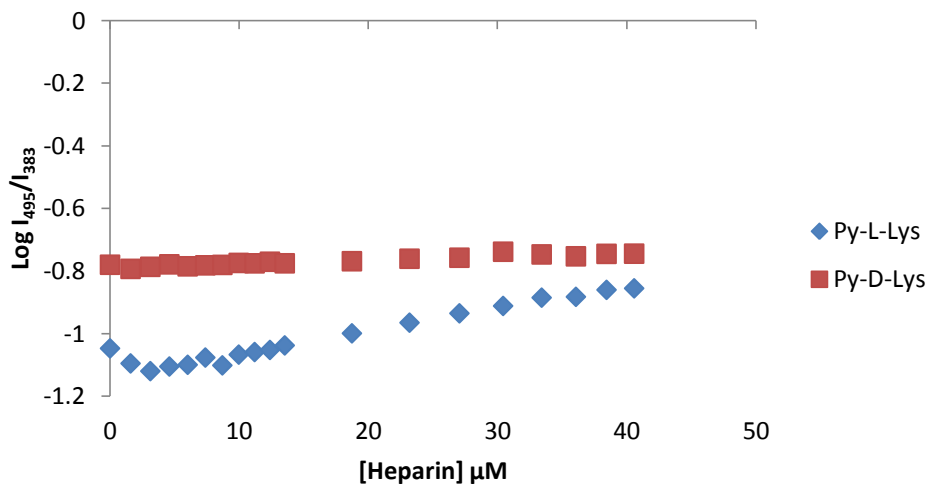


Figure 3.43: The changes of the fluorescence intensity ratio of Py-L-Lys and Py-D-Lys ($\log(I_{495}/I_{383})$) plotted against increasing heparin concentration in in 10 mM Tris HCl buffer with 150mM NaCl buffer.

3.8.6 Heparin sensing in 12.5% serum with 20 mM Tris HCl

Both PyL-Lys and Py-D-Lys were tested for binding to heparin in 12.5% serum under the same conditions as Py-G1 in Section 2.2.6. Again, the fluorescence emission at 395 nm decreased in intensity but the band at 495 nm was effectively unchanged (**Figure 3.44**). Titrating Py-D-Lys (60 μM) with heparin gave similar results as Py-L-Lys (**Figure 3.45**).

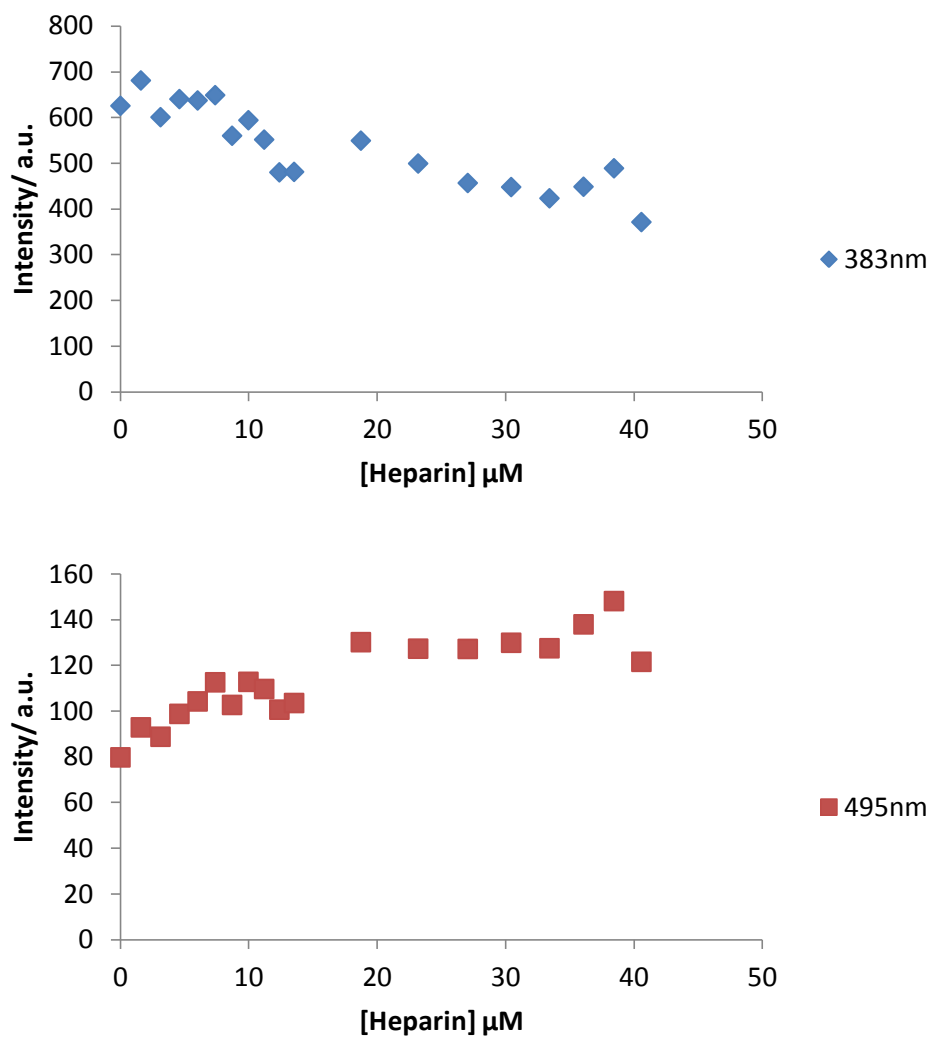


Figure 3.44: Fluorescence intensities extracted at 383 nm (Top) and 495 nm (Bottom) for the titration of heparin into Py-L-Lys in 12.5% serum with 20 mM Tris HCl.

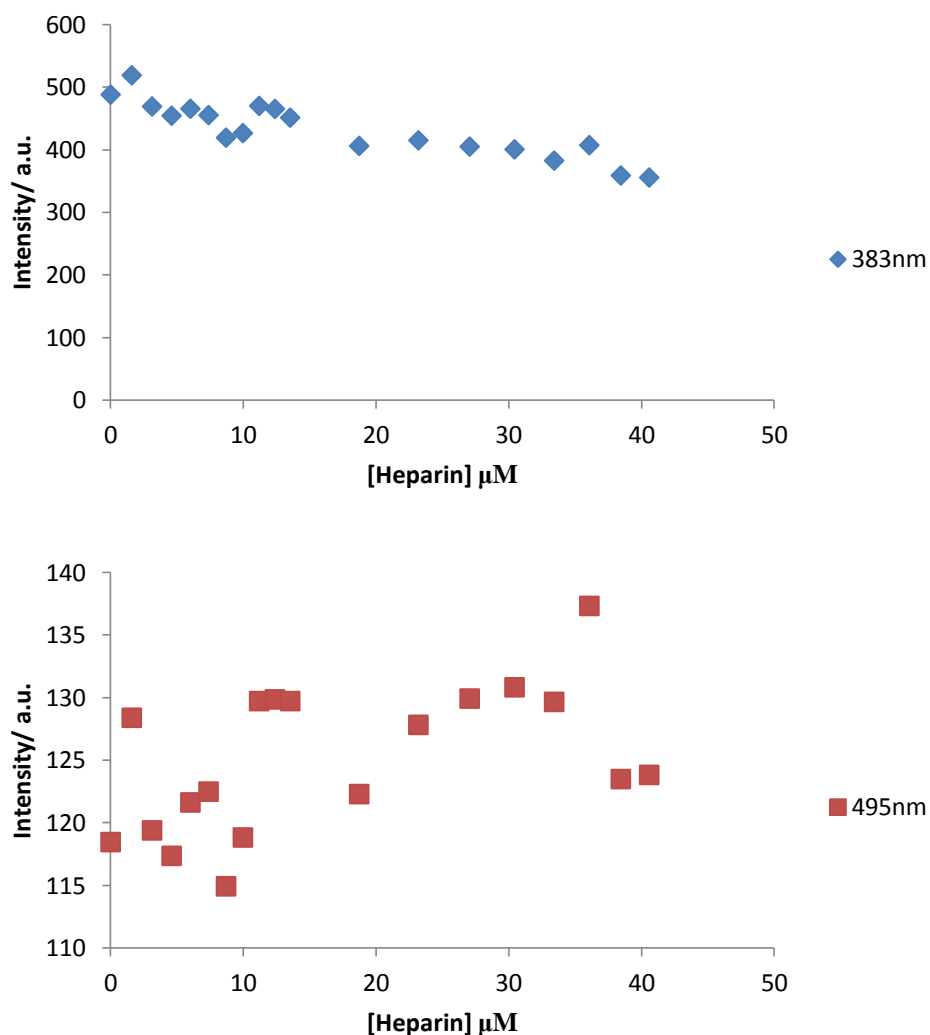


Figure 3.45: Fluorescence intensities extracted at 383 nm (Top) and 495 nm (Bottom) for the titration of heparin into Py-D-Lys in 12.5% serum with 20 mM Tris HCl.

Comparing the ratiometric response for Py-L-Lys and Py-D-Lys, again it is evident that Py-L-Lys shows the larger response mainly driven by changes in the monomer emission. Furthermore, under these conditions the response is linear. It was clear that Py-L-Lys shows better sensing of heparin than the Py-D-Lys. In particular, there is a sensory response to heparin across the clinically important concentration (1 to 10 μM). This also suggested that the L-configuration is more favoured in binding to heparin in 12.5% serum for this system (**Figure 3.46**).

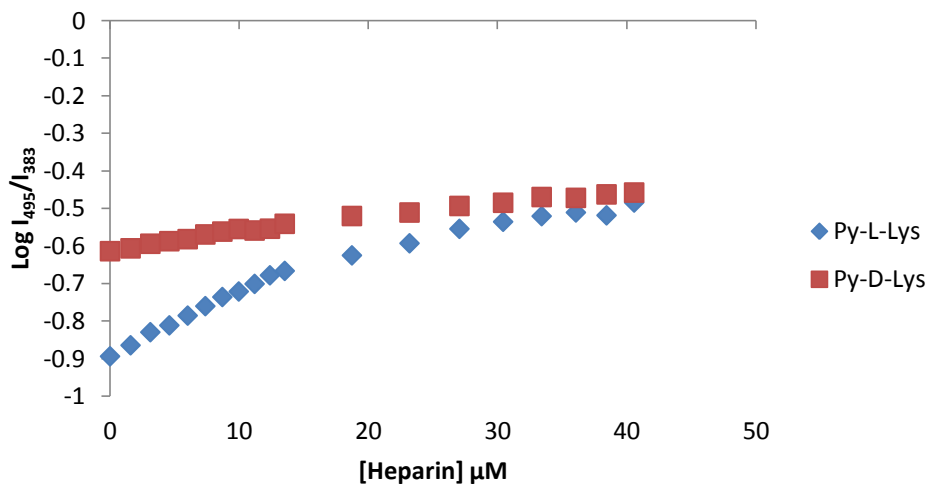


Figure 3.46: The changes of the fluorescence intensity ratio of Py-L-Lys and Py-D-Lys ($\log(I_{495}/I_{383})$) plotted against increasing heparin concentration in 12.5% serum with 20 mM Tris HCl.

3.8.7 Heparin sensing in 100% serum

In 100% serum, for Py-L-Lys, both monomer emission with peaks at 383 and 400 nm and excimer emission with peak at 495 nm did not change on increasing the concentration of heparin (**Figure 3.47**). The same was also observed for Py-D-Lys (**Figure 3.48**).

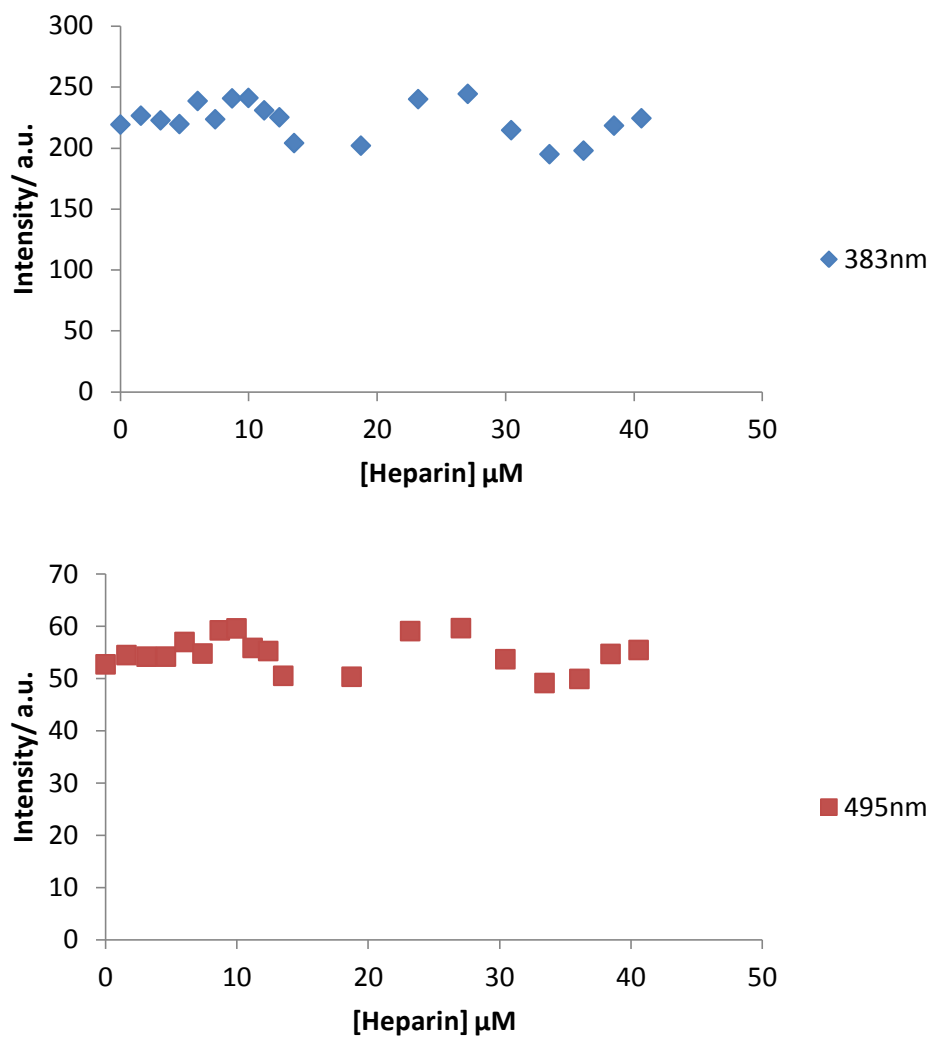


Figure 3.47: Fluorescence intensities extracted at 383 nm (Top) and 495 nm (Bottom) for the titration of heparin into Py-L-Lys in 100% serum.

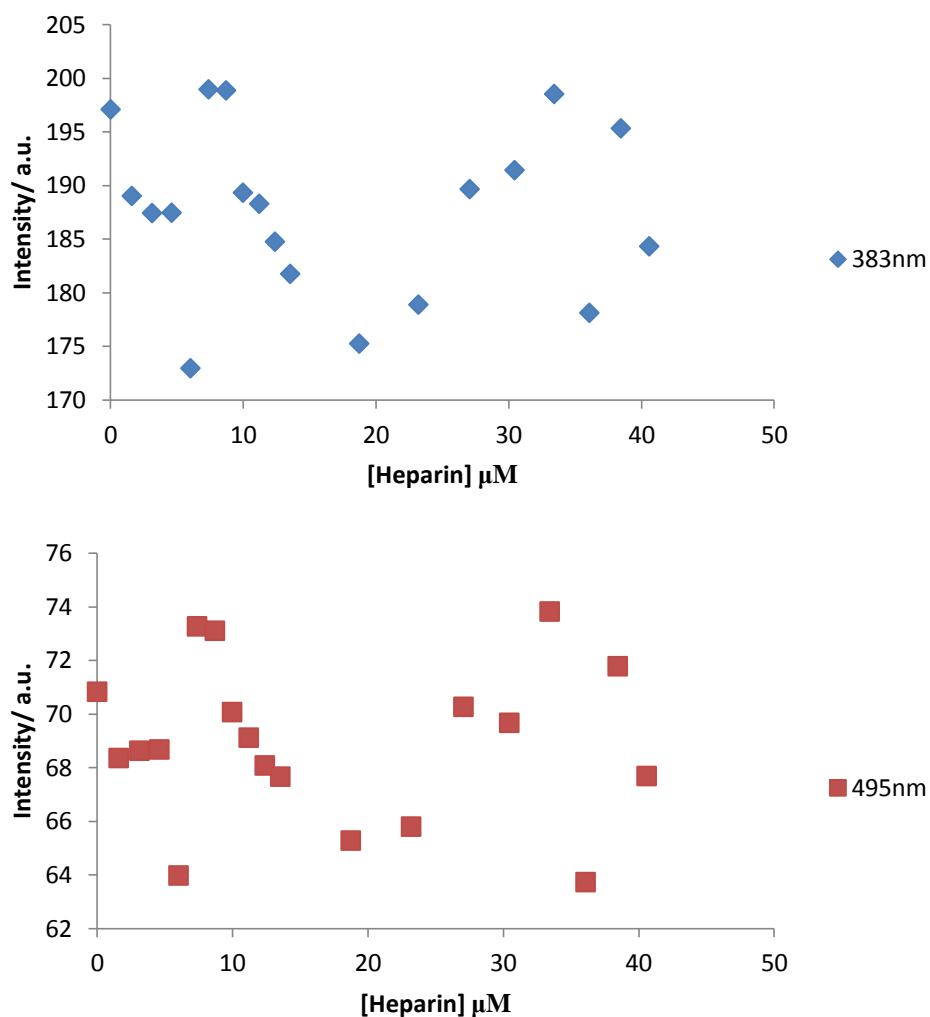


Figure 3.48: Fluorescence intensities extracted at 383 nm (Top) and 495 nm (Bottom) for the titration of heparin into Py-D-Lys in 100% serum.

From **Figure 3.49**, we can see there were no observable changes in the $\log(I_{495}/I_{383})$ plot for either compound. At this point, it could be either the background competition by albumin proteins (etc.) binding too strongly to all of the hydrophobic parts and hence preventing any excimer from being established and limiting heparin binding or the fluorescence scattering by serum itself meaning we can't detect anything. Therefore, we also performed the test with elevated concentrations of both the sensors and heparin.

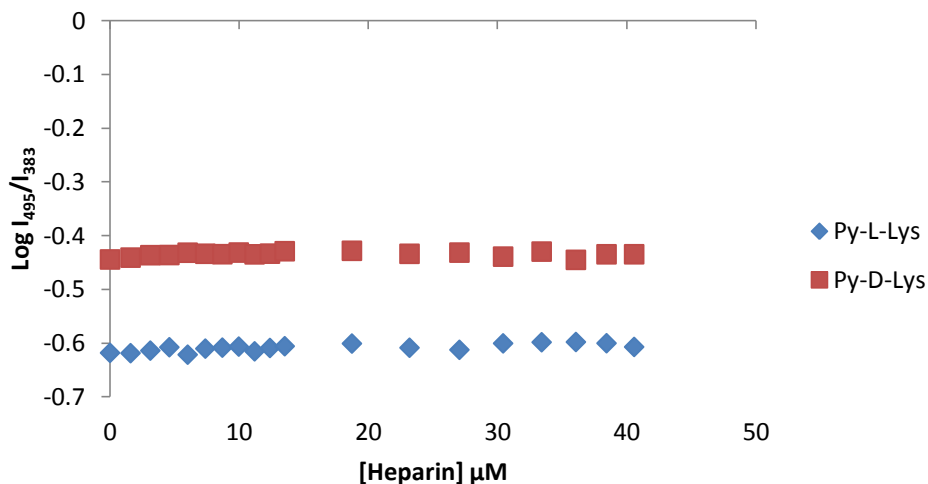


Figure 3.49: The changes of the fluorescence intensity ratio of Py-L-Lys and Py-D-Lys ($\log(I_{495}/I_{383})$) plotted against increasing heparin concentration in 100% serum.

3.8.8 Heparin sensing in 10 mM Tris HCl with 150 mM NaCl buffer at elevated concentrations.

Both sensors were examined at ca. seven times elevated concentrations (426 μM) to determine whether they could detect heparin under these conditions. Since this assay concentration was now well above the CAC value of the sensors, we can clearly see that SAMul sensing mechanism was observed in buffer. Upon addition of heparin, for both Py-L-Lys (**Figure 3.50**) and Py-D-Lys (**Figure 3.51**) the fluorescence emission intensity at 383 nm decreased while the emission band centred at 495 nm increased very significantly until it became the dominant feature of the spectrum. The emission band at 495 nm shows a large enhancement with increasing concentration of heparin and can be attributed to the enhanced formation of pyrene excimers being induced by heparin binding.

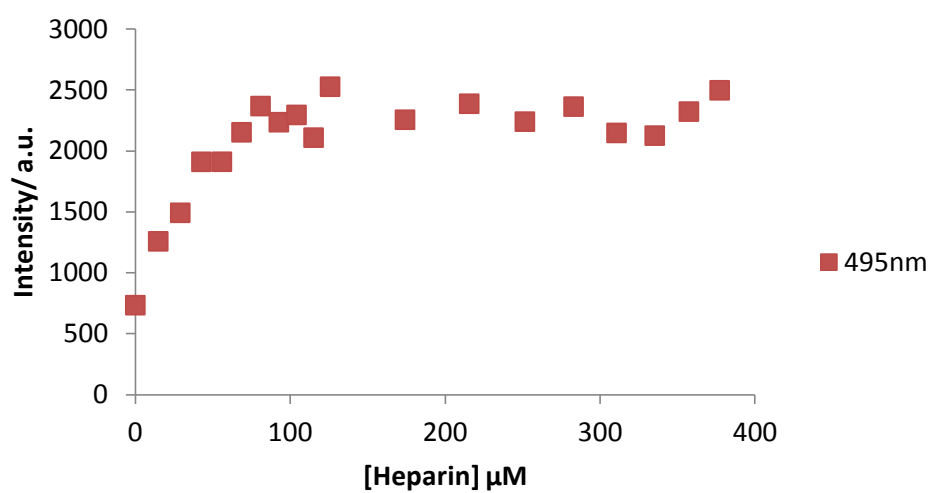
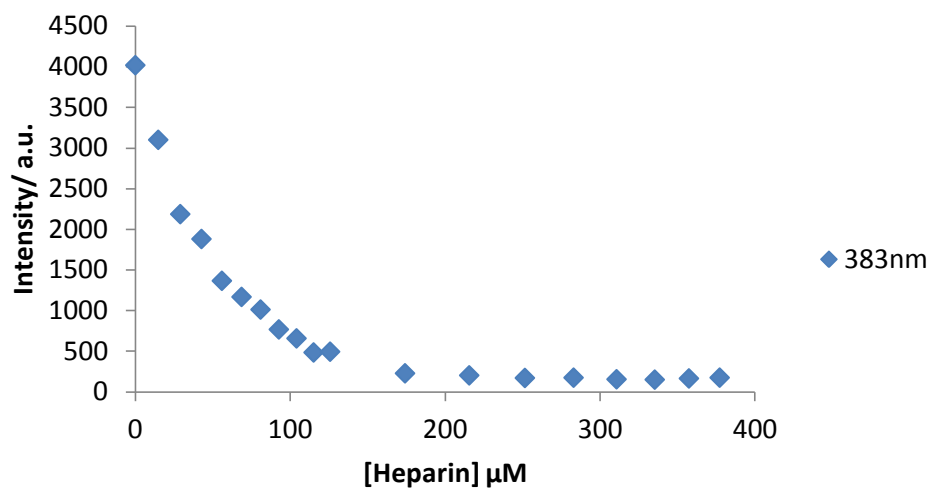


Figure 3.50: Fluorescence intensities extracted at 383 nm and 495 nm for the titration of heparin into Py-L-Lys ($426\mu\text{M}$) in buffer.

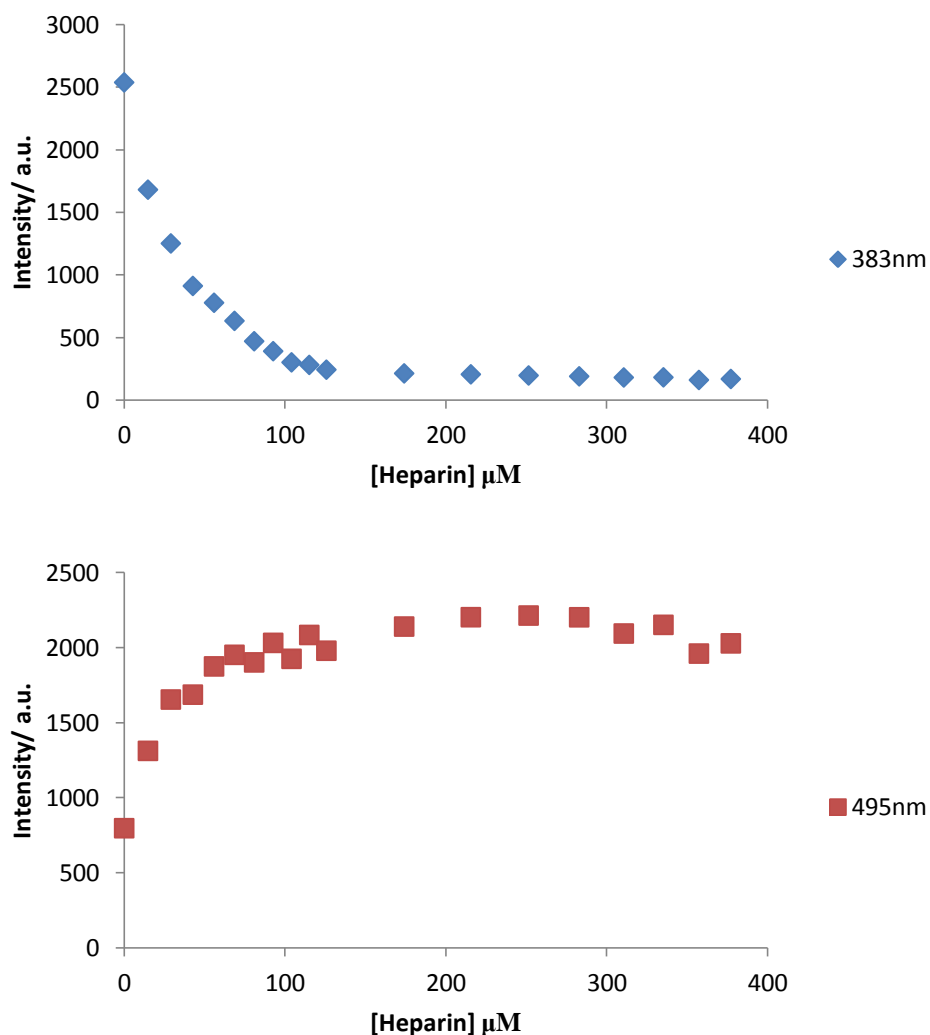


Figure 3.51: Fluorescence intensities extracted at 383 nm and 495 nm for the titration of heparin into Py-D-Lys (426μM) in buffer.

Comparing the ratiometric response for Py-L-Lys and Py-D-Lys under these conditions, both sensors showed somewhat similar and linear responses to heparin (**Figure 3.52**). When comparing the data with non-elevated concentration in Section 3.8.5, this would suggest that the SAMul approach is a more effective way of displaying ligands to ensure they can more effectively interact with heparin polyanions. The dynamic range of the sensors is large, with big fluorescent responses. However, the chiral discrimination has somewhat been lost, which may suggest that these sensors, when pre-assembled and bind primarily as a result of their charge, and therefore the effects of chiral charge organisation are being lost. It is possible that the introduction of

a glycine spacer unit, as earlier in the chapter may encourage the more effective display of the chiral ligands on surface of the nanostructures.

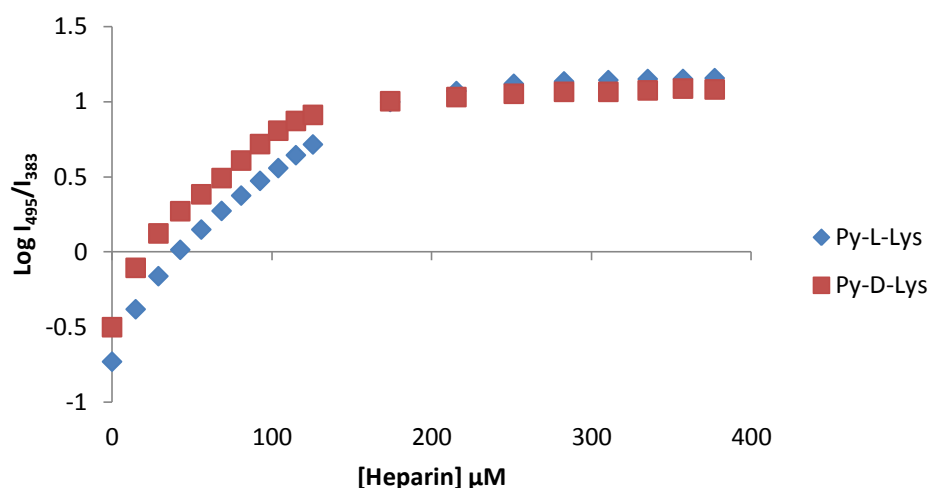


Figure 3.52: The changes of the fluorescence intensity ratio of PyL-Lys and Py-D-Lys ($\log(I_{495}/I_{383})$) plotted against increasing heparin concentration in buffer.

3.8.9 Heparin sensing in 12.5% serum with 20 mM Tris HCl at elevated concentrations

We also performed this elevated concentration assay in 12.5 % serum with 20 mM Tris HCl. In the absence of heparin, self-assembling Py-L-Lys (**Figure 3.53**) and Py-D-Lys (**Figure 3.54**) show a characteristic monomer emission, with peaks at 383 and 400 nm with a large excimer emission at 495 nm. Upon addition of heparin, the fluorescence emission intensity at 395 nm decreased while the emission band centred at 495 nm increased significantly. This would suggest that serum does not totally disrupt the self-assembled multivalency of Py-L-Lys and Py-D-Lys. Unlike when the assay was performed at lower concentrations, in this case $I_{495} > I_{383}$ once heparin is bound which indicated that increasing the concentration has significantly improved the ability of the system to stabilise the self-assembled nanostructures in these more competitive conditions. We would therefore assign this as a clear SAMul sensing mechanism.

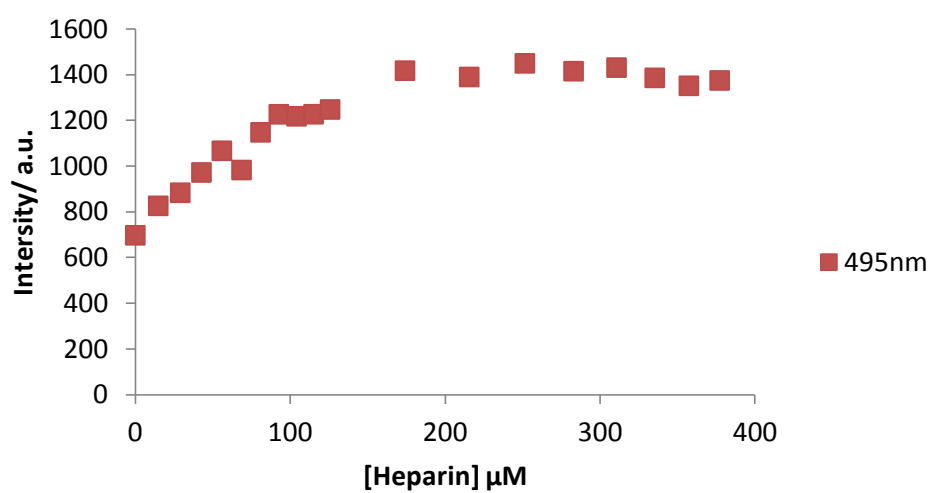
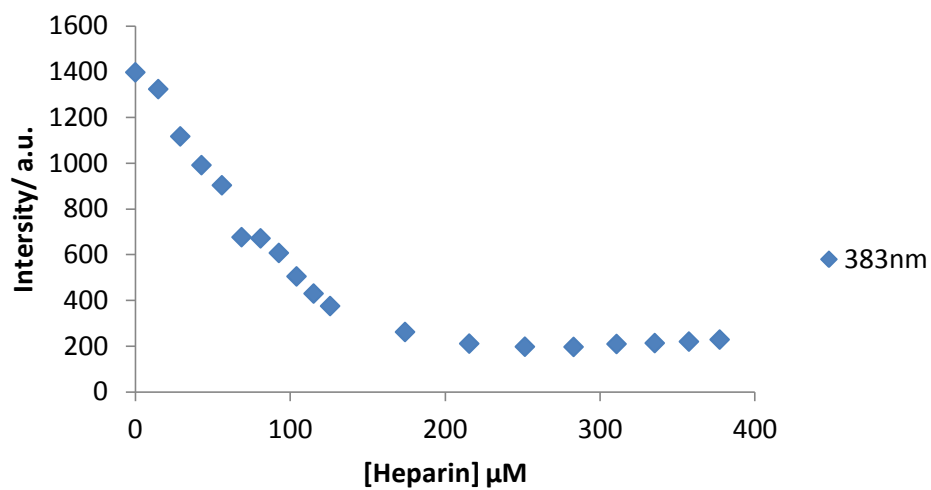


Figure 3.53: Fluorescence intensities extracted at 383 nm (Top) and 495 nm (Bottom) for the titration of heparin into Py-L-Lys in 12.5% serum with 20 mM Tris HCl.

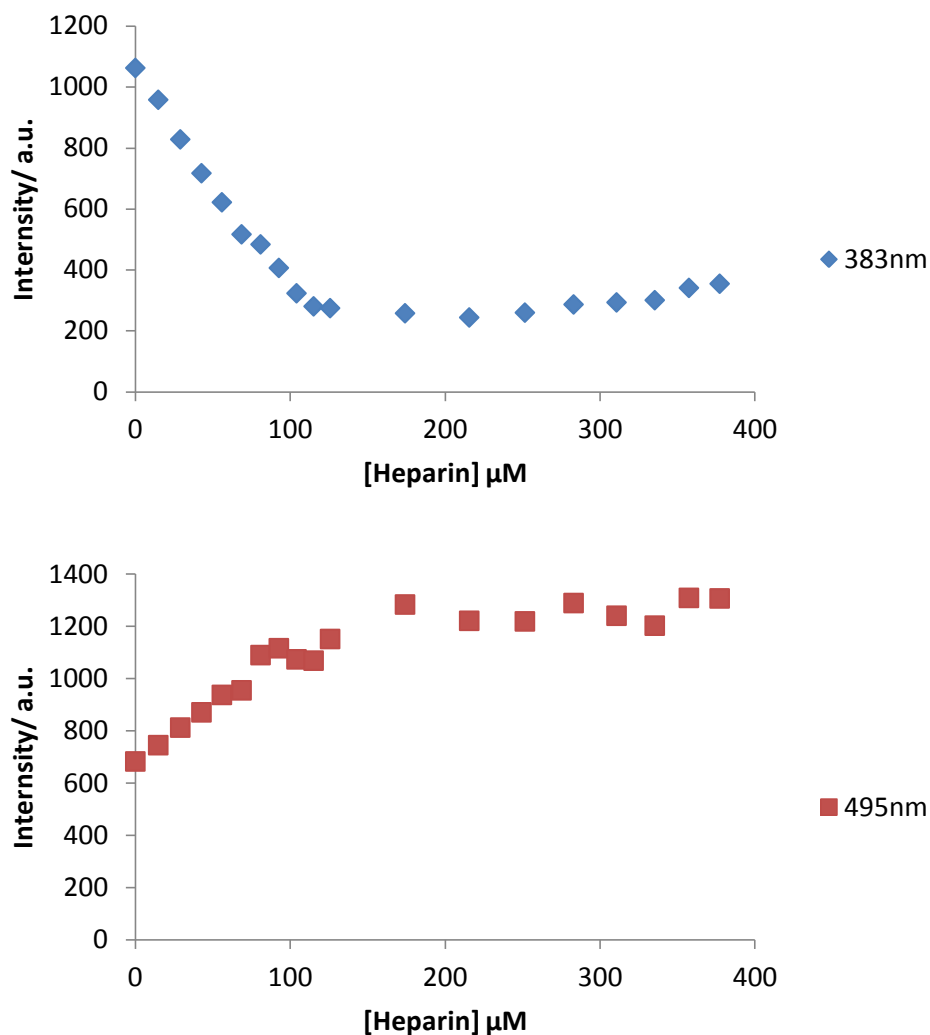


Figure 3.54: Fluorescence intensities extracted at 383 nm (Top) and 495 nm (Bottom) for the titration of heparin into Py-D-Lys in 12.5% serum with 20 mM Tris HCl.

Comparing the ratiometric response for Py-L-Lys and Py-D-Lys, both sensors showed very similar responses under these conditions (**Figure 3.55**). Both sensors gave a linear response to heparin under these assay conditions in concentrations from 10-150 μM.

While Py-DAPMA (Chapter 2) was suggested to have limited SAMul sensing response observed in serum conditions, both Py-L-Lys and Py-D-Lys had $\log(I_{495}/I_{383}) > 0$ and comparable dynamic ranges to those observed in buffer condition. This may suggest that sensor self-assembly is being relatively well maintained in this system.

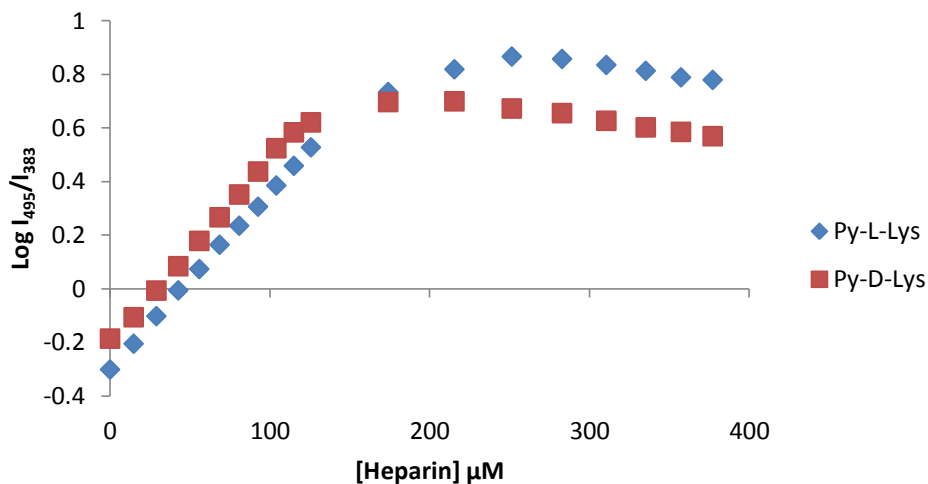


Figure 3.55: The changes of the fluorescence intensity ratio of Py-L-Lys and Py-D-Lys (426 μM) ($\log(I_{495}/I_{383})$) plotted against increasing heparin concentration in 12.5% serum with 20 mM Tris HCl.

3.8.10 Heparin sensing in 100% serum at elevated concentrations

In 100% serum, at elevated concentrations, monomer emission of Py-L-Lys (**Figure 3.56**) and Py-D-Lys (**Figure 3.57**) with peaks at 383 and 400 nm decreased and excimer emission with peak at 495 nm increased, but only slightly, on addition of heparin. This clearly suggested that Py-L-Lys and Py-D-Lys were able to sense heparin in 100% serum. However, it is also clear that there is less evidence of SAMul sensing in 100% serum than was observed in 12.5% serum or simple buffered conditions. The results would again suggest that when SAMul is fully enforced prior to heparin addition, this system shows little chiral discrimination.

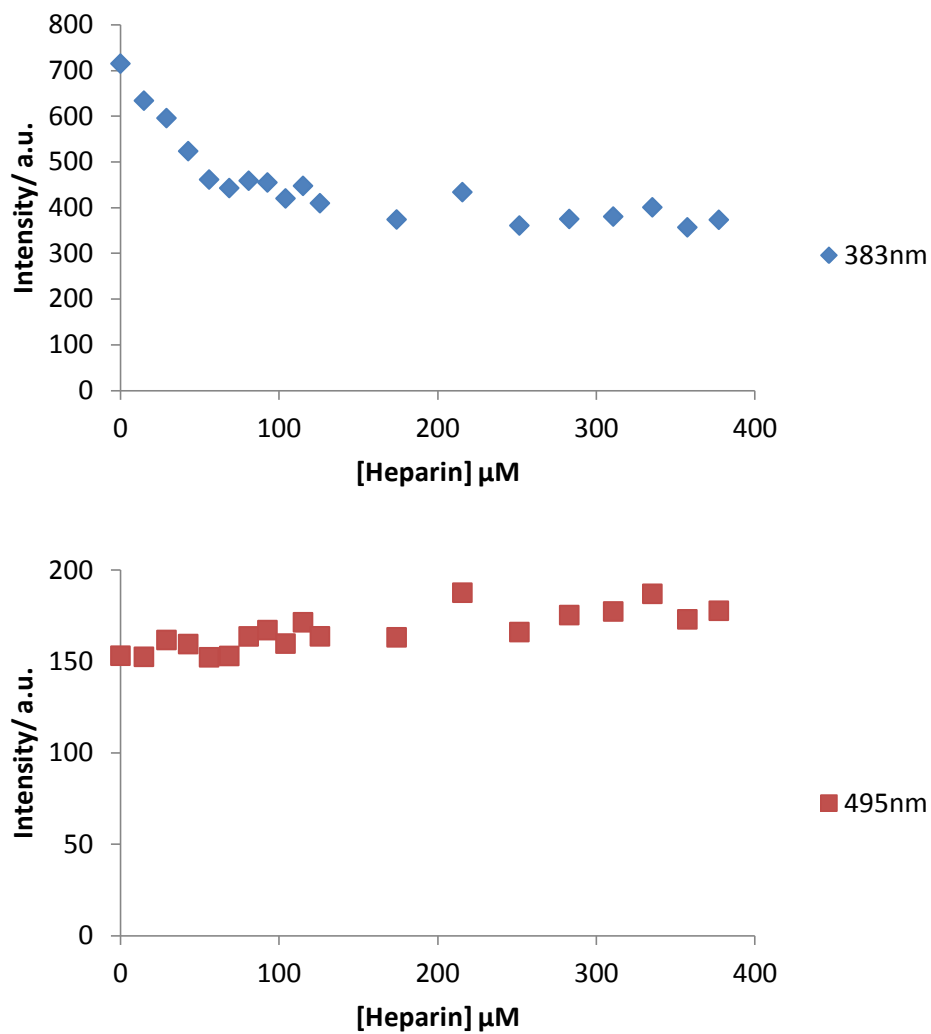


Figure 3.56: Fluorescence intensities extracted at 383 nm (Top) and 495 nm (Bottom) for the titration of heparin into Py-L-Lys (426μM) in 100% serum.

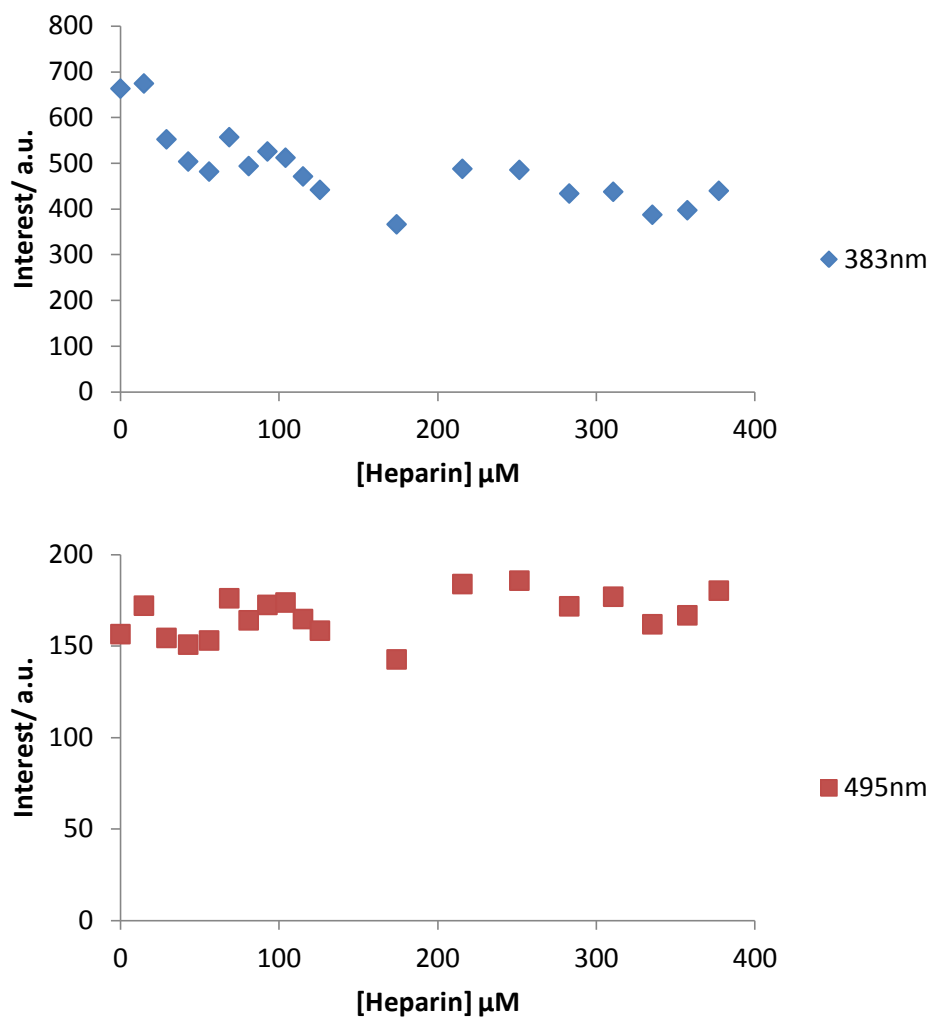


Figure 3.57: Fluorescence intensities extracted at 383 nm (Top) and 495 nm (Bottom) for the titration of heparin into Py-D-Lys (426μM) in 100% serum.

Once again, considering the ratiometric response, a linear response is observed (in this case both responses are again similar for Py-L-Lys and Py-D-Lys) (**Figure 3.58**). The dynamic range is less than observed in buffer as well as in 12.5% serum buffer condition. This may due to the serum light scattering, as well as competition from the binding and fluorescent event in serum

Overall, it is remarkable that simple dications (Py-L-Lys and Py-D-Lys) can respond to heparin polyanions in such highly competitive media. We propose that the amphiphilic ligand design, and the ability of pyrene to assemble during binding to heparin, play a significant role in assisting heparin sensing in 100% serum.

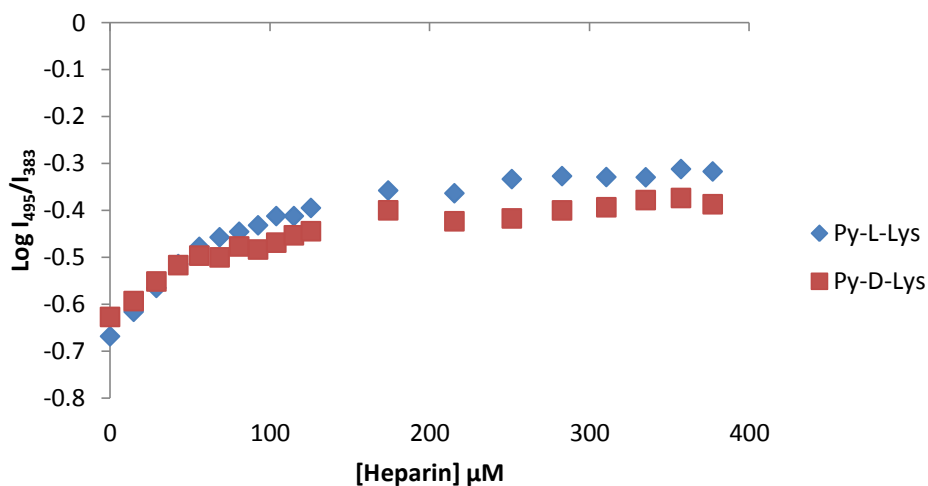


Figure 3.58: The changes of the fluorescence intensity ratio of Py-G1 (213 μM) and Py-DAPMA (426 μM) ($\log(I_{495}/I_{383})$) plotted against increasing heparin concentration in 100% serum

Intriguingly there appears to be some chiral discrimination when these sensors are applied at low concentration but not at high concentration, This may suggest that the extent of self-assembly prior to heparin binding indicates the abilities of the chiral ligands to achieves any stable discrimination on binding. Such systems may be improved on the surfaces of nanostructures by incorporating a spacer unit.

3.8.11 Conclusion and future work

Both Py-L-Lys and Py-D-Lys can act as effective heparin sensors in competitive media using a ratiometric fluorescence sensing approach, which is desirable for a clinical setting in term of detecting this biologically important polyanion. However, little chiral discrimination is observed in the binding event.

It is instructive to compare all of these results with those recently reported by Bromfield and Smith.¹⁶⁰ Although all of these systems have the same lysine ligands on their surfaces for binding to chiral polyanions the polyanions display different chiral preferences (**Table 3.3**). This would suggest that the way in which the ligands are displayed, which in turn depends on the nature of the hydrophobic component and the

overall structural characteristics, are absolutely critical. This view is strongly supported by the observation that the introduction of a spacer unit in C₁₆-Gly-Lys switches on nanoscale enantio-differentiation in contrast to C₁₆-Lys. Furthermore the impact of concentration on the chiral recognition potential of Py-Lys would also suggest that the extent of self-assembly, which impacts directly on ligand display, will help to mediate and control the binding preferences. Clearly, nanoscale recognition events are complex and it is too simplistic to imagine that a specific ligand will target a specific guest, rather, the overall nanoscale display is required to optimize binding. This in fact suggests that this field of research, still in its infancy, has considerable potential for further optimisation and development.

	DNA	Heparin
1L/1D ¹⁶⁰	L	D
2L/2D ¹⁶⁰	No preference	No preference
C ₁₆ -L/D-Lys	No preference	No preference
C ₁₆ -Gly-L/D-Lys	D	D
Py-L/D-Lys Low concentration	Not studied	L
Py-L/D-Lys High concentration	Not studied	No preference

Table 3.3: List of SAMul polyanion binder.

For future work, the study the effect of spacer groups in chiral systems such as use of another amino acid as spacer groups and the study of effect of morphology of self-assembly. Other modifications could include variation of the surface binding groups to examine the effects of different cationic ligands on DNA/heparin binding performance.

Chapter 4 NMR investigation of Heparin binding with Mallard Blue (Mal-B) and Self-Assembled Multivalent (SAMul) Heparin Binders

4.1 Introduction

In the previous chapter we explored the impact of structural changes on polyanion sensing and binding. Specifically, we have observed how modifying the hydrophobic units responsible for self-assembly can give the overall nanostructures the capacity for heparin sensing. We have also explored the impact of chirality, and more importantly the precise display of chiral ligands, on the specifics of polyanion recognition. In this chapter we explore the specifics of ligand design on interaction with polyanionic heparin in precise molecular detail.

4.1.1 Heparin NMR

As discussed in Chapter 2, heparin is a highly sulfated polysaccharide which is the most charge-dense polyanion present in biological systems and is used widely as an anti-coagulant drug.⁵⁰

Nuclear magnetic resonance (NMR) spectroscopy has been used for structural characterization of heparin, without the possibility of loss or conversion of structural information as a result of breakdown of the polymer, as established by several early studies.^{165, 166} One dimensional (1D) proton and carbon NMR have been used to elucidate the monosaccharide composition, patterns of sulfation and acetylation present in heparins isolated from different sources, as well as chemically modified heparin (**Figure 4.2**).¹⁶⁷⁻¹⁶⁹ Such studies are of key importance given the heterogeneous nature of many heparin samples, and variability from batch to batch. While 1D NMR analysis was limited by severe signal overlapping, two dimensional (2D) NMR such as heteronuclear single quantum coherence (HSQC) spectroscopy, which provides correlation between the aliphatic carbon and its attached protons, allowed the

determination of the various monosaccharide components. The spectrum contained a peak for each unique proton attached to the heteronucleus being considered (**Figure 4.3**). Recently, the use of high-field NMR analysis was employed not only to probe monosaccharide composition, but also to find the presence of impurities such as oversulfated chondroitin sulfate (OSCS) present in marketed heparin products.¹⁷⁰⁻¹⁷²

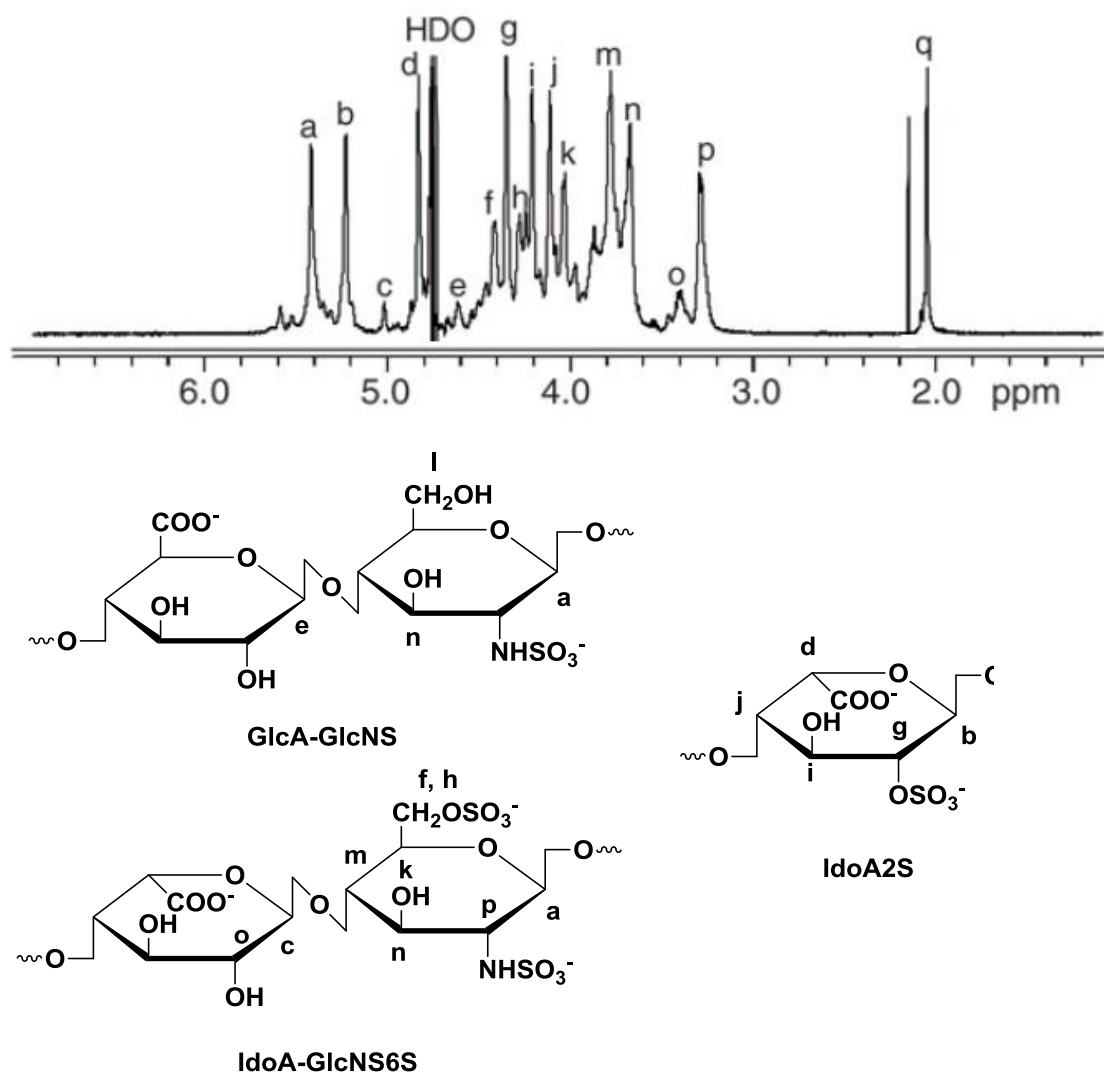


Figure 4.2: (Top) ¹H-NMR spectra acquired at 800 MHz and assignment of heparin: a, H1 GlcNS, GlcNS6S; b, H1 IdoA2S; c, H1 IdoA; d, H5 IdoA2S; e, H1 GlcA; f, H6 GlcNS6S; g, H2 IdoA2S; h, H6' GlcNS6S; i, H3 IdoA2S; j, H4 IdoA2S; k, H5 GlcNS6S; l, H6 GlcNS; m, H4 GlcNS6S; n, H3 GlcNS, GlcNS6S; o, H2 GlcA; p, H2 GlcNS6S; q, acetyl CH₃.¹⁷³ (bottom) Structures of the common disaccharide pairs in the heparin chains and assignment.

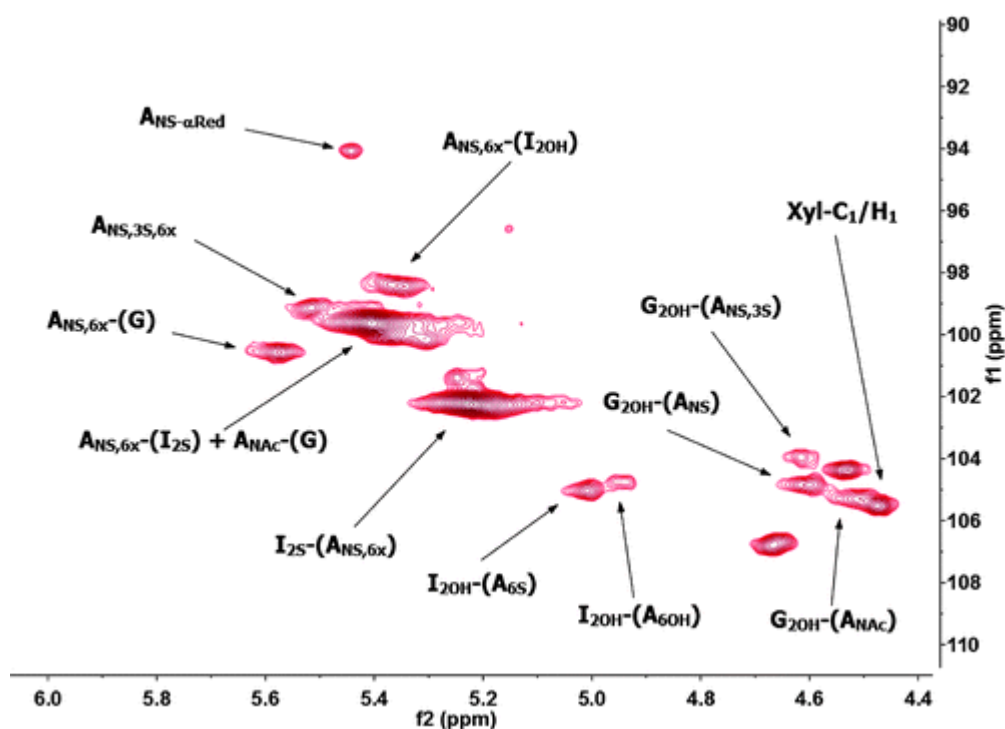
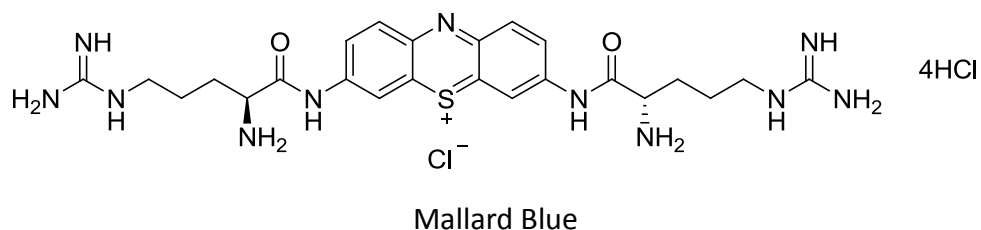


Figure 4.3: Plot of the anomeric region (4.4 to 6.1 ppm proton (f2) and 90 to 110 carbon ppm (f1)) the 2D ^1H - ^{13}C HSQC spectrum obtained on a 50 mg sample of sodiated heparin in 700 μL of D_2O .¹⁷⁴

4.1.2 Mallard Blue

In 2013, Bromfield *et al.* reported the use of Mallard Blue (Mal-B), which is a high-affinity selective heparin sensor that operates in highly competitive media.⁸⁰ We employed this dye in Chapter 3 for the competition assays of heparin binding.



The binding site of Mal-B to heparin is of particular interest. Bromfield *et al.*, who reported the use of Mal-B for heparin sensing also reported a molecular dynamics (MD) study of the interaction of both (**Figure 4.4**), and it was suggested that cationic sites on the sensor were in close proximity to anionic sites on the heparin with the sensor

binding over the heparin chain in a “groove-like” site.⁸⁰ This binding mode was in agreement with the experimentally observed stoichiometry but there was no other experimental data available to support this model. Clearly, dissecting such interactions at the molecular level would be of considerable value.

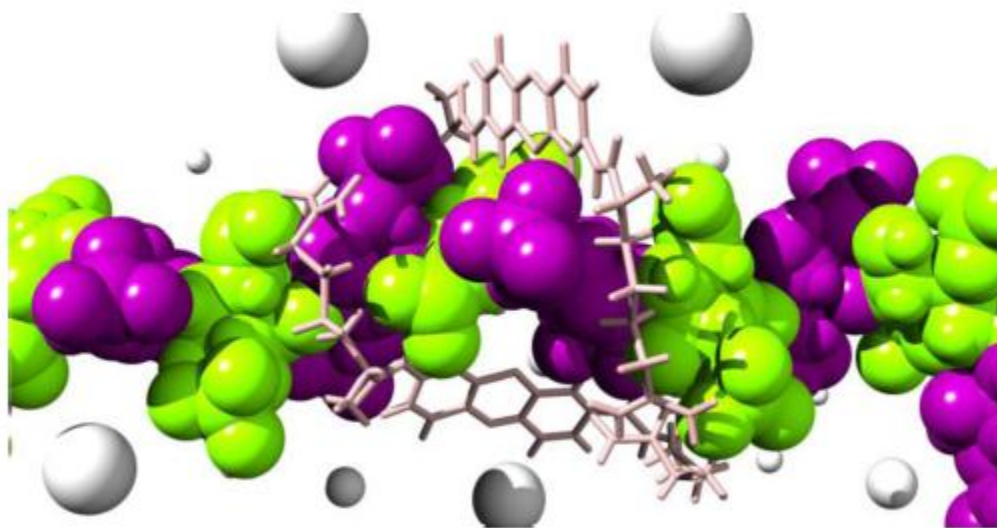


Figure 4.4: Equilibrated MD snapshot of the Mal-B-heparin system. Mal-B, rosy brown sticks; heparin (D-glucosamine units), dark magenta spheres; and CPK (L-iduronic acid units), chartreuse spheres. Some Cl⁻ and Na⁺ ions are shown as large and small white spheres, respectively. Water omitted for clarity.⁸⁰

4.1.3 NMR study of heparin interaction

Nuclear magnetic resonance (NMR) can be used for investigating intermolecular and intramolecular interactions in inclusions, ion pairs, and aggregates.^{175, 176} A decrease of electron density around a nucleus increases the chemical shift (high-frequency downfield shift), whereas an increase of electron density around a nucleus decreases the chemical shift (low-frequency upfield shift). In terms of host-guest chemistry, when a guest binds to a host through ionic interactions, electron density around the cation will decrease, which will result in an increase of chemical shift¹⁷⁷ and the chemical shift for the protons near the anion will increase.¹⁷⁸

In 2010, Feng *et al.* studied the interactions between a G5 PAMAM dendrimer and heparin via isothermal titration calorimetry (ITC), ¹H nuclear magnetic resonance (1H

NMR), pulsed-field gradient (PFG) NMR, nuclear Overhauser effect spectroscopy (NOESY), and atomic force microscopy (AFM) studies. From **Figure 4.5**, we can see that changing the molar ratios of heparin/G5 dendrimer lead to a consistent downfield shift of protons b' and d', which are methylene protons adjacent to the terminal amine groups, of G5 dendrimer. They suggested that the G5 dendrimer binds with heparin through ionic pairing between cationic amine groups on the dendrimer and sulfate/carboxylate groups on the heparin chain, and the observed chemical shift for dendrimer protons was a time-weighted average of the free state and bound state of the surface amine groups on dendrimers.¹⁷⁹ As such, this study confirmed the expected electrostatic binding mode between the nanoscale objects.

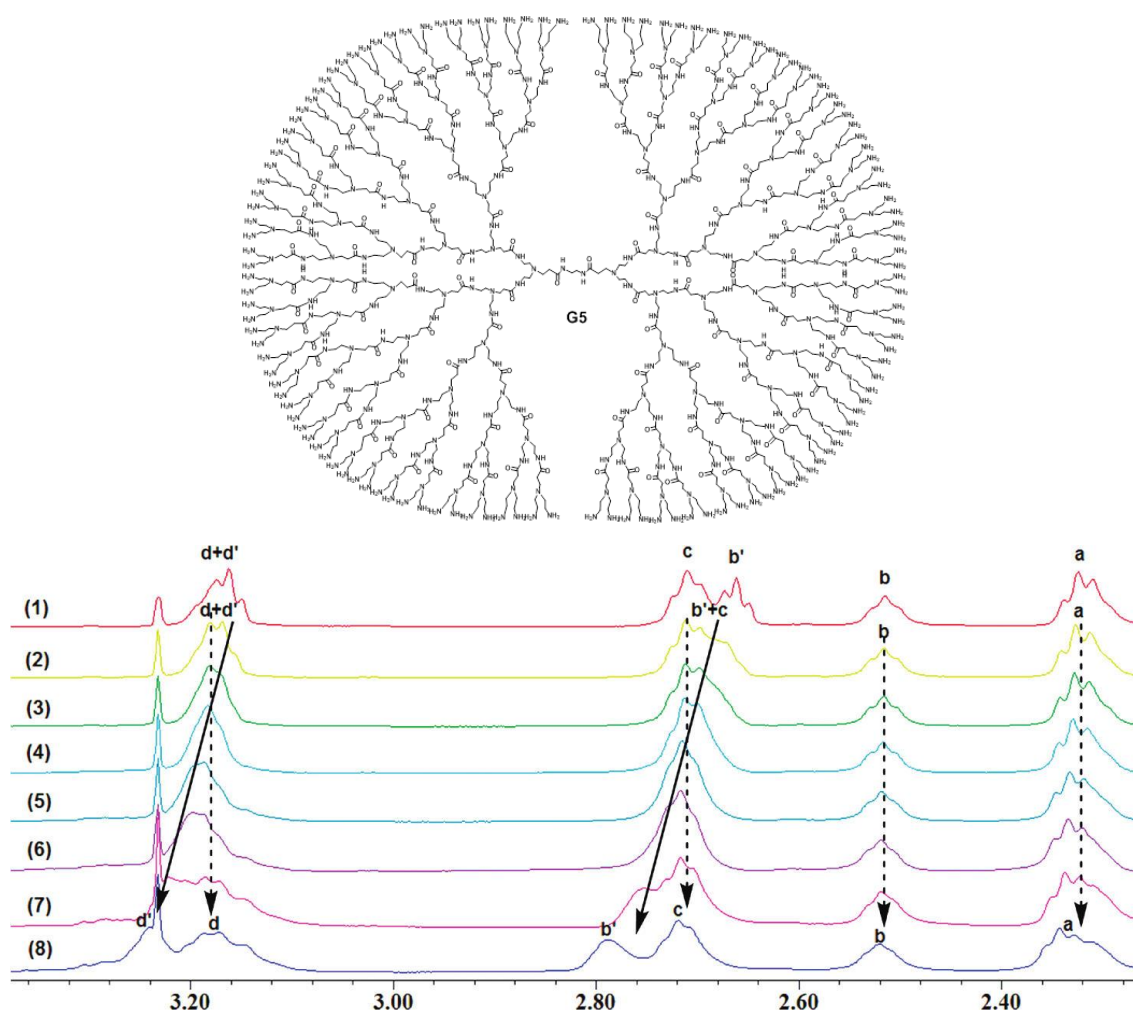


Figure 4.5: (Top) Structure of G5 PAMAM dendrimer (Bottom) ¹H NMR titration spectra of G5 dendrimer with heparin. The G5 dendrimer concentration in the samples is fixed at a concentration of 2 mg/mL. The molar ratios of heparin/G5 dendrimer in (1-8) are 0, 1, 2, 4, 8, 10, 15, and 20, respectively.¹⁷⁹

4.1.4 Project aim

Since we are interested in understanding the interaction of heparin binders with heparin using experimental data rather than just using molecular dynamics, we decided to apply the NMR technique to compare the binding of Mal-B or heparin with the molecular dynamics. In a second part of the study, we also decided to apply the NMR technique to a family of self-assembled multivalent (SAMul) heparin binders which consist of a 16 carbon chain length hydrophobic unit with different anion binding ligand head groups. In this way, we hoped to get the bottom of the precise molecular details of the interactions between heparin binding systems and this important polyanionic biomolecule.

4.2 NMR investigation of Heparin binding with Mallard Blue (Mal-B)

4.2.1 NMR spectra of heparin and Mal-B

The ^1H NMR spectrum of our commercially available sample of heparin in D_2O is shown in **Figure 4.6**. Most peaks are in the range of 3 to 5.5 ppm. This spectrum is in agreement with the report by Keire *et al.*,¹⁷² and consistent with the assumed skeleton of the polysaccharide.

The ^1H NMR spectrum of Mal-B in D_2O then is shown in **Figure 4.7** and most peaks are between 1 and 3.5 ppm (aliphatic region, Arg "arm") or 6.2 and 8.5 ppm (thionine core). The region of crossover between the spectra of heparin and Mal-B was small. As such, if heparin and Mal-B interacted with each other, we might expect to be able to detect peak shifting in the ^1H NMR.

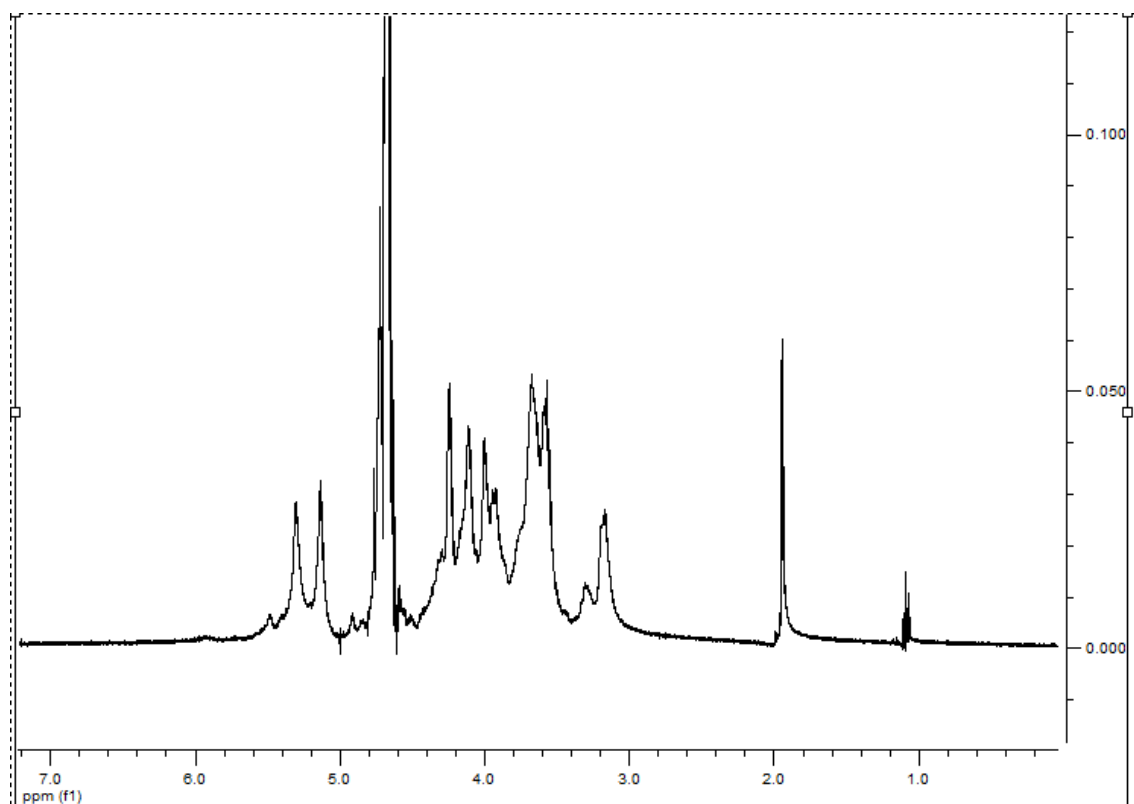


Figure 4.6: ^1H NMR spectrum of heparin in D_2O .

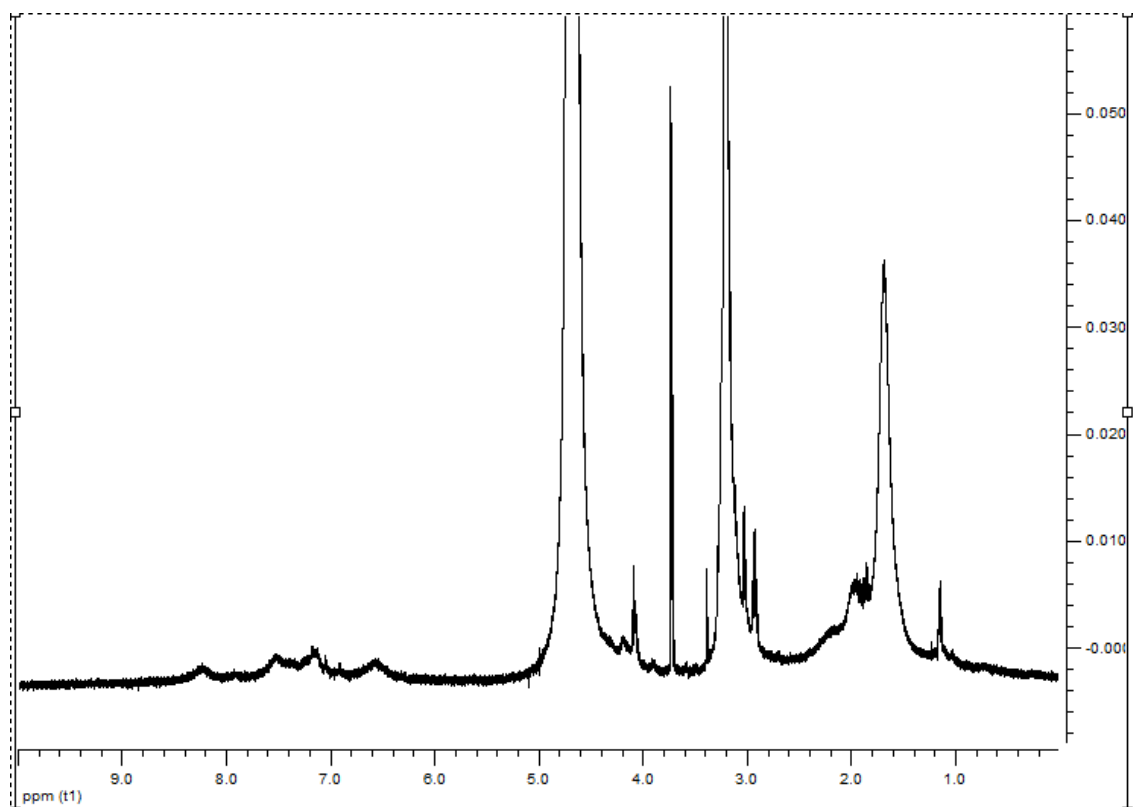


Figure 4.7: ^1H NMR spectrum of Mal-B in D_2O .

Unfortunately, the sample of Mal-B in D_2O of **Figure 4.7** was run at relatively high concentration (40 mg (92.4 mM) of Mal-B in 600 μL of D_2O). The broad, low signal to noise in the aromatic region at the spectrum suggests aggregation of Mal-B in water at these high concentrations. We have previously tested Mal-B for aggregation, which does not occur at the conditions of the UV-Vis heparin binding assay (μM) but it does begin to occur when the concentration is elevated into the mM regime.⁸⁰

4.2.2 2D NMR spectra

From the ^1H NMR spectrum of heparin, we can see significant overlap of peaks. In order to unambiguously assign the signals, we applied a 2D ^1H - ^{13}C -heteronuclear single quantum coherence (HSQC) spectroscopy experiment (**Figure 4.8**) to characterize the compound and compare the spectroscopic data with literature values (**Figure 4.9** and **Figure 4.10**).¹⁷²

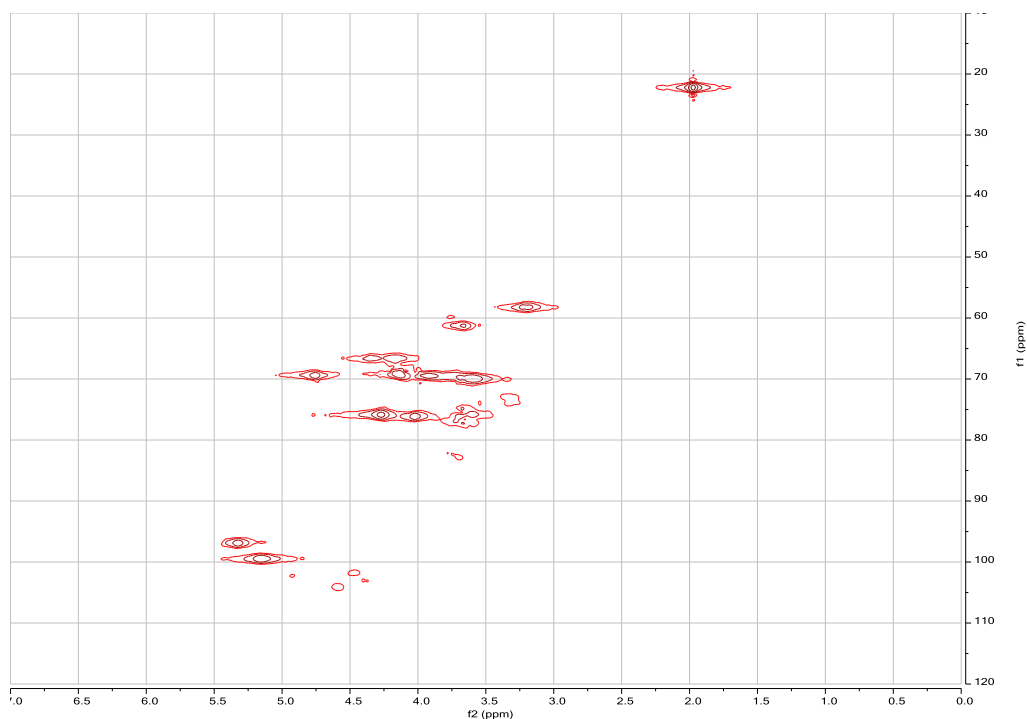


Figure 4.8: HSQC NMR spectrum of heparin in D₂O

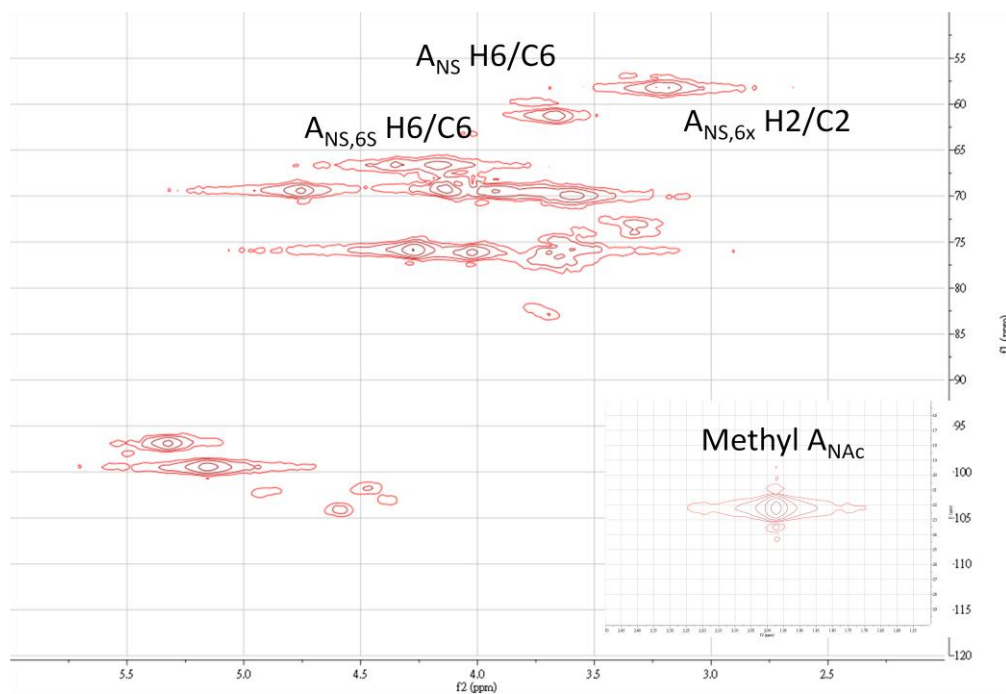


Figure 4.9: Plot of aliphatic region (3.0 to 5.0 ppm proton (f2) and 50 to 90 ppm carbon (f1)). Bottom right is the N-acetyl methyl signal. Selected signals are labeled based on the assignments of Keire *et al.*¹⁷²

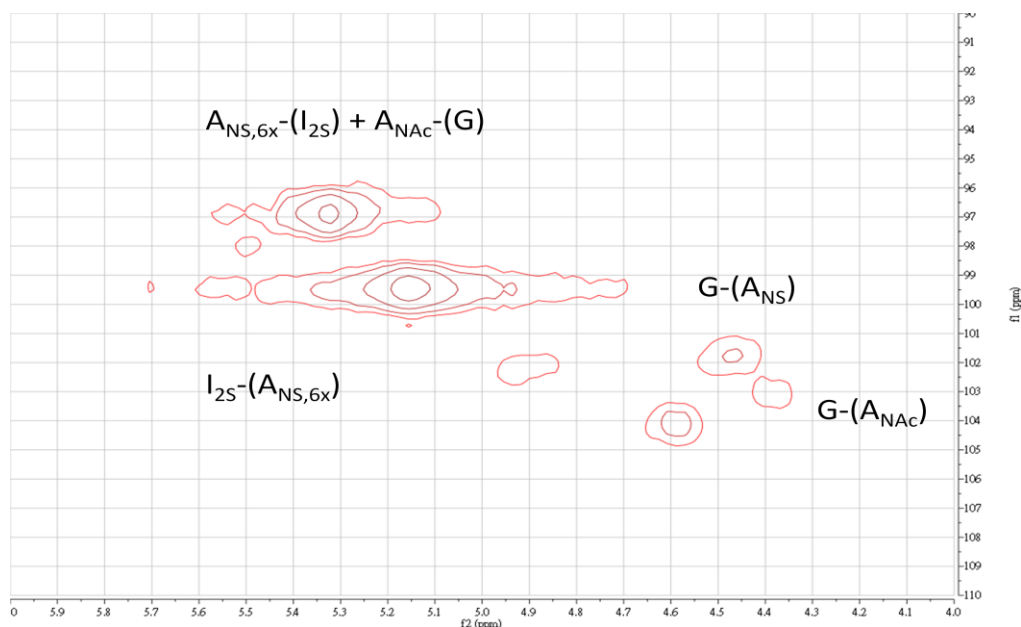


Figure 4.10: Plot of anomeric region (4.0 to 6.0 ppm proton (f2) and 90 to 110 ppm carbon (f1)). Selected signals are labeled based on the assignments of Keire *et al.*¹⁷²

The HSQC of Mal-B (high concentration sample) in D₂O did not exhibit any peaks in the aromatic region (**Figure 4.11**). We suggest that this is a result of the stacking of the Mal-B at NMR concentrations. If the stacking is, as proposed, driven by $\pi - \pi$ interactions, then the aromatic peaks would be those most subject to line broadening as they will be fully immobile in the core of the assembly. The arginine arms on periphery of aggregate would, in contrast, be more mobile.

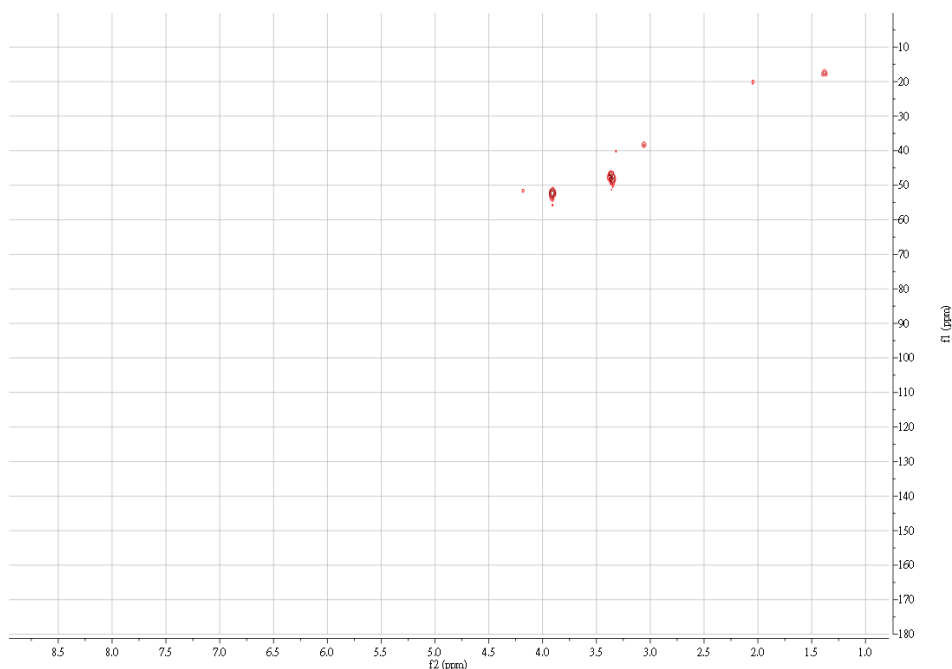


Figure 4.11: HSQC NMR spectrum of Mal-B in D₂O

4.2.3 Low concentration Mal-B NMR study

It was therefore decided to use a lower concentration of Mal-B to limit the aggregation of Mal-B. **Figure 4.12** was measured at low concentration (40 μ M) of Mal-B in D₂O and we can now clearly see the peaks in the aromatic region. Indeed these peaks are more clearly visible than was the case at much higher concentration, which is supportive of the view that aggregation was limiting signal intensity. However, when we expand the aromatic region, it is also clear that we observe more peaks than expected (**Figure 4.13**). This was thought to be possibly due to the stacking of Mal-B. It could also be possibly be the result of slow rotation about the amide bonds. Therefore the sample was heated to 50 °C overnight but then the effect became even greater (**Figure 4.14**).

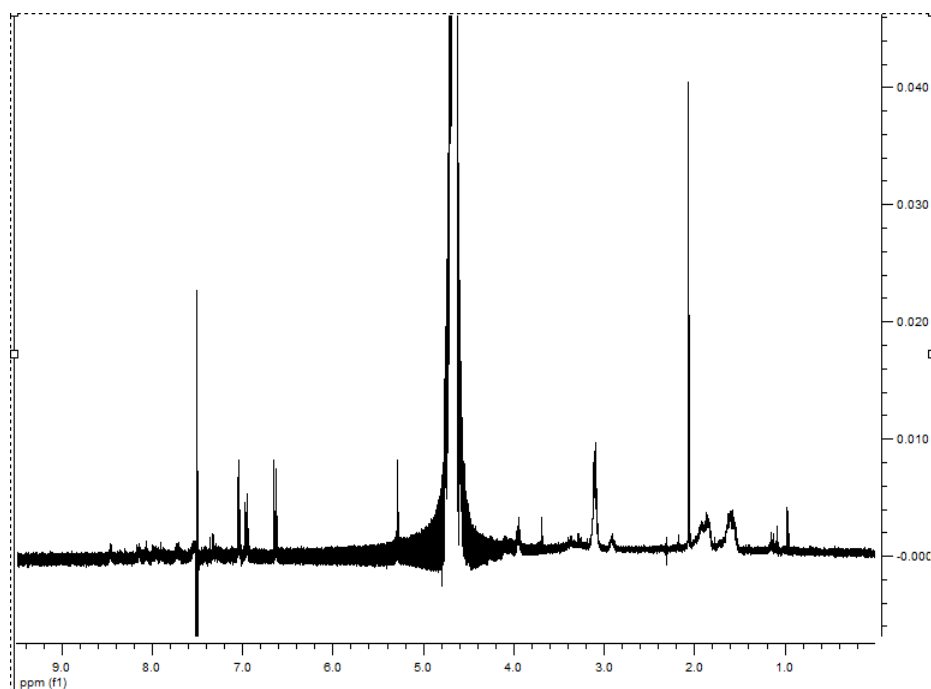


Figure 4.12: ¹H NMR spectrum of low concentration of Mal-B in D₂O.

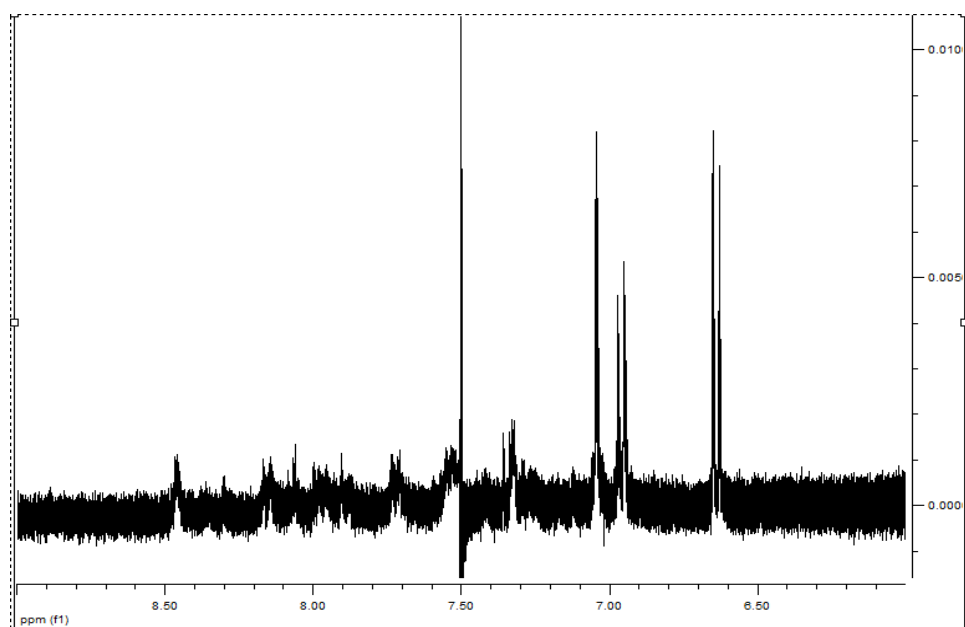


Figure 4.13: Expansion of the 6.0-9.0 ppm region of the of low concentration of Mal-B in D₂O.

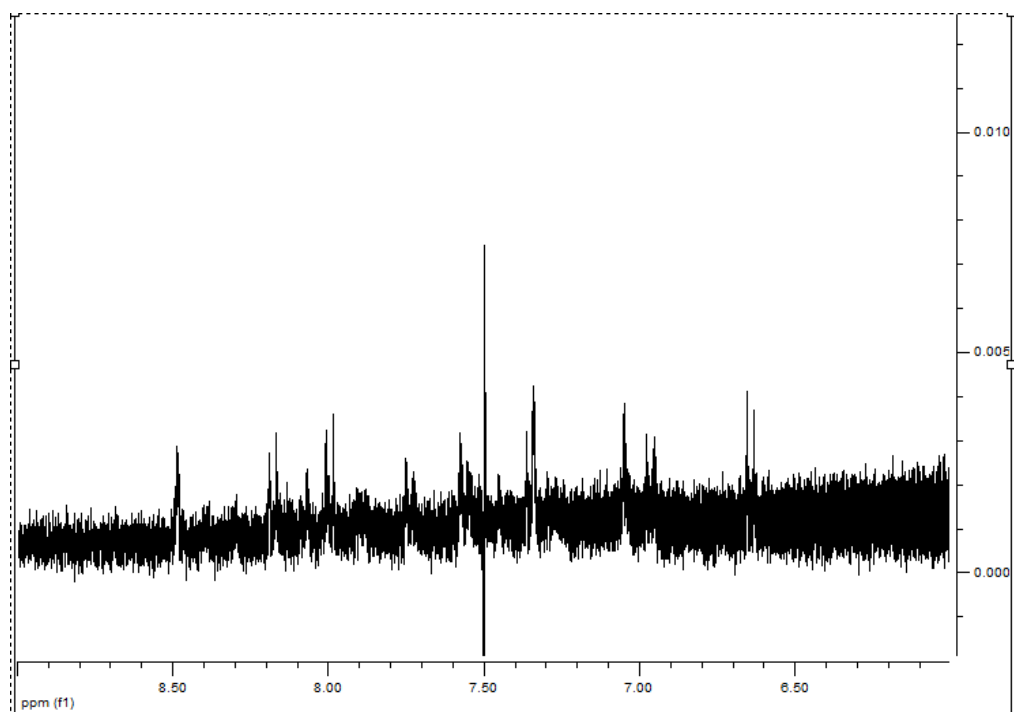


Figure 4.14: Expansion of the 6.0-9.0 ppm region of the of low concentration of Mal-B in D₂O at 50 °C overnight.

On the addition of heparin, we can see clearly that the major peaks have been shifted significantly downfield and simplified the spectrum (**Figure 4.15**). We reasoned that these significant changes on heparin binding may allow us to use titration methods to characterise the mode of binding. Clearly interaction of Mal-B with heparin significantly changes its NMR spectrum.

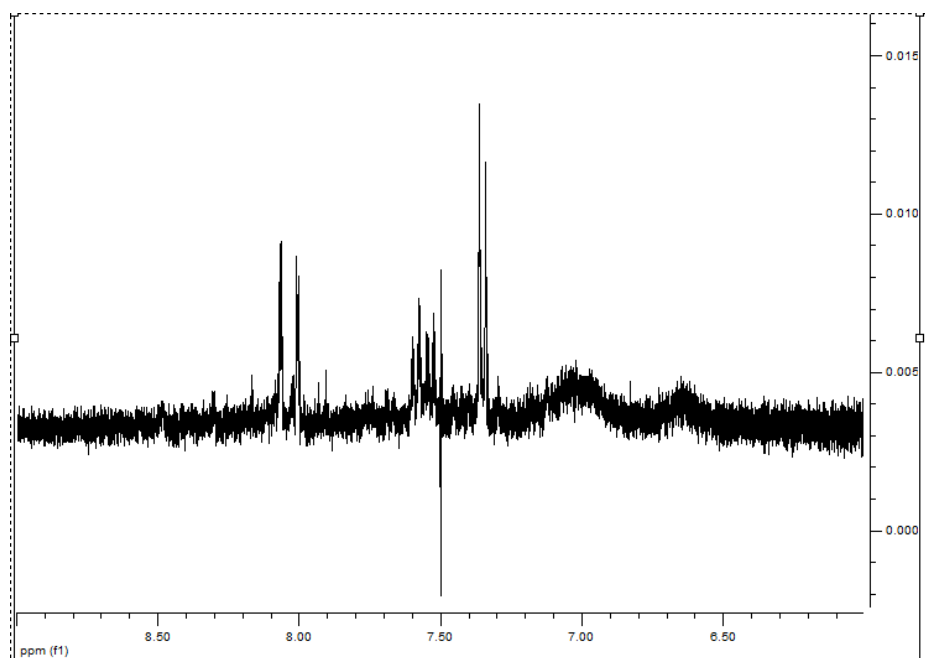


Figure 4.15: Expansion of the 6.0-9.0 ppm region of the of Mal-B with heparin in D₂O.

We then prepared Mal-B (40 μM) with the same buffer system as that used by Bromfield *et al.*⁸⁰ in their heparin binding assay (Tris HCl ,10 mM, pH 7, 150 nM NaCl). This simplified the aromatic region very significantly (**Figure 4.16**). Indeed the spectrum could now be fully assigned in which all of them are the protons on the thionine core.

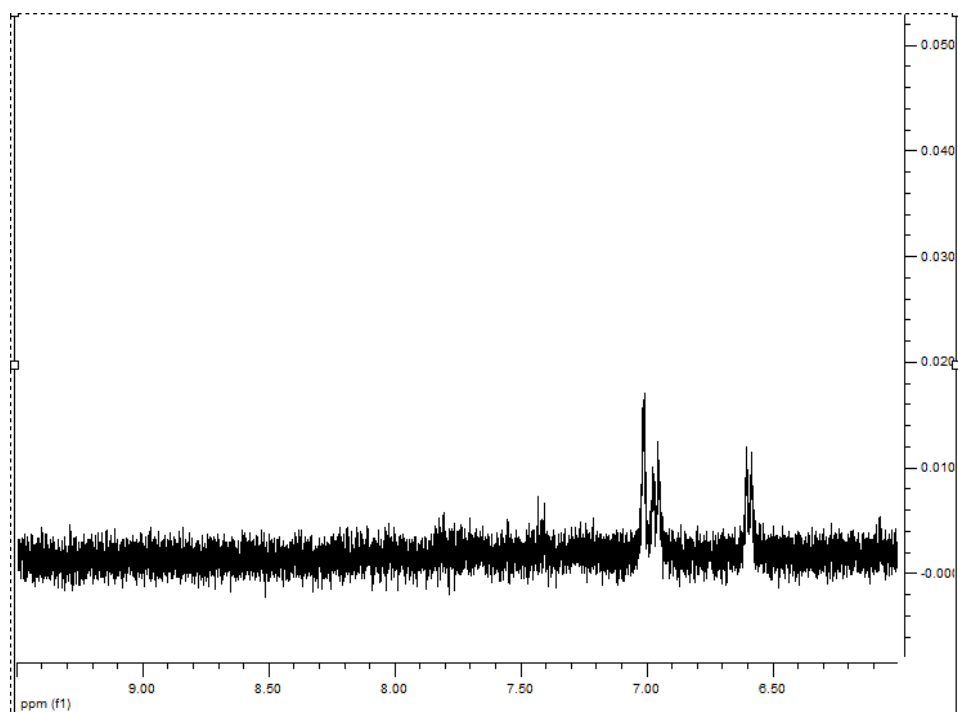


Figure 4.16: Expansion of the 6.0-9.5 ppm region of the of Mal-B (40 μ M) in Tris HCl ,10 mM, pH 7, 150 nM NaCl, D₂O.

However, using Tris HCl as buffer introduces additional signals in the ¹H NMR spectrum at ca. 3.7 ppm which will overlap with heparin saccharide signals and may affect studies of binding later on. Therefore we used a phosphate buffer (10 mM, pH 7, 150 nM NaCl) and observed that it also had limited peak splitting (**Figure 4.17**). It is therefore possible that as ionic strength increases in buffer solution, the aggregation of Mal-B is limited, perhaps because of interactions between Mal-B and anions present within the buffer. Alternatively, the pH control offered by the buffer system may help limit the number of protonation states of the Mal-B and hence simplify the NMR spectra – although usually peaks associated with different protonation should be in fast exchange. As such we prefer the explanation that control over ionic composition is limiting aggregation.

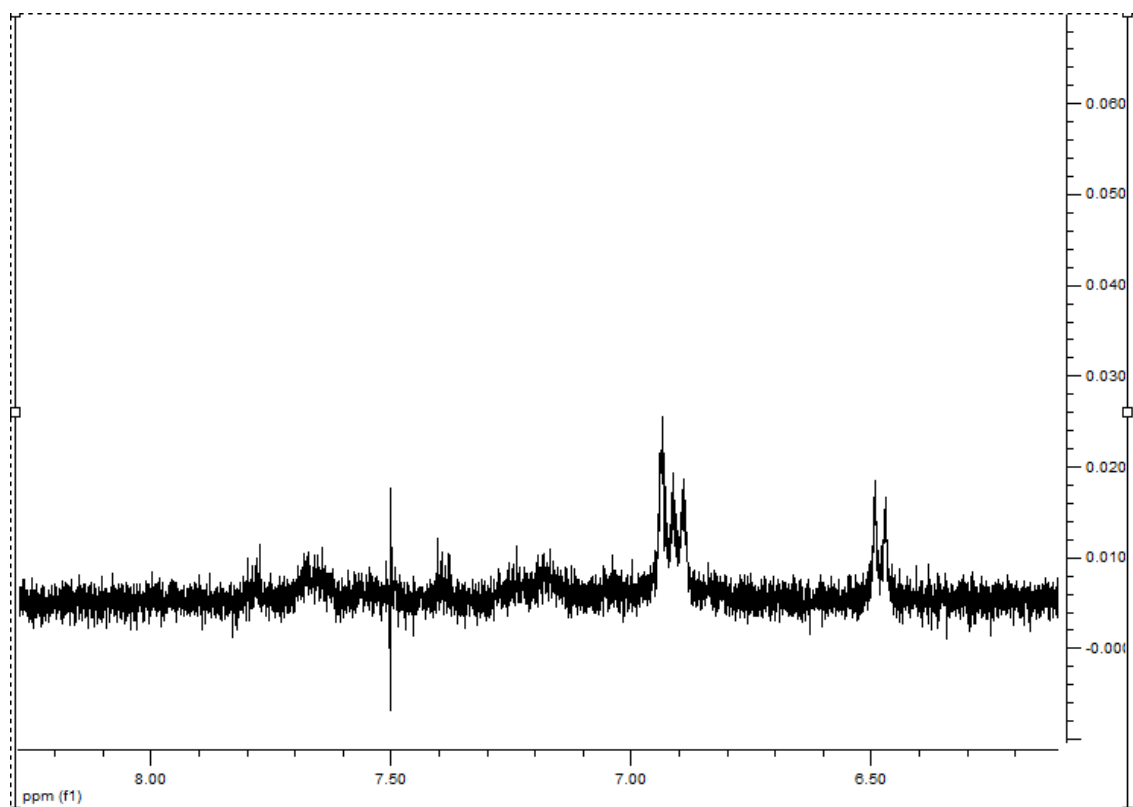


Figure 4.17: Expansion of the 6.0-8.5 ppm region of the of Mal-B in phosphate,10 mM, pH 7, 150 nM NaCl, D₂O.

4.2.4 Effect of buffer in Mal-B binding with heparin

Given the apparent importance and significance of the buffer, a binding study of Mal-B with heparin in different buffer systems was therefore performed using UV-Vis spectroscopy to investigate the impact of this factor on heparin binding and sensing. In Tris HCl buffer, as reported by Bromfield *et al.*⁸⁰ (**Figure 4.18**), the max absorbance wavelength shifts from 615 to 585 nm as the concentration of heparin increases whereas in phosphate buffer, the max absorbance does not shift at all (**Figure 4.19**). As the concentration of heparin increases, both systems decrease in absorbance which indicates the binding of heparin to Mal-B. This meant we can use either buffer system in our NMR study as binding clearly taken place. However, there were some subtle and important differences between heparin binding in the two different buffer systems.

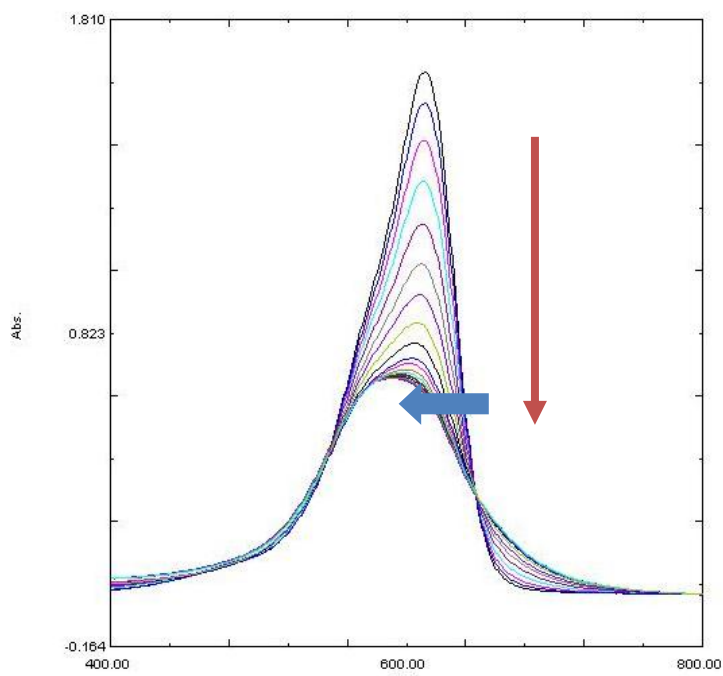


Figure 4.18: UV absorbance of Mal-B with increasing heparin concentration in Tris HCl ,10 mM, pH 7, 150 nM NaCl,

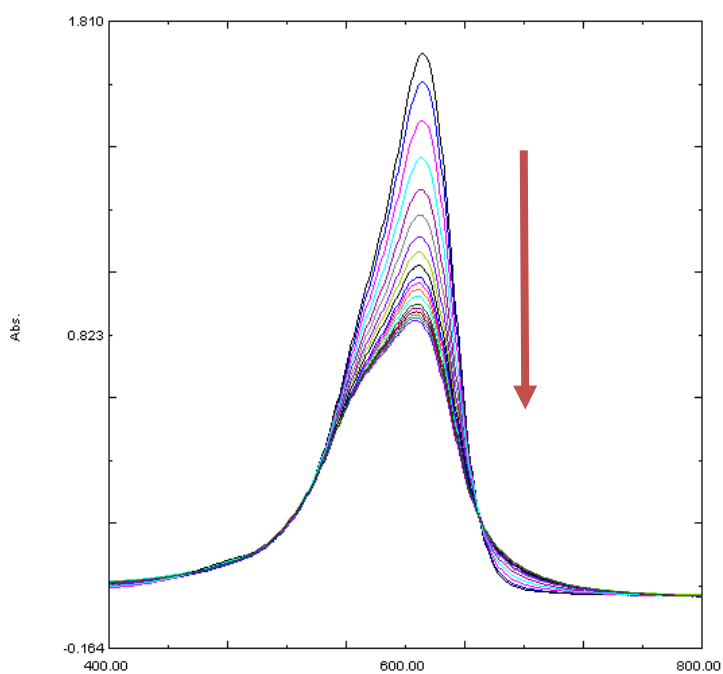


Figure 4.19: UV absorbance of Mal-B with increasing heparin concentration in phosphate ,10 mM, pH 7, 150 nM NaCl,

The above UV-Vis titration experiments were performed in triplicate and the results are shown in **Figure 4.20**. It is clear from the binding profiles that when binding

take place in Tris HCl, the titration curve is sharper - which would correspond with a stronger binding. Furthermore, the binding in Tris HCl saturates at ca. 20 μM heparin, whereas in phosphate buffer it saturates at ca. 15 μM . These observations may suggest that the phosphate anions in the buffer compete for binding to Mal-B. These differences are particularly clear when considering the normalised titration curves in **Figure 4.20**. Nonetheless, heparin binding can still be observed for Mal-B even in the presence of 10 mM phosphate (a large excess). This indicates the high degree of selectivity and binding preference between Mal-B and polyanionic heparin.

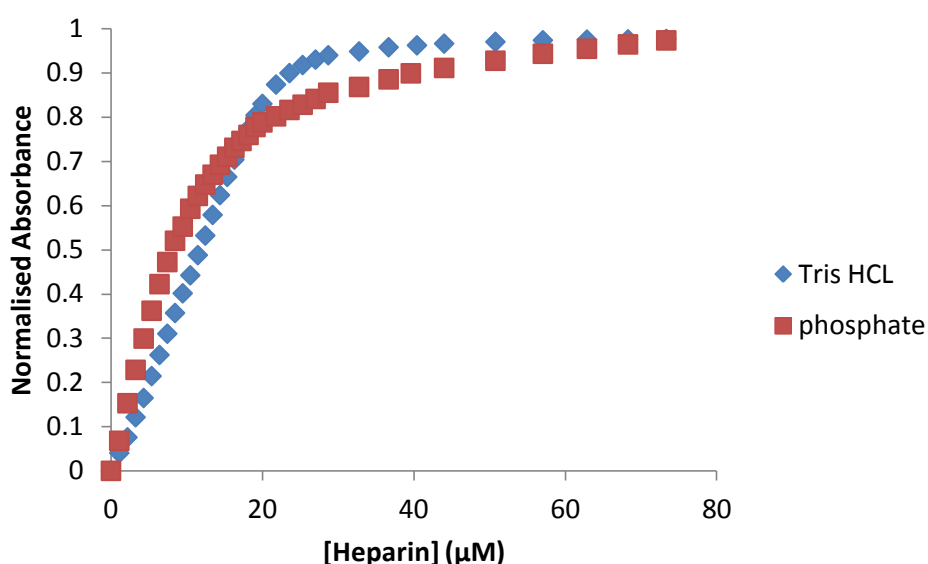


Figure 4.20: Normalised absorbance of Mal-B vs heparin concentration in different buffer systems at max absorbance 615 nm.

We then studied the UV-Vis spectra of Mal-B on changing the ratio of Tris HCl buffer and phosphate buffer. The max absorbance only shifts ~ 1 nm from 1:0 to 0:1 phosphate : Tris HCl when there is no heparin present (**Figure 4.21**). However, in the presence of heparin there is a large shift as the buffer is changed from 1:0 to 0:1 phosphate : Tris HCl (**Figure 4.22**).

Figure 4.22 clearly shows that the complex formed between Mal-B and heparin has a different optical response depending on the choice of buffer. However Mal-B

itself is relatively unchanged in the different buffers (**Figure 4.21**). We suggest that interactions with phosphate anions change the nature of the Mal-B/heparin complex, and modify the way in which these two species bind to each another.

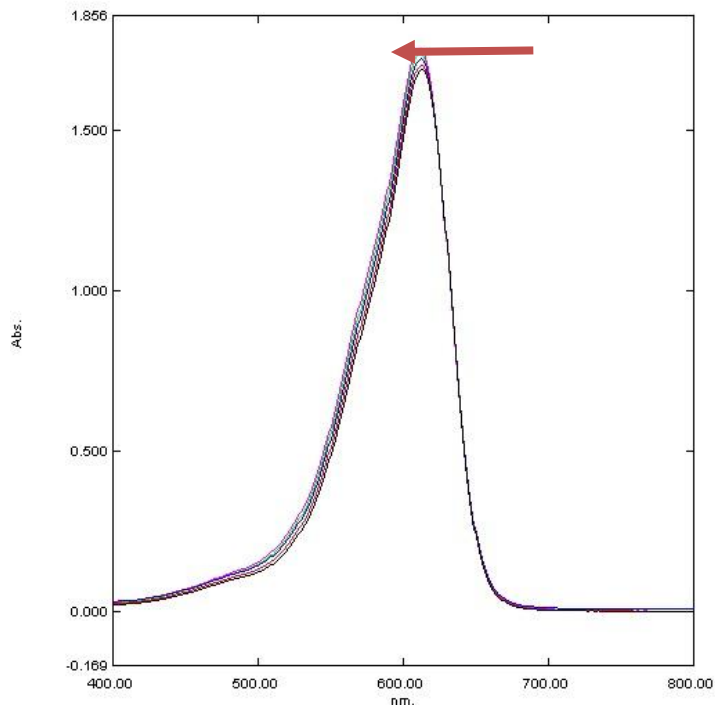


Figure 4.21: UV absorbance of Mal-B in different ratio of buffer (1:0 to 0:1 phosphate : Tris HCl)

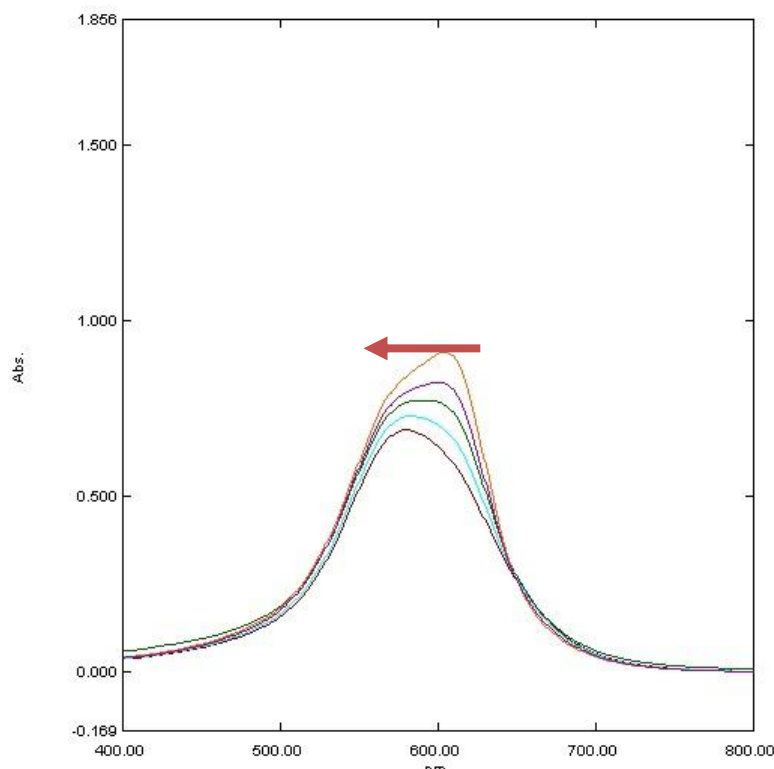


Figure 4.22: UV absorbance of Mal-B with heparin in different ratio of buffer (1:0 to 0:1 phosphate : Tris HCl)

Clearly these data demonstrated that the choice of buffer can be crucial in binding experiments and can play an active role in mediating interactions between host and guest. Others have reported related phenomena¹⁸⁰ and it is important for supramolecular chemists to keep in mind that buffers can play active roles in binding events above and beyond simple pH control.

4.2.5 Titration study of Mal-B with heparin in phosphate buffer.

We then went back to NMR to consider further the interaction between Mal-B and heparin in buffer. The ^1H NMR spectra of Mal-B (200 μM) with an increase of heparin concentration (1:0 to 1:1) in phosphate buffer are shown in **Figure 4.23**. As the concentration of heparin increased, the intensity of the Mal-B signal was lost. From **Figure 4.24**, it was clear that when Mal-B binds heparin at NMR concentrations the complex precipitated from solution. Indeed this could be observed visually.

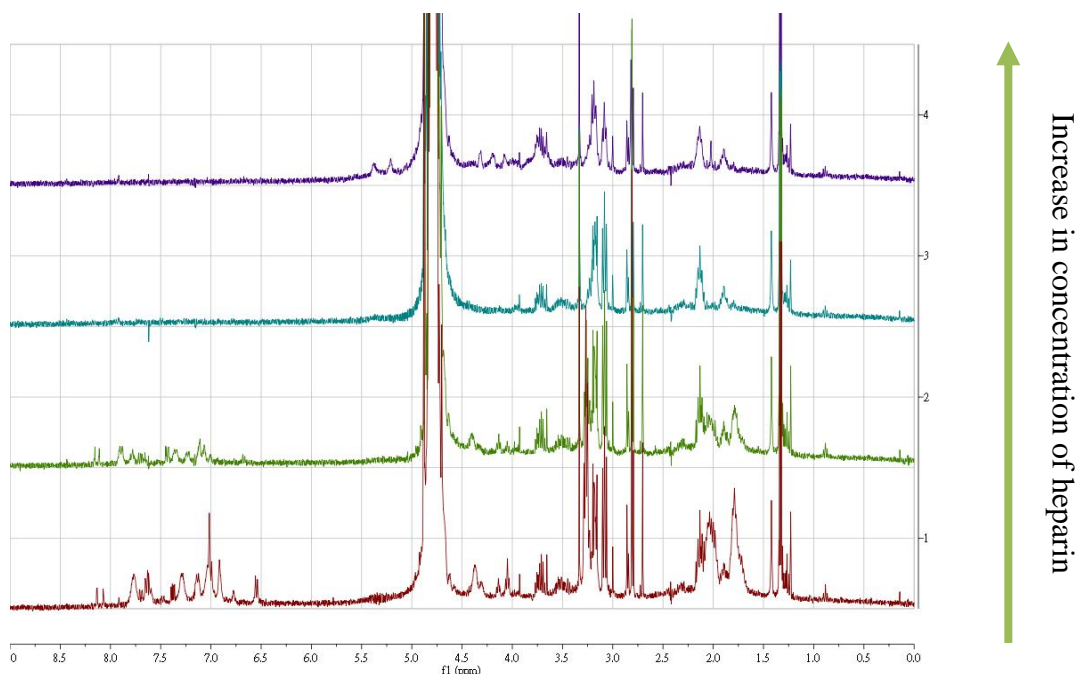


Figure 4.23: ¹H NMR spectra of Mal-B (200 μM) with increasing heparin concentration (1:0 to 1:1).



Figure 4.24: Photo of NMR tubes of Mal-B with increasing of heparin concentration

4.2.6 Conclusions

It was clear that using Tris HCl or phosphate buffer minimises peak splitting in the aromatic region of Mal-B and we suggest that this is a result of limiting aggregation of Mal-B. We reasoned this may allow us to learn about the interaction between Mal-B

and heparin via titration study in NMR. However in such studies at NMR concentrations, precipitation of the complex was observed, limiting the opportunity for analysis.

We explored the interaction between Mal-B and heparin in different buffer systems using UV-Vis spectroscopy and it was clear that the Mal-B:heparin complex has a different spectropic signature in Tris HCl and phosphate buffer. We suggest that the highly anionic nature of the phosphate buffer means that it can interact in the binding processes. There is evidence from binding curves that the binding is weaker in phosphate and we suggest that phosphate anions are involved at the nanoscale binding interface in a competitive sense.

4.3 NMR investigation of Heparin binding with Self-Assembled Multivalent (SAMul) Heparin Binders

4.3.1 Self-Assembled Multivalent (SAMul) Heparin Binders

We then went on to extend these studies to some self-assembled multivalent (SAMul) heparin binders of particular interest. We discussed SAMul heparin binders in Chapter 3. Inspired by Jones *et al.* who compared the effects of the surface ligands on dendron-DNA interaction using 1,3-diaminopropane (DAP), N,N-di-(3-aminopropyl)-N-(methyl)amine (DAPMA) and spermine functionalized low-molecular dendrons and suggested that structural influences of the surface ligands on dendrons helped to control DNA binding and gene delivery ability,¹⁸¹ we considered that there may be structural effects of surface ligands of SAMul binders on binding to heparin. Loryn Fechner, a visiting Masters student from Freie Universität Berlin, synthesised four SAMul binders with palmitic acid coupled to diamine DAP, triamines DAPMA and spermidine, and tetraamine spermine (**Figure 4.25**).

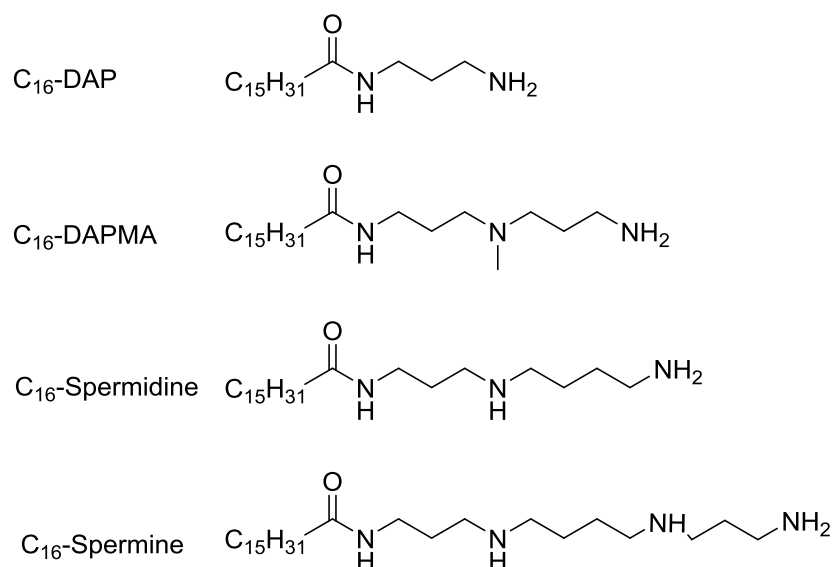


Figure 4.25: Structure of self-assembled multivalent (SAMul) heparin binders.

Fechner studied the heparin binding ability of these compounds and related, using data from the Mal-B competition assay, that the effective concentration and charge excess at 50% replacement of Mal-B for C₁₆-Spermidine indicated that it was the most effective heparin binder. The order of effectiveness (**Table 4.1**) can be summarized as

follows:

C_{16} -Spermidine (+2) > C_{16} -Spermine (+3) > C_{16} -DAPMA (+2) > C_{16} -DAP (+1)

	C_{16}-DAP	C_{16}-DAPMA	C_{16}-Spermidine	C_{16}-Spermine
CE ₅₀	0.69	0.69 ± 0.05	0.34 ± 0.05	0.49 ± 0.1
EC ₅₀ [μM]	74	37 ± 3	19 ± 3	17.5 ± 0.3
Dose [mg]	0.75	0.49 ± 0.03	0.24 ± 0.04	0.28 ± 0.01

Table 4.1 Summary of the binding parameters for heparin binding for SAMul heparin binder

C_{16} -DAP was ineffective because its solubility in water was too low for it to work in the binding assay – this is a result of its relatively small hydrophilic unit (just a single positive charge. We had perhaps expected that the most highly charged C_{16} -Spermine would be the most effective polyanion binder and as such these results were initially surprising. Furthermore, it was not clear why C_{16} -Spermidine significantly outperformed C_{16} -DAPMA when both ligands have the same +2 charge.

The results indicate that the structure of the ligand plays an important role in heparin binding ability and that an increase in the amount of positive charges does not necessarily increase binding efficiency in a simple predictable manner. Therefore we became interested in using our NMR technique to understand the interaction of different SAMul heparin binders with heparin in order to compare the binding site of these ligands and the way in which they interacted on a molecular level when binding to heparin.

4.3.2 Result and discussion

4.3.2.1 C_{16} -DAP

NMR confirmed the insolubility of C_{16} -DAP as no signals could be observed from the spectrum.

4.3.2.2 NMR titration of C₁₆-DAPMA with heparin

An NMR titration of C₁₆-DAPMA with heparin was performed where C₁₆-DAPMA (2 mg/mL) was titrated with increasing heparin concentration (1:0 to 1:1) and the ¹H NMR spectra are shown in **Figure 4.26**. We can see the signal of the binder initially decrease to zero and then increase back with broadened, shifted peaks as the concentration of heparin increases. From **Figure 4.27**, we can see that when the concentration of heparin is between 1:0.5 and 1:0.6, the NMR tubes are a clear solution with white particulate matter which matches the NMR data. The disappearance of the peaks at the 1:0.5 ratio could suggest the formation of a charge-balanced complex at this point between the heparin binder and the heparin leading to precipitates of an aggregate. However, clearly in the presence of excess heparin, the complex reorganizes and redissolves into solution. As such, this allows us to gain some insight into molecular level interactions underpinning these complexes.

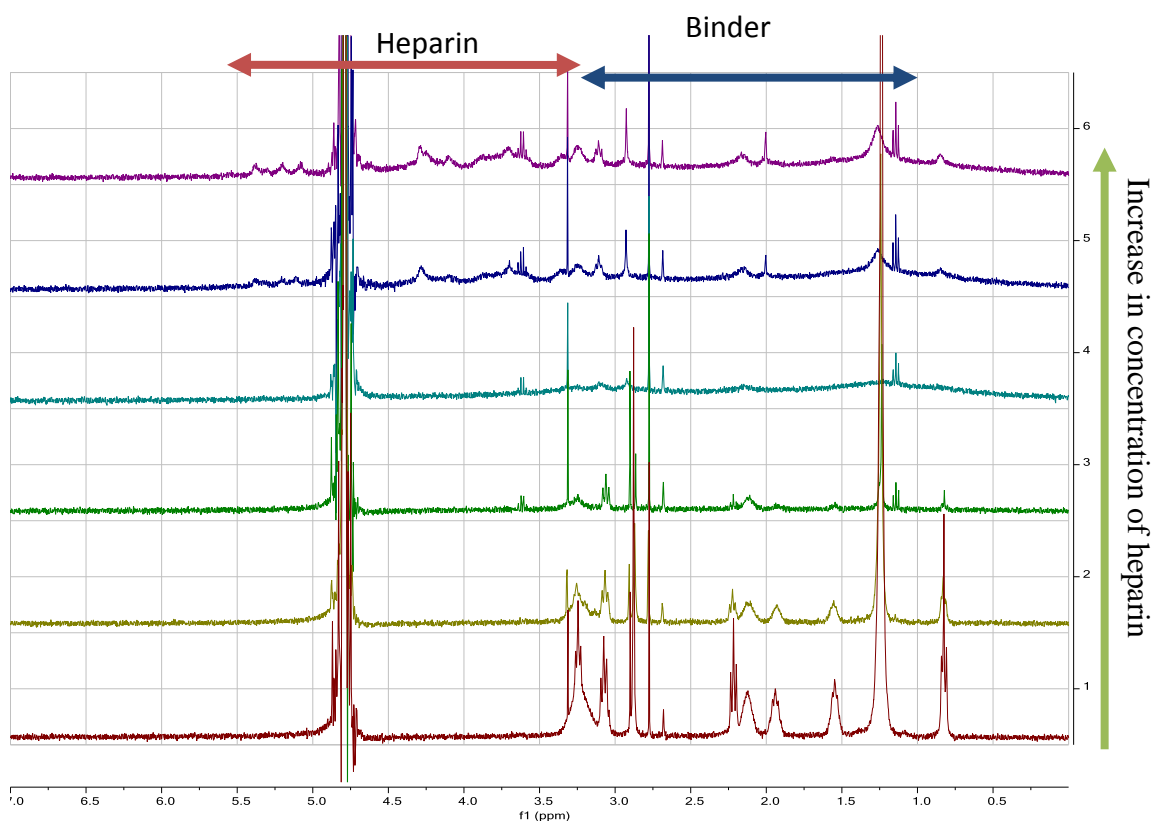


Figure 4.26: ¹H NMR spectra of C₁₆-DAPMA with increase heparin concentration (1:0 to 1:1)

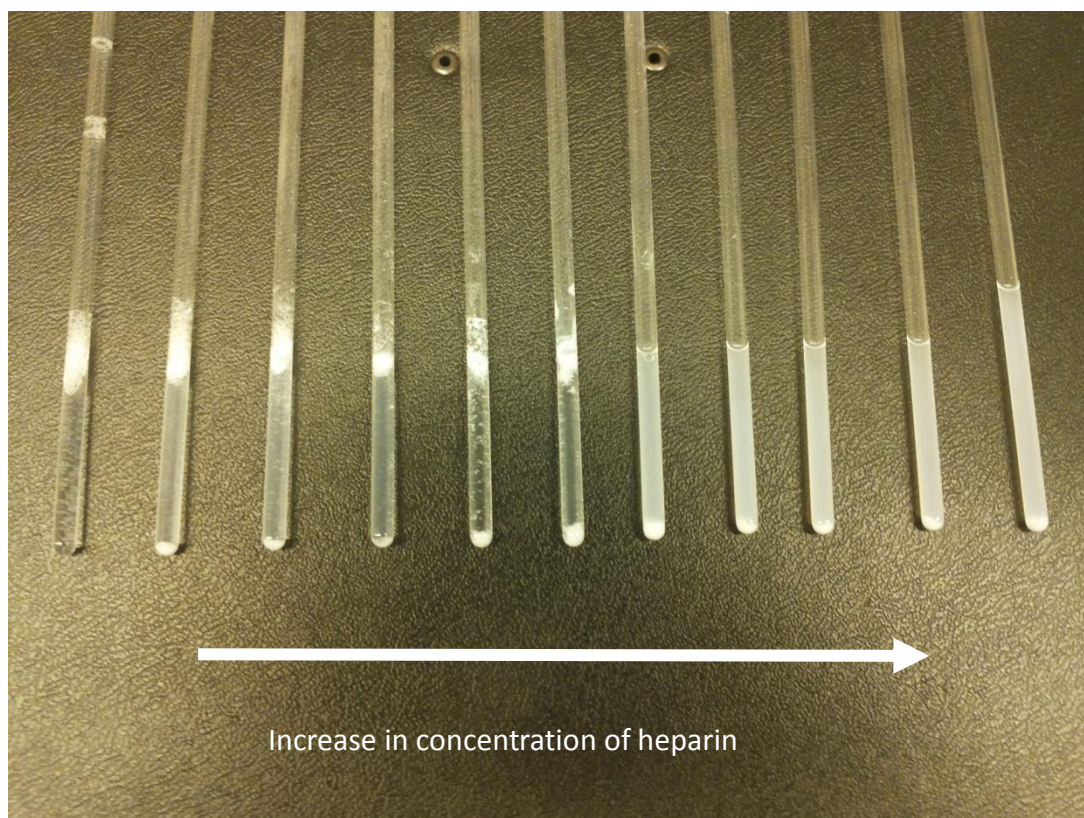


Figure 4.27: Photo of NMR tubes of C_{16} -DAPMA with increase of heparin concentration (1:0 to 1:1)

When we look more closely at the region associated primarily with C_{16} -DAPMA binder between 0 to 3.5 ppm (**Figure 4.28**), it was clear that a, $\text{CH}_2\text{N}(\text{CH}_3)$ and c, $\text{CH}_2\text{CH}_2\text{N}(\text{CH}_3)$ reappeared, slightly shifted downfield, whereas b, CH_2CONH ; d, $\text{CH}_2\text{CH}_2\text{NH}_2$; e, $\text{CH}_2\text{CH}_2\text{CONH}$ were still missing even when the compound reaches 1:1 ratio. This would agree with a view that the protonated amines are the primary site of interaction with heparin and the CH_2 group next to these sites shift downfield as they became deshielded. It is not completely clear why the other peaks disappear from the spectrum and remain unseen – we suggest that in that presence of excess heparin the peaks directly responsible for binding are exchanging between heparin chains and can be observed, while the other peaks which are not directly responsible for interacting with heparin remain in slow exchange on the NMR timescale. Molecular modelling¹⁸¹ suggests that DAPMA has a relatively hindered molecular skeleton which is less able to rotate and reorganise than some of the other amine ligands.

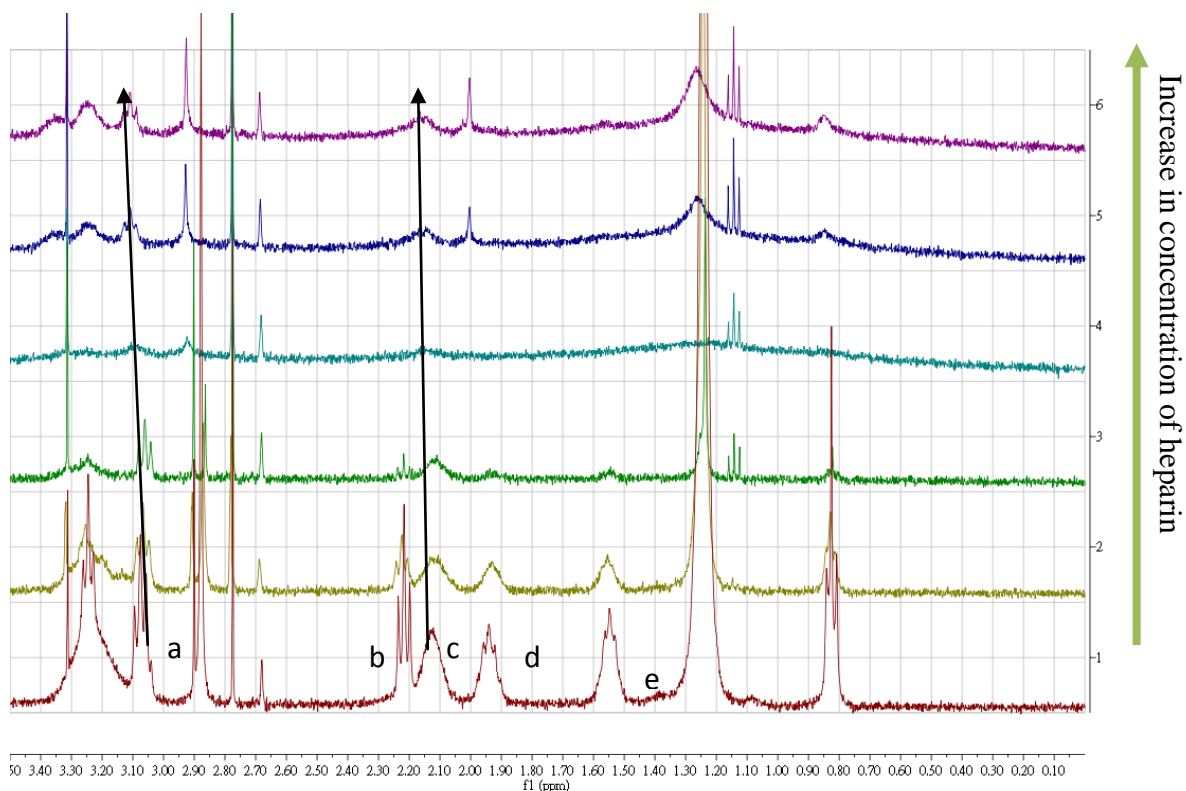
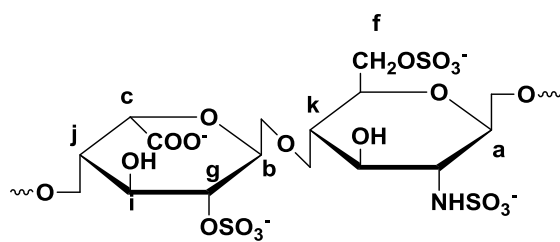


Figure 4.28: ^1H NMR spectra of C_{16} -DAPMA with increase of heparin concentration from 0 to 3.5 ppm.

We then performed the experiment in reverse adding the C_{16} -DAPMA to heparin in order to observe which heparin peaks are most affected. A ^1H NMR titration of C_{16} -DAPMA with heparin was performed where heparin (2 mg/mL) was titrated with increasing of C_{16} -DAPMA concentration (1:0 to 1:1) and the ^1H NMR spectra of are shown in **Figure 4.29**. When we look more closely at the region between 4.7 and 5.7 ppm, two peaks which are: a, H1 GlcNS, GlcNS6S; b, H1 IdoA2S; of heparin shifted slightly upfield as the concentration of C_{16} -DAPMA increased (**Figure 4.30**). In the region between 4.5 and 3.0 ppm, five peaks which are: f, H6 GlcNS6S; g, H2 IdoA2S; i, H3 IdoA2S; j, H4 IdoA2S; k, H5 GlcNS6S of heparin shifted as the concentration of C_{16} -DAPMA increased (**Figure 4.31**). This suggested that C_{16} -DAPMA interacted with these protons on heparin – however, all shifts were relatively small so it is hard to come to clear conclusions, furthermore, C_{16} -DAPMA peaks are not clearly seen at the end of the experiment and it is possible that in this titration the C_{16} -DAPMA:heparin complex

remains as an insoluble precipitate – hence its NMR peaks are not really being observed.



IdoA2S-GlcNS6S

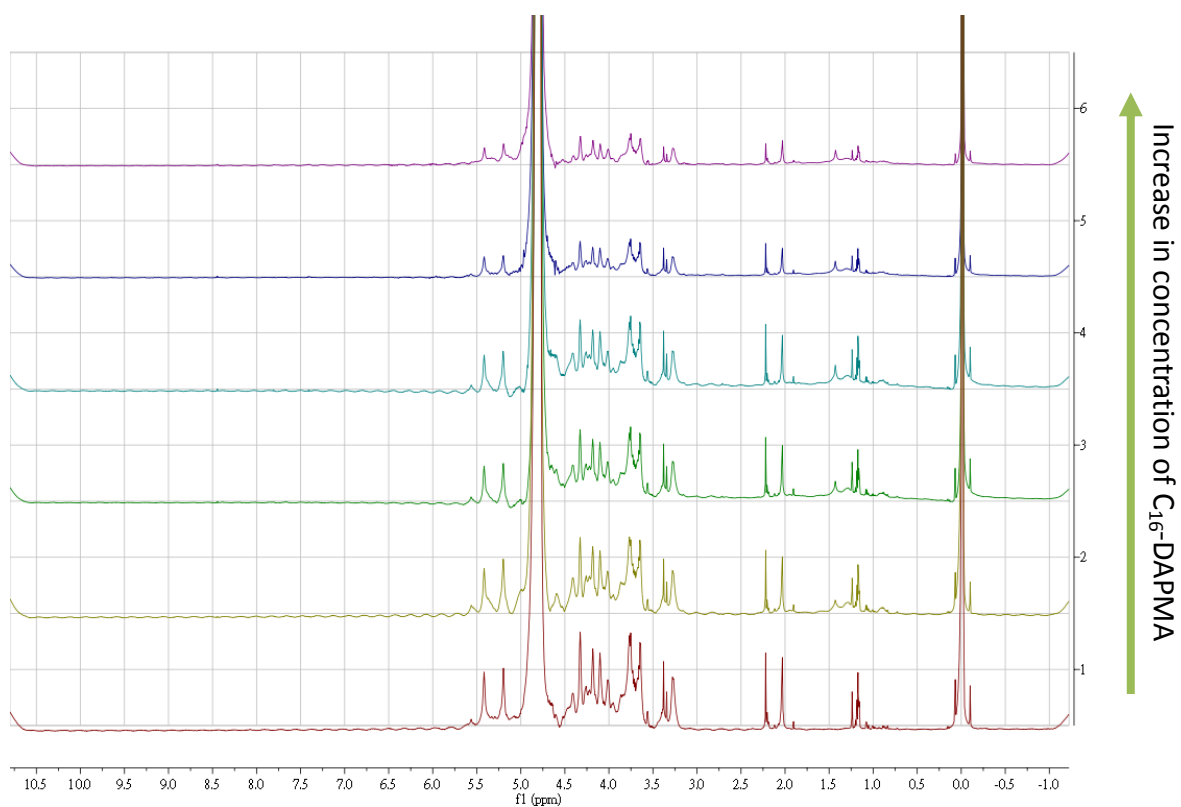


Figure 4.29: ^1H NMR spectra of heparin with increase of C_{16} -DAPMA concentration (1:0 to 1:1)

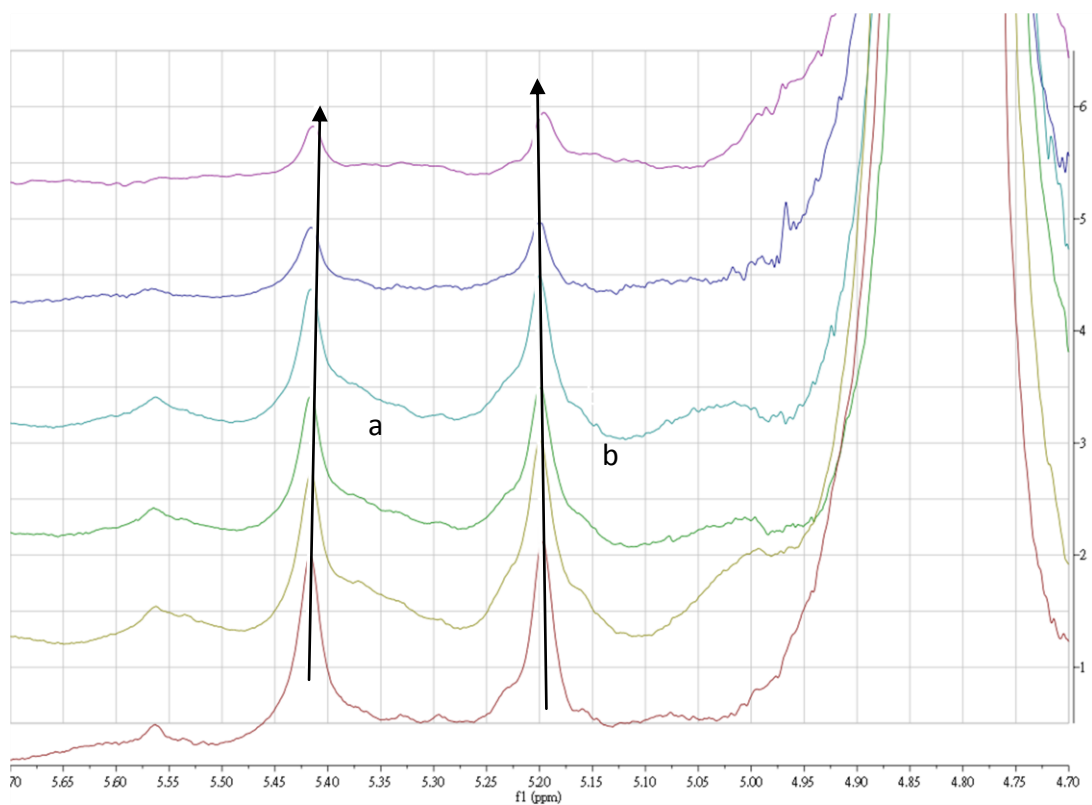


Figure 4.30: ^1H NMR spectra of heparin with increase of C_{16} -DAPMA concentration from 4.7 to 5.7 ppm

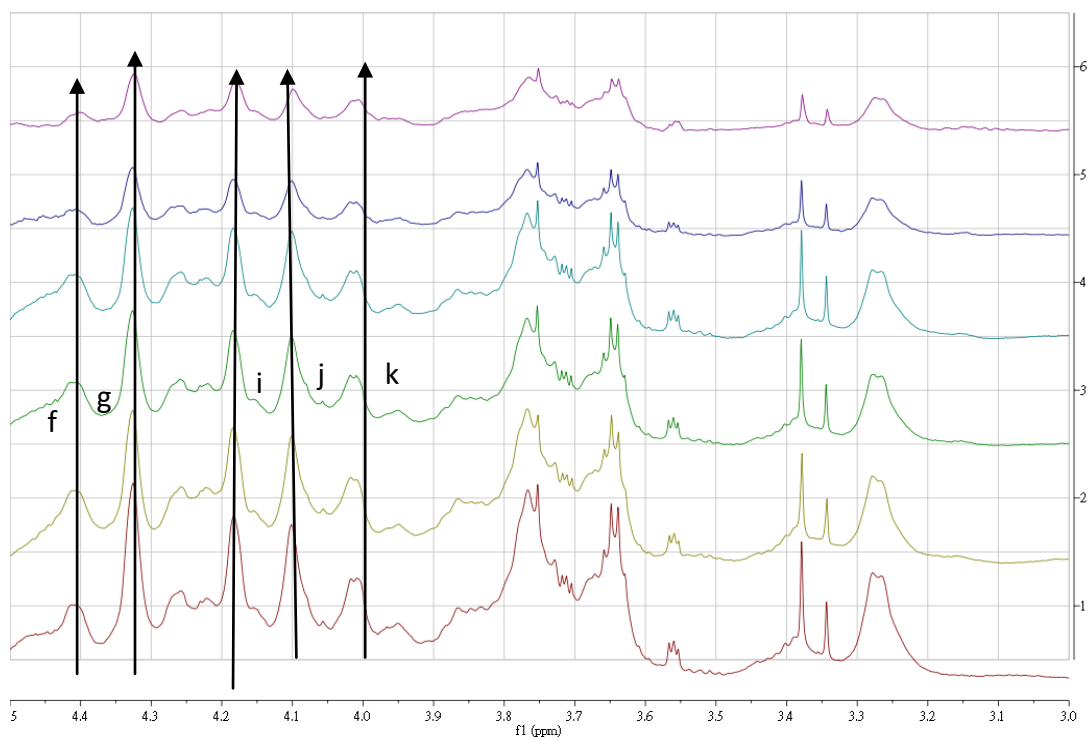


Figure 4.31: ^1H NMR spectra of heparin with increase of C_{16} -DAPMA concentration from 3.0 to 4.5 ppm

In summary, C₁₆-DAPMA binds with heparin through ionic interactions between cationic amine groups on and sulfate/carboxylate groups on the heparin chain forms an insoluble precipitate at charge equivalence. Interestingly in the presence of excess heparin the protons adjacent to the N⁺ binding sites on C₁₆-DAPMA reappeared suggesting they may be in fast exchange between heparin chains. The protons on heparin are very slightly shifted. It is worth noting that anomeric proton, H1 GlcNS, GlcNS6S shifted upfield and H1 IdoA2S shifted downfield which may suggest the “H1 GlcNS, GlcNS6S” was near the cation¹⁷⁷ whereas “H1 IdoA2S” shifted away from cation or moved closer to anion.¹⁷⁸ IdoA2S is a L sugar whereas GlcNS6S is a D sugar, this may suggest that the chiral identity of the sugar has an effect on the heparin binder as C₁₆-DAPMA is a non-chiral compound. For the non-anomeric proton, all five proton peak (H6 GlcNS6S; H2 IdoA2S; H3 IdoA2S; H4 IdoA2S; H5 GlcNS6S) that were shifted slightly downfield consistent with binding to the cationic sites.

4.3.2.3 NMR titration of C₁₆-Spermidine with heparin

The triamine spermidine, a naturally-occurring constitutional isomer of DAPMA, shares the same charge as DAPMA. However, Fechner reported that C₁₆-Spermidine is a more significantly effective heparin binder than C₁₆-DAPMA. Hence we titrated heparin into C₁₆-Spermidine to observe the effect on the C₁₆-Spermidine NMR spectrum. The ¹H NMR spectra of C₁₆-Spermidine (2 mg/mL) on increasing of heparin concentration (1:0 to 1:1) are shown in **Figure 4.32**. We can see the signal of the binder first decrease to zero and then increase back with significantly broadening, and shifted peaks as the concentration of heparin increases. This is similar overall behaviour as that observed for C₁₆-DAPMA, however in this case all the ligand peaks reappear in the presence of excess heparin.

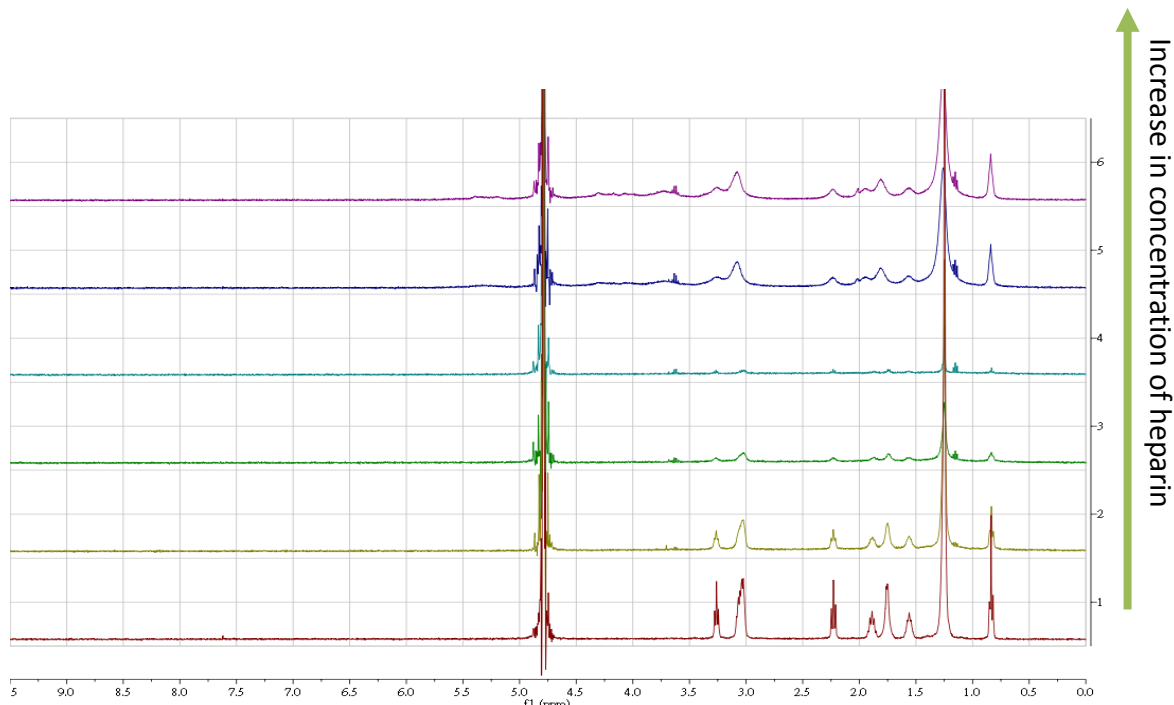


Figure 4.32: ^1H NMR spectra of C_{16} -Spermidine with increase of heparin concentration (1:0 to 1:1)

When we look more closely at the in region between 0 and 3.5 ppm (**Figure 4.33**), peak a, $\text{CH}_2\text{NH} + \text{CH}_2\text{NH}_2$ b, $\text{CH}_2\text{CH}_2\text{NHCO}$ and c $\text{CH}_2\text{CH}_2\text{NH}_2 + \text{CH}_2\text{CH}_2\text{CONH}$, all reappeared and shifted downfield whereas other peaks remained the same. We suggest that only the shifted peaks interacted with heparin. Since protons of all three peaks are next to or two bonds away from the cationic amine and they all shifted downfield, this suggests that they experience a decrease in electron density around the nucleus as a result of the ionic interaction of the binder and heparin. Interestingly, we note that for C_{16} -Spermidine the protons further from the charged nitrogen area also reappear and shift downfield, which was not the case for C_{16} -DAPMA where they remained broadened. This is indicative of a different binding interface between C_{16} -Spermidine and heparin, perhaps with larger electrostatic interactions. This would be in agreement with the better binding observed in binding assays.

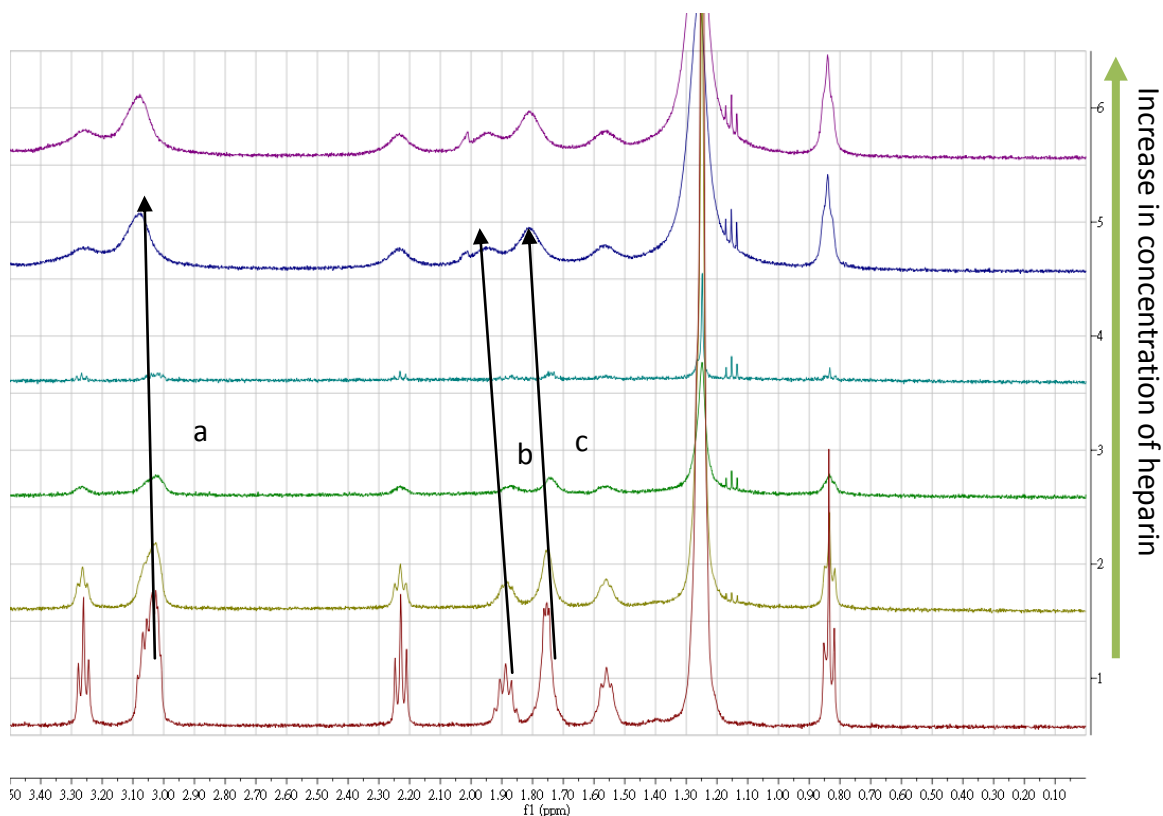
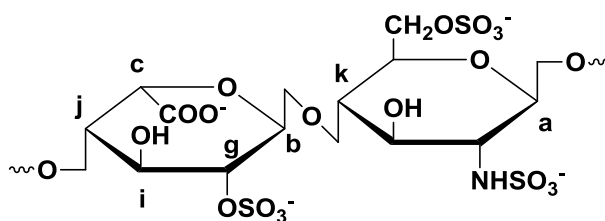


Figure 4.33: ^1H NMR spectra of C_{16} -Spermidine with increase of heparin concentration (1:0 to 1:1) from 0 to 3.5 ppm

We then reversed the experiment and titrated C_{16} -Spermidine into heparin in order to observe the effect of binding on specific regions of the heparin biopolymer. The ^1H NMR spectra of heparin (2 mg/mL) with increasing C_{16} -Spermidine concentration (1:0 to 1:1) are shown in **Figure 4.34**. When we look closer at the region between 4.7 and 5.7 ppm, two peaks which are: a, H1 GlcNS, GlcNS6S; b, H1 IdoA2S; of heparin shifted slightly as the concentration of C_{16} -Spermidine increase (**Figure 4.35**). In region between 3.0 and 4.5 ppm, four peaks which are: g, H2 IdoA2S; i, H3 IdoA2S; j, H4 IdoA2S; k, H5 GlcNS6S of heparin shifted with very small value as the concentration of C_{16} -Spermidine increase (**Figure 4.36**).



IdoA2S-GlcNS6S

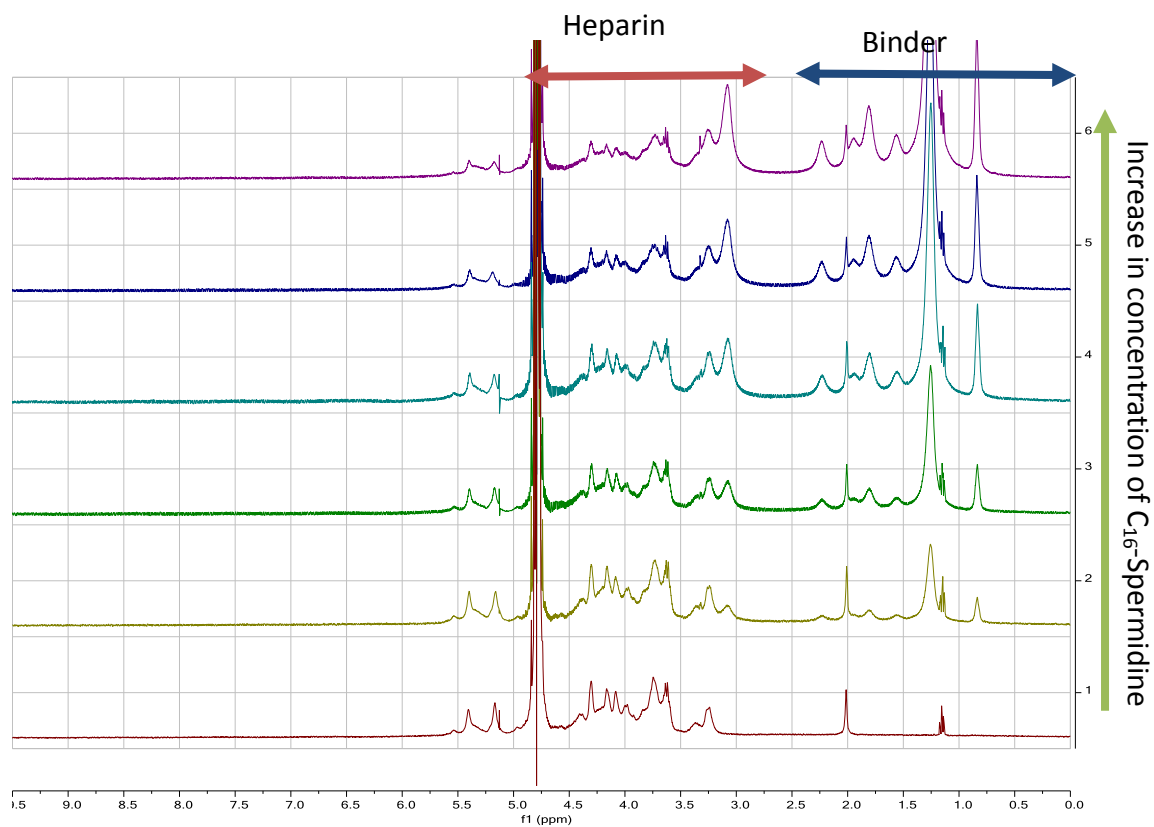


Figure 4.34: ^1H NMR spectra of heparin with increase of C_{16} -Spermidine concentration (1:0 to 1:1)

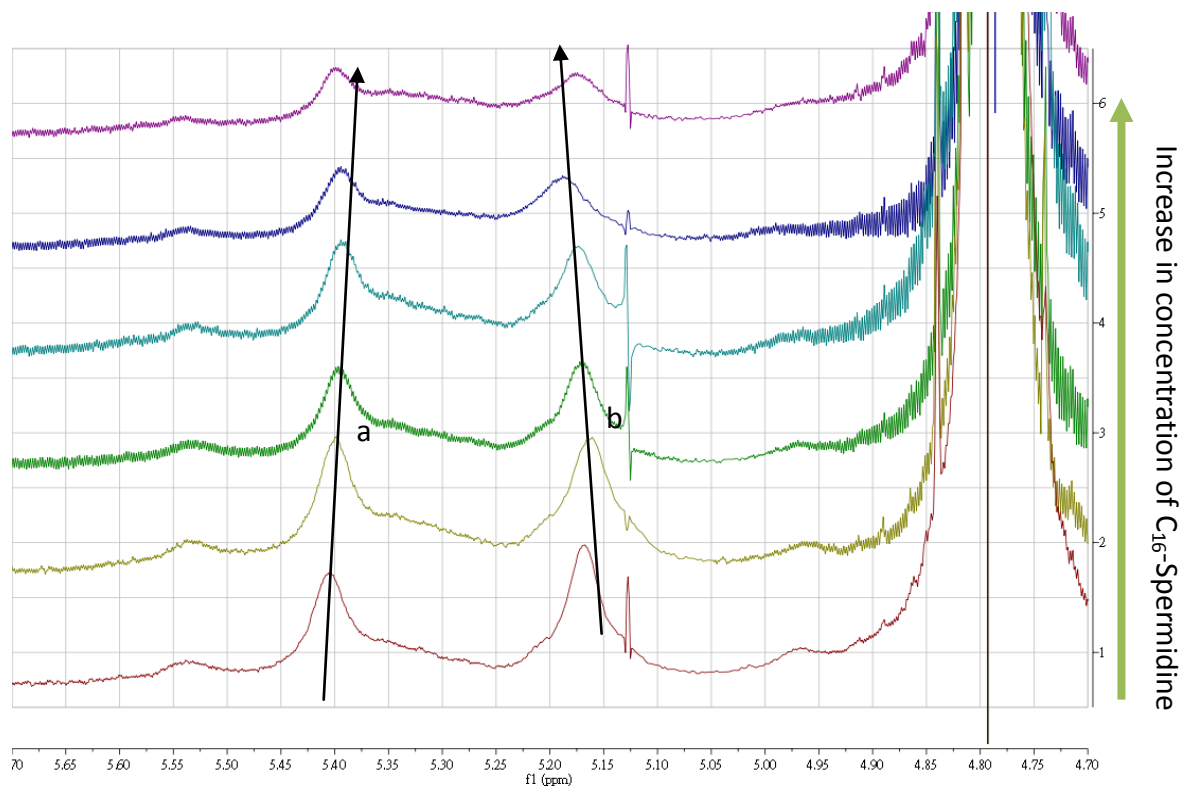


Figure 4.35: ^1H NMR spectra of heparin with increase of C_{16} -SPERMIDINE concentration from 4.7 to 5.7 ppm

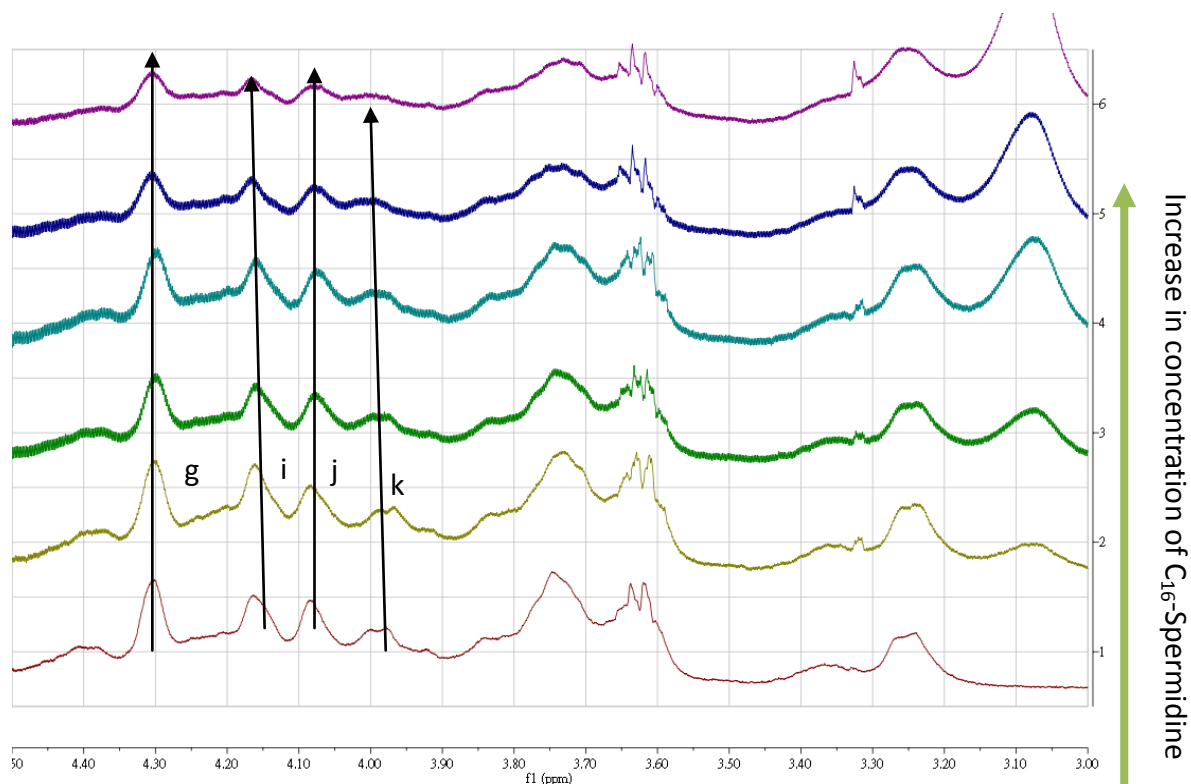


Figure 4.36: ^1H NMR spectra of heparin with increase of C_{16} -Spermidine concentration from 3.0 to 4.5 ppm

Importantly the presence of C_{16} -Spermidine was clearly observed in this titration, unlike C_{16} -DAPMA in the equivalent experiment. This suggests the complexes have very different solubilities and affinities just as a consequence of the minor ligand changes.

In summary, C_{16} -Spermidine shows difference in its NMR response compared with C_{16} -DAPMA when it binds with heparin through ionic interactions between cationic amine groups on and sulfate/carboxylate groups on heparin chain. In particular the complex retains much faster dynamics on the NMR timescale supportive of potential for complex optimisation and resulting in most of the protons on heparin being shifted.

4.3.2.4 NMR titration of C_{16} -Spermine

We then studied the more highly charged C_{16} -Spermine system to observe its interaction with heparin. The ^1H NMR spectra of C_{16} -Spermine (2 mg/mL) with increasing heparin concentration (1:0 to 1:1) are shown in **Figure 4.37**. We can see the

signals of the binder again initially decrease to zero as aggregation and precipitation occurs at charge equivalence, then increase back with broadening, and shifted peaks as the concentration of heparin increases further. This general pattern is similar to that observed for C₁₆-DAPMA and C₁₆-Spermidine.

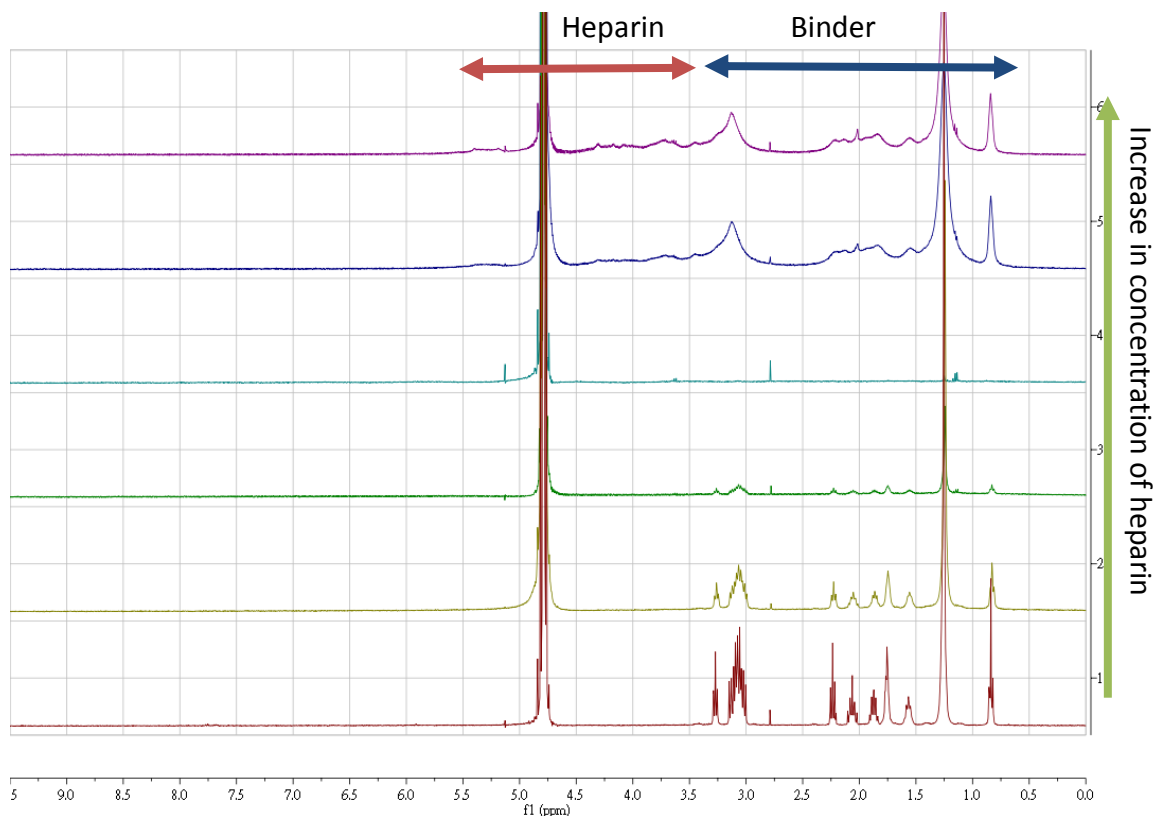


Figure 4.37: ¹H NMR spectra of C₁₆-Spermine with increase of heparin concentration (1:0 to 1:1).

When we look closer at the region between 0 and 3.5 ppm (**Figure 4.38**), it is clear that a, $\text{CH}_2\text{NH} + \text{CH}_2\text{NH}_2$, shifted, and formed a combined peak which is too broad to be assigned. We suggest they all interact with heparin. As for the other binders, we suggest that proton decrease in electron density around the nucleus as a result of the ionic interactions of the binder and heparin. Interestingly the protons two carbons away from the charges were significantly broadened but did not appear to shift to any major extent. This is closer to the behaviour of C₁₆-DAPMA than C₁₆-Spermidine and would support the view that C₁₆-Spermidine was a better binder with more effective ligand organisation dynamics than either C₁₆-DAPMA and C₁₆-Spermine.

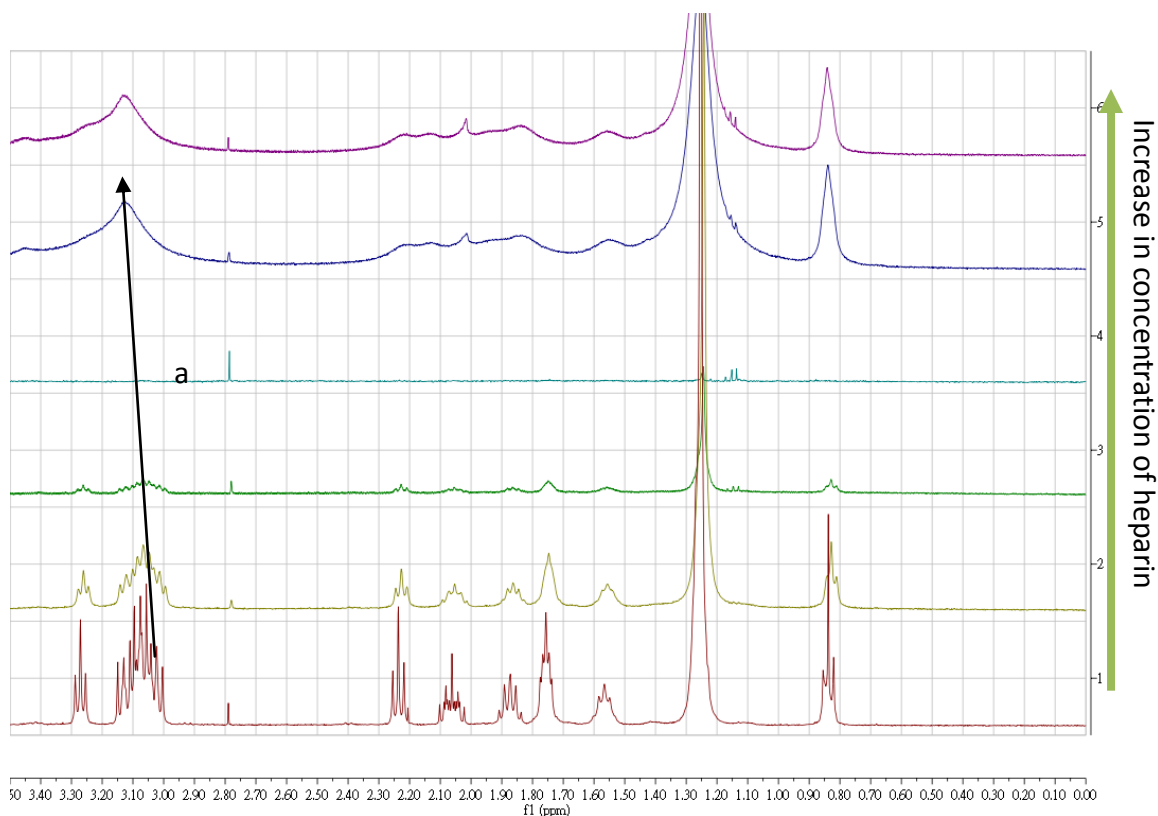
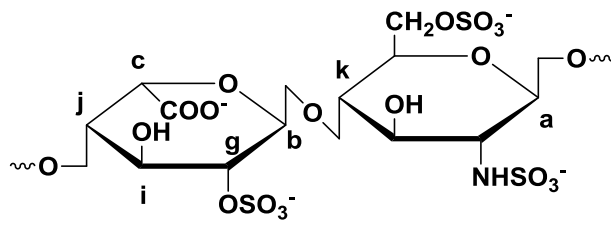


Figure 4.38: ^1H NMR spectra of C_{16} -Spermine with increase of heparin concentration (1:0 to 1:1) from 0 to 3.5 ppm

The ^1H NMR spectra of Heparin (2 mg/mL) with increasing C_{16} -Spermine concentration (1:0 to 1:1) are shown in **Figure 4.39**. When we look closer in the region between 4.7 and 5.7 ppm, two peaks which are: a, H1 GlcNS, GlcNS6S; b, H1 IdoA2S of heparin shifted slightly as the concentration of C_{16} -Spermine increased (**Figure 4.40**) As in the other cases, proton a shifted upfield while proton b shifted downfield suggesting direct effects at these anomeric position. In the region between 3.0 and 4.5 ppm, four peaks which are: d, H2 IdoA2S; e, H3 IdoA2S; f, H4 IdoA2S; g, H5 GlcNS6S of heparin shifted as the concentration of C_{16} -Spermine increased (**Figure 4.41**). However, once again, shifts were very small and might indicate that the binding here is not as effective as that for C_{16} -Spermidine. Furthermore, the C_{16} -Spermine peaks in this experiment were also much broader than those of C_{16} -Spermidine in the equivalent experiment – suggesting that the latter forms better optimised complexes.



IdoA2S-GlcNS6S

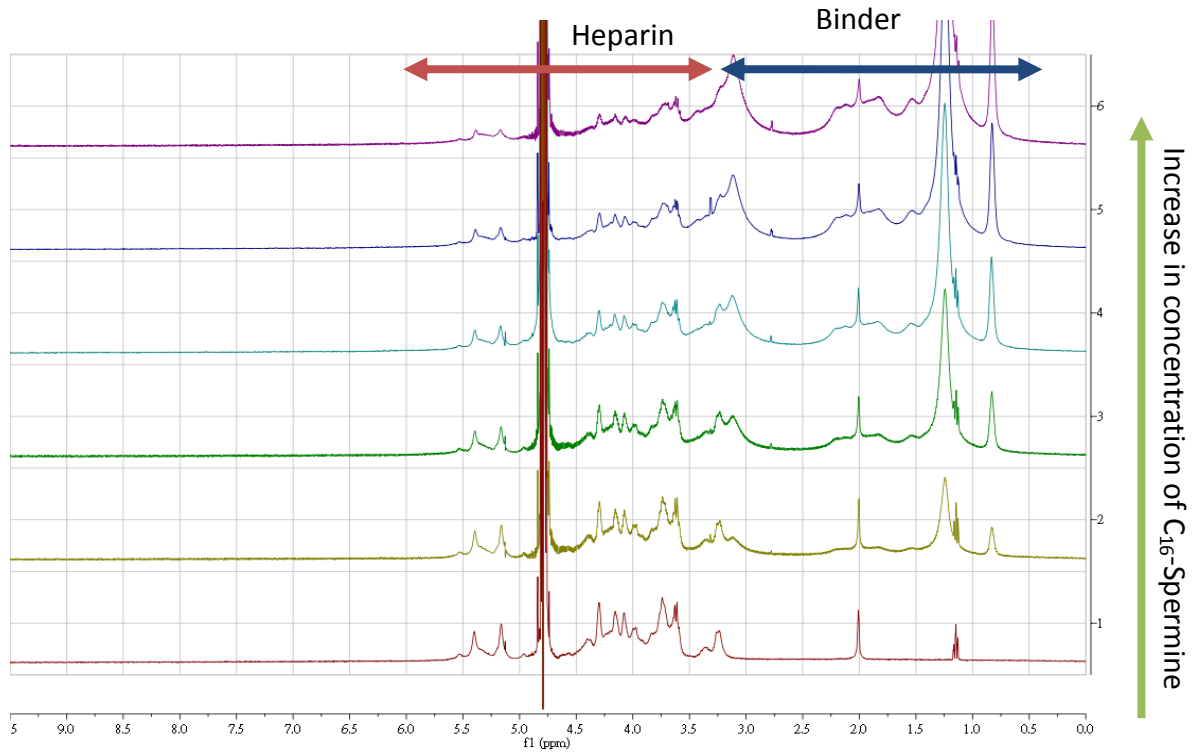


Figure 4.39: ^1H NMR spectra of heparin with increase of C_{16} -Spermine concentration (1:0 to 1:1)

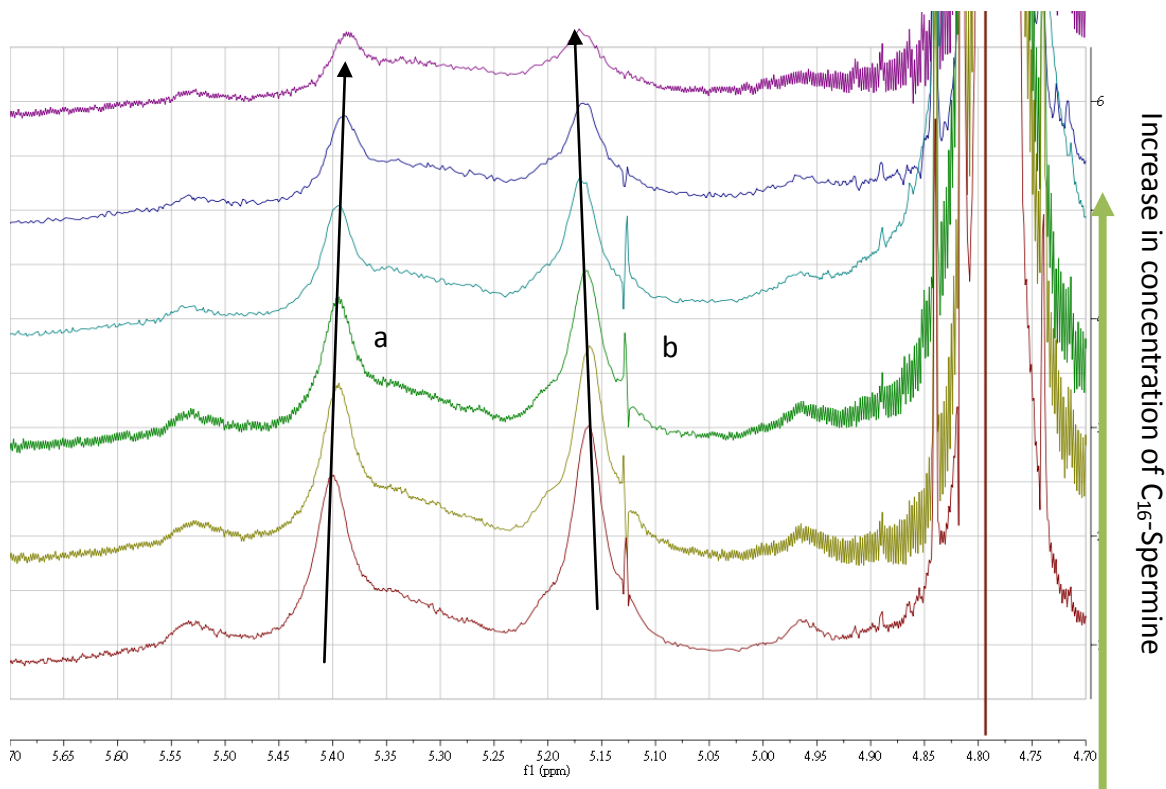


Figure 4.40: ^1H NMR spectra of heparin with increase of C_{16} -Spermine concentration from 4.7 to 5.7 ppm

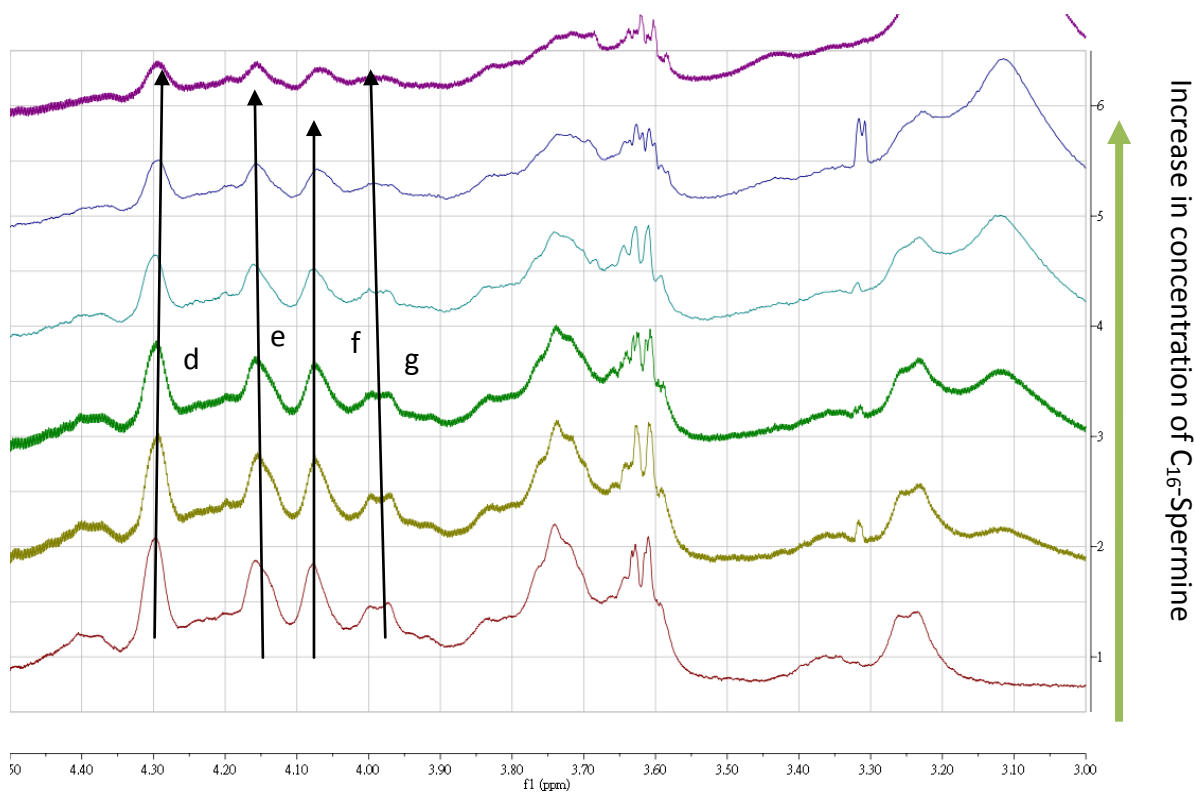
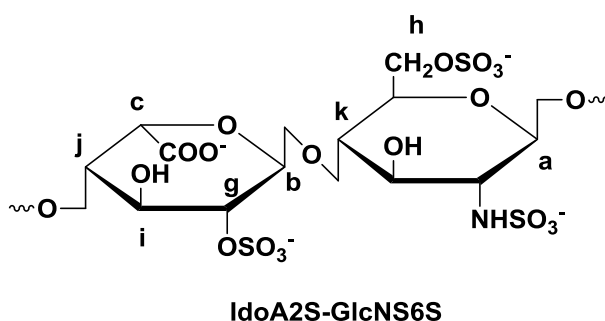


Figure 4.41: ^1H NMR spectra of heparin with increase of C_{16} -Spermine concentration from 3.0 to 4.5 ppm

In summary, C₁₆-Spermine shares a similar shifting pattern in NMR with C₁₆-DAPMA and C₁₆-Spermidine when binding with heparin through ionic interactions between cationic amine groups on the binder and sulfate/carboxylate groups on the heparin chain and resulting in most of the protons on heparin being shifted. However, peak broadening on the ligand is intermediate between C₁₆-DAPMA and C₁₆-Spermidine.

4.3.2.5 700 MHz titration study of SAMul heparin binder with heparin

Since improvements in the field strengths of magnets lead to greater resolution of signals by NMR, we initially titrated C₁₆-DAPMA into heparin to observe which heparin peaks are mostly affected at the resolution affected by a 700 MHz NMR spectrometer. An NMR titration of heparin with C₁₆-DAPMA was performed in which Heparin (2 mg/mL) with increase of C₁₆-DAPMA concentration (1:0 to 1:1) and the ¹H NMR spectra of are shown in **Figure 4.42**. When we look more closely at the region between 4.7 and 5.7 ppm, three peaks which are: a, H1 GlcNS, GlcNS6S; b, H1 IdoA2S; of heparin shifted slightly as the concentration of C₁₆-DAPMA increases (**Figure 4.43**). In the region between 4.5 and 3.0 ppm, four peaks which are: f, H6 GlcNS6S; g, H2 IdoA2S; h H6' GlcNS6S; i, H3 IdoA2S; j, H4 IdoA2S; k, H5 GlcNS6S of heparin shifted very slightly as the concentration of C₁₆-DAPMA increases (**Figure 4.44**).



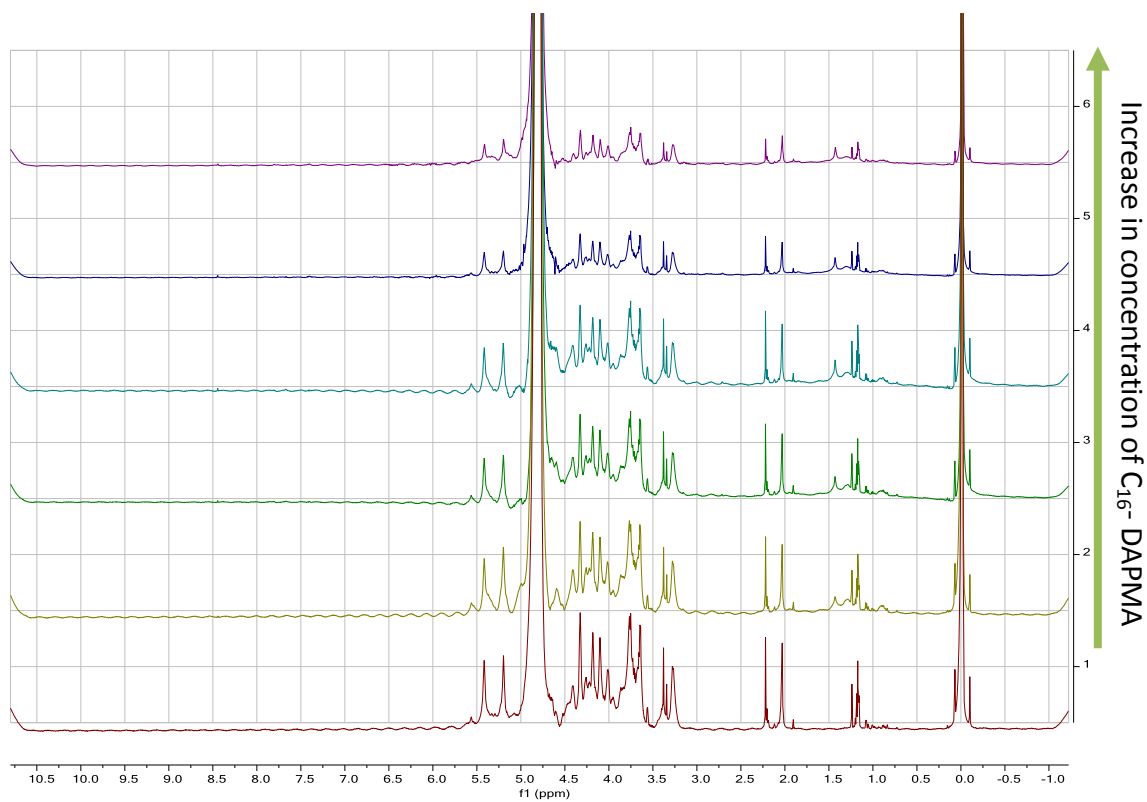


Figure 4.42: ^1H NMR spectra (700 MHz) of heparin with increase of C_{16} -DAPMA concentration (1:0 to 1:1)

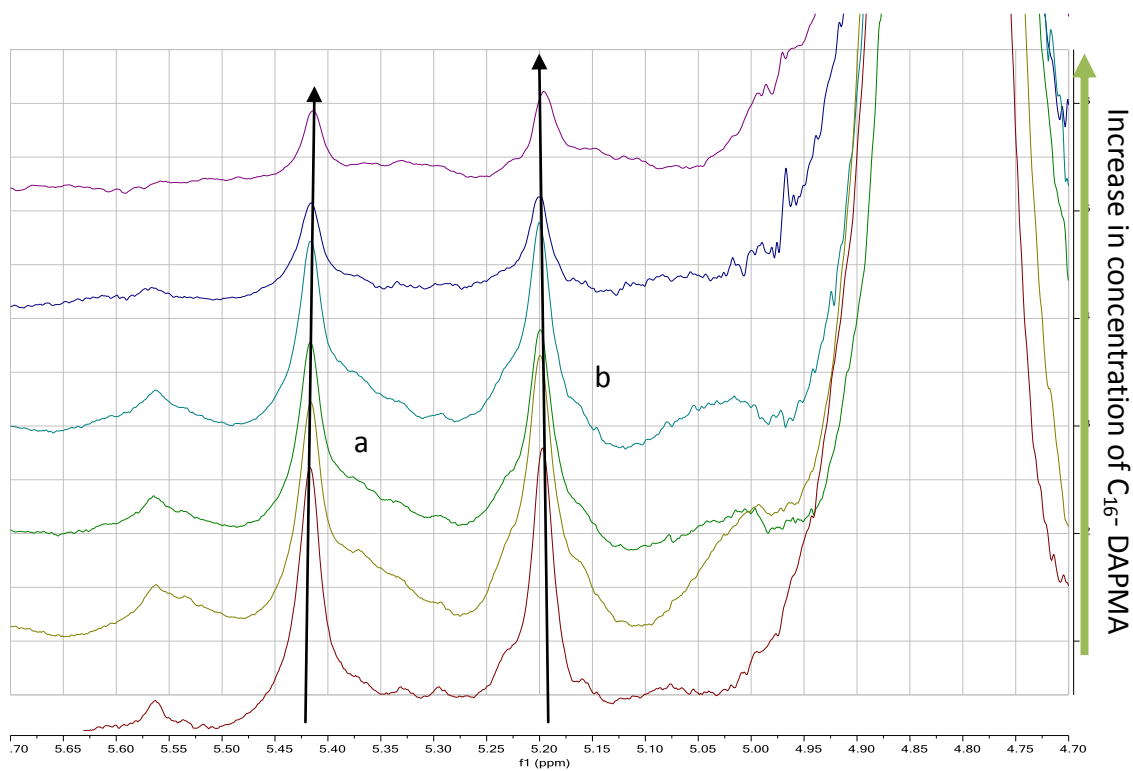


Figure 4.43: ^1H NMR spectra (700 MHz) of heparin with increase of C_{16} -DAPMA concentration from 4.7 to 5.7 ppm

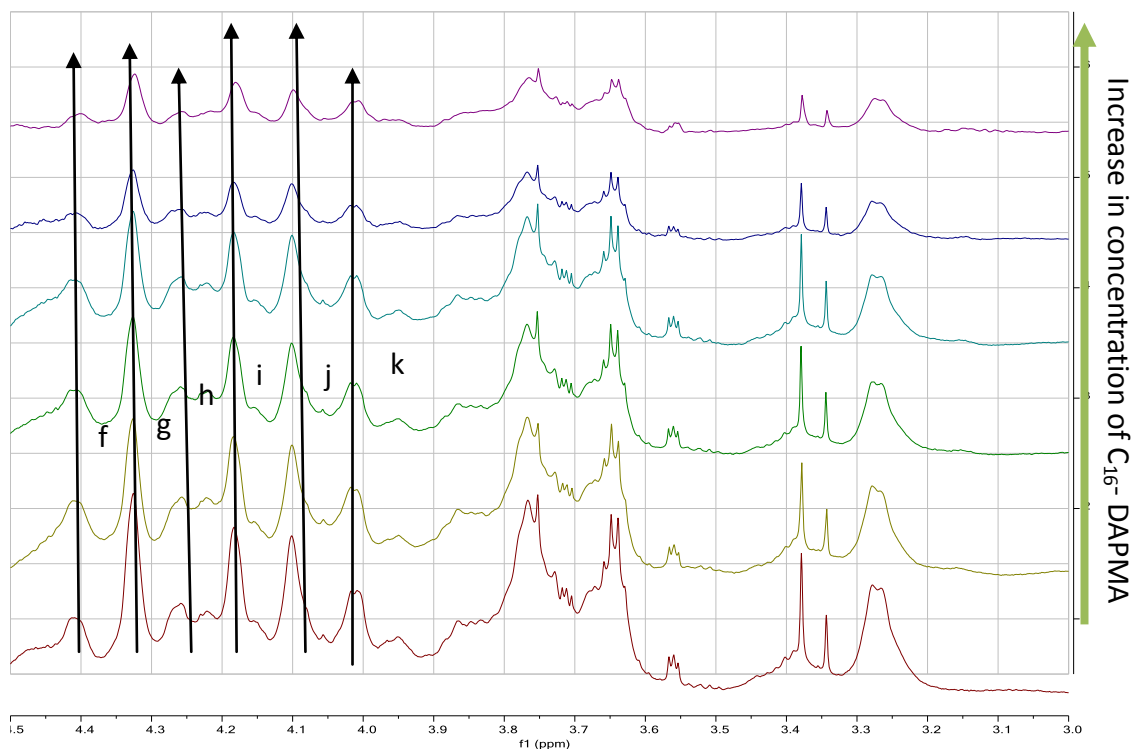


Figure 4.44: ^1H NMR spectra (700 MHz) of heparin with increase of C_{16} -DAPMA concentration from 4.5 to 3.0 ppm

As such, the results at 700 MHz were in good agreement at 400 MHz. Running the titration study at 700 MHz resolved one extra peak, H6' GlcNS6S. The titration study was also performed with C_{16} -Spermine as well as C_{16} -Spermidine in 700 MHz spectrometer, however, apart from the extra proton H6' GlcNS6S being resolved, all the shifting patterns are the same, and the experiment will not be discussed further here.

4.3.3 Conclusion and future work

On titration between heparin binders and heparin, at charge equivalence, precipitation occurred as a result of aggregate formation and no NMR signals were observed. However on addition of excess heparin to binder (or vice versa) the complexes became soluble again and it was possible to observe changes and shifted peaks which provided some insight into the binding mode. Peak shifts were relatively small but similar protons on the heparin framework were consistently affected.

All SAMul heparin binders interacted with H1 GlcNS, GlcNS6S; H1 IdoA2S; H2 IdoA2S; H3 IdoA2S; H4 IdoA2S; H5 GlcNS6S of heparin and share the same pattern in shifting in NMR. The anomeric proton H1 GlcNS, GlcNS6S shifted upfield and H1 IdoA2S shifted downfield. With 700 MHz, an extra proton that interacted with the binder H6' GlcNS6S was resolved.

On titrating heparin into binder, shifts in the binder protons could be observed. Specifically the protons adjacent to the cationic charged nitrogens were shifted downfield. For the best binder (C_{16} -Spermidine) protons two carbons away from N^+ were also shifted and quite well resolved whereas for the less effective binders (C_{16} -Spermine and C_{16} -DAPMA) these more distant protons remained very broadened (or invisible) and there was little evidence of shifting. This strongly suggests that different ligands on the periphery of these SAMul nanostructures have different dynamics at the binding interface with polyanionic heparin. We suggest that the dynamics at this interface are of key importance in the binding strength – this view may support modelling performed by Pricl and co-workers on these systems,¹⁸² which related to similar data in the literature.¹⁸¹ This modelling focuses on the impact of ligand dynamics and reorganisation on the entropy of binding and hence the binding affinity.

In summary, NMR can provide some insight to the binding events at the nanoscale and appears particularly useful for uncovering the role of ligands and dynamics in mediating binding.

For future work, the study of other SAMul heparin binders such as C_{16} -L/D-Lys and C_{16} -Gly-L/D-Lys discussed in Chapter 3 and therefore understand the effect of the spacer group toward heparin binding

Chapter 5 Orthogonal Nanoscale adhesion of Nanotubes and DNA using SAMul System

5.0 Overview

In the previous chapters, we have discussed the sensing and binding of polyanionic targets, heparin and DNA, by synthetic systems. We have used NMR techniques to gain insight into the molecular detail of their interactions and shown that the combination of self-assembly and multivalency is a promising strategy by which we can obtain adhesion to polyanionic nanoscale surfaces. In this chapter, we aim to demonstrate, in a proof-of-principle study, that such interactions can be applied as a general methodology in order to bring together nanoscale building blocks in new and controllable ways. As such, we initially need a brief introduction about some of the key structures used in the methodology which we may want to manipulate. The synthetic work in this chapter contributed to S. M. Bromfield, P. Posocco, C. W. Chan, M. Calderon, S. E. Guimond, J. E. Turnbull, S. Prichard and D. K. Smith, *Chem. Sci.*, 2014, 5, 1484-1492.⁴³

5.1 Nanomaterial

5.1.1 Carbon nanotubes

Carbon nanotubes (CNTs) were first reported by Oberlin *et al.* in 1976¹⁸³ and consist of rolled graphene sheets with diameters in the nanometre range and lengths in the micrometre range. In 1991, Iijima reported that multi-walled carbon nanotubes were found in the insoluble material of arc-burned graphite rods¹⁸⁴ and this gave rise to a great interest in CNT research and development.

CNTs can be produced by arc discharge, laser ablation or chemical vapor deposition (CVD).¹⁸⁵ The arc discharge method uses two electrodes with at least one electrode being made of graphite through which a direct current (DC) is passed in a gaseous atmosphere. The laser ablation method uses an intense laser beam to ablate vaporize a target consisting of a mixture of graphite and metal catalyst in a flow of inert

gas. The CVD method involves catalyst-assisted decomposition of hydrocarbons and growth of CNTs over the catalyst in a temperature range of 300–1200 °C.¹⁸⁶ Hence CNTs prepared by the above methods contain carbonaceous impurities such as amorphous carbon, fullerenes, and carbon nanoparticles and metal catalyst particles.

CNTs can be purified via chemical or physical methods, or a combination of both. The chemical method purifies CNTs via gas phase, liquid phase and electrochemical approaches whereas the physical method can involve filtration, centrifugation, solubilization with functional groups, high temperature annealing and other techniques such as chromatography.¹⁸⁶

CNTs can exist as a single layer, (single-walled carbon nanotube, SWCNT, **Figure 5.1**), or multiple layers nested within one another (multi-walled carbon nanotube, MWCNT). CNTs are also known to have applications in areas such as resilient composite materials, field emission, energy storage, and molecular electronics.¹⁸⁷⁻¹⁹⁰ As such they can be considered to be nanomaterials of considerable interest and importance.

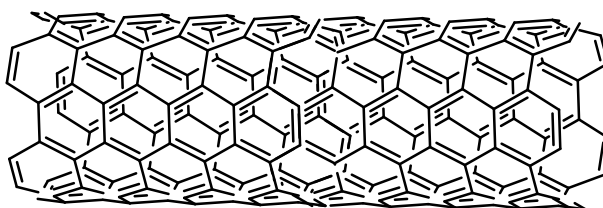


Figure 5.1: Single-wall carbon nanotube.

5.1.2 Functionalising CNTs

Although CNTs have a wide range of potential applications, they are undermined by the low solubility of these structures in either water or organic solvents and incident aggregation of the CNTs.¹⁹¹ However, CNTs can gain solubility via functionalising them through both covalent¹⁹² and non-covalent means.

Covalent methods typically involve either oxidation in an acidic medium or 1,3-dipolar cycloaddition, producing substituted structures with much of the carbon

nanotubes' unique aromatic character being disrupted by the modifying groups.¹⁹² It should be noted that covalent modification can be difficult to control with functionalisation occurring at a number of different sites or to different sheets. Examples of covalent functionalisation are illustrated in **Figure 5.2**.

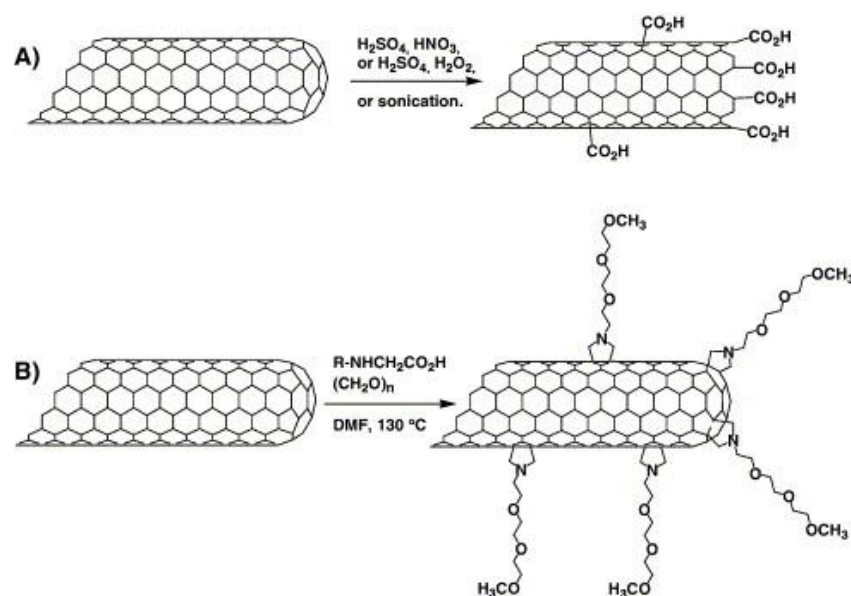


Figure 5.2: (A) CNT treated with acid to cut them and form carboxylic groups at the tips and the sidewalls. (B) CNT undergoing 1,3 dipolar cycloaddition by reacting an α -amino acid derivative with para-formaldehyde. $\text{R} = \text{CH}_3\text{O}(\text{CH}_2\text{CH}_2\text{O})_2\text{CH}_2\text{CH}_2$.¹⁹²

Covalent modification of the surface may have effects on the internal electronic properties of CNTs by disrupting conjugation pathways. Hence, effective functionalisation of the carbon nanotubes by non-covalent methods has attracted increasing recent interest.¹⁹³ The aromatic and hydrophobic character of CNTs allows non-covalent functionalisation via π - π stacking or van der Waals interactions (**Figure 5.3**). This approach can leave the electronic properties of the CNT intact.

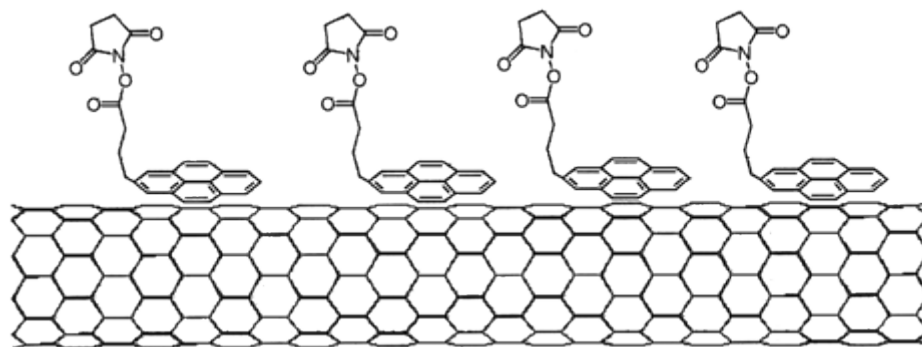


Figure 5.3: 1-Pyrenebutanoic acid, succinimidyl ester irreversibly adsorbing onto the sidewall of a SWCNT via π - π stacking.¹⁹³

5.1.3 Dendrons and carbon nanotubes

Dendrons and hyperbranched dendritic structures provide a particularly interesting approach for non-covalent functionalisation of carbon nanotubes. The presence of multiple surface groups on the periphery of the branched nanostructures provides a large surface area for interactions with the solvent, while the orthogonal groups at the dendron focal point can interact with the carbon nanostructure. As such there is a capacity to use such structures to mediate interactions between CNTs and solvent via directed non-covalent interactions. Wurm *et al.* demonstrated how this principle using α,ω_n -heterotelechelic hyperbranched polyethers and its pyrene analogue can bind to MWCNTs, using hydrophilic block copolymers, with multiple hydroxyl end head groups to help solubilise the assembly in an aqueous medium (see **Figure 5.4**).¹⁹⁴ This gave rise to water soluble CNTs.

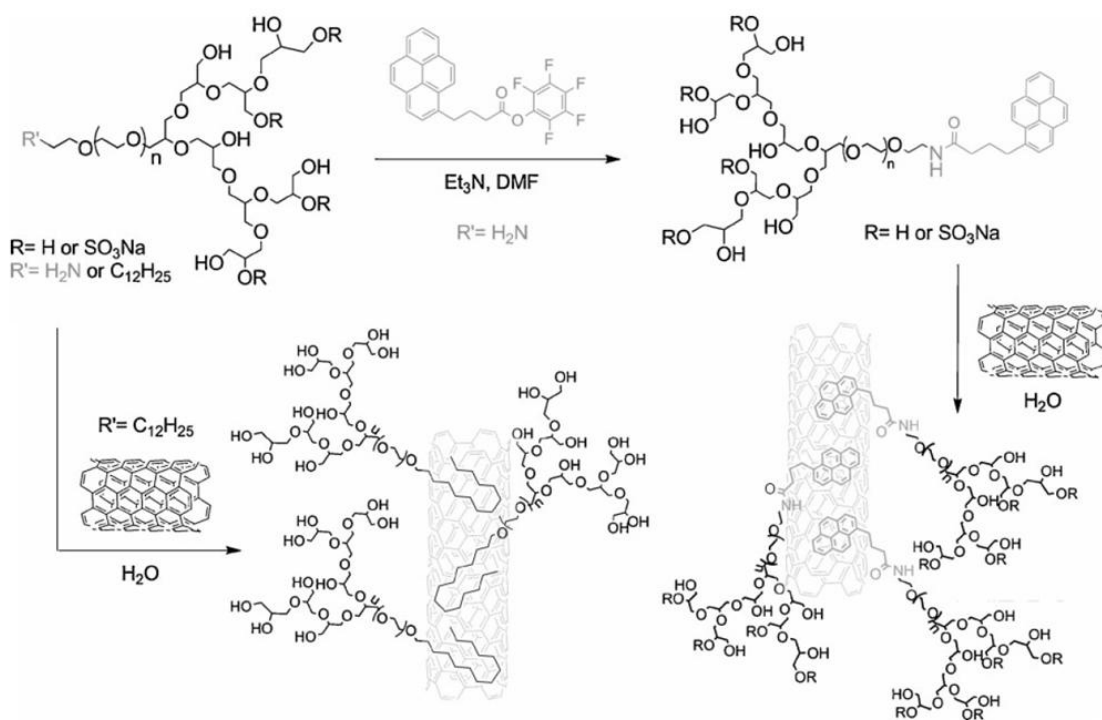


Figure 5.4: Non-covalent modification of MWCNT inducing water solubility.¹⁹⁴

On the other hand, Bahun *et al.* used an inverse strategy in which the dendritic surface groups interacted in a multivalent way with the CNT while the polymer (Polystyrene) at the dendritic focal point helped mediate solubility. As such, these pyrene-functionalized linear-dendritic hybrid polymers dissolved CNTs in organic solvents such as THF.¹⁹⁵ (see **Figure 5.5**).

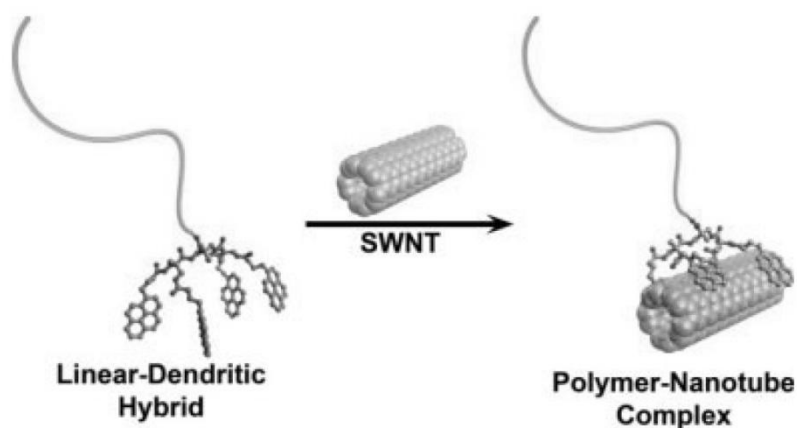


Figure 5.5: Schematic illustration of the interaction between a linear-dendritic hybrid polymer (second generation dendron) and a SWNT.¹⁹⁵

5.1.4 CNTs in biomedical applications.

CNTs have been of interest to many researchers as nanovectors for the highly efficient delivery of drugs and biomolecules.¹⁹⁶ They can be functionalised non-covalently or covalently with drugs, biomolecules and nanoparticles and have been suggested as carriers with great potential for the development of new-generation delivery systems for drugs and biomolecules (for an overall view, see **Figure 5.6**). Clearly there is significant interest in the ability to interface CNT with biologically relevant molecules of therapeutic interest. In the section below, we focus on cellular uptake and potential in gene delivery as just one example of this work.

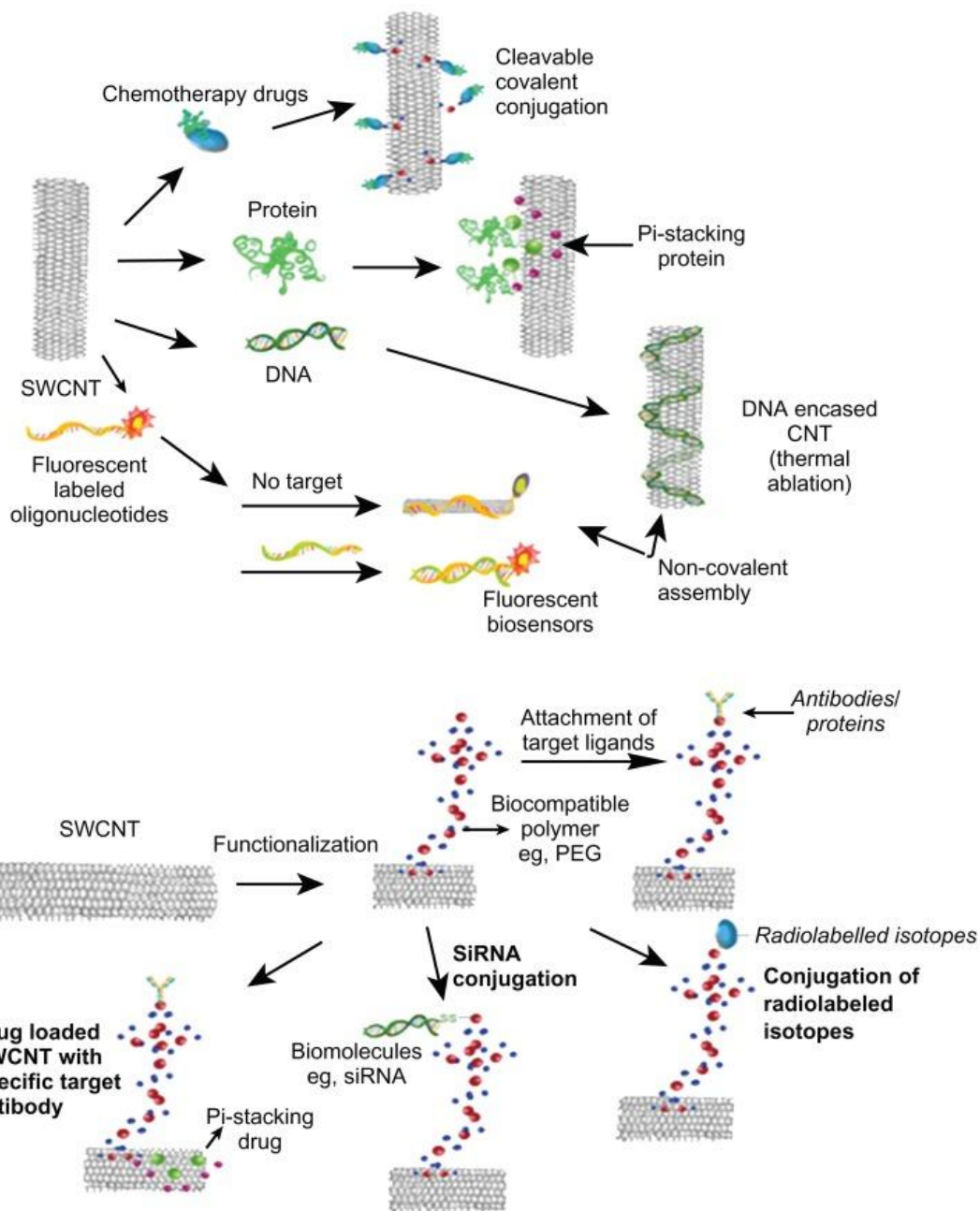


Figure 5.6: Overview of functionalization of carbon nanotubes (CNTs) using different molecules and their biomedical applications. Figure adapted from Ref¹⁹⁶.

5.1.5 Cellular uptake of CNTs

There are two possible major pathways by which CNTs can cross the cellular membrane.¹⁹⁷ The first is an endocytosis dependent pathway which may be either receptor-mediated or non-receptor mediated and the second is based on an endocytosis independent pathway which includes diffusion, membrane fusion, or

direct pore transport of the extracellular material into the cell (**Figure 5.7 a, b**). In general, such systems are taken up across cellular membrane via the first endocytosis-mediated passway. However, CNTs can also be taken via the second, more direct mechanism. The second approach is a direct translocation of CNT through the plasma membrane into the cytoplasm, which has been termed by some researchers as the “nanoneedle” mechanism.¹⁹⁸ This pathway includes processes such as diffusion, membrane fusion, and direct pore transport (**Figure 5.7 c**). This relatively unique mechanism means CNTs have seen particular interest for their unique ability to intervene within cells, although of course this also raises the risk of uncontrolled uptake and hence toxicity.

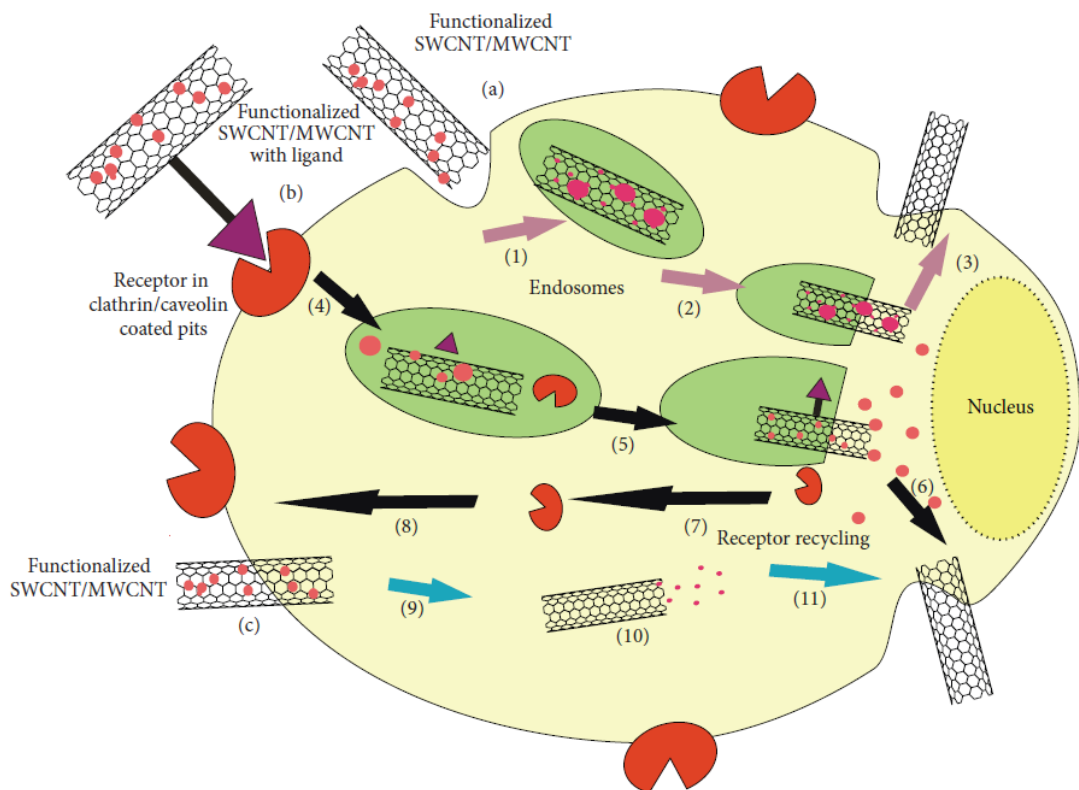


Figure 5.7: Pathways for the penetration of CNTs into the cell. (a) Non-receptor mediated endocytosis: (1) membrane that surrounds the drug loaded functionalized CNTs, (2) internalization of drug loaded CNTs, and (3) release of drug; (b) receptor mediated endocytosis: (4) membrane surrounds the CNT-receptor conjugate by forming endosomes followed by internalization, (5) release of drug, and (6, 7, 8) regeneration of receptor; (c) endocytosis independent pathway: (9) direct penetration of drug loaded functionalized CNT and (10) release of the drug.¹⁹⁷

5.1.6 CNTs as gene delivery vector

In 2004, Bianco *et al.* reported the first work using carbon nanotubes as a novel gene delivery vector system with covalently-modified carbon nanotubes using the Prato reaction, a method based on the 1,3-dipolar cycloaddition of azomethine ylides which had been used to introduce amines (**Figure 5.8**).¹⁹⁹ The cationic amine functionalized carbon nanotube was able to condense plasmid polyanionic DNA to form supramolecular complexes with globular conformations through electrostatic interactions.²⁰⁰ The level of gene expression depended on the charge ratio between the ammonium groups on the SWNT surface and the phosphate groups of the DNA backbone. Moreover, the DNA carbon nanotube (DNA-CNT) complexes did not appear to exert any mitogenic or toxic effect on activated or non-activated lymphocytes.

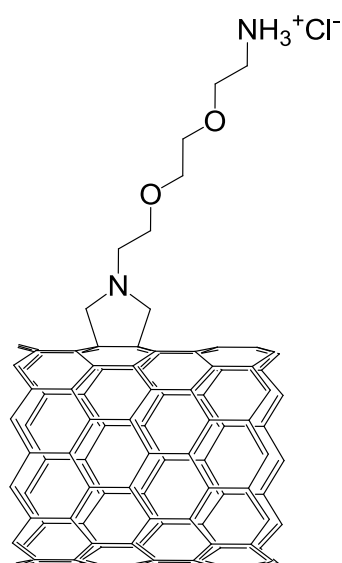


Figure 5.8: Azomethine ylides functionalized carbon nanotube.

Non-covalent functionalisation of CNTs with amphiphilic molecules is of great importance because, in contrast to covalent functionalisation, the π -network of graphene sheets is not disturbed, and their extraordinary physical properties remain intact.²⁰¹ Furthermore, it avoids complex and relatively uncontrolled covalent functionalisation reactions.

Surfactants such as sodium dodecyl sulfate,²⁰² sodium dodecyl-

benzenesulfonate,²⁰³ cetyltrimethylammonium bromide (CTAB),²⁰⁴ and the Triton-X series²⁰⁵ have been shown to enhance the stability and dispersibility of CNTs in the culture medium by absorbing onto the surface of CNTs, thereby reducing cytotoxicity.¹⁹⁶ Dispersion of SWCNTs helps to diminish SWCNT cytotoxicity.²⁰⁶ Studies with polyoxyethylene sorbitan monooleate, a surfactant, also enhanced the dispersibility of CNTs and showed no toxicity to human lung mesothelial (MSTO-211-H) cells.²⁰⁷

Therefore, achieving functionalisation of carbon nanotubes by non-covalent means while at the same time facilitating strong CNT-polyanion binding became an interesting topic to explore.

5.2 Project Aim

In general terms, we reasoned it is of great interest to understand generic adhesion processes between diverse nanoscale structures and design system which can interact simultaneously and controllable with two different nanostructures. In this way we should be able to study the advantages/properties of each of the nanostructures within a single hybrid. As such, we became interested in enabling carbon nanotubes, or graphene sheets, to interact with anionic biomolecules. For this study, we selected DNA as the polyanion of interest rather than heparin because of the potential applications of such organised nano-hybrids. Such systems might have applications in gene delivery. **Figure 5.9** shows our general schematic approach in which we design a bi-functional supramolecular dendron with a hydrophobic unit capable of binding to CNTs and polycationic ligands capable of binding to polyanionic DNA. Such a systems can be considered to be “nanoscale glue” and it should be noted that this approach to the supramolecular organisation of nanoscale matter has broader scope and potential than only binding CNTs or DNA. As such, this project can be considered as a proof-of-principle to demonstrate the potential of such “nano-glues”.

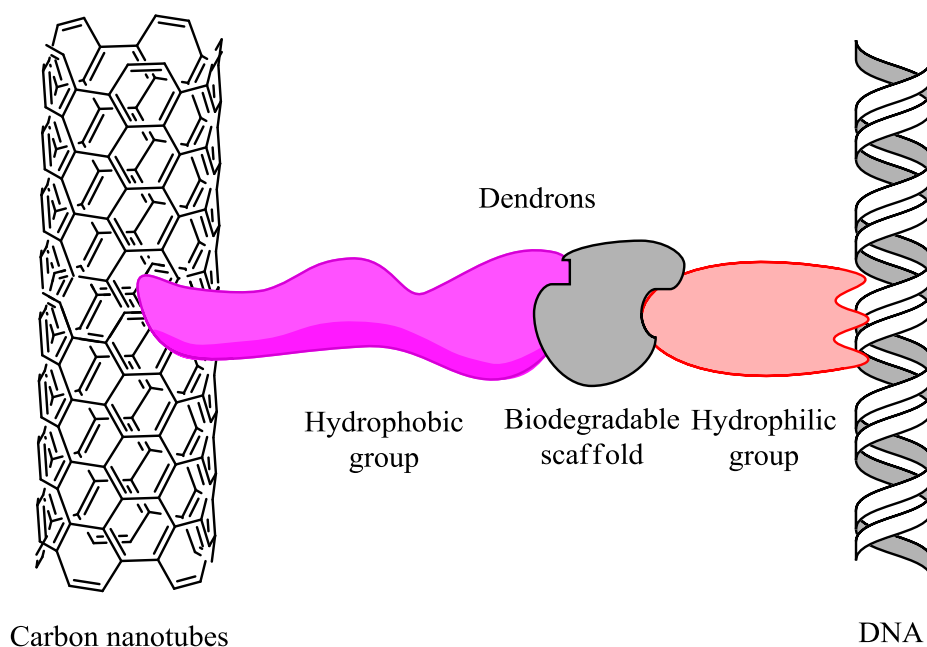
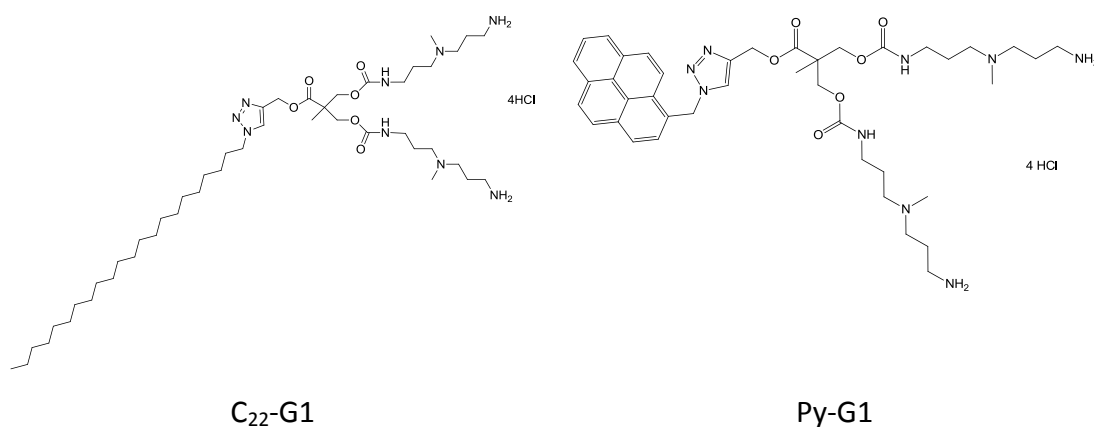


Figure 5.9: Schematic drawing of dendrons as a "nanoglu" that glue two different nanoscale building blocks together such as double helical DNA and a carbon nanotube.

5.3 Compound Design

This project therefore aims to employ self-assembling dendrons to 'glue together' different orthogonal nanoscale building blocks, such as SWCNT and DNA. Initial target molecules were C₂₂-G1 and Py-G1. These compounds contain hydrophobic units to potentially bind to the SWCNT and polyamine ligands to bind to DNA.



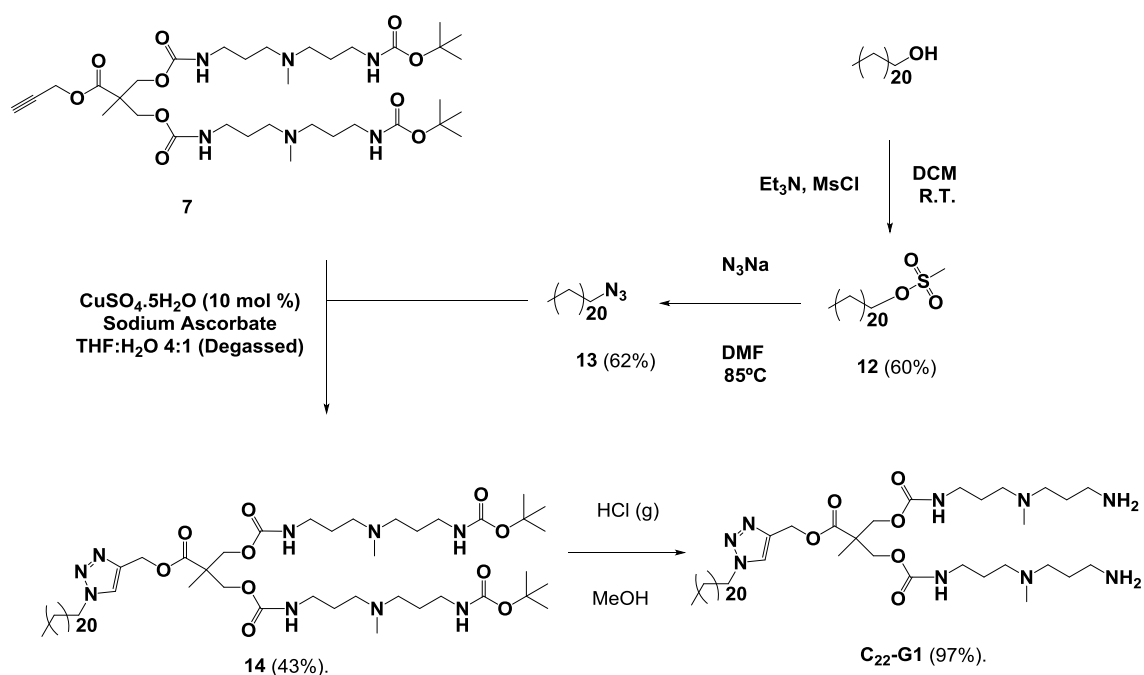
C₂₂-G1 was first reported by Rodrigo *et al.*⁹³ as a self-assembling dendron for heparin binding. The amine surface groups were shown to bind DNA as reported by

Barnard *et al.*,²⁰⁸ however this published structure had not been investigated for DNA binding potential. Furthermore the hydrophobic tail should have potential to bind with SWCNT. In addition to studying C₂₂-G1, we proposed to employ Py-G1, as we reasoned the pyrene group may bind with higher affinity to SWCNT as a consequence of the pyrene's π - π stacking mechanism. The synthesis and heparin-sensing potential of this SAMul binder were described in Chapter 2. So Clearly Py-G1 has the ability to bind polyanions – although once again, its DNA binding potential had not yet been assessed.

5.4 Result and Discussion

5.4.1 Synthesis of C₂₂-G1

To synthesise C₂₂-G1, the procedure reported by Rodrigo *et al.*⁹³ was followed. The synthesis of alkyne-functionalised dendron, **7**, was same as reported in Chapter 2. Then “click” chemistry was used to attach 1-azidodocosane **13** to **7** and the resulting **14** was purified by gel permeation chromatography. Target C₂₂-G1 was obtained by removing the protecting groups of **14** using HCl gas in methanol (**Scheme 5.1**).



Scheme 5.1: Synthesis of C₂₂-G1

It should be noted that some of the compounds synthesised by me in this project

were used in a full study of the heparin binding potential of these carried out by Dr S. M. Bromfield. The results of this study were published in *Chemical Science*⁴³ but are not discussed in detail here as the analysis was carried out primarily by Bromfield.

Some of the spectroscopic assignment of these compounds were revisited. When compared with the published report of Rodrigo *et al.*,⁹³ compound **14** showed a proton at 5.20 ppm, which was not reported. This proton had ²J or ³J correlation to 3 carbons at 123.4, 142.3 and 173.1 ppm in the HMBC. Based on the correlation from HMBC this peak was assigned as the CH₂O adjacent to the triazole unit with ¹H NMR (400MHz, CDCl₃) δ: 5.20 and ¹³C NMR (100MHz, CDCl₃) δ: 58.3 (see **Figure 5.10**). This proton and this carbon had been missed in the previous assignment.

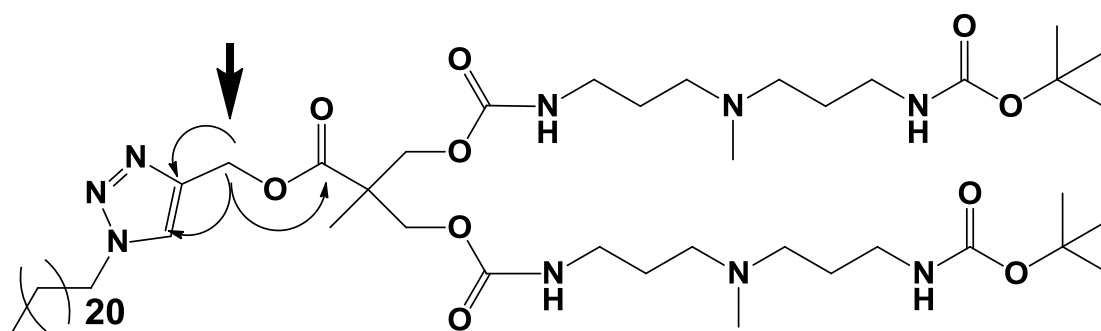
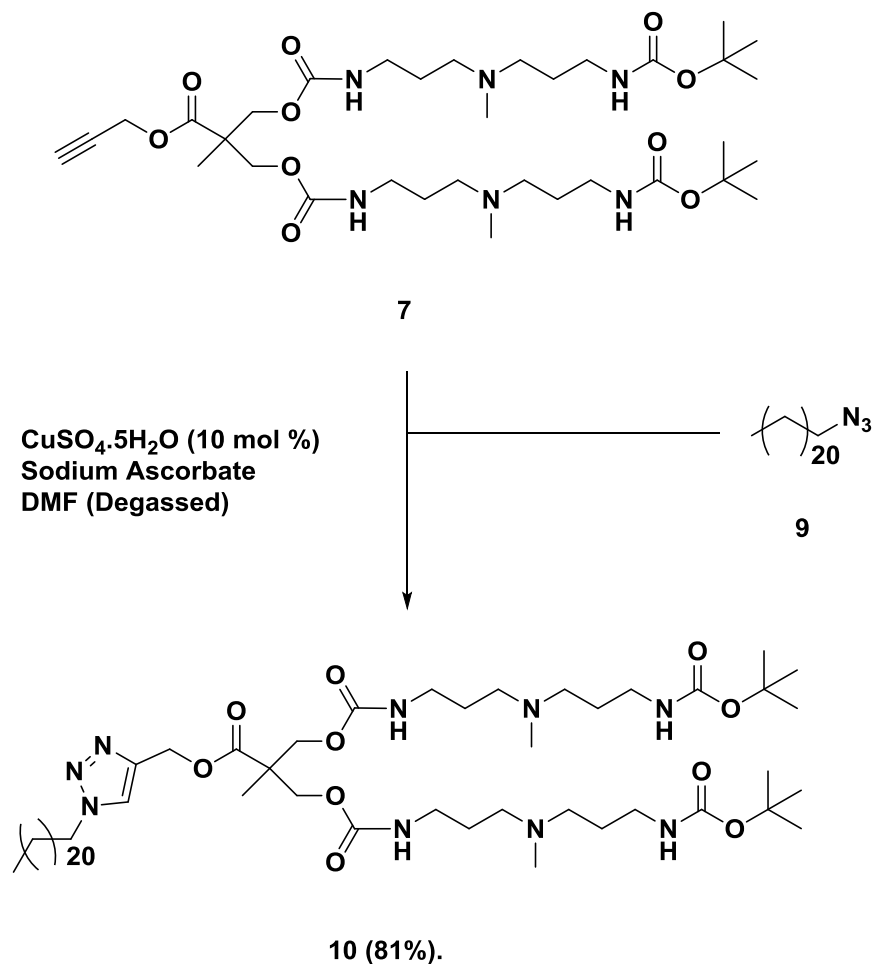


Figure 5.10: HMBC correlations observed for proton at 5.20 ppm in compound **10** in CDCl₃

The deprotected target compound, C₂₂-G1, also had a missing proton and carbon assignment for the CH₂O adjacent to the triazole. This was now assigned as ¹H NMR (400MHz, MeOD-*d*₄) δ:5.15 and ¹³C NMR (100MHz, MeOD-*d*₄) δ: 142.3. All other characterisation was in full agreement with the published report by Rodrigo *et al.*⁹³

In Chapter 2, the click chemistry step for the synthesis of protected Py-G1 suggested that the yield could be significantly enhanced by changing the solvent from aqueous THF to dry and degassed DMF. Therefore, the synthesis of protected C₂₂-G1 was repeated with the new method, as reported for protected Py-G1, to see whether the yield could be improved.



The yield using the new method was found to be 81%, which was significantly higher than what was reported by Rodrigo *et al.*⁹³ with 40%. As such, this indicated that this optimised method should be employed for the synthesis of all of this class of compounds in future studies.

5.4.2 Critical Aggregation Concentration (CAC) of C₂₂-G1 and Py-G1

The CAC of C₂₂-G1 was reported by Rodrigo *et al.*⁹³ as $3.88 \pm 0.25 \mu\text{M}$ in 0.01M PBS buffer using a Nile Red assay,¹¹¹ in which the solubilization of the hydrophobic dye monitored by fluorescence spectroscopy acts as a probe for the minimum concentration at which self-assembly can take place in 0.01M PBS buffer (phosphate-buffered saline at pH 7.4). In this study, the CAC of C₂₂-G1 was found as $16 \pm 4 \mu\text{M}$ using the same Nile Red assay method as reported by Rodrigo *et al.*⁹³ but in 0.01M SHE buffer made up with: NaCl [9.4 mM], EDTA [20 μM] and HEPES [2 mM] at pH

7 (see **Figure 5.11**).

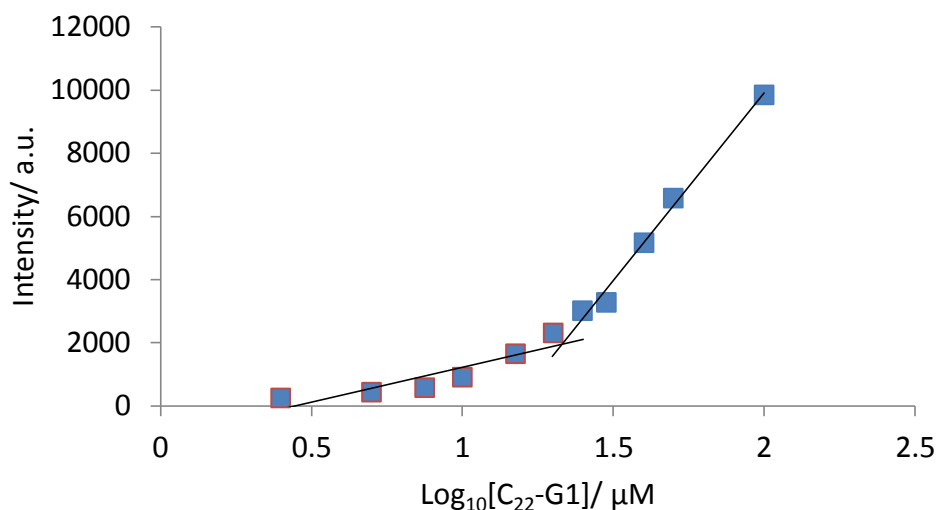


Figure 5.11: Fluorescence intensity of Nile Red in the presence of increasing amounts of C₂₂-G1 in SHE Buffer

The result suggested that the CAC of C₂₂-G1 in SHE Buffer is higher than that in PBS buffer. This may be due to PBS buffer having higher ionic strength than SHE buffer which helps drive the self-assembly. Specifically interactions between the phosphate anions (10 mM) in PBS and cationic C₂₂-G1 would be expected to encourage self-assembly. In 2013, Javadian *et al.* reported that the CAC value of ester-containing cationic gemini surfactants, dodecyl esterquat and dodecyl betainate decreased as the concentration of NaBr increased because the addition of salt causes the neutralization and screening of the charge of head groups and reduction of repulsive electrostatic interactions.²⁰⁹ Indeed it is quite well-known that salt can act to screen electrostatic repulsion and lower CAC.²¹⁰ Therefore, we suggest it is not unsurprising that the CAC of C₂₂-G1 in SHE Buffer was higher than that observed in PBS buffer.

The CAC of Py-G1 was also determined in SHE buffer using the method described in Chapter 2. It was found that when Py-G1 was excited at 363 nm, a emission band with max emission at 495 nm was observed and this band could therefore be monitored to determine the CAC. This band is concentration dependent because excimer formation is favoured in the interior of the micelle when the pyrene groups are close together in

space. The CAC of Py-G1 was found to be $21 \pm 4 \mu\text{M}$ in 0.01 M SHE buffer (**Figure 5.12**).

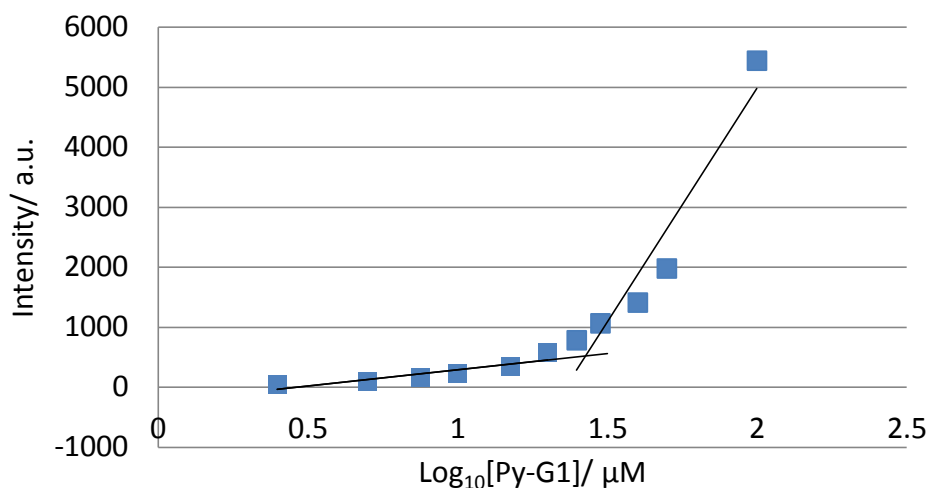


Figure 5.12: Fluorescence intensity at 495 nm of Py-G1 in the presence of increasing amounts of Py-G1 in SHE Buffer (0.01 M).

The difference between the CAC value of Py-G1 in PBS buffer ($19 \pm 2 \mu\text{M}$, reported in Chapter 2) and SHE buffer ($21 \pm 3 \mu\text{M}$) was not as significant as that for C₂₂-G1. This may be due to the more rigid structure of the aromatic rings of pyrene causing the assembly to have less overall dynamic flexibility and hence less dependence on ionic strength or interactions with components of the buffer solution. Overall, however, the data suggest that C₂₂-G1 self assembles more effectively than Py-G1.

5.4.3 DNA assay C₂₂-G1 and Py-G1

The DNA binding ability of C₂₂-G1 and Py-G1 was then measured via the displacement of the intercalating agent ethidium bromide (EthBr) from DNA as monitored by fluorescence spectroscopy in SHE buffer with DNA ($4.0 \mu\text{M}$) and EthBr ($5.07 \mu\text{M}$).^{211, 212} The CE₅₀ value is the charge excess required for the 50% displacement of ethidium bromide in the fluorescence displacement assay and the EC₅₀ value is the concentration of binder required for the 50% displacement of ethidium bromide in the fluorescence displacement assay. C₂₂-G1 was found to have a CE₅₀ = 1.5 ± 0.2 and EC₅₀ = $1.5 \pm 0.2 \mu\text{M}$ whereas Py-G1 was found to have a CE₅₀ = 2.7 ± 0.3 and EC₅₀ = 2.7 ± 0.3

μM (see **Figure 5.13**). Although these values are very dependent upon assay conditions they are an ideal way of comparing the performance of the two analogous DNA binders.

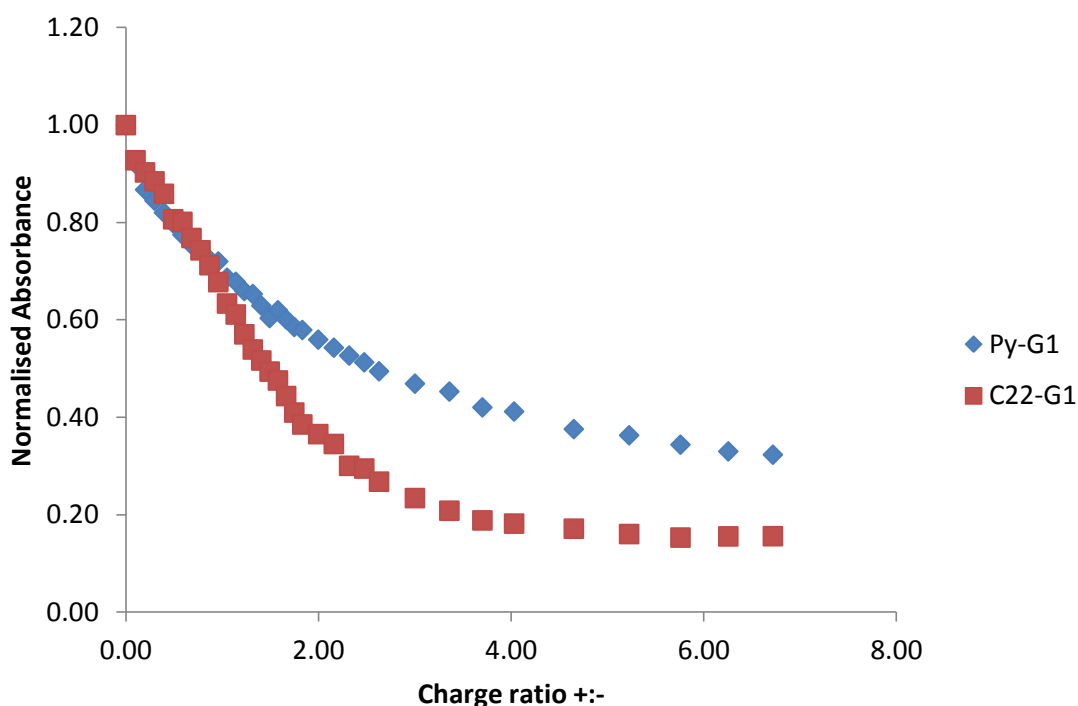


Figure 5.13: Charge ratio vs. normalised fluorescence from the EthBr displacement assay used to determine CE_{50} values for C₂₂-G1 and Py-G1.

Considering the whole titration plot, rather than only the point at which 50% displacement is observed, it is worth noting that in the initial part of the assay, when only small amounts of binder are present, the binding is relatively similar. However, once more binder is present, Py-G1 becomes increasingly ineffective at displacing EthBr. This suggests that the initial binding sites on DNA bind equally well to micelles formed by C₂₂-G1 and Py-G1. However as the DNA become more saturated with nanoscale binders, C₂₂-G1 begins to significantly outperform Py-G1. This might suggest that the former system with the more flexible hydrophobic chain, may have greater potential to adapt and bind to these less favourable secondary binding sites, Similar effects have previously been discussed in other systems binding to polyanionic targets.^{160, 213} As such we suggest the difference between C₂₂-G1 and Py-G1 in binding to DNA lies not in

the initial primary binding sites but in the more crowded secondary binding environments.

Overall, the data suggested that C₂₂-G1 binds DNA better than Py-G1. This may be because of more effective multivalent binding, particularly in the secondary binding sites. Barnard *et al.* in 2011 reported a family of second-generation dendrons with four triamine surface ligands capable of binding to DNA, degradable aliphatic-ester dendritic scaffolds, and hydrophobic units at their focal points (see **Figure 5.14**).²⁰⁸ The results suggested that Z-G2 did not aggregate and also indicated an inverse relationship between the length of the hydrophobic chain and the CMC value (C₁₂-G2 > C₁₆-G2 > C₂₂-G2). At the same time, the CE₅₀ values of EthBr displacement assay decreased from C₁₆-G2 to C₂₂-G2 whereas Z-G2 and C₁₂-G2 were unable to effectively displace ethidium bromide from the DNA double helix under the conditions investigated. This suggested that self-assembly activated multivalent binding when the CAC was reached and hence effective DNA binding only occurred for the assembled nanostructures. C₂₂-G1 self-assembles more effectively than Py-G1 (lower CAC value for C₂₂-G1), we also noted that Py-G1 may be expected to form a more rigid self-assembled structure with less dependence on assay conditions. This supports the view that C₂₂-G1 binds DNA better than Py-G1 by more effective activation of flexible and responsive multivalent binding when the CAC is reached.

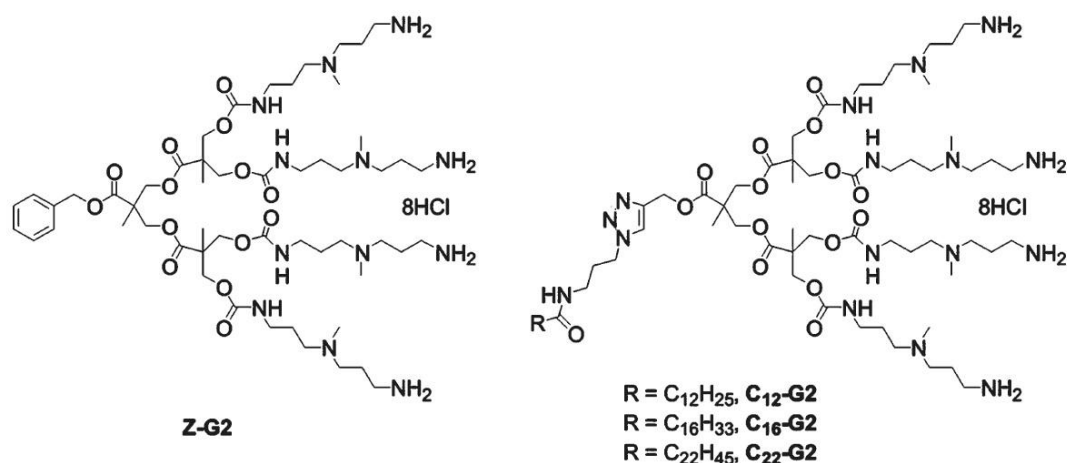


Figure 5.14: Dendrons investigated by Barnard *et al.*²⁰⁸

5.4.4 Carbon nanotube assay

We then moved on to consider the ability of our dendrons to bind the other nanoscale component of interest, i.e. the carbon nanotubes. The simplest way to consider interaction with CNTs is through a simple solubilisation assay. CNTs are not soluble in water, but in the presence of a solubilising ligand should be capable of being more effectively dissolved and to disperse in this medium. We therefore developed a sonication/dissolution assay to probe CNTs binding.

To find out the optimised sonication time needed for C₂₂-G1 to bind with SWCNT, SWCNT (~5 mg) was added into a cuvette with 2 ml of deionized water, and sonicated for 5, 10, 15 and 20 min and the spectra recorded. C₂₂-G1 (0.51 mg) was added to 1 ml of deionized water, shaken well, added to another cuvette with SWCNT (~5 mg) and deionized water, sonicated for 5, 10, 15 and 20 min and the spectra recorded. The results are shown with the intensity at 400 nm being used to detect the dispersion of the CNTs into the aqueous solution (**Figure 5.15**).

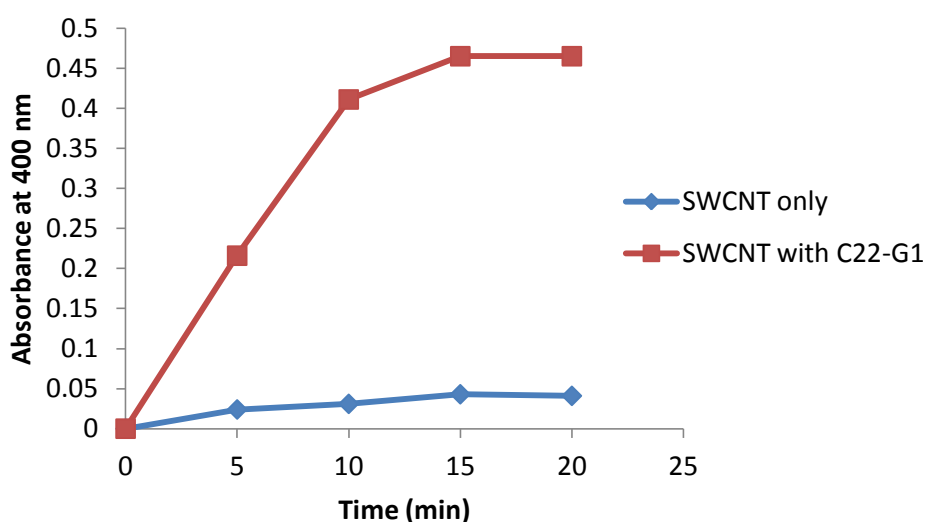


Figure 5.15: UV Absorbance at 400 nm vs time sonicated for SWCNT with/without C₂₂-G1 in H₂O

Sonication of SWCNT in the presence of C₂₂-G1 clearly led to the solubilization of the nanotubes in water when compared with the results without C₂₂-G1. Moreover, there

was no difference in absorbance at 400 nm after sonication for 15 min or 20 min. As such, the results to optimise the assay indicated that 15 min of sonication is sufficient for most of the C₂₂-G1 to bind with, and hence, solubilise SWCNT.

After sonication, there was sometimes a problem in these initial experiments with the inhomogeneous nature of some of the samples. We therefore decided to introduce a centrifugation step to reduce light scattering effects. SWCNT (~5 mg) was added into 4 tubes each with 2 ml of deionized water in them. They were then sonicated for 15 min, followed by centrifugation at 2000 RPM for 30 min. The supernatant solution was then carefully transferred to cuvettes for recording. The samples were then returned to the centrifugation tubes, and aliquots of C₂₂-G1 were then added into the 4 tubes respectively and then sonicated for 15 min and centrifuged at 2000 RPM for 30 min and the spectra recorded. The above process was repeated at centrifuge speeds of 3000 and 4000 RPM. **Figure 5.16** to **Figure 5.18** present the differences in the absorbance at 400 nm before and after addition of dendron.

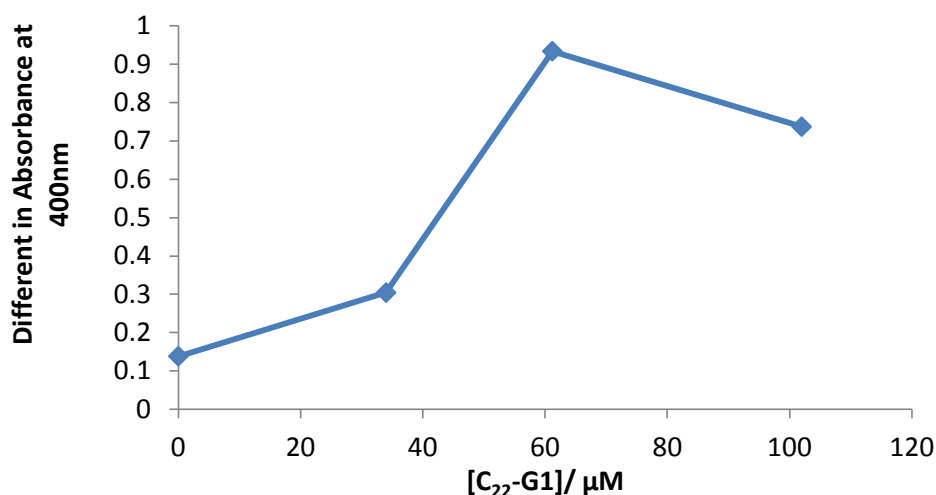


Figure 5.16: Difference in Absorbance of SWCNT in H₂O before and after adding C₂₂-G1 vs [C₂₂-G1] at 2000 RPM

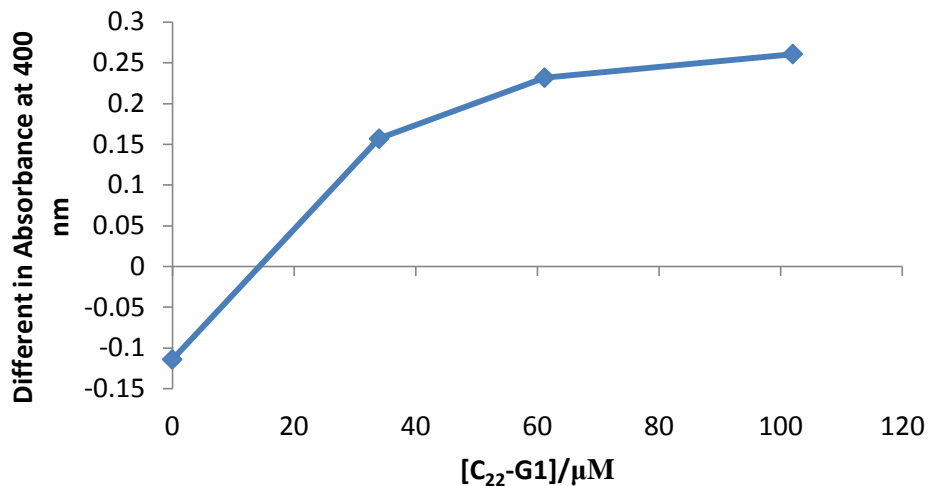


Figure 5.17: Difference in Absorbance of SWCNT in H₂O before and after adding C₂₂-G1 vs [C₂₂-G1] at 3000 RPM

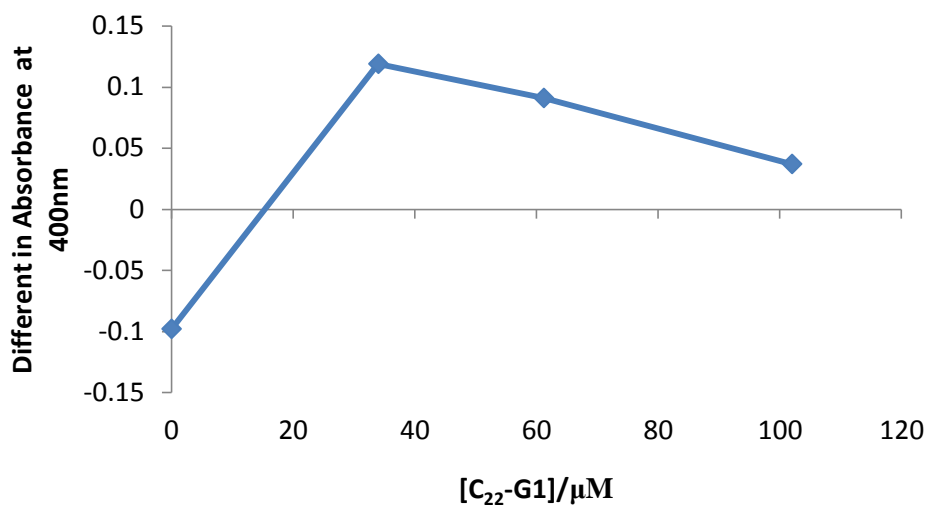


Figure 5.18: Difference in Absorbance of SWCNT in H₂O before and after adding C₂₂-G1 vs [C₂₂-G1] at 4000 RPM

At 2000 RPM, there was still a lot of inhomogeneous material present, leading to lots of light scattering, while at 4000 RPM, even the nanoscale complexes appeared to have been centrifuged out of the sample, leading to low absorbance values. It is well known that centrifugation can lead to sedimentation of larger nanoscale aggregates. As such we believe the assay at 3000 RPM fairly and optimally reflects the ability of C₂₂-G1 to "solubilise" SWCNT into water.

After it was found that sonication for 15 mins and centrifugation at 3000 RPM (1450 g min^{-1}) could be used as a standard procedure when quantifying the SWCNT binding, both C₂₂-G1 and Py-G1 were tested with SWCNT in SHE buffer. The results showed that as the concentration of C₂₂-G1 and Py-G1 increased, there was better uptake SWCNT for C₂₂-G1 (**Figure 5.19**). The result suggested that C₂₂-G1 showed effective uptake of SWCNTs. However, using this assay, Py-G1 could not be seen to uptake SWCNT. It was clear that for C₂₂-G1, SWCNT uptake is detected at concentrations above 25 μM and above. This is in-line with the observed CAC of this self-assembling system. However, it should also be noted that the optical properties of pyrene may be interfering with this assay as it absorbs in the UV-Vis at a similar wavelength.

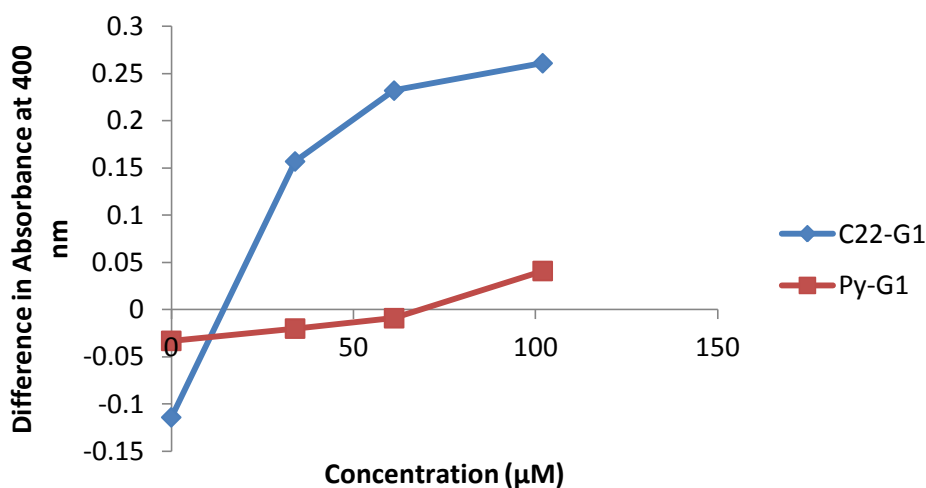


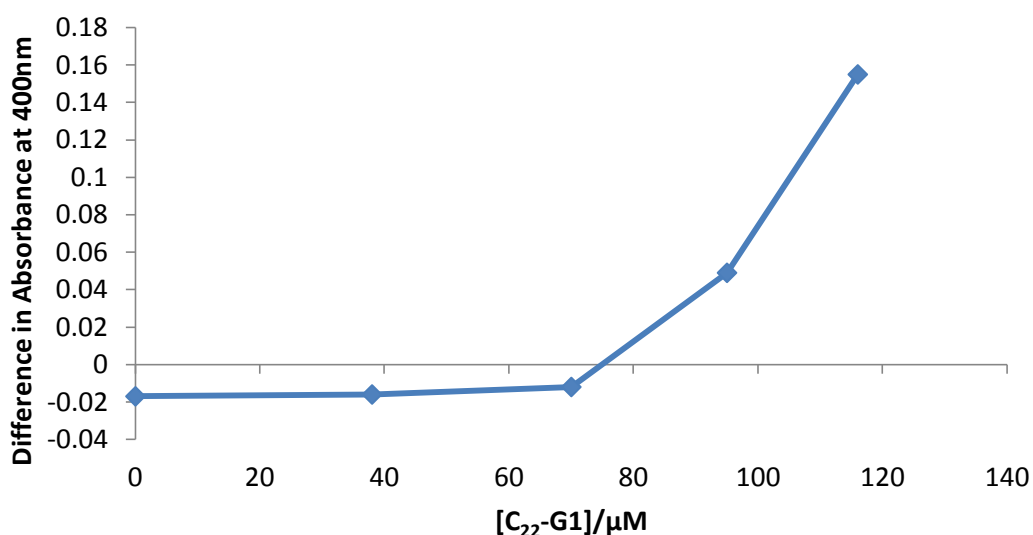
Figure 5.19: Difference in absorbance at 400 nm of SWCNT in SHE buffer before and after adding binder and centrifugation.

5.4.5 CNTs and DNA binding assay of C₂₂-G1

Having demonstrated that C₂₂-G1 was both the most effective DNA binder and the most easily monitored system for CNT binding, we then had to demonstrate the capacity of this system to bind simultaneously to both nanostructures and hence act as a “nanoglue”.

An assay was therefore developed which combined both the CNT binding assay and the DNA binding assay. This should allow monitoring of both DNA and CNT binding together if we see increase in UV-Vis in absorbance at 400 nm (uptake of SWCNTs) and a decrease in fluorescence emission intensity at 590 nm (DNA binding monitored via EthBr displacement) as the concentration of C₂₂-G1 increases.

SWCNT (~5 mg) were therefore added there into five tubes each with 2 ml of EthBr concentration of 5.07 μ M and DNA at 4.0 μ M in SHE buffer in them. They were then sonicated for 15 min, followed by centrifugation at 3000 RPM for 30 min. The solution was carefully transferred to cuvettes for recording and returned to the centrifugation tubes. Aliquots of C₂₂-G1 mixed with in EthBr (5.07 μ M) and DNA (4.0 μ M) in SHE buffer were then added into the 5 tubes respectively and then sonicated for 15 min and centrifuged at 3000 RPM for 30 min and the spectra recorded.



From the data, it is clear that as the concentration of C₂₂-G1 increases, the absorbance difference also increases which suggests some CNT uptake in the present of DNA and EthBr. Notably CNT uptake only appears above dendron concentrations of ca. 70 μ M. This is higher than what was observed in the absence of DNA where uptake was observed from 25 μ M. This might suggest that interaction with DNA limits the ability to bind SWCNTs,. Perhaps by stabilising the aggregates of C₂₂-G1 and limiting

their ability to reorganise and bind to the SWCNTs surface with their hydrophobic chain. Although it is clear that as the concentration increases, this SWCNT binding can still occur.

However, when we compare the fluorescence intensity of free EthBr, EthBr + DNA, EthBr + SWCNTs and EthBr + DNA + SWCNTs (See **Table 5.1**), it became evident that the presence of SWCNT quenched the fluorescence of EthBr. As such the EthBr assay was not valid as a method for quantifying the DNA binding in this case. Hence we needed to find a new method that might enable monitoring of DNA and CNT binding together. As such we turned to transmission electron microscopy (TEM).

	EthBr	EthBr + DNA	EthBr + SWCNT	EthBr + SWCNT + DNA
Fluorescence intensity	65.75	332.6	3.255	3.834

Table 5.1: Fluorescence intensity recorded at 590 nm.

5.4.6 Transmission Electron Microscopy (TEM)

The morphology of the C₂₂-G1 and CNT was characterised by TEM following the deposition of solution-phase aliquots onto a formvar grid, staining with uranyl acetate and drying. C₂₂-G1 appeared to aggregate into micellar assemblies, with approximate diameters of *ca.* 7 nm, as previously reported by Rodrigo *et al.* (**Figure 5.20, left**),⁹³ and the CNT sample we were using could clearly be categorized as a single layer walled (SWCNT) (**Figure 5.20, right**).

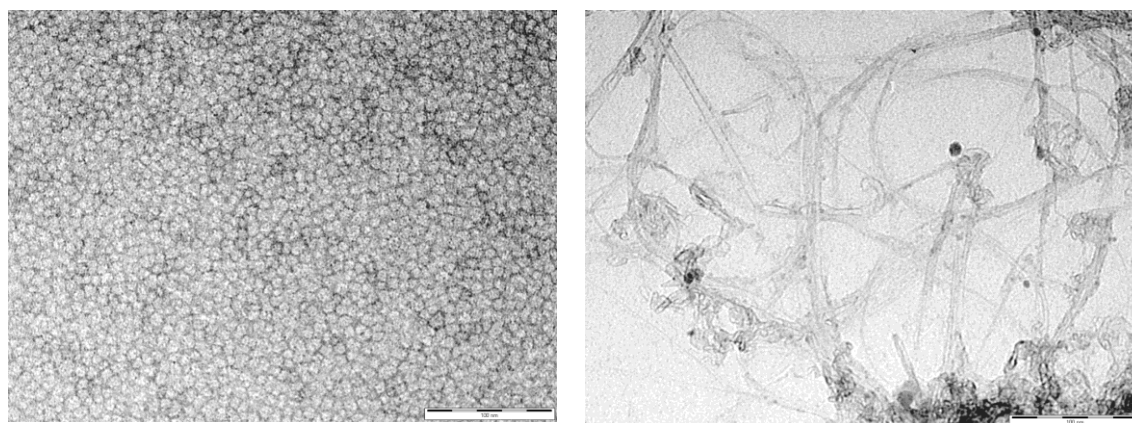


Figure 5.20: TEM image of (left) C₂₂-G1 and (right) CNT (100nm)

The C₂₂-G1 was then imaged in the presence of DNA (**Figure 5.21**). The micellar objects appeared to remain fully intact and co-assemble with the polyanionic components. The nano-aggregate formed had similar morphology as observed when it bound with heparin as reported by Rodrigo *et al.*⁹³ This may suggest the micelles aggregates along the polyanionic backbone of DNA as a consequence of electrostatic interactions (**Figure 5.22**). Indeed these nanoscale aggregates can be considered to result from an effective ionic “close packing” of the two different counter-ionic component. Inpartally, these images demonstrate that the micelle assemblies formed by C₂₂-G1 are not disrupted by the present of DNA, as sometimes happens when such contracts are brought into contract with a polyanion. Indeed, the micelles clearly have a very significant stability even when the ligand surface are bound to nanoscale DNA.

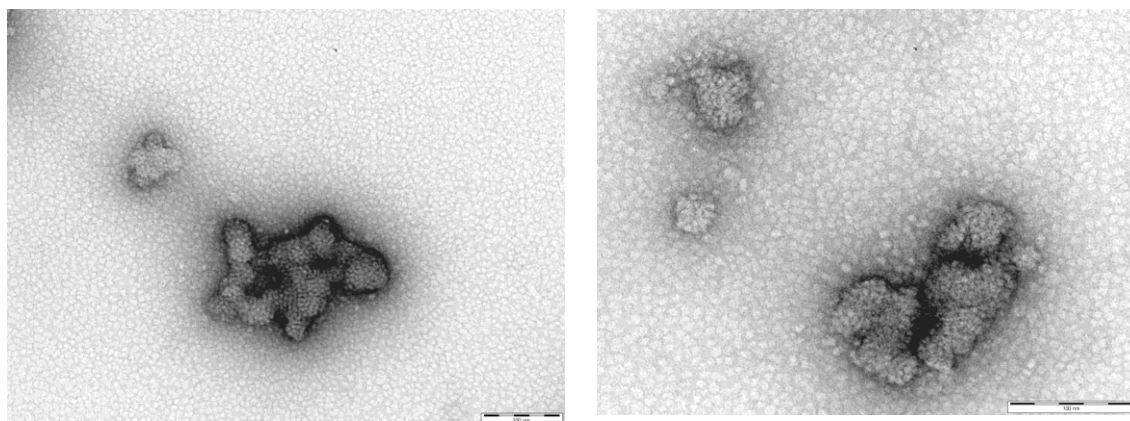


Figure 5.21: TEM of C₂₂-G1 with DNA (100 nm)

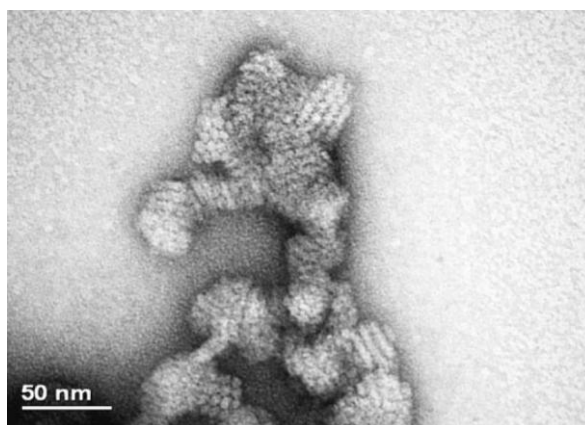


Figure 5.22: TEM of C₂₂-G1 with heparin.⁹³

Bromfield et al. reported modelling of C₂₂-G1 bind binding to heparin in 2014 (**Figure 5.23**).⁴³ They suggested that the larger self-assembled micelles generated by C₂₂-G1 exploit 32 (out of 96) positive charges to constantly bind one heparin chain in an efficient manner. Clearly as more polyanion chains are brought into contact with the micelle they can then satisfy the surface ligands – without disrupting the overall micellar nanostructure.

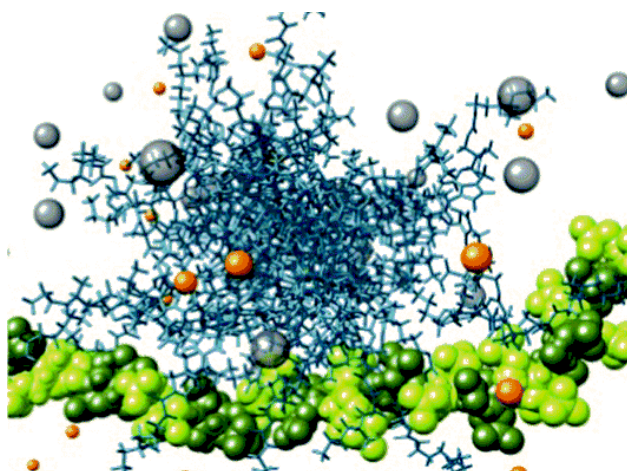


Figure 5.23: Atomistic models of self-assembled C₂₂-G1 is shown as teal sticks, with heparin is in dark olive green (L-iduronic acid) and light green (D-glucosamine) spheres. Water molecules are omitted for clarity while some Na⁺ and Cl⁻ ions are shown as orange and grey spheres, respectively.⁴³

We then investigated for the morphology of C₂₂-G1 in the present of SWCNT. SWCNTs (~5 mg) were weighed out in a tube and C₂₂-G1 in deionised water was added, sonicated for 15 min and centrifuged at 3000 RPM for 30 min. The solution was carefully transferred into a sample vial ready for TEM. The solution was then deposited as solution-phase aliquots onto a formvar grid, staining with uranyl acetate and dried.

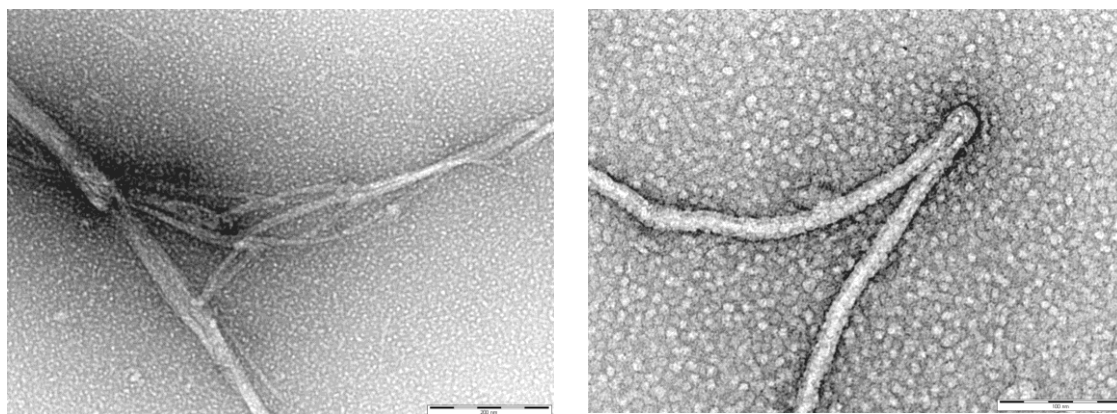


Figure 5.24: TEM image of C₂₂-G1 with CNT (100nm)

From **Figure 5.24**, it was visually clear that the C₂₂-G1 allowed CNT to be taken up into solution as the solution became coloured. We suggest its own hydrophobic tail bound with CNT and the cationic amine surface groups allow dispersion in solution. From the TEM image (**Figure 5.24**), it was evident that C₂₂-G1 was being dispersed on the surface of the CNT which gained a brighter contrast.

Hence, we wanted to test whether TEM help could demonstrate that C₂₂-G1 binds with CNTs via its hydrophobic tail and DNA with the cationic amine surface groups. To the solution of C₂₂-G1 with CNT (1 mL) which was prepared for the TEM image beforehand, was added with 1 ml of DNA solution (0.2 mg/mL). The mixed solution was then deposited in solution-phase aliquots onto a formvar grid, staining with uranyl acetate and dried.

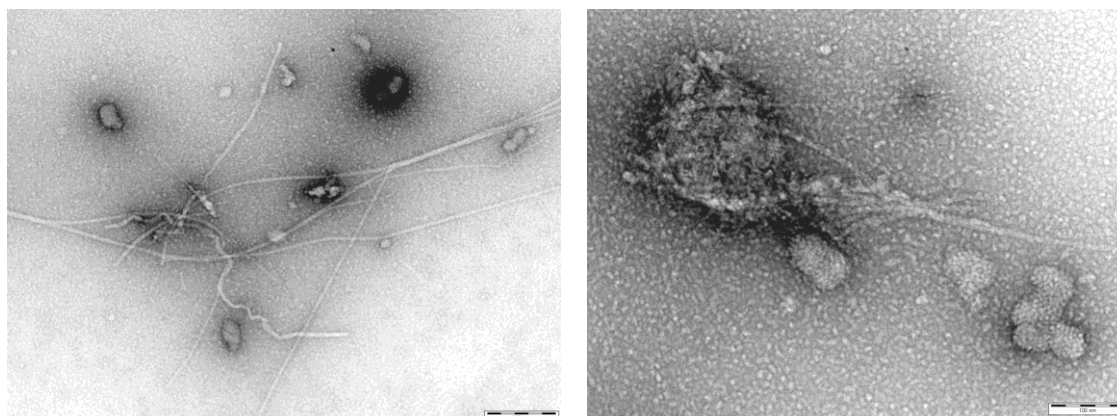


Figure 5.25: TEM image of C₂₂-G1 + CNT + DNA (100 nm)

From **Figure 5.25**, the excess C₂₂-G1 which was not bound with CNTs in **Figure 5.24** was now also bound with the DNA in the solution with clear micelle clustering being observed in the image, like in **Figure 5.21**. This suggested that in order to visualise the binding of all three at the same time, we needed to filter the excess C₂₂-G1 after we bind it with CNT then only the modified nanotubes should bind with DNA for visual characterisation.

The effect of the filtration step was probed on the C₂₂-G1-CNT complexes. SWCNTs (~5 mg) were weighed out and C₂₂-G1 in deionised water was added, then sonicated for 15 min and centrifuged at 3000 RPM for 30 min. The solution was carefully transferred to Amicon Ultra centrifugal filter units, with a regenerated cellulose filter 100 kDa, and centrifuged at 3000 rpm for 10 min, washed three times with deionised water and finally recovered by resuspending in 1 mL of deionised water. The resulting solution was transferred into a sample vial for the TEM. The solution was then deposited in solution-phase aliquots onto a formvar grid, staining with uranyl acetate and drying.

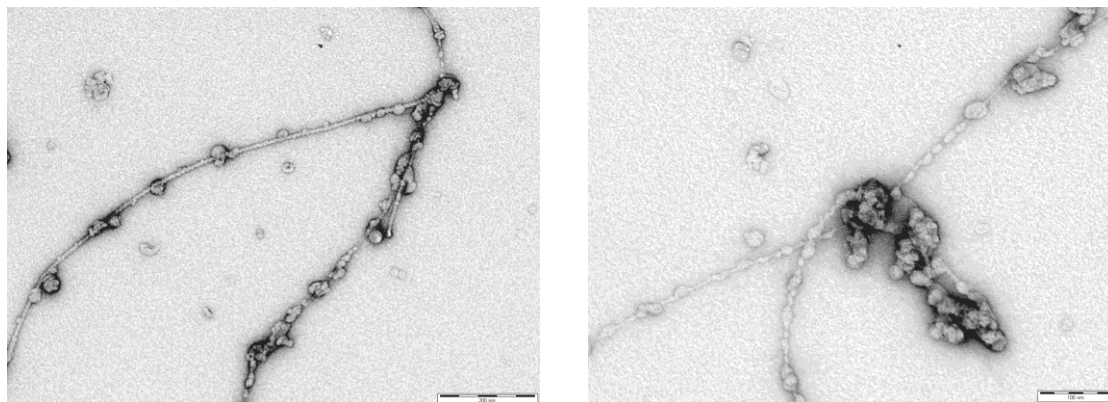


Figure 5.26: TEM image of C₂₂-G1 with CNT after filtration (100nm)

From the TEM image of C₂₂-G1 with CNT (**Figure 5.26**), after the removal of excess C₂₂-G1, it was clear that the C₂₂-G1 was retained mostly in micellar aggregates and surrounded the surface of the CNT. The background “free” C₂₂-G1 micelles observed in **Figure 5.24** are no longer observed and have clearly been removed by the filtration step. Next, to the solution of C₂₂-G1 with CNT after filtration (1 mL), previously prepared for the TEM image, was added DNA solution (0.2 mg/mL), and the mixture was then

deposited in solution-phase aliquots onto a formvar grid, staining with uranyl acetate and dried.

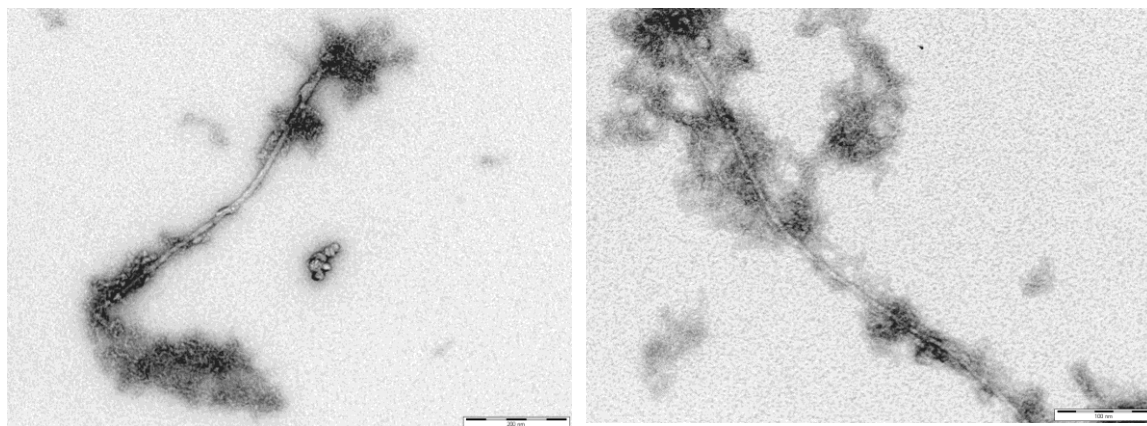


Figure 5.27: TEM image of C₂₂-G1 + CNT + DNA after filtration (100 nm)

From **Figure 5.27**, we could see dark regions corresponding to DNA warping on the surface of CNT. This suggested that our C₂₂-G1 can indeed act as nanoglue that bind DNA and CNT together. Moreover, the micellar aggregates still seem to remain largely intact, connecting the two orthogonal nanostructures together.

We then applied the same method as before for Py-G1 to determine visually whether Py-G1 can act as nanoglue or not. Py-G1 was first imaged in the presence of DNA, and it had similar morphology as did C₂₂-G1 bound with DNA, which suggested that clusters of micellar assemblies of Py-G1 aggregate along the backbone of DNA as a consequence of electrostatic interactions in a “close packed” cation/anion arrangement (**Figure 5.28**).

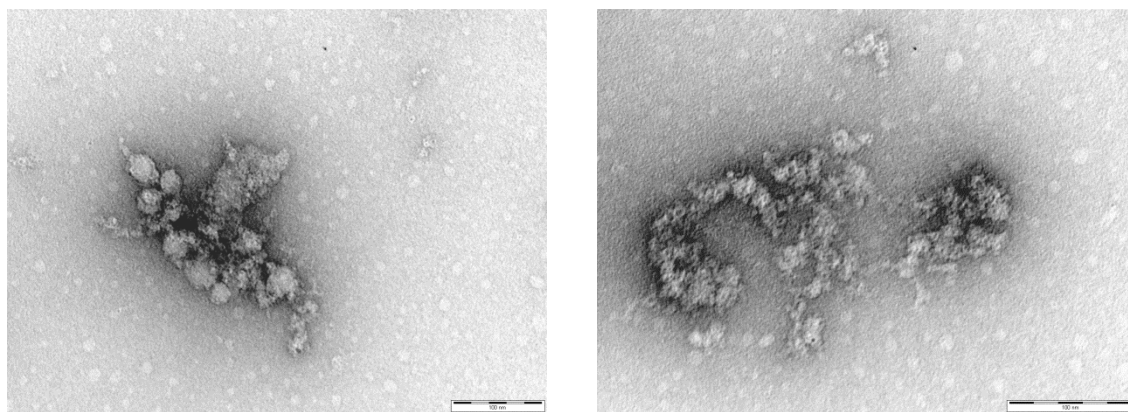


Figure 5.28: TEM image of Py-G1 with DNA (100 nm)

We then studied the morphology of the Py-G1 with CNT using the same method as optimised for C₂₂-G1. From **Figure 5.29**, it was clear that the Py-G1 remained mostly in vesicular or clusters of micellar assemblies and surrounded the surface of the CNT. In contrast to the UV-Vis assay described in Section 5.4.4, this clearly suggests that Py-G1 can indeed uptake SWCNTs and would agree with the view that the optical properties of pyrene were interfering with this previous assay. We can also see a much larger size of Py-G1 assemblies on the surface of the CNT due to the fact that Py-G1 form much bigger assemblies in solution (~10 to 40 nm from DLS) compared with as C₂₂-G1 which forms well-defined micelles with diameters of ca. 9 nm.⁴³

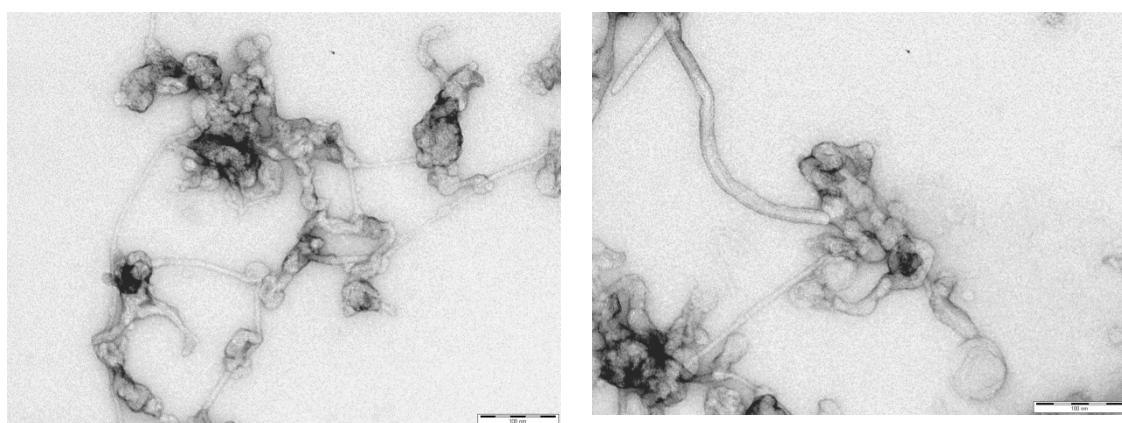


Figure 5.29: TEM image of Py-G1 with CNT after filtration (100nm)

We then probed the ability of Py-G1 act as nanogule to simultaneously bind CNT

and DNA. To the solution of Py-G1 with CNT after filtration (1 mL) which was prepared for the TEM image beforehand, was added with DNA solution and the mixture was then deposited in solution-phase aliquots onto a formvar grid, staining with uranyl acetate and dried.

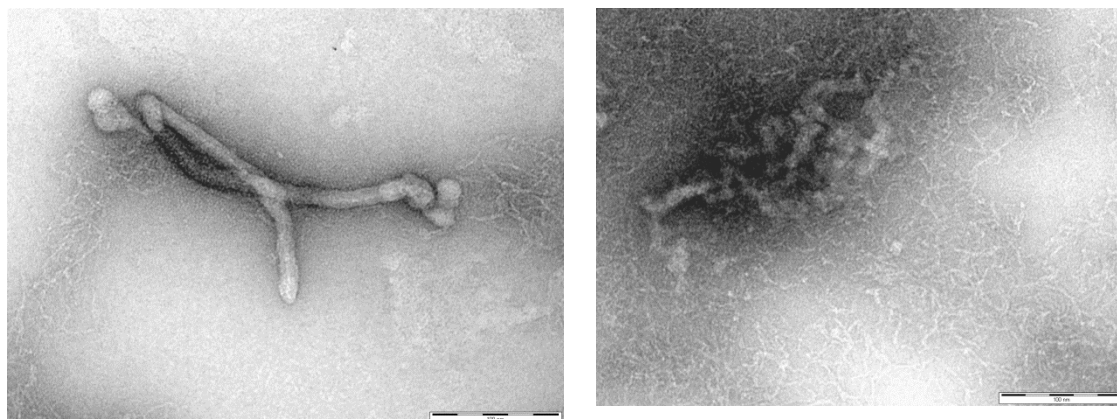


Figure 5.30: TEM image of Py-G1 + CNT + DNA after filtration (100 nm)

From **Figure 5.30**, we could see some evidence of DNA surrounding the surface of CNT. Although the images were not as clear as for C₂₂-G1, this therefore provides some evidence that Py-G1 can also act as a nanoglue that binds DNA and CNT together.

5.5 Summary and future work

C₂₂-G1 was successfully synthesised. After changing the solvent for the click chemistry step we successfully achieved excellent yields for C₂₂-G1. We also revisited the characterisation of this molecule and contributed material for a major publication dealing with this heparin binder.⁴³

Both C₂₂-G1 and Py-G1 self-assemble and bind to DNA and SWCNT respectively. The effect of buffer on the CAC of C₂₂-G1 appeared to be stronger than the CAC of Py-G1. C₂₂-G1 was also more effective than Py-G1 in binding to DNA (lower CE₅₀ and EC₅₀) and SWCNT (higher absorbance differences when increase in concentration of C₂₂-G1 than Py-G1). We suggest this reflects the flexible hydrophobic chain enabling better self-assembly and more responsive binding surfaces than the more rigid pyrene. As such we considered C₂₂-G1 to be our primary candidate to act as nanoglue and

allow the adhesion of these orthogonal nanostructures.

Although our attempt to quantitatively assay simultaneous DNA and SWCNT binding was unsuccessful, it is clear that TEM imaging allow us to monitor the binding of both DNA and CNT. Filtration of the excess binder prior to monitoring simultaneous DNA and CNT binding together was essential. But once this had been done, it could clearly be observed for C₂₂-G1 that the three different nanostructures were being effectively linked together in solution.

As such we consider this as proof-of-principle for the way in which SAMul nanosystems can act to bind more than one nanosystem at the same time, and shows that surface ligands and hydrophobic core can possess orthogonal supramolecular organization, ensuring new interface between different nanoscale material – in this case, nanotubes and DNA.

For future work, it is of interest to move towards to gene delivery experiment for the C₂₂-G1/Py-G1 with DNA and CNT investigate adhesion of other diverse nanostructures, such as graphene/fullene.

Chapter 6 Experimental

6.1 General Materials and Methods

All reagents were obtained from commercial sources and were used without further purification. Sodium salt heparin from porcine intestinal mucosa with a molecular weight between $15,000 \pm 2,000$ Da (1 kU = 1000 units) was obtained from Calbiochem®. Trizma® hydrochloride (Tris HCl) obtained from Sigma Aldrich. Phosphate buffer was obtained from Fisher Scientific. Column chromatography was performed on silica gel 60 (35-70 μm) supplied by Fluka Ltd. Preparative gel permeation chromatography (GPC) was performed on Biobeads SX-1 supplied by Bio-Rad. Thin layer chromatography (TLC) was performed on Merck aluminum-backed plates, coated with 0.25 nm silica gel 60. ^1H , ^{13}C , ^1H - ^1H COSY, ^1H - ^{13}C HSQC and ^1H - ^{13}C HMBC NMR were recorded on a JEOL ECX400 (^1H 400 MHz, ^{13}C 100 MHz) spectrometer. ^1H NMR at 700 Mhz was recorded on a Bruker Avance (16.4 T) 700 MHz. ESI and HR-ESI mass spectra were recorded on a Bruker Daltonics Microtof mass spectrometer. For the acquisition of the UV-vis absorption spectra, a Shimadzu UV2041-PC instrument was used. A Thermo Scientific Heraeus Biofuge Primo was used for centrifugation. IR spectra were measured PerkinElmer Spectrum Two™ IR Spectrometers with ATR-IR. Circular Dichroism was carried out on a Jasco J810 CD Spectrophotometer (150w Xe lamp). Fluorescence emission was measured on a Hitachi F-4500 spectrofluorimeter. All Mal-B solutions were incubated at 50°C for 24 hours prior to use and stored in the dark. For the purpose of calculations, the molecular weight of heparin is assumed as that of the sodiated analogue of the heparin repeat unit (L-iduronic acid and β -D-glucuronic acid), namely $665.40 \text{ g mol}^{-1}$.

6.2 Assay Methods

Pyrene-derivatives Critical Aggregation Concentration (CAC) Assay

A stock solution of the pyrene-derivatives was made up in PBS/SHE buffer at various concentrations. Aliquots of the stock solution were taken and diluted with PBS/SHE to the desired concentration in a 1 ml assay volume. The fluorescence emission was measured on a Hitachi F-4500 spectrofluorimeter using an excitation wavelength of

363 nm. Fluorescence intensity was extracted at 495 nm. Experiments were performed in triplicate.

Dynamic light scattering (DLS)

Dynamic light scattering data were measured at 1 mg/mL using a Zetasizer Nano (Malvern Instruments Ltd., Worcestershire, UK), based on the principle of measurement of the backscattered light fluctuations at an angle of 173° and the calculation of an autocorrelation function. Data were recorded from 15–20 runs per single measurement, each of which was carried out at 25°C using folded capillary cells (DTS 1060). Monomer solutions were freshly prepared by dissolving an appropriate amount of dry compound in filtered aqueous media (e.g. 10 mM Tris HCl, 150 mM NaCl). All samples were agitated and incubated at 25°C for 10 minutes prior to measurement. Data are reported based on volume distribution.

TEM Imaging

Dendron solutions were prepared in clean water at 1 mg/mL. Samples imaged in the presence of heparin and DNA were introduced at 1 mg/ mL. Once prepared, aliquots of each solution were loaded on a formvar grid, negatively stained with uranyl acetate and allowed to dry before imaging. Image taken from FEI Tecnai 12 BioTWIN G2 transmission electron microscope with SIS CCD camera

Heparin Sensing Assay Using Fluorescence

Aliquots of dendron solution were made up to 10 ml in volumetric flasks with 10 mM Tris HCl with 150 mM NaCl buffer solution or 12.5% Human Serum in 20 mM Tris HCl buffer or 100% Human Serum to yield stock solutions of the sensor. 5 mL of this solution was then added to heparin to yield a stock solution of sensor/heparin. 1 ml of stock sensor solution was added to the cuvette and titrated with stock sensor/heparin solution so that the cuvette ended up with 2 ml solution. The fluorescence emission was measured on a Hitachi F-4500 spectrofluorimeter using an excitation wavelength of 363 nm. Fluorescence intensity was extracted at 383 and 495

nm. Experiments were performed in triplicate.

Nile Red Encapsulation¹⁶¹

A 2.5 mM Nile Red stock solution was made in EtOH. A dendron stock solution was made up in PBS/SHE buffer at various concentrations. Aliquots of the stock solution were taken and diluted with PBS/SHE to the desired concentration in a 1 ml assay volume. Nile red (1 μ l) was added and the fluorescence emission was measured on a Hitachi F-4500 spectrofluorimeter using an excitation wavelength of 550 nm. Fluorescence intensity was recorded at 635 nm. Experiments were performed in triplicate.

Ethidium Bromide Displacement^{211, 212}

A solution of Calf Thymus DNA (8.0 μ M) was prepared in SHE Buffer (2 mM HEPES, 0.05 mM EDTA, 150mM NaCl) at pH 7.5. Ethidium bromide was diluted with SHE Buffer to give a final concentration of 10.14 μ M. Background ethidium bromide fluorescence was measured at 5.07 μ M. The dendron stock solution, at varying concentration depending on the charge of the dendron, was prepared in a 50:50 solution of the ethidium bromide and DNA solutions to give a final EthBr concentration of 5.07 μ M and DNA at 4.0 μ M with respect to one DNA base (M_r 330 g mol^{-1}). Appropriate amounts of the dendron solution were added to 2 ml of a stock containing EthBr (5.07 μ M) and DNA (4.0 μ M) to achieve the desired N:P ratio. The fluorescence was measured on a Hitachi F-4500 spectrofluorimeter using an excitation wavelength of 540 nm. Fluorescence intensity was recorded at 595 nm. The fluorescence values were normalised to a solution containing only DNA (4.0 μ M) and EthBr (5.07 μ M). Experiments were performed in triplicate.

Heparin Displacement Assay using Mal-B In Buffer

A cuvette containing 2 mL of MalB (25 μ M), heparin (27 μ M) and NaCl (150 mM) in Tris HCl (10 mM) was titrated with binder stock solution to give the cuvette suitable binder-heparin charge ratios. The binder stock solution was composed of the original MalB/heparin/NaCl/Tris HCl stock solution endowed additionally with a concentration

of binder such that, after addition of 10 μL binder stock, the cuvette charge ratio (+ : -) is increased by 0.037. After each addition, the cuvette was inverted to ensure good mixing and the absorbance at 615 nm was recorded against a Tris HCl (10 mM) baseline. Absorbance was normalised between a solution of MalB (25 μM), NaCl (150 mM) in Tris HCl (10 mM) and one containing MalB (25 μM), heparin (27 μM), NaCl (150 mM) in Tris HCl (10 mM).

Binding of Heparin to Mal-B.

A cuvette was charged with 2 mL of a stock solution of MalB (25 μM) in NaCl (150 mM) and Tris HCl (10 mM) or phosphate buffer (10 mM). This solution was titrated with a stock solution of heparin (200 μM) in MalB (25 μM), NaCl (150 mM) and Tris HCl (10 mM) or phosphate buffer (10 mM) to a final cuvette volume of 3 mL. The absorbance at 615 nm was recorded after each addition. Experiments were performed in triplicate.

NMR method

^1H and ^1H - ^{13}C HSQC NMR heparin spectra were obtained with 100mg of sodiated heparin in 600 μL of D_2O on a JEOL ECX400 (^1H 400 MHz, ^{13}C 100 MHz) spectrometer.

^1H and ^1H - ^{13}C HSQC NMR Mal-B spectra were obtained with 40mg of Mal-B in 600 μL of D_2O on a JEOL ECX400 (^1H 400 MHz, ^{13}C 100 MHz) spectrometer.

^1H NMR Mal-B spectra at low concentration were obtained with 0.4 mg of Mal-B in 600 μL of D_2O in selected solvent buffer on a JEOL ECX400 (^1H 400 MHz) spectrometer.

NMR titration study for Mal-B with increasing heparin concentration.

Mal-B stock solution was made up in buffer solution in D_2O at 0.66 mg /mL to yield a stock solution of Mal-B. This solution was then added to heparin to yield a stock solution of Mal-B/heparin which was 1:1, (w/w). Aliquots of the stock solution of Mal-B were taken and diluted with the stock solution of Mal-B/heparin to provide the desired ratio in a 600 μL volume in NMR tube.

NMR titration study for SAMul Heparin Binder at 2mg/ mL with increasing heparin concentration.

A dendron stock solution was made up in D₂O at 2mg /mL to yield a stock solution of dendron. This solution was then added to heparin to yield a stock solution of dendron /heparin which was 1:1, (w/w). Aliquots of the stock solution of dendron were taken and diluted with stock solution of dendron/heparin to give the desired ratio in a 600 µL volume in NMR tube.

NMR titration study for heparin at 2mg/ mL with increasing SAMul Heparin Binder concentration.

A heparin stock solution was made up in D₂O at 2mg /ml to yield a stock solution of heparin. This solution was then added to dendron to yield a stock solution of heparin/dendron which are 1:1, w/w. Aliquots of the stock solution of heparin were taken and diluted with stock solution of heparin/dendron to give the desired ratio in a 600 µL volume in NMR tube.

Optimised SWCNT uptake assay

SWCNT (~5 mg) was added into five tubes each with 2 ml of SHE buffer. They were then sonicated for 15 min, followed by centrifugation at 3000 RPM for 30 min. The solution was carefully transferred to cuvettes for recording by UV-vis absorption spectroscopy and put back into the tubes. Aliquots of dendron solution in SHE buffer were then added into the 5 tubes respectively and sonicated for 15 min and centrifuged at 3000 RPM for 30 min and the spectra recorded.

CNT and DNA binding assay

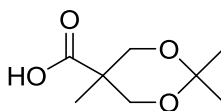
SWCNT (~5 mg) were added there into five tubes each with 2 ml of EthBr concentration of 5.07 µM and DNA at 4.0 µM in SHE buffer in them. They were then sonicated for 15 min, followed by centrifugation at 3000 RPM for 30 min. The solution was carefully transferred to cuvettes for recording and returned to the centrifugation tubes. Aliquots of dendron solution mixed with in EthBr (5.07 µM) and DNA (4.0 µM) in SHE buffer were then added into the 5 tubes respectively and then sonicated for 15 min and

centrifuged at 3000 RPM for 30 min and the spectra recorded.

TEM imaging for CNT and DNA binding assay

SWCNTs (~5 mg) were weighed out and C₂₂-G1 in deionised water was added, then sonicated for 15 min and centrifuged at 3000 RPM for 30 min. The solution was carefully transferred to an Amicon Ultra centrifugal filter units, with a regenerated cellulose filter 100 kDa, and centrifuged at 3000 rpm for 10 min, washed three times with deionised water and finally recovered by resuspending in 1 mL of deionised water. The resulting solution was transferred into a sample vial and added to DNA solution (0.2 mg/mL). The mixture was then deposited in solution-phase aliquots onto a formvar grid, stained with uranyl acetate and dried.

Synthesis of Isopropylidene-2,2-bis(hydroxymethyl) propionic acid.⁹⁴⁻⁹⁸



Molecular Formula = C₈H₁₄O₄

Molecular Weight = 174.19

2,2-Bis(hydroxymethyl) propionic acid (15.0 g, 111.8 mmol), 2,2-dimethoxypropane (20 ml, 162.7 mmol) and *p*-toluene sulfonic acid monohydrate (1.0 g, 5.3 mmol) were dissolved in acetone (60 ml) and the reaction mixture was stirred at room temperature for 3 h. The acid catalyst was neutralised with NH₄OH in EtOH (1 ml, 50:50) and stirred for 10 minutes to allow a precipitate to form. The solvent was removed *in vacuo* and the resulting product was dissolved in DCM and extracted with H₂O (2 x 30 ml). The organic phase was dried over MgSO₄, filtered and the filtrate evaporated *in vacuo* yielding the product as white crystals (10.49 g, 59.9 mmol, 54%).

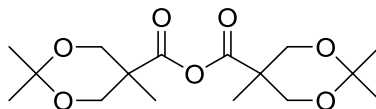
$R_f = 0.47$ (9:1 DCM: MeOH).

¹H NMR (400 MHz, CDCl₃) δ: 11.82 (br s, CO₂H, 1H); 4.18 (d, CH_{ax}H_{eq}O, ²J = 12, 2H); 3.66 (d, CH_{ax}H_{eq}O, ²J = 12, 2H); 1.44 (s, OC(CH₃)₂, 3H); 1.41 (s, OC(CH₃)₂, 3H); 1.21 (s, CH₃, 3H).

¹³C NMR (100 MHz, CDCl₃) δ: 180.3 (CO₂H); 98.3 (OC(CH₃)₂); 65.8 (2 x CH₂O); 41.7, (quaternary C); 25.2, 21.0, 18.4 (3 x CH₃).

ESI-MS: Calcd. $[M+Na]^+(C_8H_{14}NaO_4)$ $m/z = 197.0784$. Found $[M+Na]^+ m/z = 197.0793$.

Synthesis of Isopropylidene-2,2-bis(hydroxymethyl) propionic anhydride.⁹⁴⁻⁹⁸



Molecular Formula = $C_{16}H_{26}O_7$

Molecular Weight = 330.37

Isopropylidene-2,2-bis(oxymethyl)propionic acid (9.0 g, 51.6 mmol) was dissolved in DCM (50 ml), and a solution of DCC (5.3 g, 25.8 mmol) dissolved in DCM (40 ml) was added. The reaction mixture was stirred at room temperature for 3 h and then filtered through celite. The solvent was removed *in vacuo* and the residue taken up in EtOAc. Residual DCU was then removed by refiltering the solution through a glass filter. The filtrate was evaporated *in vacuo* yielding a pure product as a viscous oil (7.61 g, 23.0 mmol, 45%).

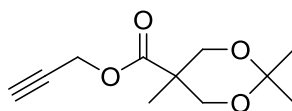
$R_f = 0.38$ (9:1 DCM: MeOH)

1H NMR (400 MHz, $CDCl_3$) δ : 4.18 (d, $\underline{CH}_{ax}\underline{H}_{eq}O$, $^2J = 12$, 4H); 3.68 (d, $\underline{CH}_{ax}\underline{H}_{eq}O$, $^2J = 12$, 4H); 1.41 (s, CH_3 , 6H); 1.37 (s, CH_3 , 6H); 1.20 (s, CH_3 , 6H).

^{13}C NMR (100 MHz, $CDCl_3$) δ : 169.3 (C=O); 98.1 ($O\underline{C}(CH_3)_2$); 65.4 (2 x CH_2O); 43.4, ($C(O)\underline{C}(CH_3)(CH_2)_2$); 25.5, 21.1, 17.3 (3 x CH_3).

ESI-MS: Calcd. $[M+Na]^+(C_{16}H_{26}NaO_7)$ $m/z = 353.1571$. Found $[M+Na]^+ m/z = 353.1576$.

Synthesis of Propyne isopropylidene-2,2-bis(hydroxymethyl) propionate.⁹⁴⁻⁹⁸



Molecular Formula = $C_{11}H_{16}O_4$

Molecular Weight = 212.24

Propargyl alcohol (0.73 ml, 12.6 mmol) and DMAP (0.23 g, 19 mmol) were dissolved in pyridine (3.06 ml, 3 equivalents) and DCM (10 ml). Isopropylidene-2,2-bis(hydroxymethyl) propionic anhydride (5.0 g, 15.13 mmol) dissolved in DCM (20 ml) was

then added. The reaction mixture was stirred overnight at room temperature. The reaction was quenched with H₂O (5 ml) and diluted with DCM (50 ml). The solution was washed with NaHSO₄ (3 x 30 ml, 1.33 M), 10% Na₂CO₃ (3 x 30 ml) and sat. brine (30 ml). The organic phase was dried over MgSO₄, filtered and the filtrate evaporated *in vacuo* yielding a product as a pale yellow oil (3.53 g, 16.6 mmol, 100 %).

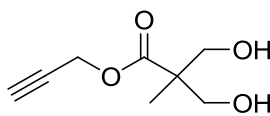
$R_f = 0.87$ (9:1 DCM: MeOH)

¹H NMR (400 MHz, CDCl₃) δ : 4.69 (d, CH₂C≡CH, ⁴J = 2.6, 2H); 4.16 (d, CH_{ax}H_{eq}O, ²J = 11.9, 2H); 3.61 (d, CH_{ax}H_{eq}O, ²J = 11.9, 2H); 2.45 (t, C≡CH, ⁴J = 2.6, 1H); 1.38 (s, CH₃, 3H); 1.34 (s, CH₃, 3H); 1.16 (s, CH₃, 3H).

¹³C NMR (100 MHz, CDCl₃) δ : 173.3 (C=O); 97.9 (OC(CH₃)₂); 77.4 (C≡CH); 74.9 (C≡CH); 65.7 (CH₂O); 52.2 (CH₂C≡CH); 41.7 (C(O)C(CH₃)(CH₂)₂); 24.5, 22.4, 18.3 (3 x CH₃).

ESI-MS: Calcd. [M+Na]⁺ (C₁₁H₁₆NaO₄) $m/z = 235.0941$. Found. [M+Na]⁺ $m/z = 235.0947$.

Synthesis of Propyne-[G1]-OH⁹⁴⁻⁹⁸



Molecular Formula = C₈H₁₂O₄

Molecular Weight = 172.18

Propyne-[G1]-isopropylidene (3.41 g, 16.1 mmol) was dissolved in MeOH (115 ml, 25 mg/ml) and concentrated H₂SO₄ (2.3 ml, 2% v/v) was added. After stirring overnight at room temperature the reaction mixture was neutralised with NH₄OH in MeOH (8 ml, 1:1), upon which a white precipitate of ammonium sulfate forms. The mixture was stirred for 30 minutes and the salt was then removed by filtering the solution through celite and the filtrate evaporated *in vacuo*. The crude product was taken up in CHCl₃ and filtered to remove any further impurities. The solvent was then removed *in vacuo* yielding a pure product as a yellow oil (2.41 g, 14.00 mmol, 92%).

$R_f = 0.45$ (9:1 DCM: MeOH)

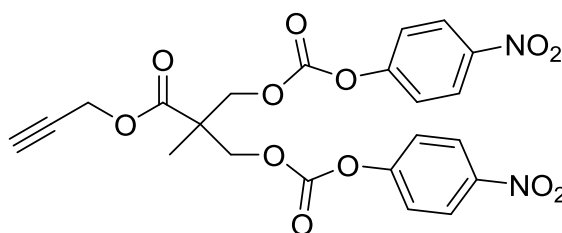
¹H NMR (400 MHz, CDCl₃) δ : 4.66 (d, CH₂C≡CH, ⁴J = 2.4, 2H); 3.80 (d, CH_aH_bOH, ²J = 11.3, 2H); 3.65 (d, CH_aH_bOH, ²J = 11.3, 2H); 2.49 (t, C≡CH, ⁴J = 2.4, 1H); 1.05 (s, CH₃, 3H).

¹³C NMR (100 MHz, CDCl₃) δ : 175.0 (C=O); 77.3 (C≡CH); 75.2 (C≡CH); 67.6 (CH₂OH);

52.4 ($\text{CH}_2\text{C}\equiv\text{CH}$); 49.3 ($\text{C}(\text{O})\text{C}(\text{CH}_3)(\text{CH}_2)_2$); 19.0 (CH_3).

ESI-MS: Calcd. $[\text{M}+\text{Na}]^+$ ($\text{C}_8\text{H}_{12}\text{NaO}_4$) $m/z = 195.0628$. Found. $[\text{M}+\text{Na}]^+ m/z = 195.0623$.

Synthesis of Propyne-[G1]- *p*-nitrophenyl carbonate⁹³



Molecular Formula = $\text{C}_{22}\text{H}_{18}\text{N}_2\text{O}_{12}$

Molecular Weight = 502.38

Propyne-[G1]-OH (2.00 g, 11.62 mmol) was dissolved in dry dichloromethane (DCM, 30 ml) and pyridine (5.46 ml, 67.8 mmol) was added, followed by *p*-nitrophenylchloroformate (9.37 g, 46.48 mmol) dissolved in dry DCM (100 ml). The reaction mixture was stirred overnight at room temperature under a nitrogen atmosphere. The mixture was then diluted with DCM (50 ml) and washed with NaHSO_4 (2 x 50ml, 1.33M) and sat. brine (50 ml). The organic phase was dried over MgSO_4 , filtered and the filtrate evaporated *in vacuo* to provide the crude product as a white solid (8.2 g). 500 mg of crude product was purified by GPC (DCM) to yield a pure product as an off-white solid (210 mg, 0.42 mmol, 59 %).

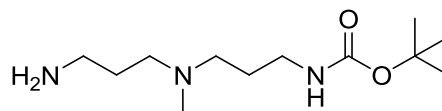
$R_f = 0.46$ (DCM, UV).

^1H NMR (400MHz, CDCl_3) δ : 8.27 (d, $\text{CHC}(\text{NO}_2)\text{CH}$, J 9.2 Hz, 2H); 8.26 (d, $\text{CHC}(\text{NO}_2)\text{CH}$, J 9.2 Hz, 2H); 7.38 (d, *p*-nitrophenyl H, J 9.2 Hz, 2H); 7.37 (d, *p*-nitrophenyl H, J 9.2 Hz, 2H); 4.80 (d, $\text{CH}_2\text{C}\equiv\text{CH}$, $J = 2.4$ Hz, 2H); 4.60 (d, CH_2O , J 11.2 Hz, 2H); 4.50 (d, CH_2OH , $J = 11.2$ Hz, 2H); 2.51 (t, $\text{C}\equiv\text{CH}$, $J = 2.4$ Hz, 1H); 1.43 (s, CH_3 , 3H).

^{13}C NMR (CDCl_3 , 100MHz) δ : 17.0 (C=O); 155.2 (OC=O); 152.1 145.5, 125.33121.7 (4x ArC); 75.7 ($\text{C}\equiv\text{CH}$); 69.0 (CH_2O), 53.2 ($\text{CH}_2\text{C}\equiv\text{CH}$); 46.6($\text{C}(\text{O})\text{C}(\text{CH}_3)(\text{CH}_2)_2$); 17.6 (CH_3).

ESI-MS: Calcd. $[\text{M}+\text{H}]^+$ ($\text{C}_{22}\text{H}_{19}\text{N}_2\text{O}_{12}$) $m/z = 503.0933$; Obs. $[\text{M}+\text{H}]^+ m/z = 503.0944$.

Synthesis of *tert*-Butyl 3-((3-aminopropyl)(methyl)amino)propyl carbamate⁴



Molecular Formula = C₁₂H₂₇N₃O₂

Molecular Weight = 245.36

N,N-di-(3-aminopropyl)-*N*-methylamine (50 ml, 310 mmol) was dissolved in THF (250 ml) and cooled to 0°C. Di-(*tert*-butyl)dicarbonate (25 g, 110 mmol) which dissolved in THF (50 ml) was added drop-wise over 2 h. The reaction was then quenched with 25 ml of water. The solvent was removed *in vacuo* and the residue was taken up in aqueous NaOH (pH>10) and extracted with DCM. The organic layers were then washed with citrate (pH 4-5). The water layers were combined and basified to pH >10 with 1 M NaOH. The mono-protected product was then extracted with DCM. The organic phases were combined, dried over MgSO₄, filtered and the filtrate evaporated *in vacuo* yielding the product as a colourless oil (8.5 g, 34.6 mmol, 31% with respect to di-(*tert*-butyl)dicarbonate).

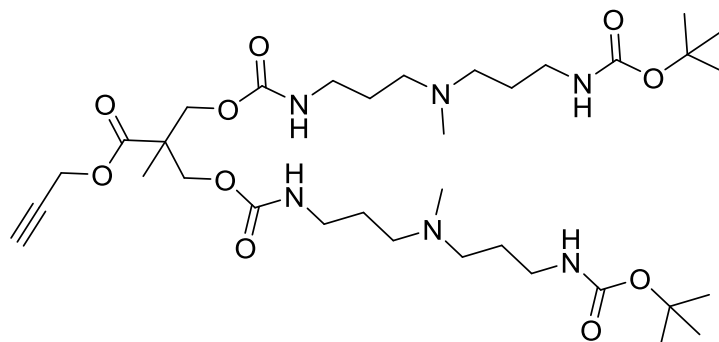
*R*_f = 0.3 (4:1 MeOH: aqueous ammonia).

¹H NMR (400 MHz, DMSO-d₆) δ: 6.79 (br t, ³*J* = 5.6, NH, 1H); 2.89 (q, CH₂NHCO, ³*J* = 6.8 Hz, 2H); 2.53 (t, CH₂NH₂, ³*J* = 6.8 Hz, 2H); 2.26 (t, CH₂N(CH₃), ³*J* = 6.8 Hz, 2H); 2.22 (t, CH₂N(CH₃), ³*J* = 6.8 Hz, 2H); 2.08 (s, N(CH₃), 3H); 1.52 (q, CH₂CH₂NH₂, ³*J* = 6.8 Hz, 2H); 1.44 (q, CH₂CH₂NCH₃, ³*J* = 6.8 Hz, 2H); 1.35 (s, 9H, C(CH₃)₃).

¹³C NMR (100 MHz, DMSO-d₆) δ: 155.2 (CONH); 77.2 (C(CH₃)₃); 55.6, 55.4 (CH₂N(CH₃)); 41.7 (N(CH₃)); 39.8 (CH₂NHCO); 38.3 (CH₂NH₂); 30.5 (CH₂CH₂ N(CH₃)); 28.2 (C(CH₃)₃); 27.7 (CH₂CH₂NH₂).

ESI-MS: Calcd. [M+H]⁺ (C₁₂H₂₈N₃O₂) *m/z* = 246.2176. Found [M+H]⁺ *m/z* = 246.2186.

Synthesis of Propyne-[G1]-mono-Boc-DAPMA⁹³



Molecular Formula = C₃₄H₆₂N₆O₁₀

Molecular Weight = 714.45

A solution of propyne-[G1]- *p*-nitrophenyl carbonate (210 mg, 0.42mmol) in dry DCM (15 ml) was added to an excess of *tert*-Butyl 3-((3aminopropyl)(methyl)amino) propyl carbamate (615.3 mg, 2.52mmol) dissolved in dry DCM (20 ml). A solution of DMAP (51.03 mg, 0.42 mmol, 1 equivalent) and DIPEA (108.15 mg, 0.84mmol, 2 equivalents) in dry DCM (40 ml) was added and the reaction mixture was stirred for 48 hours under a nitrogen atmosphere. The solvent was then evaporated *in vacuo* to yield the crude product as a yellow oil. The crude product was purified by gel permeation chromatography to give the pure product as an orange foam (270 mg, 0.38 mmol, 90%).

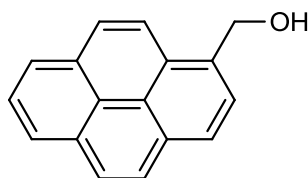
R_f = 0.65 (95:5 MeOH:NH₄OH).

¹H NMR (400MHz, CDCl₃) δ : 6.03 (br s, NH, 2H); 5.40 (br s, NH, 2H); 4.68 (s, CH₂C≡CH, 2H); 4.25-4.11 (m, CH₂O, 4H); 3.26-3.09 (m, CH₂NH, 8H); 2.48 (t, C≡CH, J = 2.4Hz, 1H); 2.44-2.33 (m, 2x N(CH₃), 6H), 1.85-1.70 (m, CH₂CH₂NH, 4H); 1.40 (s, C(CH₃)₃, 18H); 1.22 (s, CH₃, 3H).

¹³C NMR (CDCl₃, 100MHz) δ : 172.5 (C=O), 156.0 (C=ONH); 78.8 (C(CH₃)₃); 77.2 (C≡CH); 75.1 (C≡CH); 65.5 (CH₂O); 55.3, 55.7 (CH₂N(CH₃)); 52.3 (CH₂C≡CH); 46.8 (C(O)C(CH₃)(CH₂)₂); 41.4 (N(CH₃)); 39.8, 38.9 (CH₂NH); 28.45 (C(CH₃)₃); 26.8, 26.1 (CH₂CH₂NH, CH₂CH₂N(CH₃)); 17.8 (CH₃).

ESIMS: Calcd. [M+H]⁺ (C₃₄H₆₃N₆O₁₀) m/z = 715.4600; Obs. [M+H]⁺ m/z = 715.4596.

Synthesis of 1-Pyrenemethanol¹⁰⁰



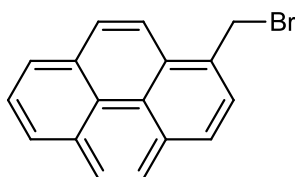
Molecular Formula = C₁₇H₁₂O

Molecular Weight = 232.28

1-Pyrenecarboxaldehyde (0.50 g, 2.2 mmol) was stirred at 0 °C in THF. A solution of NaBH₄ (0.25 g, 6.5 mmol) in 100% ethanol (15 mL) was prepared and ten drops of 1 M NaOH was added. This solution was added to the aldehyde and stirred at 0 °C for 15 min, which changed from a yellow-green color to milky-white. The mixture was quenched with 10% HCl (v/v), diluted with water (50 mL) and extracted with CH₂Cl₂ (3 × 30 mL). The combined organic fractions were washed with NaHCO₃ and water successively (30 mL each), and dried over MgSO₄. Filtration and evaporation yielded the desired alcohol, (0.494 g, 2.13 mmol, 97%).

¹H NMR (400MHz, CDCl₃) δ: 8.05-8.38 (m, 9H, Ar-H); 5.41 (s, 2H, ArCH₂);

Synthesis of 1-Bromomethyl pyrene¹⁰⁰



Molecular Formula = C₁₇H₁₁Br

Molecular Weight = 295.17

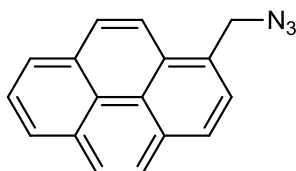
1-Pyrenemethanol (0.487 g, 2.09 mmol) was taken in toluene (60 mL). The resulting suspension was cooled to 0°C and PBr₃ (0.24 mL, 2.48 mmol) was added to it drop wise. The reaction mixture was stirred at 0°C for 1 h and at room temperature for 12 h. After the reaction was complete, saturated Na₂CO₃ (50 mL) was added to it slowly under ice-cold condition, resulting in the formation of two layers. The toluene layer was separated, passed over Na₂SO₄, after which the solvent was removed to give a yellowish solid product (0.574g, 1.94 mmol, 93 %). This product was used directly for

the next step without further purification.

^1H NMR (400MHz, CDCl_3) δ : 5.26 (s, 2H, ArCH_2); 8.02-8.40 (m, 9H, Ar-H).

^{13}C NMR (100MHz, CDCl_3) δ : 132.0, 131.2, 130.8, 129.1, 128.2, 128.0, 127.7, 127.3, 126.3, 125.6, 125.6, 125.1, 124.9, 124.6, 122.8 (Ar-C); 32.2 (Ar- CH_2)

Synthesis of 1-Azidomethyl pyrene¹⁰⁰



Molecular Formula = $\text{C}_{17}\text{H}_{11}\text{N}_3$

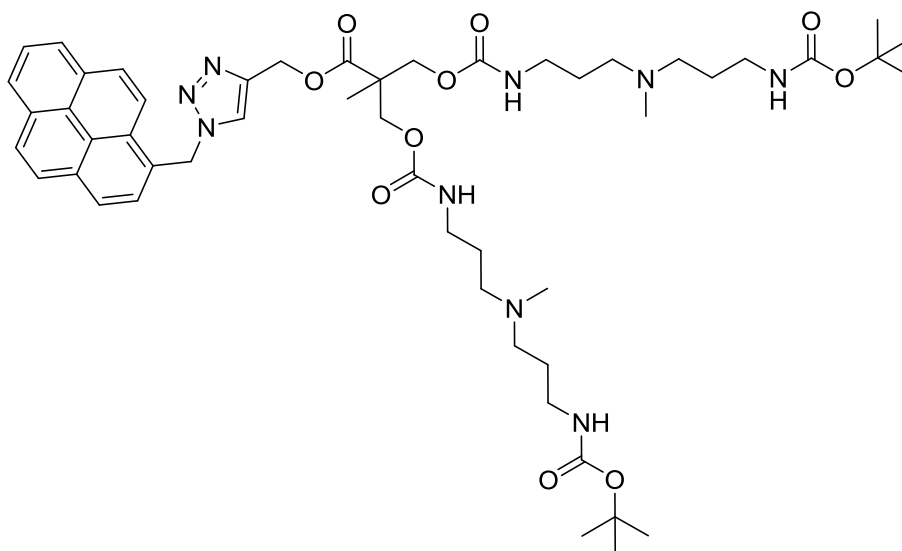
Molecular Weight = 257.29

1-Bromomethyl pyrene (0.564 g, 1.91 mmol) was dissolved in 35 mL of dry DMF. Then NaN_3 (0.496 g, 7.64 mmol) was added to it and the reaction mixture was stirred at 50 °C for 5 h. After the reaction was complete, 20 mL of H_2O was added to it and the contents were extracted with EtOAc. The EtOAc layer was washed with brine, passed over Na_2SO_4 and purified on a silica column using petroleum ether and EtOAc as the eluent to get the yellow solid product (0.476g, 1.85 mmol, 97 %).

^1H NMR (400MHz, CDCl_3) δ : 5.04 (s, 2H, ArCH_2); 7.98-8.25 (m, 9H, Ar-H).

^{13}C NMR (100MHz, CDCl_3) δ : 131.7, 131.2, 130.7, 129.2, 128.4, 128.2, 127.9, 127.4, 127.3, 126.2, 125.6, 125.5, 125.0, 124.6, 122.6 (Ar-C); 53.1 (Ar- CH_2)

Synthesis of Py-G1-Boc



Molecular Formula = C₅₆H₁₀₇N₉O₁₀

Molecular Weight = 1065.81

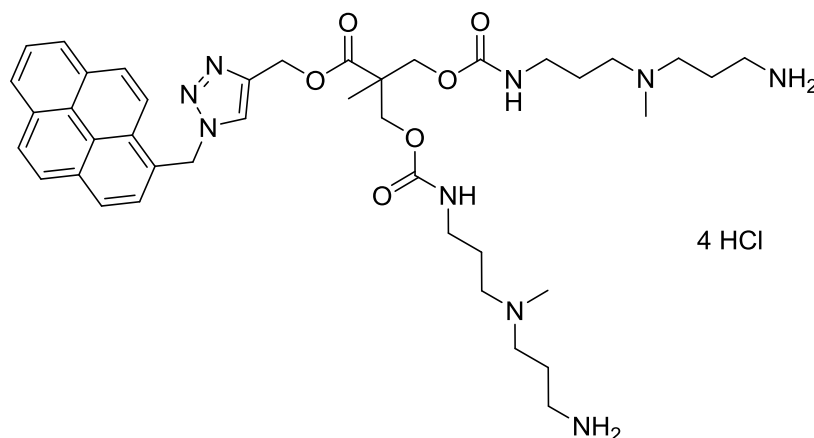
Propyne-[G1]-mono-Boc-DAPMA (0.100 g, 0.14 mmol) was dissolved in degassed DMF (10 ml) along with 1-azidomethyl pyrene (0.036 g, 0.14 mmol), CuSO₄•5H₂O (3.49 mg, 14 μmol, 10 mol%) and sodium ascorbate (2.66 mg, 28 μmol, 20 mol%). The reaction mixture was stirred 72 hours at room temperature under N₂. The DMF was then removed in vacuo at room temperature and the residue taken up in DCM (20 ml). The solution was washed with H₂O (2 x 10 ml), dried over MgSO₄ and the solvent was evaporated in vacuo to leave the crude product (0.102 g). The crude product was purified by GPC (DCM) affording the desired product as a yellow solid (0.098 g, 0.101 mmol, 72 %).

¹H NMR (400MHz, CDCl₃) δ: 8.38-7.90 (m, 9H, Ar-H); 7.45 (br s, CH triazole, 1H); 6.21 (s, 2H, ArCH₂); 5.80 (br s, NH, 2H); 5.38 (br s, NH, 2H); 5.11 (s, CH₂O triazole, 2H); 4.22-4.12 (m, CH₂O, 6H); 3.24-3.05 (m, CH₂NH, 8H); 2.39-2.31 (m, CH₂N(CH₃), 8H); 2.15 (s, N(CH₃), 6H); 1.61 (app. q, CH₂CH₂NH, J = 6.8 Hz, 8H); 1.40 (s, C(CH₃)₃, 18H).

¹³C NMR (100MHz, CDCl₃) δ: 173.1(CONH); 156.1 (OCONH); 155.9 (OCONH); 142.35 (C triazole); 131.7, 131.2, 130.7, 129.2, 128.4, 128.2, 127.9, 127.4, 127.3, 126.2, 125.6, 125.5, 125.0, 124.6, 122.6 (Ar-C); 123.47 (CH triazole); 78.79(C(CH₃)₃); 65.60 (CH₂O); 58.3 (CH₂O triazole) 56.06, 55.64 (CH₂N(CH₃)); 52.0 (Ar-CH₂N triazole); 46.88 (C_{quat});

41.67 (N(CH₃)); 40.08, 39.15 (CH₂NH); 28.37 (C_{quat}(CH₃)); 26.42, 26.40 (CH₂CH₂NH);
 IR (cm⁻¹): 3378m (N-H), 2923m (C-H), 1697s (C=O), 1601w, 1530m (CONH), 1461m,
 1248s, 1128s, 1022m, 845m, 708m.
 ESI-MS: Calcd. [M+2H]²⁺ (C₅₁H₇₅N₉O₁₀) *m/z* = 486.7813; Found [M+H]⁺ *m/z* = 486.7808
 (100%).

Synthesis of Py-G1



Molecular Formula = C₄₁H₆₁Cl₄N₉O₆

Molecular Weight = 917.17

Py-G1--Boc-DAPMA (98 mg, 101 μmol) was dissolved in MeOH (20 ml) and HCl gas was bubbled through the solution for 20 s. The reaction mixture was stirred at room temperature for 3 hours. The solvent was removed *in vacuo* to afford the product as a yellow foam (41mg, 45μmol, 44%).

R_f = 0.00 (NH₄OH).

¹H NMR (400 MHz, MeOD-*d*₄) δ: 7.90-8.38 (m, 9H, Ar-*H*); 7.45 (br s, CH triazole, 1H); 6.21 (s, 2H, ArCH₂); 5.80 (br s, NH, 2H); 5.38 (br s, NH, 2H); 5.19 (br s, CH₂O triazole, 2H); 4.22-4.12 (m, CH₂O, 6H); 3.05-3.24 (m, CH₂NH, 8H); 2.31-2.39 (m, CH₂N(CH₃), 8H); 2.15 (s, N(CH₃), 6H); 1.61 (app q, CH₂CH₂NH, *J* = 6.8 Hz, 8H).

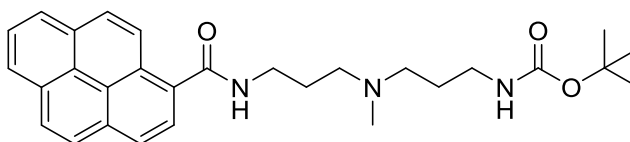
¹³C NMR (100 MHz, MeOD-*d*₄) δ: 173.1(C=O); 156.1 (OCONH); 142.35 (C triazole); 131.7, 131.2, 130.7, 129.2, 128.4, 128.2, 127.9, 127.4, 127.3, 126.2, 125.6, 125.5, 125.0, 124.6, 122.6 (Ar-C); 123.47 (CH triazole); 65.60 (CH₂O); 58.3 (CH₂O triazole) 56.06, 55.64 (CH₂N(CH₃)); 56.0 (Ar-CH₂N triazole); 46.88 (C_{quat}); 41.67 (N(CH₃)); 40.08, 39.15 (CH₂NH);

28.37 (C_{quat}(CH₃)); 26.42, 26.40 (CH₂CH₂NH);

IR (cm⁻¹): 3362w (N-H), 2957m (C-H), 1708s (C=O), 1600m, 1529m (CONH), 1462w, 1246m, 1131m, 1084 w, 846w, 707w

ESI-MS *m/z*: Calcd. [M+2H]²⁺ (C₄₁H₅₉N₉O₆) 386.7289; Found [M+H]⁺386.7285. (100%)

Synthesis of Py-DAPMA-Boc



Chemical Formula: C₂₉H₃₅N₃O₃

Molecular Weight: 473.62

Pyrenecarboxylic acid (100 mg, 0.406 mmol) was dissolved in DCM (40 ml) and TBTU (130 mg, 0.406 mmol) and Et₃N (5 ml) were added. The mixture was stirred for 5 min, then mono-Boc-protected *N,N*-di-(3-aminopropyl)-*N*-methylamine (99.6 mg, 0.406 mmol) was dissolved in CH₂Cl₂ (20 ml) and added to the mixture. The solution was left stirring overnight. The solvent was evaporated *in vacuo* and the product purified by column chromatography (SiO₂ in MeOH : DCM 1:9). The product was obtained as pale yellow solid (0.156 g, 81%, 0.33 mmol).

R_f = 0.25 (1:9 MeOH:DCM).

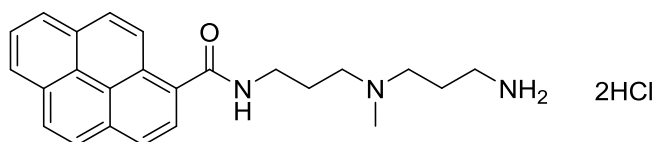
¹H NMR (400 MHz, CDCl₃) δ: 8.38-7.90 (m, 9H, Ar-H); 6.18 (br s, NH, 2H); 3.40 (d, CH₂NH, *J* = 6.8 Hz, 2H); 3.00 – 2.91(m, CH₂N(CH₃), 4H) 2.90-2.82 (m, CH₂N(CH₃), 2H); 2.54 (s, N(CH₃), 3H); 1.91, 1.61 (q, CH₂CH₂NH, *J* = 6.8 Hz, 4H); 1.40 (s, C(CH₃)₃, 9H).

¹³C NMR (100 MHz, CDCl₃) δ: 171.42 (C=O); 156.90 (C=ONH); 132.29, 130.76, 130.22, 129.53, 128.49, 128.39, 128.15, 126.88, 126.25, 125.81, 125.65, 124.89, 124.21, 124.09, 123.94, 123.82 (Ar-C); 79.61 (C(CH₃)₃); 54.05, 53.93 (CH₂N(CH₃)); 39.51 (N(CH₃)); 37.14, 36.93 (CH₂NH); 28.30 (C(CH₃)₃); 24.64, 24.30 (CH₂CH₂NH).

IR (cm⁻¹): 3283w (N-H), 2929w (C-H), 1691s (C=O), 1633s, 1519s (CONH), 1363s, 1246s, 1163s, 844s, 712m.

ESI-MS *m/z*: Calcd. (C₂₉H₃₆N₃O₃) [M+H]⁺ 474.2751; Obs. [M+H]⁺*m/z* 474.2736 (100%).

Synthesis of Py-DAPMA



Chemical Formula: $C_{24}H_{29}Cl_2N_3O$

Molecular Weight: 446.42

Py-DAPMA-Boc (100 mg, 0.211 mmol) was dissolved in MeOH (20 ml) and HCl gas was bubbled through the solution for 20 s. The reaction mixture was stirred at room temperature for 3 h. The solvent was removed *in vacuo* to afford the product as a brown oil (89 mg, 200 μ mol, 95%).

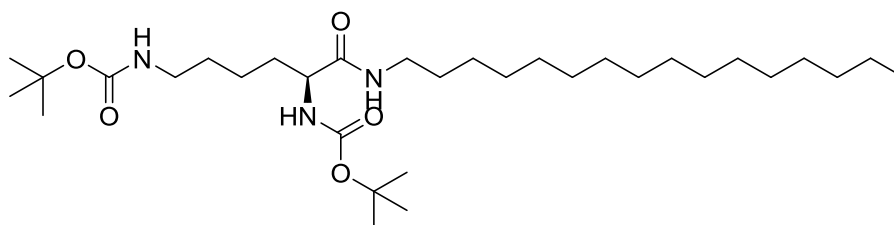
$R_f = 0.00$ (NH_4OH).

1H NMR (400 MHz, MeOD- d_4) δ : 8.01-7.55 (m, 9H, Ar-H); 3.70-3.55 (m, CH_2NH , 2H); 3.20-2.90 (m, $CH_2N(CH_3)$, $CH_2N(CH_3)$, $N(CH_3)$ 9H) 2.30-2.00 (m, CH_2CH_2NH , 4H). peaks were relatively broad owing to aggregation at NMR concentrations.

^{13}C NMR (100 MHz, MeOD- d_4) δ : 171.89 (C=O); 132.56, 131.02, 130.46, 130.02, 128.50, 128.20, 126.86, 126.32, 125.82, 125.63, 125.03, 124.27, 124.19, 123.89 (Ar-C); 54.45, 53.16 ($CH_2N(CH_3)$); 39.61 ($N(CH_3)$); 37.05, , 36.89 (CH_2NH); 24.39, 23.33 (CH_2CH_2NH)
IR cm^{-1} : 3385m (N-H), 2958m (C-H), 1708s (C=O), 1624m, 1528s (CONH), 1459s, 1244m, 1050s, 847s, 708m.

ESI-MS m/z : Calcd. $[M+H]^+$ ($C_{24}H_{28}N_3O$) 374.2227; Found $[M+H]^+$ 374.2227 (100%).

Synthesis of C_{16} -L-Lys-(Boc) $_2$



Chemical Formula: $C_{32}H_{63}N_3O_5$

Molecular Weight: 569.87

L-Lys-(Boc) $_2$ (500 mg, 1.44 mmol) was dissolved in DCM (40 ml) and TBTU (463 mg, 1.44 mmol.) and NEt_3 (5 ml) were added. The mixture was stirred for 5 minutes, then the 1-hexadecylamine (390 mg , 1.44 mmol) was dissolved in DCM (20 ml) and added to

the mixture. The solution was left stirring overnight. The solvent was evaporated *in vacuo*. After evaporation of the solvent the product was dissolved again in EtOAc (50 ml) and washed 1.33M NaHSO₄ (2x 15 ml), sat. NaHCO₃ (2x 15 ml), H₂O (3x 15 ml) and sat. NaCl solution (15 ml). After column chromatography (SiO₂ in Hexane : EtOAc 1:1), it was obtained as pale yellow solid in 0.466 g (56 %, 0.81 mmol).

$R_f = 0.25$ (Hexane : EtOAc 1:1)

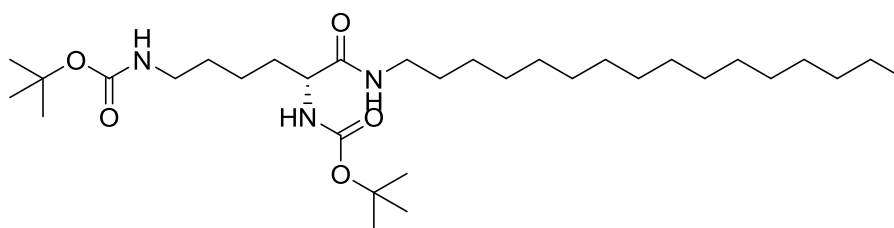
¹H NMR (400 MHz, CDCl₃) δ : 6.72 (s, CHNH, 1H), 5.45 (s, CH₂NH, 1H), 4.82 (s, CH₂NH, 1H), 4.01 (dd app. q, $J = 4.4$ Hz, CH(NHBoc), 1H), 3.20-3.04 (m, CH(NHBoc)CH₂, 2H); 1.69, 1.52 (comp m, CH₂CH₂CH₂NHBoc, 4H), 1.34 (br s, C(CH₃)₃ + CH₂, 22H), 1.15 (br s, CH₂, 28H), 0.78 (t, $J = 6.5$ Hz, CH₃, 3H).

¹³C NMR (100MHz, CDCl₃) δ : 172.18 (C=O); 156.16, 155.88, (C=O, Boc); 79.65, 78.91, (C(CH₃)₃); 54.33 (CHCONH); 39.99 (CH₂NHBoc), 39.46 (CONHCH₂); 32.31, 31.90, 29.69, 29.66, 29.61, 29.57, 29.52, 29.35, 29.32 (CH₂); 28.43, 28.33, C(CH₃)₃; 26.92 22.73, 22.67 (CH₂); 14.10 (CH₃)

IR cm⁻¹: 3341m (N-H), 2918m, 2850m(C-H), 1685s (C=O), 1648m, 1532s (CONH), 1244m, 1166s, 655m.

ESI-MS: Calcd. [M+H]⁺ (C₃₂H₆₄N₃O₅) $m/z = 570.4840$; Obs. [M+H]⁺ $m/z = 570.4868$.

Synthesis of C₁₆-D-Lys-(Boc)₂



Chemical Formula: C₃₂H₆₃N₃O₅

Molecular Weight: 569.87

D-Lys-(Boc)₂ (500 mg, 1.44 mmol) was dissolved in DCM (40 ml) and TBTU (463 mg, 1.44 mmol.) and NEt₃ (5 ml) were added. The mixture was stirred for 5 minutes, then the 1-hexadecylamine (390 mg, 1.44 mmol) was dissolved in DCM (20 ml) and added to the mixture. The solution was left stirring overnight. The solvent was evaporated *in vacuo*. After evaporation of the solvent the product was dissolved again in EtOAc (50 ml) and washed 1.33M NaHSO₄ (2x 15 ml), sat. NaHCO₃ (2x 15 ml), H₂O (3x 15 ml) and

sat. NaCl solution (15 ml).. After column chromatography (SiO₂ in Hexane : EtOAc 1:1), it was obtained as pale yellow solid in 0.452 g (55 %, 0.79 mmol).

$R_f = 0.25$ (Hexane : EtOAc 1:1)

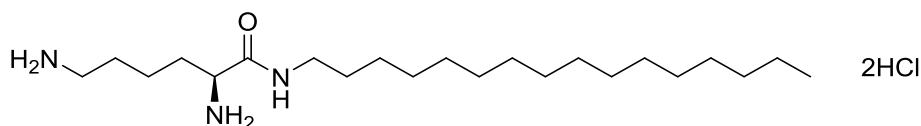
¹H NMR (400 MHz, CDCl₃) δ : 6.72 (s, CHNH, 1H), 5.45 (s, CH₂NH, 1H), 4.82 (s, CH₂NH, 1H), 4.01 (dd app. q, $J = 4.4$ Hz, CH(NHBoc), 1H), 3.20-3.04 (m, CH(NHBoc)CH₂, 2H); 1.69, 1.52 (comp m, CH₂CH₂CH₂NHBoc, 4H), 1.34 (br s, C(CH₃)₃ + CH₂, 22H), 1.15 (br s, CH₂, 28H), 0.78 (t, $J = 6.5$ Hz, CH₃, 3H).

¹³C NMR (100MHz, CDCl₃) δ : 172.18 (C=O); 156.16, 155.88, (C=O, Boc); 79.65, 78.91, (C(CH₃)₃); 54.33 (CHCONH); 39.99 (CH₂NHBoc), 39.46 (CONHCH₂); 32.31, 31.90, 29.69, 29.66, 29.61, 29.57, 29.52, 29.35, 29.32 (CH₂); 28.43, 28.33, C(CH₃)₃; 26.92 22.73, 22.67 (CH₂); 14.10 (CH₃)

IR cm⁻¹: 3342m (N-H), 2919m, 2852m(C-H), 1687s (C=O), 1650m, 1530s (CONH), 1246m, 1167s, 657m.

ESI-MS: Calcd. [M+H]⁺ (C₃₂H₆₄N₃O₅) $m/z = 570.4840$; Obs. [M+H]⁺ $m/z = 570.4839$.

Synthesis of C₁₆-L-Lys



Chemical Formula: C₂₂H₄₇N₃O

Molecular Weight: 369.64

C₁₆-L-Lys-(Boc)₂ (100 mg, 175 μ mol) was dissolved in MeOH (20 ml) and HCl gas was bubbled through the solution for 20 s. The reaction mixture was stirred at room temperature for 3 hours. The solvent was removed *in vacuo* to afford the product as an off white foam (73 mg, 166 μ mol, 95%).

$R_f = 0.00$ (NH₄OH).

¹H NMR (400 MHz, MeOD-*d*₄) δ : 3.88 (dd app t, $J = 4.4$ Hz, CH(NH₂), 1H), 3.21 (t, $J = 7.0$ Hz, CH₂NHCO, 2H); 2.94 (t, $J = 8.0$ Hz, CH₂NH₂, 2H) 1.88, 1.72 1.50 (comp m, CH₂CH₂CH₂CH₂NH₂, 6H), 1.28-1.26 (m, CH₂, 28H), 0.88 (t, $J = 6.5$ Hz, CH₃, 3H).

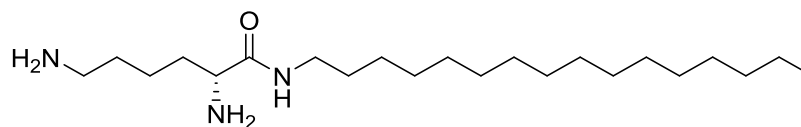
¹³C NMR (100MHz, MeOD-*D*₄) δ : 169.82 (C=O); 54.16 (CHCONH); 40.66 (CH₂NH₂); 40.26 (CH₂NH); 33.06, 32.13, 30.79, 30.76, 30.71, 30.47, 30.40, 30.27, 28.80, 28.71,

28.04, 27.99, 23.73, 23.00 (CH₂); 14.48 (CH₃).

IR cm⁻¹: 2916m, 2848m(C-H),, 1667m, 1566s (CONH), 1269w, 720m.

ESI-MS: Calcd. [M+H]⁺ (C₂₂H₄₈N₃O) m/z = 370.3792; Obs. [M+H]⁺ m/z=370.3772.

Synthesis of C₁₆-D-Lys



Chemical Formula: C₂₂H₄₇N₃O

Exact Mass: 369.37

C₁₆-D-Lys-(Boc)₂ (100 mg, 175 μmol) was dissolved in MeOH (20 ml) and HCl gas was bubbled through the solution for 20 s. The reaction mixture was stirred at room temperature for 3 hours. The solvent was removed *in vacuo* to afford the product as an off white foam (74 mg, 167 μmol, 96%).

R_f = 0.00 (NH₄OH).

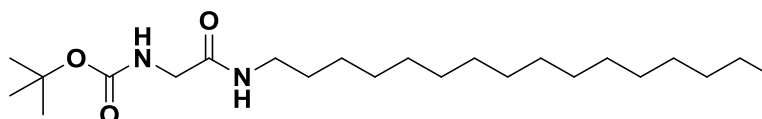
¹H NMR (400 MHz, MeOD-*d*₄) δ: 3.88 (dd app t, *J* = 4.4. Hz, CH(NH₂), 1H), 3.21 (t, *J* = 7.0 Hz, CH₂NHCO, 2H); 2.94 (t, *J* = 8.0 Hz, CH₂NH₂, 2H) 1.88, 1.72 1.50 (comp m, CH₂CH₂CH₂CH₂NH₂, 6H), 1.28-1.26 (m, CH₂, 28H), 0.88 (t, *J* = 6.5 Hz, CH₃, 3H).

¹³C NMR (100MHz, MeOD-*D*₄) δ: 169.82 (C=O); 54.16 (CHCONH); 40.66 (CH₂NH₂,); 40.26 (CH₂NH); 33.06, 32.13, 30.79, 30.76, 30.71, 30.47, 30.40, 30.27, 28.80, 28.71, 28.04, 27.99, 23.73, 23.00 (CH₂); 14.48 (CH₃).

IR cm⁻¹: 2916m, 2849m(C-H),, 1665m, 1561s (CONH), 1269w, 720m

ESI-MS: Calcd. [M+H]⁺ (C₂₂H₄₈N₃O) m/z = 370.3792; Obs. [M+H]⁺ m/z = 370.3788.

Synthesis of C₁₆-Gly-boc



Chemical Formula: C₂₃H₄₆N₂O₃

Molecular Weight: 398.63

Boc-Gly-OH (1.48 g, 8.42 mmol) was dissolved in DCM (40 ml) and TBTU (463 mg, 8.32

mmol.) and NEt_3 (5 ml) were added. The mixture was stirred for 5 minutes, then the 1-hexadecylamine (2 g , 8.42 mmol) was dissolved in DCM (20 ml) and added to the mixture. The solution was left stirring overnight. The solvent was evaporated *in vacuo*. After evaporation of the solvent the product was dissolved again in EtOAc (50 ml) and washed 1.33M NaHSO_4 (2x 15 ml), sat. NaHCO_3 (2x 15 ml), H_2O (3x 15 ml) and sat. NaCl solution (15 ml). The solvent was evaporated *in vacuo* and the product was obtained as white solid in 1.3 g (64 % , 5.39 mmol).

$R_f = 0.40$ (Hexane : EtOAc 1:1).

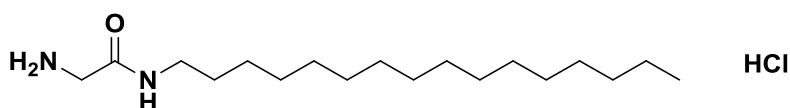
$R_f = 0.40$ (Hexane : EtOAc 1:1). $^1\text{H NMR}$ (400 MHz, CDCl_3) δ : 6.11 (br s, NH, 1H); 5.15 (br s, NH, 1H); 3.76 (d, $J = 4.4$ Hz, COCH_2NH , 2H); 3.25 (q, $J = 4.4$ Hz, CH_2NHCO , 2H) 1.67, 1.50-1.28 (comp m, $\text{C}(\text{CH}_3)_3 + \text{CH}_2$, 37H), 0.86 (t, CH_3 , $J = 8.0$ Hz, 3H).

$^{13}\text{C NMR}$ (100MHz, CDCl_3) δ : 169.34, 156.47 (C=O); 80.45 $\text{C}(\text{CH}_3)_3$; 39.59 (COCH_2NH); 32.01 (CH_2NHCO); 29.78, 29.75, 29.68, 29.62, 29.60, 29.45, 29.37 (CH_2); 28.38 ($\text{C}(\text{CH}_3)_3$) 26.94, 22.7 (CH_2); 14.22 (CH_3).

IR cm^{-1} : 3287m (N-H), 2916m ,2848m(C-H), 1693s (C=O), 1642s, 1530m (CONH), 1249m, 1170s, 719m.

ESI-MS: Calcd. $[\text{M}+\text{Na}]^+$ ($\text{C}_{23}\text{H}_{46}\text{N}_2\text{O}_3\text{Na}$) $m/z = 421.3401$; Obs. $[\text{M}+\text{H}]^+$ $m/z = 421.3390(100\%)$

Synthesis of C_{16} -Gly



Chemical Formula: $\text{C}_{18}\text{H}_{39}\text{ClN}_2\text{O}$

Molecular Weight: 334.97

C_{16} -Gly-boc (600 mg, 1.51 mmol) was dissolved in MeOH (20 ml) and HCl gas was bubbled through the solution for 20 s. The reaction mixture was stirred at room temperature for 3 hours. The solvent was removed *in vacuo* to afford the product as an off white foam (481 mg, 1.43 mmol, 96%).

$R_f = 0.00$ (NH_4OH).

$^1\text{H NMR}$ (400 MHz, $\text{MeOD}-d_4$) δ : 3.65, (s, CH_2NH_2 , 2H); 3.28 (t, $J = 8.0$ Hz, CH_2NHCO , 2H)

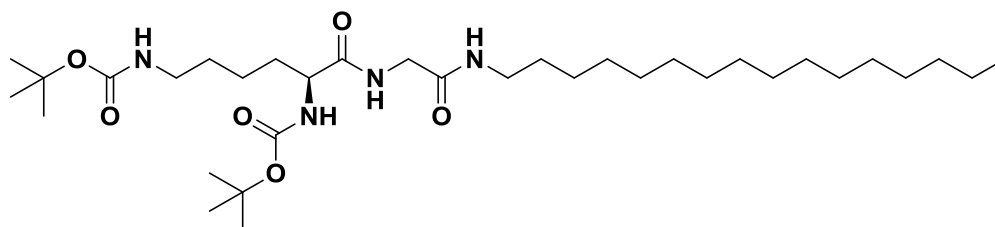
1.49 (app. q, $J = 8.0$ Hz, $\text{CH}_2\text{CH}_2\text{NHCO}$ 2H); 1.35-1.20 (comp m, CH_2 , 26H), 0.90 (t, $J = 7.0$ Hz, CH_3 , 3H).

^{13}C NMR (100MHz, $\text{MeOD-}d_4$) δ : 165.68 (C=O); 40.66 (CH_2NH_2); 40.26 (CH_2NHCO); 31.75, 29.45, 29.37, 29.02, 26.65 22.41 (CH_2); 13.11. (CH_3).

IR cm^{-1} : 3287m (N-H), 2914m, 2848m(C-H), , 1642s, 1470s (CONH), 1114w, 661m.

ESI-MS: Calcd. $[\text{M}+\text{H}]^+$ ($\text{C}_{18}\text{H}_{39}\text{N}_2\text{O}$) $m/z = 299.3057$; Obs. $[\text{M}+\text{H}]^+$ $m/z = 299.3068$ (60%).

Synthesis of C_{16} -Gly-L-Lys-Boc



Chemical Formula: $\text{C}_{34}\text{H}_{66}\text{N}_4\text{O}_6$

Molecular Weight: 626.92

L-Lys-(Boc) $_2$ (283 mg, 0.60 mmol) was dissolved in DCM (40 ml) and TBTU (191.7 mg, 1.44 mmol.) and NEt_3 (5 ml) were added. The mixture was stirred for 5 minutes, then the C_{16} -Gly (200 mg, 0.60 mmol) was dissolved in DCM (20 ml) and added to the mixture. The solution was left stirring overnight. The solvent was evaporated *in vacuo*. After evaporation of the solvent the product was dissolved again in EtOAc (50 ml) and washed 1.33M NaHSO_4 (2x 15 ml), sat. NaHCO_3 (2x 15 ml), H_2O (3x 15 ml) and sat. NaCl solution (15 ml). The solvent was evaporated *in vacuo* and the product was obtained as pale yellow solid in 150 mg (40 %, 0.24 mmol).

$R_f = 0.30$ (Hexane : EtOAc 1:1).

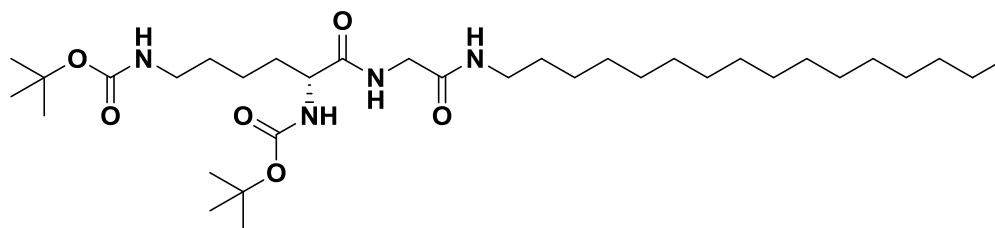
^1H NMR (400 MHz, CDCl_3) δ : 7.49 (s, NH, 1H), 7.09 (s, NH, 1H), 5.85 (s, NH, 1H), 5.27 (s, NH, 1H), 4.12 (dd app q, $J = 4.4$ Hz, $\text{CH}(\text{NHBoc})$, 1H), 3.81 (s, NHCH_2CONH , 2H) 3.20-3.04 (m, CH_2NH , 4H); 1.69-1.52 (comp m, $\text{CH}_2\text{CH}_2\text{CH}_2\text{NHBoc}$, 4H), 1.35-1.33 (m, $\text{C}(\text{CH}_3)_3 + \text{CH}_2$, 22H), 1.16-1.14 (m, CH_2 , 26H), 0.77 (t, $J = 7.0$ Hz, CH_3 , 3H).

^{13}C NMR (100MHz, CDCl_3) δ : 173.31, 169.08 (C=O); 156.45, 156.34 (CONHBoc) 79.98, 78.99, ($\text{C}(\text{CH}_3)_3$); 55.32 (COCHNH); 43.07 (CH_2NHBoc), 39.68 (NHCH_2CO) 31.39, 29.70, 29.69, 29.66, 29.59, 29.55, 29.42, 29.36 (CH_2); 29.36, 28.47 ($\text{C}(\text{CH}_3)_3$); 26.98, 22.68 (CH_2) 14.13 (CH_3).

IR cm^{-1} : 3301 m (N-H), 2922 m , 2852 m (C-H), 1692 s (C=O), 1649 m , 1525 s (CONH), 1248 m , 1168 s , 719 m .

ESI-MS: Calcd. $[\text{M}+\text{Na}]^+$ ($\text{C}_{36}\text{H}_{66}\text{N}_4\text{NaO}_6$) m/z = 649.4875; Obs. $[\text{M}+\text{H}]^+$ m/z = 649.4862 (100%)

Synthesis of C_{16} -Gly-D-Lys-Boc



Chemical Formula: $\text{C}_{34}\text{H}_{66}\text{N}_4\text{O}_6$

Molecular Weight: 626.92

D-Lys-(Boc)₂ (283 mg, 0.60 mmol) was dissolved in DCM (40 ml) and TBTU (191.7 mg, 1.44 mmol.) and NEt_3 (5 ml) were added. The mixture was stirred for 5 minutes, then the C_{16} -Gly (200 mg, 0.60 mmol) was dissolved in DCM (20 ml) and added to the mixture. The solution was left stirring overnight. The solvent was evaporated *in vacuo*. After evaporation of the solvent the product was dissolved again in EtOAc (50 ml) and washed 1.33M NaHSO_4 (2x 15 ml), sat. NaHCO_3 (2x 15 ml), H_2O (3x 15 ml) and sat. NaCl solution (15 ml). The solvent was evaporated *in vacuo* and the product was obtained as pale yellow solid in 150 mg (40 %, 0.24 mmol).

R_f = 0.30 (Hexane : EtOAc 1:1).

^1H NMR (400 MHz, CDCl_3) δ : 7.49 (s, NH, 1H), 7.09 (s, NH, 1H), 5.85 (s, NH, 1H), 5.27 (s, NH, 1H), 4.12 (dd app q, J = 4.4 Hz, $\text{CH}(\text{NHBoc})$, 1H), 3.81 (s, NHCH_2CONH , 2H), 3.20-3.04 (m, CH_2NH , 4H); 1.69-1.52 (comp m, $\text{CH}_2\text{CH}_2\text{CH}_2\text{NHBoc}$, 4H), 1.35-1.33 (m, $\text{C}(\text{CH}_3)_3 + \text{CH}_2$, 22H), 1.16-1.14 (m, CH_2 , 26H), 0.77 (t, J = 7.0 Hz, CH_3 , 3H).

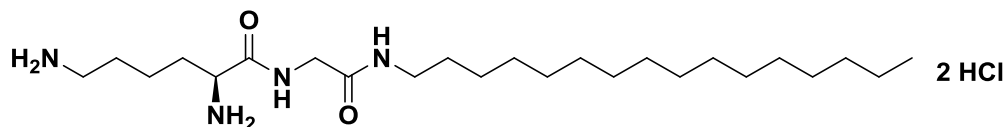
^{13}C NMR (100MHz, CDCl_3) δ : 173.31, 169.08 (C=O); 156.45, 156.34 (CONHBoc) 79.98, 78.99, ($\text{C}(\text{CH}_3)_3$); 55.32 (COCHNH); 43.07 (CH_2NHBoc), 39.68 (NHCH_2CO) 31.39, 29.70, 29.69, 29.66, 29.59, 29.55, 29.42, 29.36 (CH_2); 29.36, 28.47 ($\text{C}(\text{CH}_3)$); 26.98, 22.68 (CH_2) 14.13 (CH_3).

IR cm^{-1} : 3303 m (N-H), 2923 m , 2851 m (C-H), 1694 s (C=O), 1651 m , 1523 s (CONH),

1250m, 1167s, 720m.

ESI-MS: Calcd. $[M+Na]^+$ ($C_{36}H_{66}N_4NaO_6$) $m/z = 649.4875$; Obs. $[M+H]^+$ $m/z = 649.4857$ (100%)

Synthesis of C₁₆-Gly-L-Lys



Chemical Formula: $C_{24}H_{52}Cl_2N_4O_2$

Molecular Weight: 499.61

C₁₆-Gly-L-Lys-(Boc)₂ (100 mg, 159 μ mol) was dissolved in MeOH (20 ml) and HCl gas was bubbled through the solution for 20 s. The reaction mixture was stirred at room temperature for 3 hours. The solvent was removed *in vacuo* to afford the product as an off white foam (75 mg, 151 μ mol, 95%).

$R_f = 0.00$ (NH_4OH).

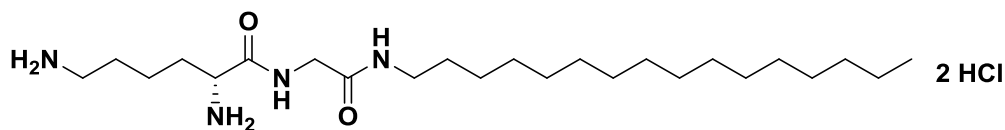
¹H NMR (400 MHz, MeOD-*d*₄) δ : 4.12 (t, CH_2NH , $J = 4.4$ Hz, 2H), 3.81 (s, $NHCH_2CONH$, 2H) 3.20 (m, CH_2NHCO , 2H); 2.96 (t, $CONHCH_2$, $J = 7.5$ Hz, 2H); 1.92, (m, $NHCOCH_2CH_2$, 2H) 1.69, 1.52 (m, $CH_2CH_2CH_2NH_2 + CH_2$, 6H), 1.35-1.33 (m, $C(CH_3)_3 + CH_2$, 26H), 0.77 (t, $J = 7.0$ Hz, CH_3 , 3H).

¹³C NMR (100MHz, MeOD-*d*₄) δ : 169.51, 169.22 ($C=O$); 52.90 ($CHCONH$); 41.77 (CH_2NH_2); 39.29 ($CONHCH_2$); 31.75, 30.45, 29.47, 29.44, 29.40, 29.16, 29.06, 26.71, 26.63, 22.42, 21.31 (CH_2); 13.15. (CH_3).

IR cm^{-1} : 3229m (N-H), 2916m, 2849m(C-H), 1654m, 1562s (CONH), 1251m, 720m.

ESI-MS: Calcd. $[M+H]^+$ ($C_{24}H_{51}N_4O_2$) $m/z = 427.4007$; Obs. $[M+H]^+$ $m/z = 427.3987$.

Synthesis of C₁₆-Gly-D-Lys



Chemical Formula: $C_{24}H_{52}Cl_2N_4O_2$

Molecular Weight: 499.61

C₁₆-Gly-D-Lys-(Boc)₂ (100 mg, 159 μmol) was dissolved in MeOH (20 ml) and HCl gas was bubbled through the solution for 20 s. The reaction mixture was stirred at room temperature for 3 hours. The solvent was removed *in vacuo* to afford the product as an off white foam (74 mg, 167 μmol, 94%).

$R_f = 0.00$ (NH₄OH).

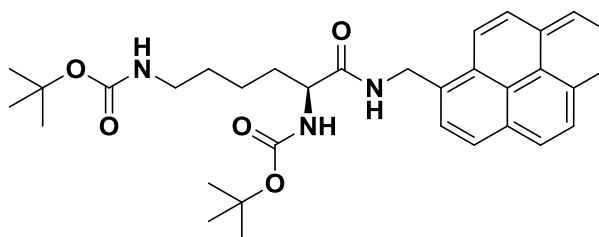
¹H NMR (400 MHz, MeOD-*d*₄) δ: 4.12 (t, CH₂NH, $J = 4.4$ Hz, 2H), 3.81 (s, NHCH₂CONH, 2H) 3.20 (m, CH₂NHCO, 2H); 2.96 (t, CONHCH₂, $J = 7.5$ Hz, 2H); 1.92, (m, NHCOCH₂CH₂, 2H) 1.69, 1.52 (m, CH₂CH₂CH₂NH₂ + CH₂, 6H), 1.35-1.33 (m, C(CH₃)₃ + CH₂, 26H), 0.77 (t, $J = 7.0$ Hz, CH₃, 3H).

¹³C NMR (100MHz, MeOD-*d*₄) δ: 169.51, 169.22 (C=O); 52.90 (CHCONH); 41.77 (CH₂NH₂); 39.29 (CONHCH₂); 31.75, 30.45, 29.47, 29.44, 29.40, 29.16, 29.06, 26.71, 26.63, 22.42, 21.31 (CH₂); 13.15. (CH₃).

IR cm⁻¹: 3230*m* (N-H), 2917*m*, 2847*m*(C-H), 1652*m*, 1563*s* (CONH), 1252*m*, 721*m*.

ESI-MS: Calcd. [M+H]⁺ (C₂₄H₅₁N₄O₂) $m/z = 427.4007$; Obs. [M+H]⁺ $m/z = 427.4005$.

Synthesis of Py-L-Lys-Boc



Chemical Formula: C₃₃H₄₁N₃O₅

Molecular Weight: 559.71

L-lys-(Boc)₂ (129 mg, 0.48 mmol) was dissolved in DCM (40 ml) and TBTU (120 mg, 0.48 mmol.) and NEt₃ (5 ml) were added. The mixture was stirred for 5 minutes, then the 1-pyrenemethylamine (100 mg, 0.48 mmol) was dissolved in DCM (20 ml) and added to the mixture. The solution was left stirring overnight. The solvent was evaporated *in vacuo*. After column chromatography (SiO₂ in MeOH : DCM 1:9), it was obtained as pale yellow solid in 252 mg (93 %, 0.45 mmol).

$R_f = 0.5$ (MeOH : DCM 1:9).

¹H NMR (400 MHz, CDCl₃) δ: 8.10-7.70 (m, Ar-H, 9H); 7.09 (br s, NH, 1H); 5.43 (br s, NH,

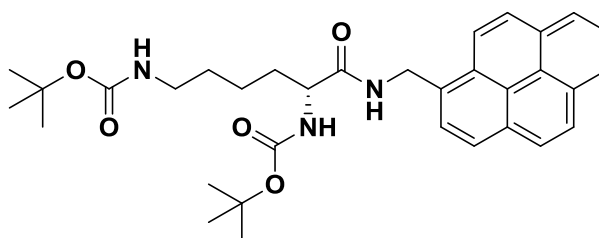
1H); 4.95 (m, ArCH₂NH, 2H) 4.73 (br s, NH, 1H); 4.10 (m, COCH, 1H); 3.00 (m, CH₂NH, 2H); 1.91, 1.61 (comp m, CH₂CH₂CH₂NH₂, 4H); 1.40, 1.30 (m, CH₂ + C(CH₃)₃, 20H) Peaks were relatively broad owing to aggregation at NMR concentrations.

¹³C NMR (100 MHz, CDCl₃) δ: 172.22 (C=O); 156.23 (C=ONH); 131.18, 131.04, 130.98, 130.71, 128.80, 128.03, 127.32, 126.76, 126.01, 125.27, 124.88, 124.72, 124.63, 122.74 (Ar-C); 79.94, 79.11 (C(CH₃)₃); 41.68 (ArCH₂NH) 40.02 (CH₂NH); 38.66 (CHNH) 32.21 (CH₂CHNH); 29.70 (CH₂CH₂NH); 28.53, 28.49 (2 × C(CH₃)₃); 26.34 (CH₂CH₂CH₂NH).

IR cm⁻¹: 3322m (N-H), 2979m, 2931m 2847w(C-H), 1681s (C=O) 1651m, 1518s (CONH), 1246m, 1164s, 844m.

ESI-MS: Calcd. [M+Na]⁺ (C₃₃H₄₁N₃O₅Na) m/z = 581.2938; Obs. [M+H]⁺ m/z = 582.2929. (100%)

Synthesis of Py-D-Lys-Boc



Chemical Formula: C₃₃H₄₁N₃O₅

Molecular Weight: 559.71

D-lys-(Boc)₂ (129 mg, 0.48 mmol) was dissolved in DCM (40 ml) and TBTU (120 mg, 0.48 mmol.) and NEt₃ (5 ml) were added. The mixture was stirred for 5 minutes, then the 1-pyrenemethylamine (100 mg, 0.48 mmol) was dissolved in DCM (20 ml) and added to the mixture. The solution was left stirring overnight. The solvent was evaporated *in vacuo*. After column chromatography (SiO₂ in MeOH : DCM 1:9), it was obtained as pale yellow solid in 196 mg (73 %, 0.35 mmol).

R_f = 0.50 (MeOH : DCM 1:9).

¹H NMR (400 MHz, CDCl₃) δ: 8.10-7.70 (m, Ar-H, 9H); 7.09 (br s, NH, 1H); 5.43 (br s, NH, 1H); 4.95 (m, ArCH₂NH, 2H) 4.73 (br s, NH, 1H); 4.10 (m, COCH, 1H); 3.00 (m, CH₂NH, 2H); 1.91, 1.61 (comp m, CH₂CH₂CH₂NH₂, 4H); 1.40, 1.30 (m, CH₂ + C(CH₃)₃, 20H) Peaks were relatively broad owing to aggregation at NMR concentrations.

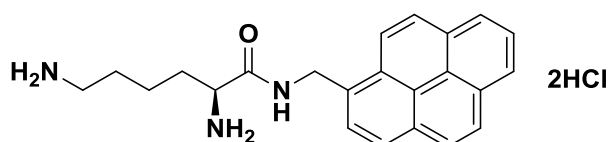
¹³C NMR (100 MHz, CDCl₃) δ: 172.22 (C=O); 156.23 (C=ONH); 131.18, 131.04, 130.98,

130.71, 128.80, 128.03, 127.32, 126.76, 126.01, 125.27, 124.88, 124.72, 124.63, 122.74 (Ar-C); 79.94, 79.11 (C(CH₃)₃); 41.68 (ArCH₂NH) 40.02 (CH₂NH); 38.66 (CHNH) 32.21 (CH₂CHNH); 29.70 (CH₂CH₂NH); 28.53, 28.49 (2 × C(CH₃)₃); 26.34 (CH₂CH₂CH₂NH).

IR cm⁻¹: 3322m (N-H), 2979m, 2931m 2847w(C-H), 1681s (C=O) 1651m, 1518s (CONH), 1246m, 1164s, 844m.

ESI-MS: Calcd. [M+Na]⁺ (C₃₃H₄₁N₃O₅Na) *m/z* = 581.2938; Obs. [M+H]⁺ *m/z* = 582.2932. (100%)

Synthesis of Py-L-Lys



Chemical Formula: C₂₃H₂₇Cl₂N₃O

Molecular Weight: 432.39

Py-L-Lys-(Boc)₂ (100 mg, 179 μmol) was dissolved in MeOH (20 ml) and HCl gas was bubbled through the solution for 20 s. The reaction mixture was stirred at room temperature for 3 hours. The solvent was removed *in vacuo* to afford the product as a brown foam (74 mg, 167 μmol, 97%).

R_f = 0.00 (NH₄OH).

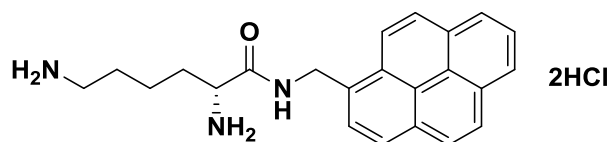
¹H NMR (400 MHz, MeoD-*d*₄) δ: 8.10-7.70 (m, Ar-H, 9H); 5.20 (m, ArCH₂NH, 2H); 3.90 (m, COCH, 1H); 3.00 (m, CH₂NH, 2H); 1.91, 1.61, 1.35 (comp m, CH₂CH₂CH₂CH₂NH₂, 6H); Peaks were relatively broad owing to aggregation at NMR concentrations.

¹³C NMR (100 MHz, MeoD-*d*₄) δ: 168.30 (C=ONH); 131.23, 131.21, 131.11, 130.88, 130.66, 128.59, 127.63, 127.16, 127.14, 127.05, 125.90, 125.13, 125.03, 124.60, 124.58, 124.49, 124.36, 122.66 (Ar-C); 41.30 (ArCH₂NH) 38.90 (CH₂NH); 37.97 (CHNH) 33.51 (CH₂CHNH); 30.92 (CH₂CH₂NH); 26.65 (CH₂CH₂CH₂NH).

IR cm⁻¹: 3321m (N-H), 2939m, 2930m 2865w(C-H), 1681s (C=O) 1642m, 1516s (CONH), 1246m, 1165s, 842m.

ESI-MS: Calcd. [M+H]⁺ (C₂₃H₂₆N₃O) *m/z* = 360.2070; Obs. [M+H]⁺ *m/z* = 360.2072. (100%)

Synthesis of Py-D-Lys



Chemical Formula: $C_{23}H_{27}Cl_2N_3O$

Molecular Weight: 432.39

Py-D-Lys-(Boc)₂ (100 mg, 179 μ mol) was dissolved in MeOH (20 ml) and HCl gas was bubbled through the solution for 20 s. The reaction mixture was stirred at room temperature for 3 hours. The solvent was removed *in vacuo* to afford the product as a brown foam (74 mg, 167 μ mol, 96%).

R_f = 0.00 (NH₄OH).

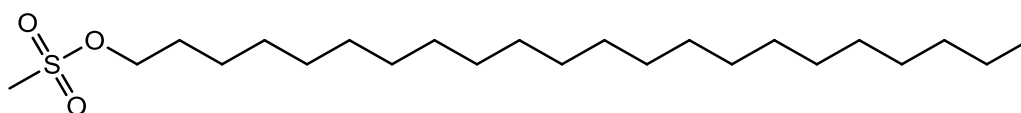
¹H NMR (400 MHz, CDCl₃) δ : 8.10-7.70 (m, Ar-H, 9H); 5.20 (m, ArCH₂NH, 2H); 3.90 (m, COCH, 1H); 3.00 (m, CH₂NH, 2H); 1.91, 1.61, 1.35 (comp m, CH₂CH₂CH₂CH₂NH₂, 6H). Peaks were relatively broad owing to aggregation at NMR concentrations.

¹³C NMR (100 MHz, CDCl₃) δ : 172.22 (C=O); 156.23 (C=ONH); 131.18, 131.04, 130.98, 130.71, 128.80, 128.03, 127.32, 126.76, 126.01, 125.27, 124.88, 124.72, 124.63, 122.74 (Ar-C); 41.68 (ArCH₂NH) 40.02 (CH₂NH); 38.66 (CHNH) 32.21 (CH₂CHNH); 29.70 (CH₂CH₂NH); 26.34 (CH₂CH₂CH₂NH).

IR cm⁻¹: 3328m (N-H), 2981m, 2927m, 2865m(C-H), 1677s (C=O) 1650m, 1505s (CONH), 1247m, 1165s, 842m.

ESI-MS: Calcd. [M+H]⁺ (C₂₃H₂₆N₃O) m/z = 360.2070; Obs. [M+H]⁺ m/z = 360.2067. (100%)

Synthesis of docosyl mesylate²¹⁴



Molecular Formula = C₂₃H₄₈O₃S

Molecular Weight = 404.33

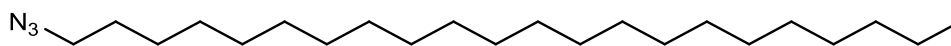
To a solution of the 1-docoanol (5.29g, 16.2 mmol) and Et₃N (5.23 mL, 37.3 mmol) in

DCM, mesyl chloride (2mL, 25.7 mmol) was added through a syringe. The resulting solution was stirred for 3h. The yellow reaction was washed sequentially with water (14 mL), 2M HCl (14mL), water (14mL), saturated NaHCO₃ (14mL), and water (14mL). The organic solution was dried with MgSO₄ and concentrated to give a white-yellow solid (3.92g, 9.69 mmol 60%). The ¹H NMR spectra of the respective crude products docosyl mesylate suggested that the material was suitable for the next step without further purification.

¹H NMR (400 MHz, CDCl₃) δ: 4.55 (t, CH₂O, *J* = 6.4 Hz, 2H); 2.99 (s, CH₃SO₃, *J* = 7.2 Hz, 3H); 1.73 (c, CH₂CH₂O, *J* = 7.2, 2H); 1.42-1.18 (m, 18 x CH₂, 36H); 0.861 (s, CH₃, *J* = 6.8, 3H).

¹³C NMR (100 MHz, CDCl₃,) δ: 70.2 (CH₂O); 37.4 (CH₃SO₃); 29.7, 29.7, 29.6, 29.6, 29.5, 29.4, 29.4, 29.1 (CH₂); 29.0 (CH₂CH₂O); 25.4 (CH₂); 22.7 (CH₂); 14.1 (CH₃).

Synthesis of 1-azidodocosane²¹⁴



Molecular Formula = C₂₂H₄₅N₃

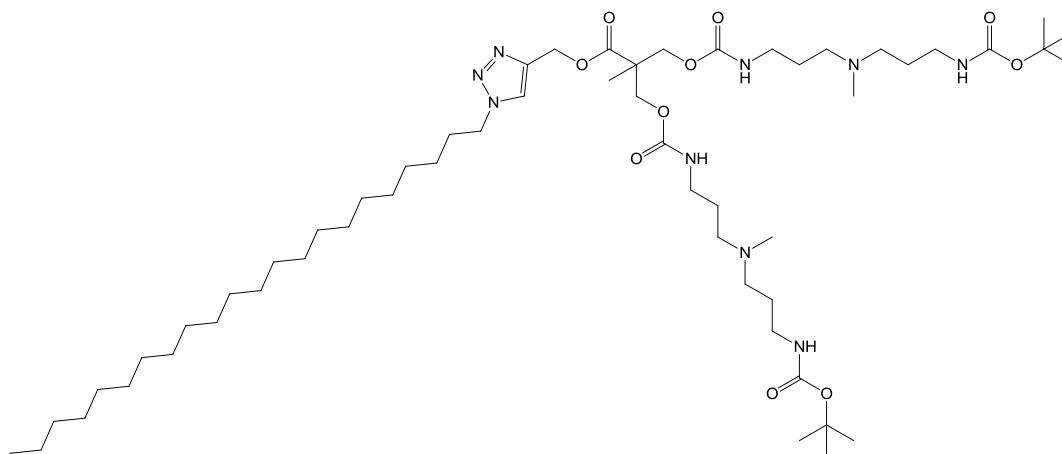
Molecular Weight = 351.36

To the solution of docosyl mesylate (2.77g, 6.84 mmol) in DMF (52 mL), NaN₃ (1.28 g, 19.5 mmol) was added. The mixture was stirred at room temperature for 30 min, and then refluxed at 85 °C for 4 h. Afterwards, the reaction was cooled before portions of hexane (104 mL) and water (10.5 mL) were added. The organic layer was separated, then washed successively with saturated NaHCO₃ (10.5 mL) and saturated NaCl (10.5 mL). The organic layer was dried with Na₂SO₄ and concentrated to give product as sticky white solid.

¹H NMR (400 MHz, CDCl₃) δ: 3.24 (t, CH₂N₃, *J* = 7.2 Hz, 2H); 1.58 (c, CH₂CH₂N₃, *J* = 7.2, 2H); 1.38-1.18 (m, 18 x CH₂, 36H); 0.86 (s, CH₃, *J* = 6.8, 3H).

¹³C NMR (100 MHz, CDCl₃,) δ: 51.3 (CH₂N₃); 31.7, 29.4, 29.4, 29.4, 29.4, 29.3, 29.2, 29.1, 28.9, 28.6, 26.4 (CH₂); 22.4 (CH₂CH₃); 13.8 (CH₃).

Synthesis of C₂₂-G1-mono-Boc-DAPMA⁹³



Molecular Formula = C₅₆H₁₀₇N₉O₁₀

Molecular Weight = 1065.81

Propyne-[G1]-mono-Boc-DAPMA (160 mg, 0.22mmol) was dissolved in degassed 4:1 THF: H₂O (10ml) along with 1-azidodocosane (75.23 mg, 0.22mmol), CuSO₄·5H₂O (5.5 mg, 22μmol, 10 mol%) and sodium ascorbate (8.72 mg, 44μmol, 20 mol%). The reaction mixture was stirred overnight at room temperature. The THF was then removed *in vacuo* at room temperature and the residue taken up in DCM (20 ml). The solution was washed with H₂O (2 x 10 ml), dried over MgSO₄ and the solvent was evaporated *in vacuo* to leave the crude product (130 mg). The crude product was purified by GPC (DCM) affording the desired product as yellow solid (130 mg, 95μmol, 43%).

R_f = 0.18 (MeOH); 0.75 (95:5 MeOH:NH₄OH).

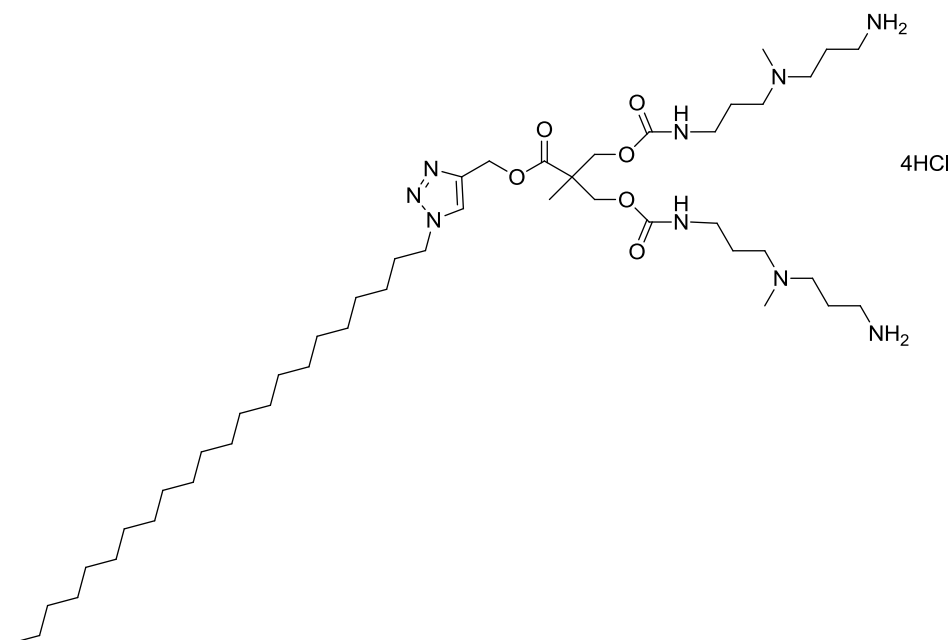
¹H NMR(400MHz, CDCl₃) δ: 7.59 (br s, CH triazole, 1H); 5.89 (br s, NH, 2H); 5.38 (br s, NH, 2H); 5.20 (s, CH₂O triazole, 2H); 4.30 (t, CH₂N triazole, J = 7.2 Hz, 2H); 4.22-4.12 (m, CH₂O, 6H); 3.05-3.24 (m, CH₂NH, 8H); 2.31-2.39 (m, CH₂N(CH₃), 8H); 2.15 (s, N(CH₃), 6H); 1.87 (t, CH₂CH₂N triazole, J = 6.8 Hz, 2H); 1.61 (q, CH₂CH₂NH, J = 6.8 Hz, 8H); 1.40 (s, C(CH₃)₃, 18H); 1.22 (s, CH₂, CH₃, 41H); 0.84 (t, CH₂CH₃, J = 6.4 Hz, 3H).

¹³C NMR (100MHz, CDCl₃) δ: 173.1(C=O); 156.1 (C=ONH); 155.9 (C=ONH); 142.35 (C triazole); 123.47 (CH triazole); 78.79(C(CH₃)₃); 65.60 (CH₂O); 58.3 (CH₂O triazole) 56.06, 55.64 (CH₂N(CH₃)); 52.57 (CH₂C≡CH); 50.35 (CH₂N triazole); 46.88(C(O)C(CH₃)(CH₂)₂); 41.67 (N(CH₃)); 40.08, 39.15 (CH₂NH); 31.83, 30.21, 29.61, 29.58, 29.57, 29.53, 29.46,

29.33; 29.27, 28.93 (CH₂); 28.37 (C(O)C(CH₃)(CH₂)₂); 26.42, 26.40 (CH₂CH₂NH); 22.60 (CH₂CH₃); 17.28 (CH₃); 14.04 (CH₂CH₃).

ESI-MS: Calcd. [M+2H]²⁺ (C₅₆H₁₀₉N₉O₁₀) *m/z* = 533.9143; Obs. [M+2H]²⁺
m/z = 533.9122.

Synthesis of C₂₂-G1⁹³



Molecular Formula = C₄₆H₉₁N₉O₆

Molecular Weight = 865.71

Boc-protected compound **10** (103 mg, 95 μmol) was dissolved in MeOH (20 ml) and HCl gas was bubbled through the solution for 20 s. The reaction mixture was stirred at room temperature for 3 hours. The solvent was removed *in vacuo* to afford the product as an off white foam (93mg, 92μmol, 97%).

R_f = 0.00 (NH₄OH).

¹H NMR (400MHz, MeOD-*d*₄) δ: 8.22 (br s, CH triazole, 1H); 5.20 (br s, NH, 2H); 5.15 (s, CH₂O triazole, 2H); 4.40 (t, CH₂N triazole, *J* 6 Hz, 2H); 4.15-4.09 (m, CH₂O, 6H); 3.31-2.96 (m, CH₂NH, CH₂N(CH₃), 16H); 2.85 (s, N(CH₃), 6H); 2.11 (br s, CH₂CH₂NH, 8H); 1.97-1.82 (m, CH₂CH₂N triazole, 2H); 1.20 (s, CH₂, CH₃, 21H); 0.82 (t, CH₂CH₃, *J* = 7.2 Hz, 3H).

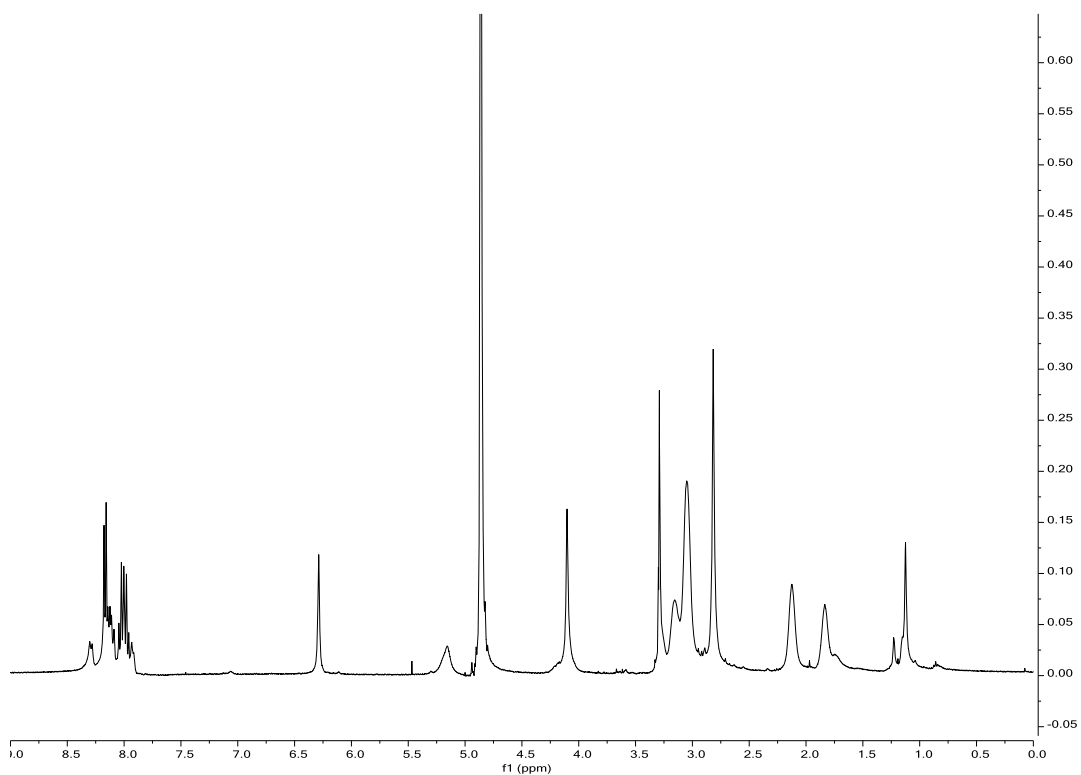
¹³C NMR (100MHz, MeOD-*d*₄) δ: 158.5 (C=ONH); 66.9 (CH₂O); 57.5 (CH₂O triazole); 55.5

(CH₂ triazole); 54.9 (CH₂N(CH₃)); 54.4(C(O)C(CH₃(CH₂)₂); 52.2 (CH₂N triazole); 40.7 (N(CH₃)); 38.8, 38.0(CH₂NH); 33.1, 31.2, 30.8, 30.7, 30.6, 30.5, 30.1, 27.5, 25.9 (CH₂); 23.7, 23.6(CH₂CH₂NH); 17.9 (CH₃); 14.5 (CH₂CH₃).

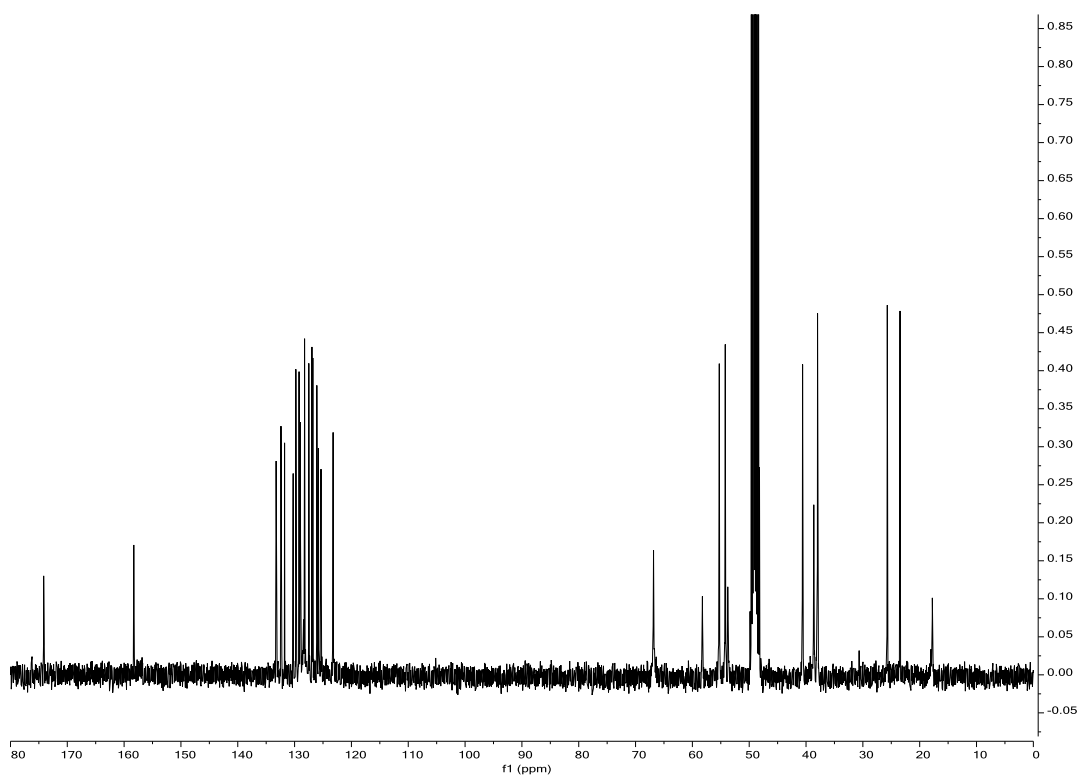
ESI-MS: Calcd. [M+H]⁺(C₄₆H₉₂N₉O₆) *m/z* = 866.7165; Obs. [M+H]⁺ *m/z* = 866.7127.

Appendices

Appendix one: NMR spectra of Py-G1

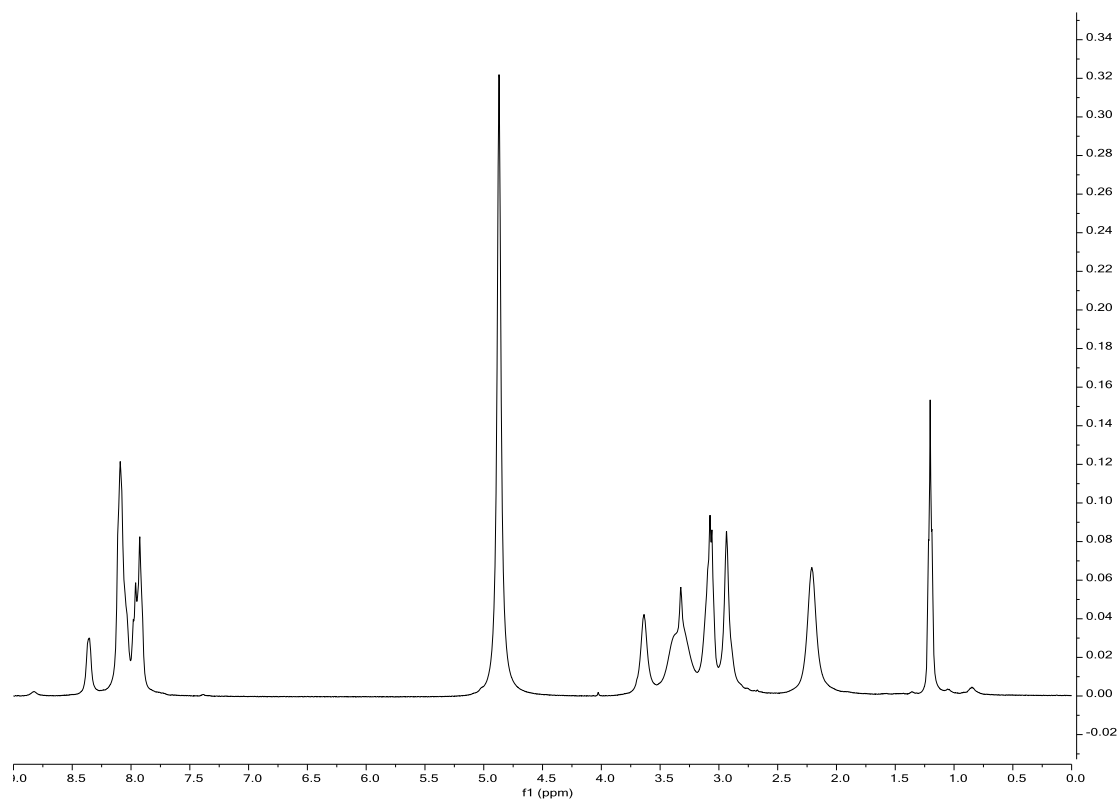


^1H NMR spectra of Py-G1

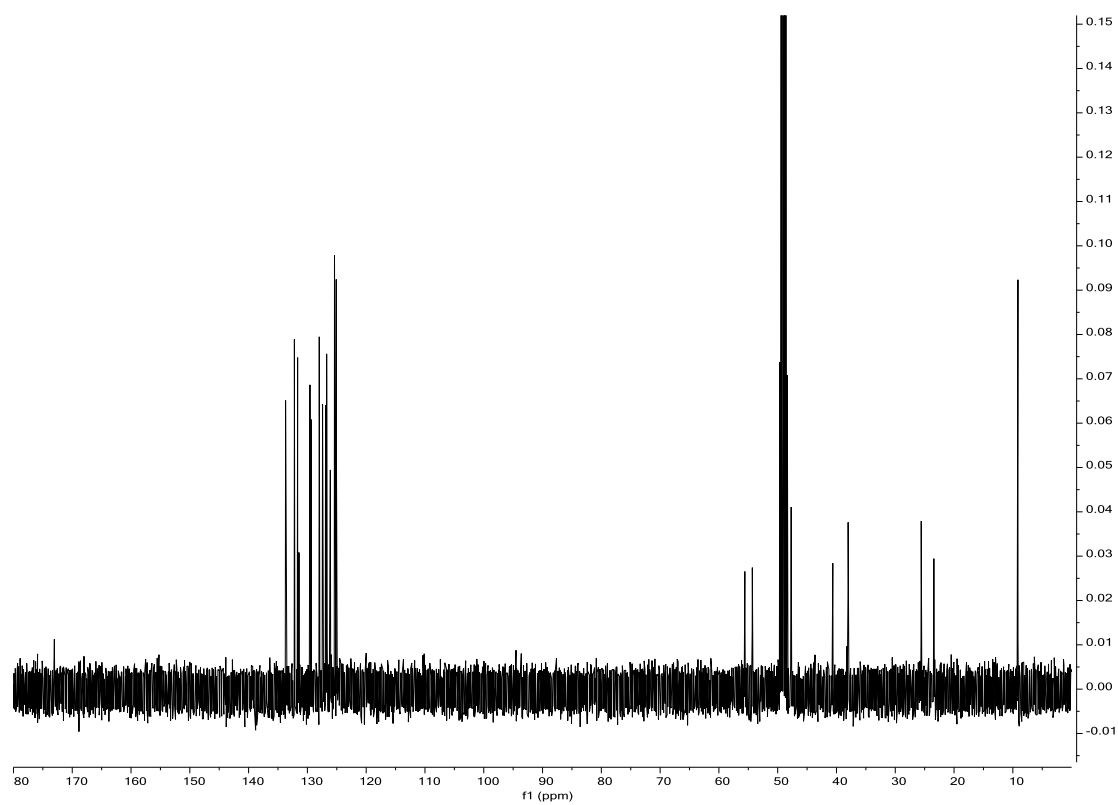


^{13}C NMR spectra of Py-G1

Appendix two: NMR spectra of Py-DAPMA

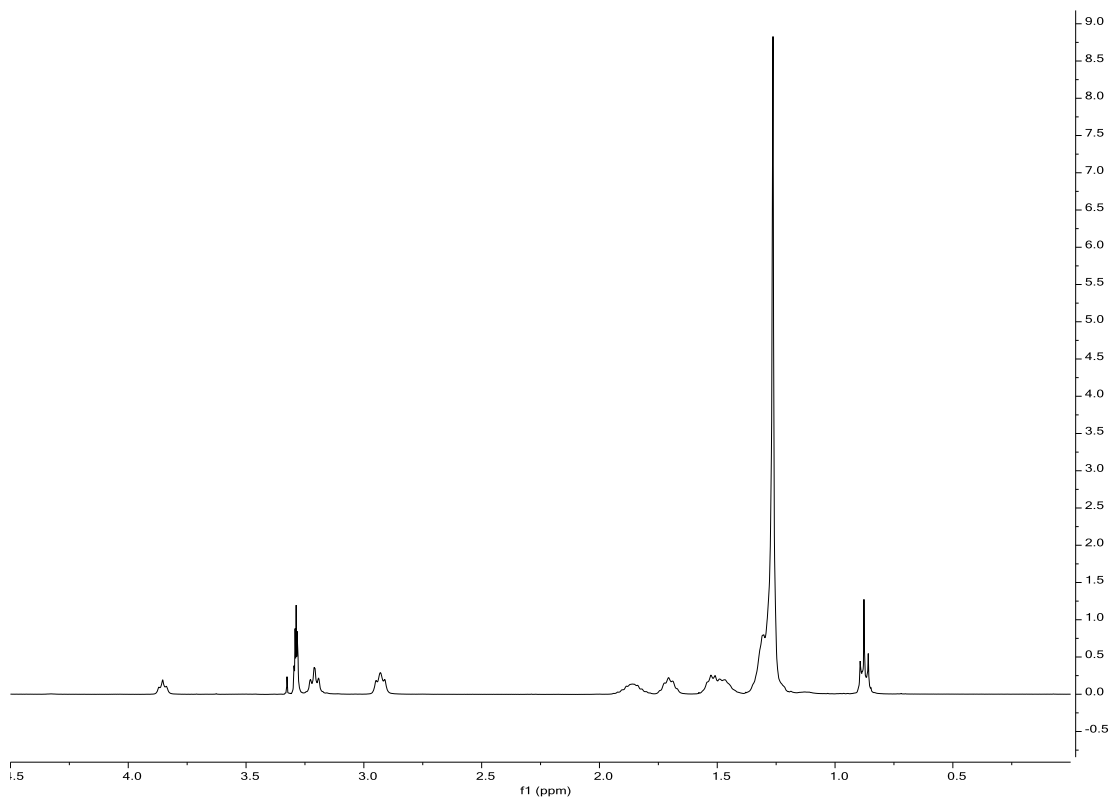


^1H NMR spectra of Py-DAPMA

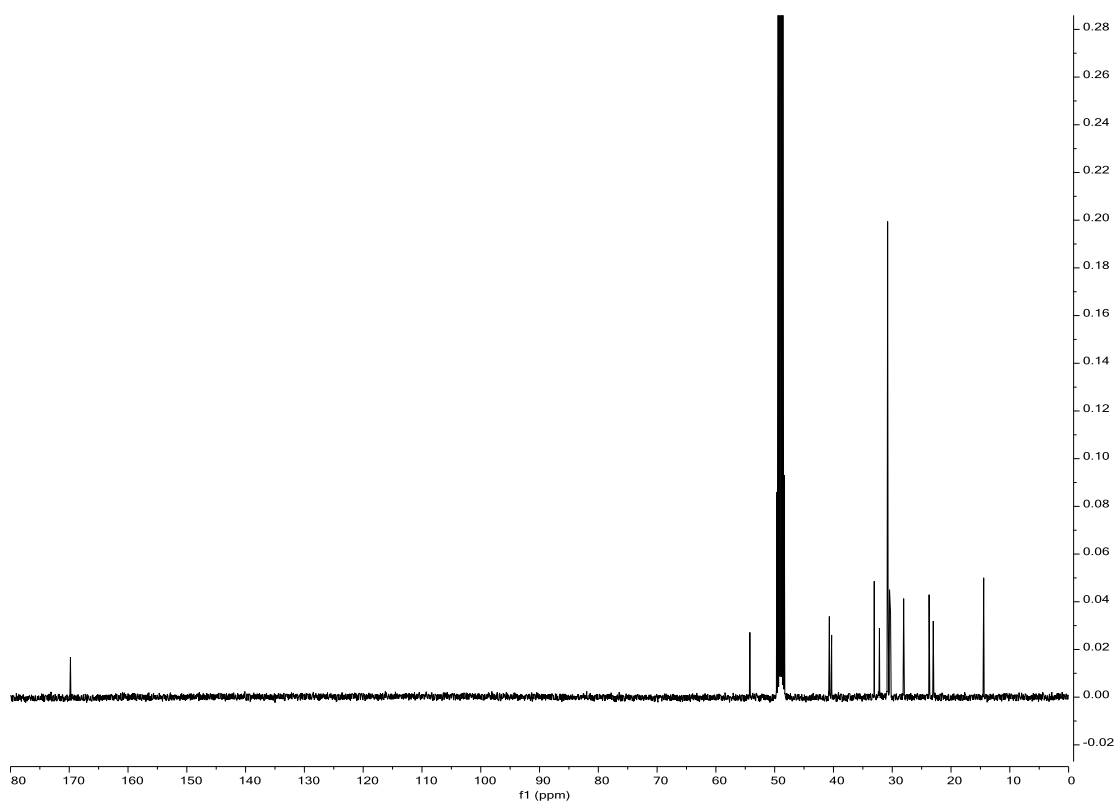


^{13}C NMR spectra of Py-DAPMA

Appendix three: NMR spectra of C₁₆-L-Lys

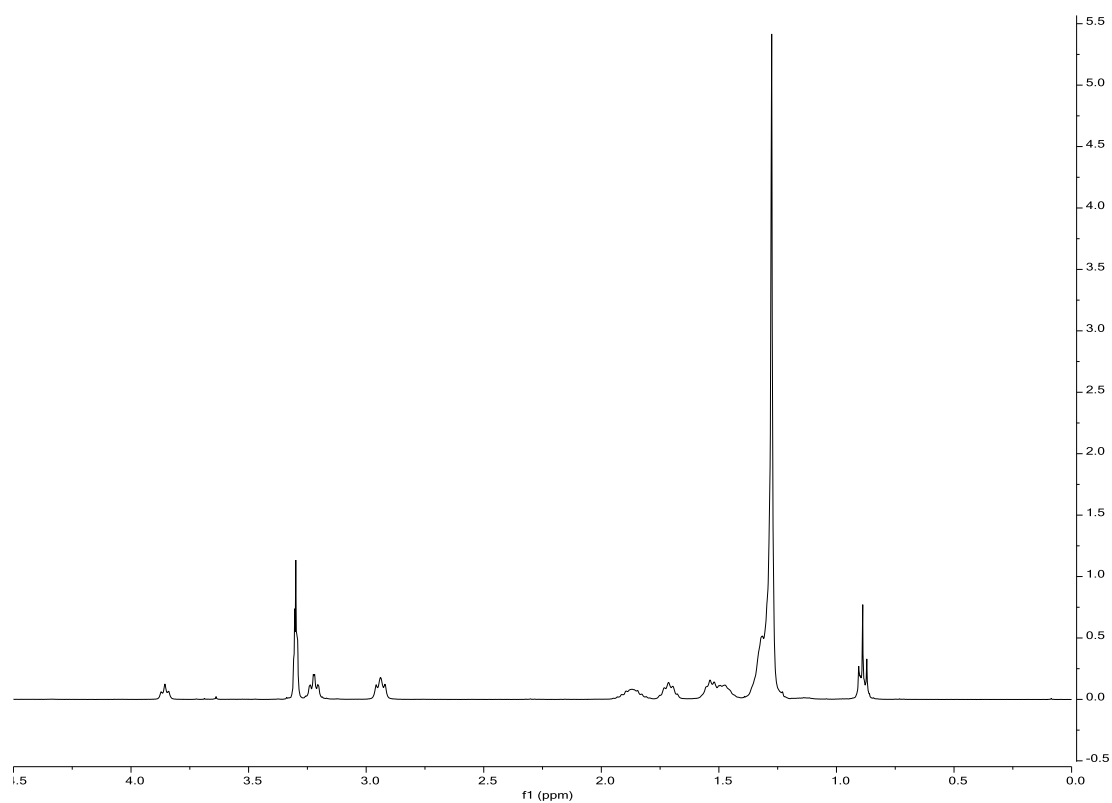


¹H NMR spectra of C₁₆-L-Lys

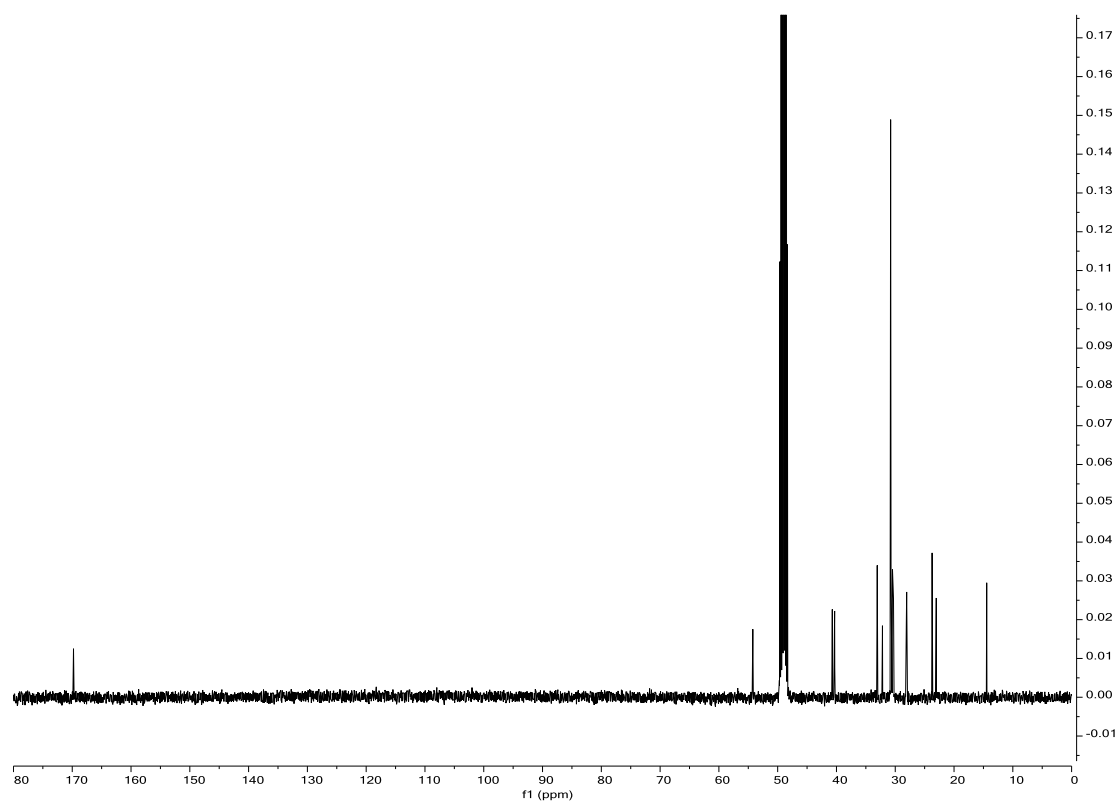


¹³C NMR spectra of C₁₆-L-Lys

Appendix four: NMR spectra of C₁₆-D-Lys

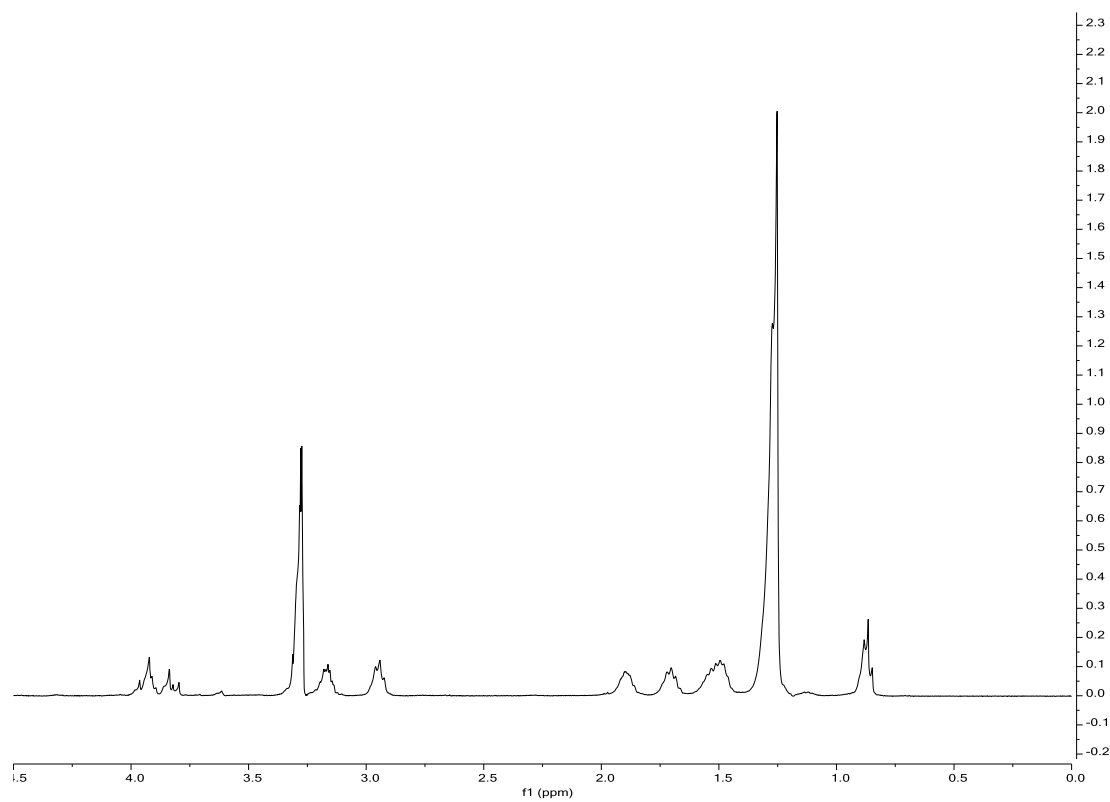


¹H NMR spectra of C₁₆-D-Lys

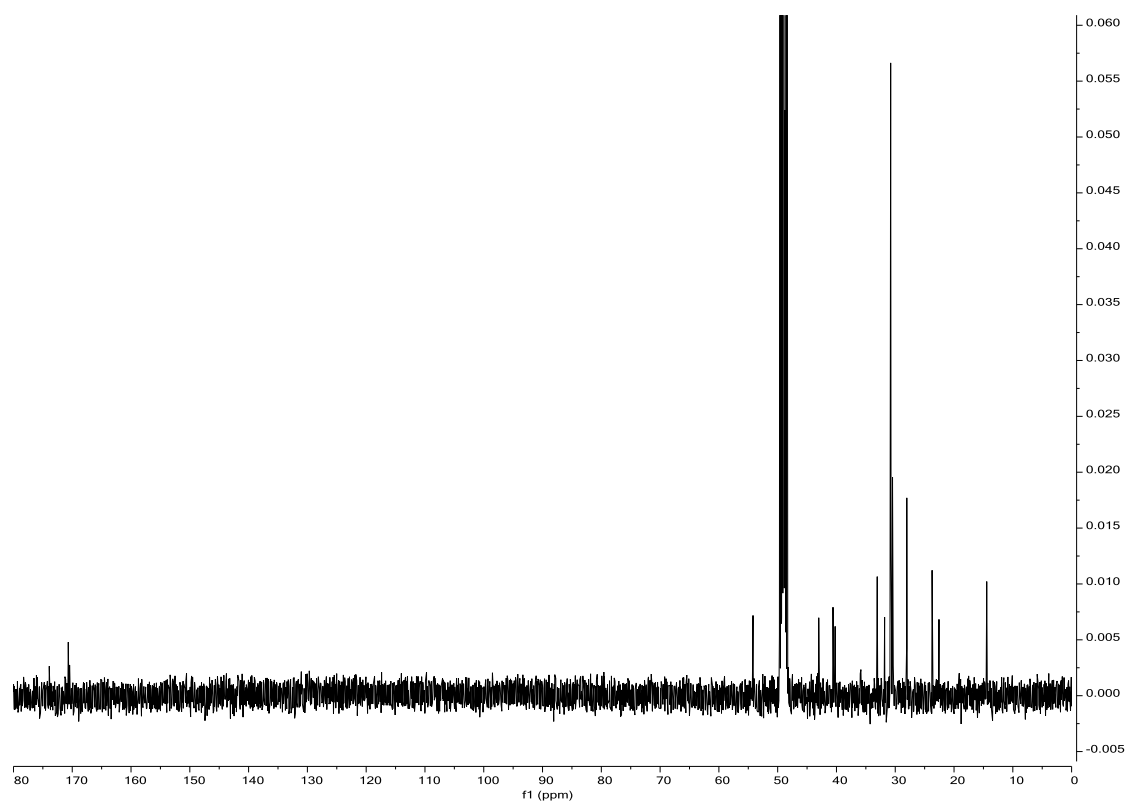


¹³C NMR spectra of C₁₆-D-Lys

Appendix five: NMR spectra of C₁₆-Gly-L-Lys

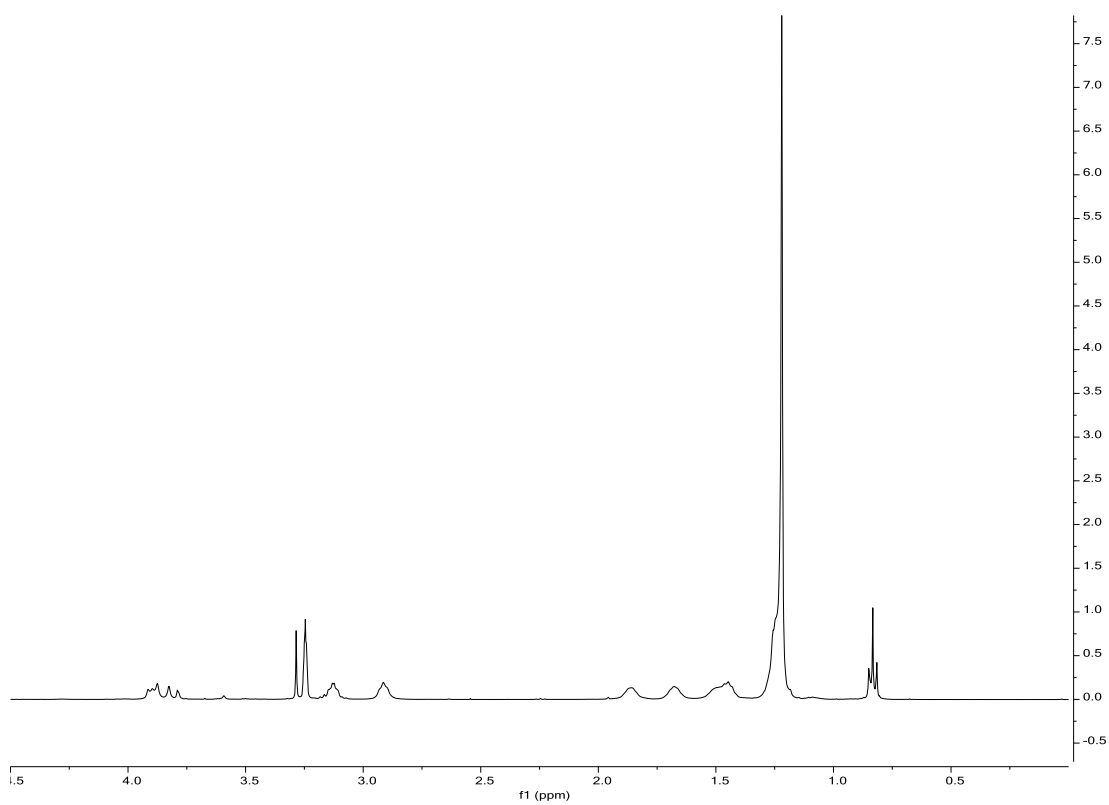


¹H NMR spectra of C₁₆-Gly-L-Lys

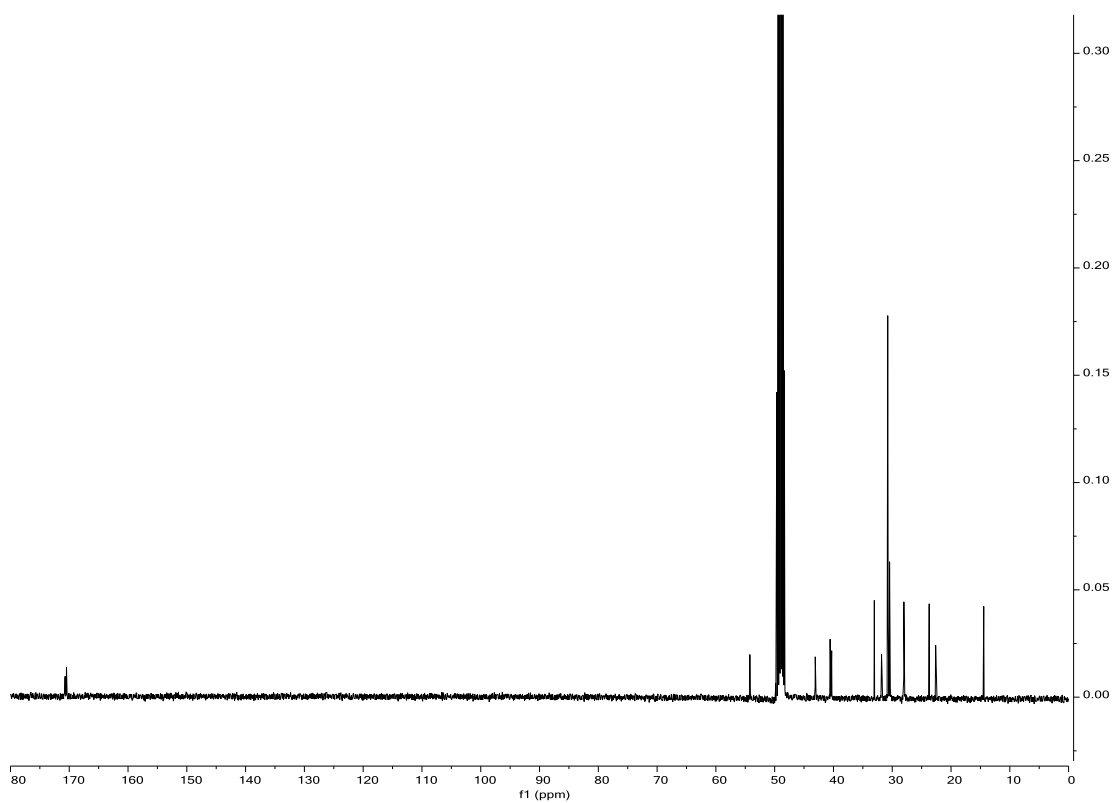


¹³C NMR spectra of C₁₆-Gly-L-Lys

Appendix six: NMR spectra of C₁₆-Gly-D-Lys

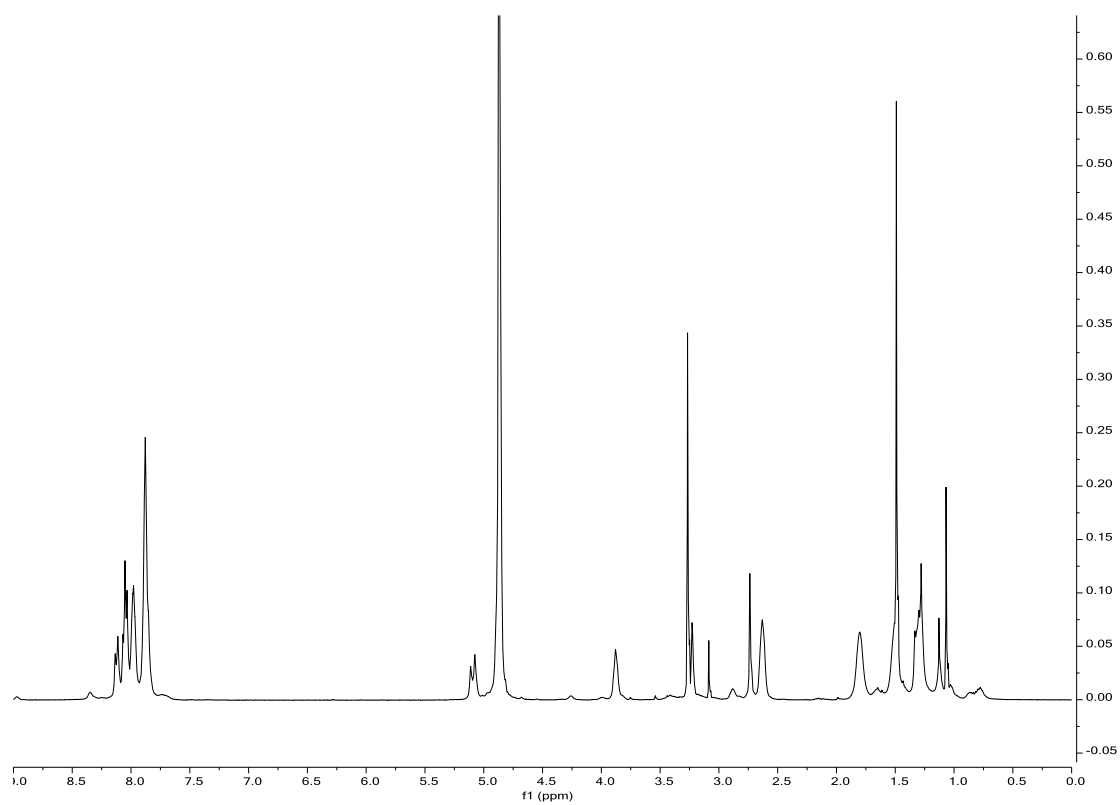


¹H NMR spectra of C₁₆-Gly-D-Lys

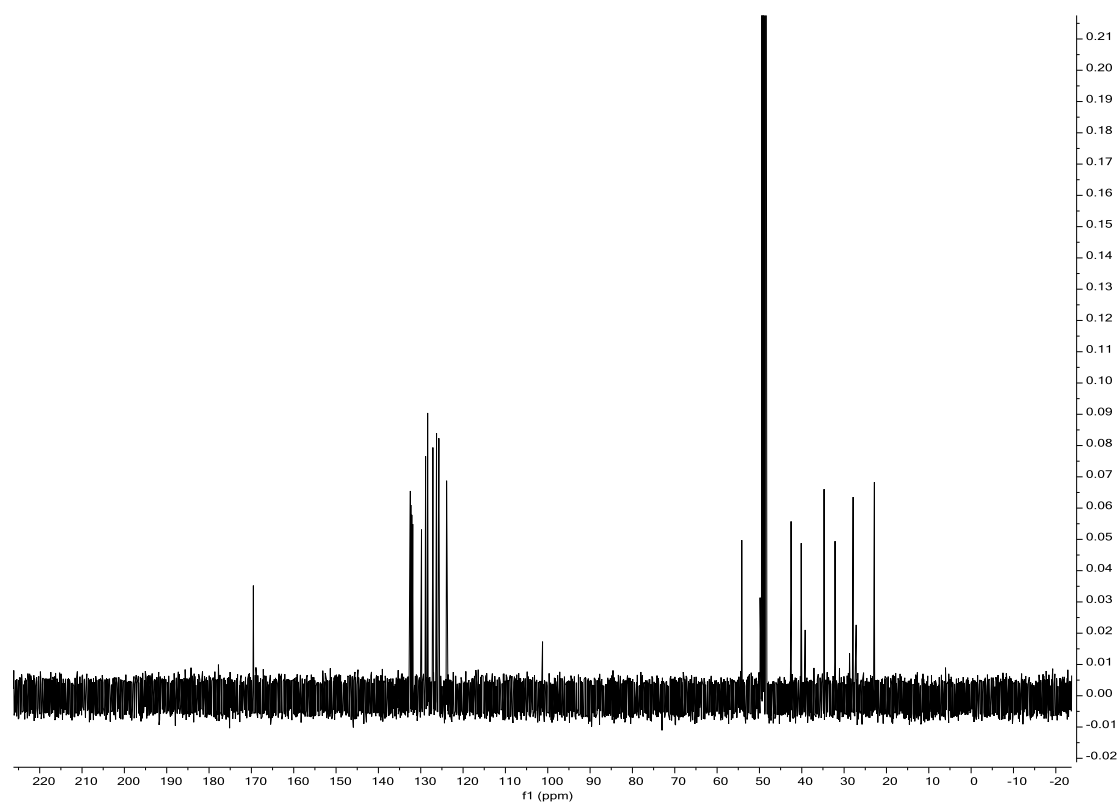


¹³C NMR spectra of C₁₆-Gly-D-Lys

Appendix seven: NMR spectra of Py-L-Lys

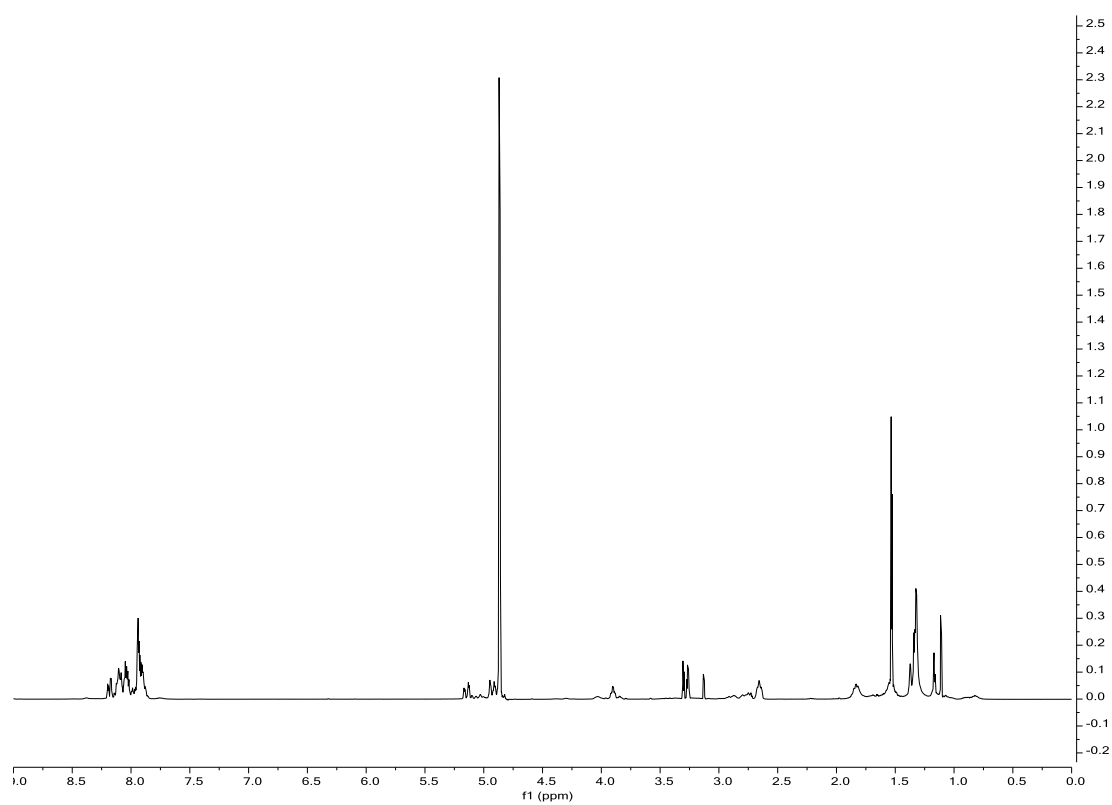


^1H NMR spectra of Py-L-Lys

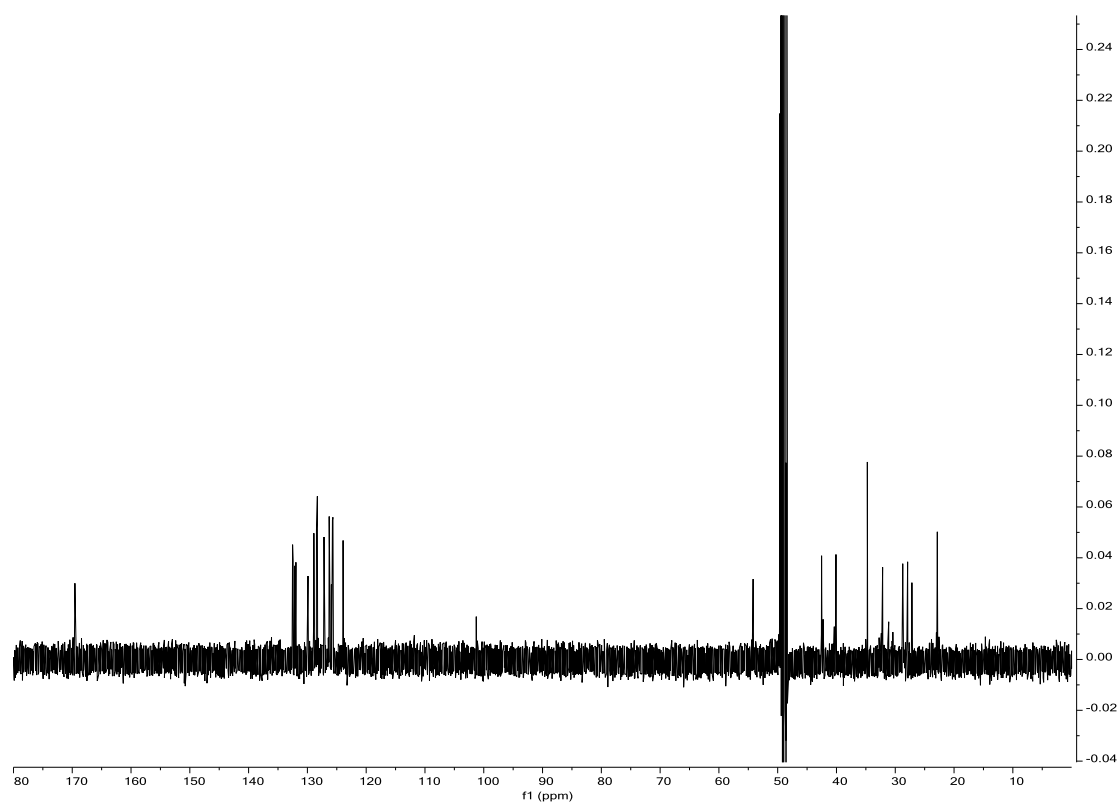


^{13}C NMR spectra of Py-L-Lys

Appendix eight: NMR spectra of Py-D-Lys

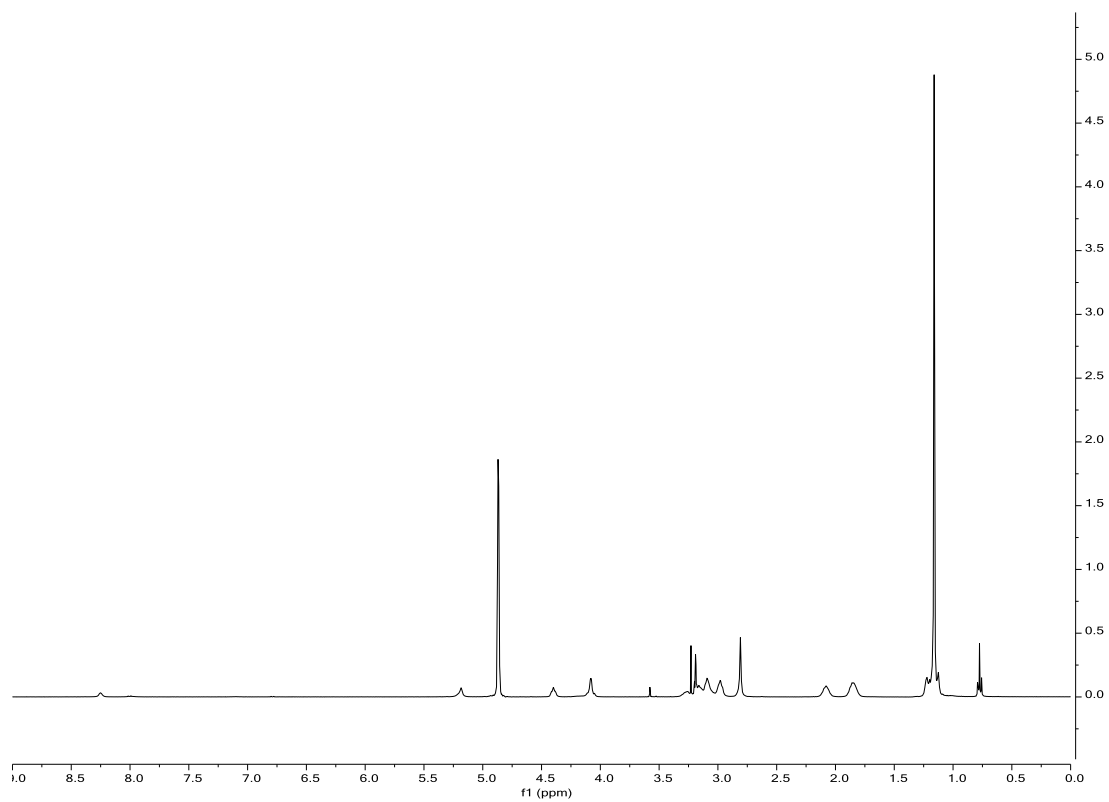


^1H NMR spectra of Py-D-Lys

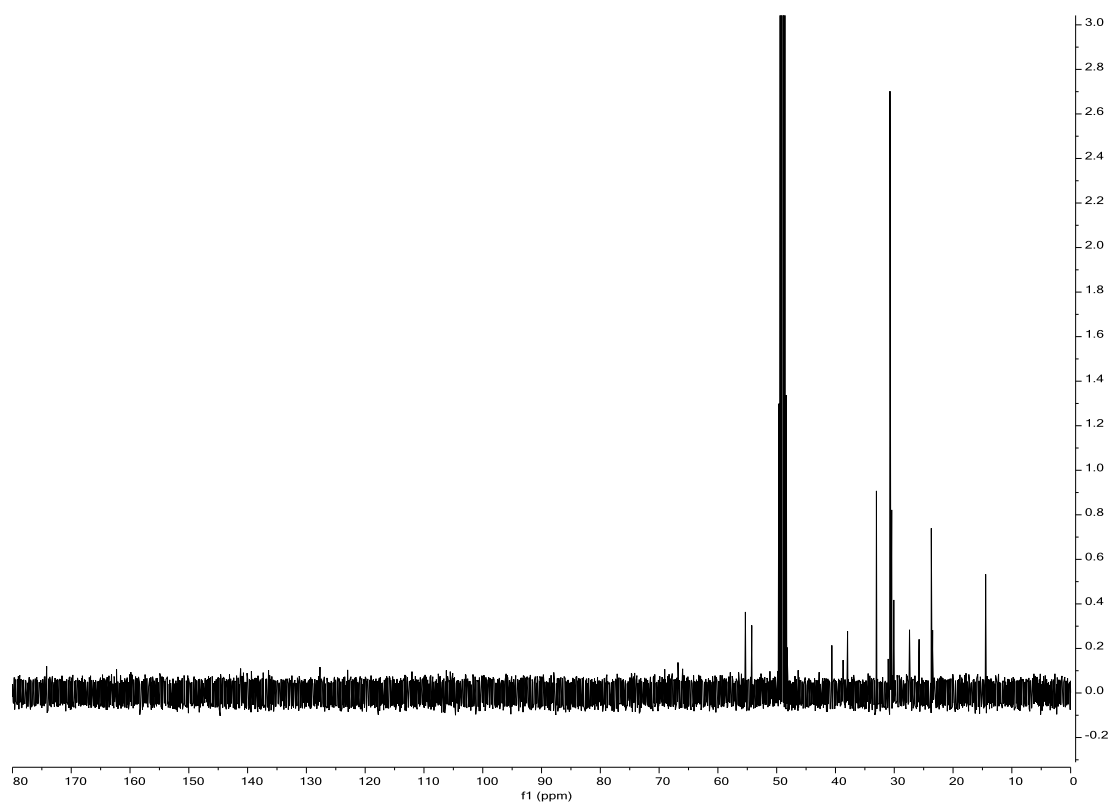


^{13}C NMR spectra of Py-D-Lys

Appendix nine: NMR spectra of C₂₂-G1



¹H NMR spectra of C₂₂-G1



¹³C NMR spectra of C₂₂-G1

Abbreviations

aPTT	Activated partial thromboplastin time
ATIII	Antithrombin III
AuNPs	Gold nanoparticles
br	Broad
bis-MPA	2,2-Bis(hydroxymethyl)propionic acid
Boc	<i>tert</i> -Butyloxycarbonyl
CAC	Critical Aggregation Concentration
CD	Circular dichroism
CE50	Charge excess or charge efficiency at 50% binding
CNT	Carbon nanotube
<i>d</i>	Doublet (NMR)
DAP	Diaminopropane
DMRIE	1,2-Dimyristyloxypropyl-3-dimethyl-hydroxyethyl ammonium bromide
DAPMA	<i>N,N</i> -Di-(3-aminopropyl)- <i>N</i> -methylamine
DCC	<i>N,N'</i> -Dicyclohexylcarbodiimide
DCM	Dichloromethane
DIPEA	Diisopropylethylamine
DLS	Dynamic light scattering
DMF	Dimethylformamide
DOFLA	Diversity-oriented fluorescent library approach
DOGS	Diocetyl-amido-glycylspermine
DOGSHDO	1,2-Dioleoyl- <i>sn</i> -glycero-3'-succinyl-1,6-hexanediol ornithine
DOPE	1,2-Dioleoyl- <i>L</i> - α -glycero-3-phosphatidylethanolamine
DORIE	1,2-Dioleoyloxypropyl-3-dimethyl-hydroxyethyl ammonium bromide
DOSPA	2,3-Dioleoyloxy- <i>N</i> -[2(sperminecarboxamido)ethyl]- <i>N,N</i> -dimethyl-1-propanaminiumtrifluoroacetate
DOTAP	1,2-Dioleoyl-3-trimethylammonium propane
DOTMA	<i>N</i> -[1(2,3-Dioleoyloxy)propyl]- <i>N,N,N</i> -trimethylammonium chloride
EC50	Effective concentration at 50% binding
EDTA	Ethylenediaminetetraacetic acid
ESI-MS	Electrospray ionisation mass spectrometry
EthBr	Ethidium bromide
GPC	Gel permeation chromatography
HSQC	Heteronuclear single-quantum correlation spectroscopy
HMBS	Heteronuclear multiple-bond correlation spectroscopy
IR	Infra Red

<i>J</i>	Coupling frequency
<i>m</i>	Medium (IR)
<i>m</i>	Multiplet (NMR)
Mal-B	Mallard blue
MD	Molecular dynamics
MWCNT	Multi-walled carbon nanotube
Mr	Relative molecular mass
<i>m/z</i>	Mass/charge ratio (Mass spectrometry)
NMR	Nuclear magnetic resonance
PAMAM	Poly(amidoamine)
PBS	Phosphate buffered saline
PBr ₃	Phosphorus tribromide
PDI	Polydispersity index (DLS)
PEI	Poly(ethyleneimine)
PLL	Poly(L-lysine)
PPI	Poly(propyleneimine)
ppm	Parts per million (NMR)
<i>q</i>	Quartet (NMR)
RNA	Ribonucleic acid
R _f	Retention factor
<i>s</i>	Strong (IR)
<i>s</i>	Singlet (NMR)
SAMul	Self-assembled multivalency
SWCNT	Single-walled carbon nanotube
<i>t</i>	Triplet (NMR)
TBTU	<i>O</i> -(Benzotriazol-1-yl)- <i>N,N,N',N'</i> -tetramethyluronium tetrafluoroborate
TEM	Transmission electron microscopy
THF	Tetrahydrofuran
TLC	Thin layer chromatography
TsOH	<i>para</i> -Toluene sulfonic acid
UV	Ultra-violet
Vis	Visible (light)
<i>w</i>	Weak (IR)

References

1. J.-M. Lehn, *Proc. Natl. Acad. Sci. U. S. A.*, 2002, **99**, 4763-4768.
2. G. R. Desiraju, *Nature*, 2001, **412**, 397-400.
3. J. Rebek, *Angew. Chem. Int. Ed. Engl.*, 1990, **29**, 245-255.
4. D. B. Amabilino and J. F. Stoddart, *Chem. Rev.*, 1995, **95**, 2725-2828.
5. M. C. T. Fyfe and J. F. Stoddart, *Acc. Chem. Res.*, 1997, **30**, 393-401.
6. N. Bordenave, B. R. Hamaker and M. G. Ferruzzi, *Food. Funct.*, 2014, **5**, 18-34.
7. G. M. Whitesides, J. P. Mathias and C. T. Seto, *Science*, 1991, **254**, 1312-1319.
8. J.-M. Lehn, *Proc. Natl. Acad. Sci. U. S. A.*, 2002, **99**, 4763-4768.
9. J.-M. Lehn, *Science*, 2002, **295**, 2400-2403.
10. A. Klug, *Angew. Chem. Int. Ed. Engl.*, 1983, **22**, 565-582.
11. G. M. Whitesides and R. F. Ismagilov, *Science*, 1999, **284**, 89-92.
12. J. D. Watson and F. H. C. Crick, *Nature*, 1953, **171**, 737-738.
13. L. Pray, *Nature Education*, 2008, **1**, 100.
14. D. Philp and J. F. Stoddart, *Angew. Chem. Int. Ed. Engl.*, 1996, **35**, 1155-1196.
15. M. M. Murr, G. S. Thakur, Y. Li, H. Tsuruta, I. Mezic and D. E. Morse, *Nano Today*, 2009, **4**, 116-124.
16. J.-F. Xu, L.-Y. Niu, Y.-Z. Chen, L.-Z. Wu, C.-H. Tung and Q.-Z. Yang, *Org. Lett.*, 2014, **16**, 4016-4019.
17. D. C. Sherrington and K. A. Taskinen, *Chem. Soc. Rev.*, 2001, **30**, 83-93.
18. E. Gazit, *FASEB J.*, 2002, **16**, 77-83.
19. A. A. Profit, V. Felsen, J. Chinwong, E.-R. E. Mojica and R. Z. B. Desamero, *Proteins*, 2013, **81**, 690-703.
20. M. Bernardi, M. Giulianini and J. C. Grossman, *ACS Nano*, 2010, **4**, 6599-6606.
21. Y. Li, T. Liu, H. Liu, M.-Z. Tian and Y. Li, *Acc. Chem. Res.*, 2014, **47**, 1186-1198.
22. S. Liu and B. C. Gibb, *Chem. Commun.*, 2008, 3709-3716.
23. S. Leininger, B. Olenyuk and P. J. Stang, *Chem. Rev.*, 2000, **100**, 853-908.
24. R. Zou, Q. Wang, J. Wu, J. Wu, C. Schmuck and H. Tian, *Chem. Soc. Rev.*, 2015, **44**, 5200-5219.
25. S. Grimme, *Angew. Chem. Int. Ed.*, 2008, **47**, 3430-3434.
26. M. O. Sinnokrot, E. F. Valeev and C. D. Sherrill, *J. Am. Chem. Soc.*, 2002, **124**,

10887-10893.

27. H. Engelkamp, S. Middelbeek, R. J. M and Nolte, *Science*, 1999, **284**, 785-788.
28. D. Chandler, *Nature*, 2005, **437**, 640-647.
29. X. L. Chi, A. J. Guerin, R. A. Haycock, C. A. Hunter and L. D. Sarson, *J. Chem. Soc.-Chem. Commun.*, 1995, 2563-2565.
30. D. K. Smith, A. R. Hirst, C. S. Love, J. G. Hardy, S. V. Brignell and B. Huang, *Prog. Polym. Sci.*, 2005, **30**, 220-293.
31. P. Posocco, S. Pricl, S. Jones, A. Barnard and D. K. Smith, *Chem. Sci.*, 2010, **1**, 393-404.
32. J. N. Israelachvili, D. J. Mitchell and B. W. Ninham, *J. Chem. Soc., Faraday Trans. II*, 1976, **72**, 1525-1568.
33. J. N. Israelachvili, S. Marcelja and R. G. Horn, *Quart. Rev. Biophys.*, 1980, **13**, 121-200.
34. A. Ballesteros-Gómez, M. D. Sicilia and S. Rubio, *Anal. Chim. Acta.*, 2010, **677**, 108-130.
35. P. Zhang, X. Xu, M. Zhang, J. Wang, G. Bai and H. Yan, *Langmuir*, 2015, **31**, 7919-7925.
36. S. Zhang, H.-J. Sun, A. D. Hughes, B. Draghici, J. Lejniaks, P. Leowanawat, A. Bertin, L. Otero De Leon, O. V. Kulikov, Y. Chen, D. J. Pochan, P. A. Heiney and V. Percec, *ACS Nano*, 2014, **8**, 1554-1565.
37. C. Fasting, C. A. Schalley, M. Weber, O. Seitz, S. Hecht, B. Kokschi, J. Dervedde, C. Graf, E.-W. Knapp and R. Haag, *Angew. Chem. Int. Ed.*, 2012, **51**, 10472-10498.
38. A. Barnard and D. K. Smith, *Angew. Chem. Int. Ed.*, 2012, **51**, 6572-6581.
39. P. M. Levine, T. P. Carberry, J. M. Holub and K. Kirshenbaum, *Med. Chem. Commun.*, 2013, **4**, 493-509.
40. G. M. Pavan, A. Danani, S. Pricl and D. K. Smith, *J. Am. Chem. Soc.*, 2009, **131**, 9686-9694.
41. M. Mammen, S. K. Choi and G. M. Whitesides, *Angew. Chem. Int. Ed.*, 1998, **37**, 2755-2794.
42. J. J. Lundquist and E. J. Toone, *Chem. Rev.*, 2002, **102**, 555-578.
43. S. M. Bromfield, P. Posocco, C. W. Chan, M. Calderon, S. E. Guimond, J. E.

- Turnbull, S. Pricl and D. K. Smith, *Chem. Sci.*, 2014, **5**, 1484-1492.
44. A. Barnard, P. Posocco, M. Fermeglia, A. Tschiche, M. Calderon, S. Pricl and D. K. Smith, *Org. Biomol. Chem.*, 2014, **12**, 446-455.
45. D. J. Welsh, P. Posocco, S. Pricl and D. K. Smith, *Org. Biomol. Chem.*, 2013, **11**, 3177-3186.
46. Y.-B. Lim, K.-S. Moon and M. Lee, *Chem. Soc. Rev.*, 2009, **38**, 925-934.
47. J. E. Kingery-Wood, K. W. Williams, G. B. Sigal and G. M. Whitesides, *J. Am. Chem. Soc.*, 1992, **114**, 7303-7305.
48. K. Petkau-Milroy and L. Brunsveld, *Eur. J. Org. Chem.*, 2013, **2013**, 3470-3476.
49. C. W. Chan and D. K. Smith, *Chem. Commun.*, 2016, **52**, 3785-3788.
50. D. L. Rabenstein, *Nat. Prod. Rep.*, 2002, **19**, 312-331.
51. S. M. Bromfield, E. Wilde and D. K. Smith, *Chem. Soc. Rev.*, 2013, **42**, 9184-9195.
52. J. Choay, M. Petitou, J. C. Lormeau, P. Sinäy, B. Casu and G. Gatti, *Biochem. Biophys. Res. Commun.*, 1983, **116**, 492-499.
53. D. L. Rabenstein, *Nat. Prod. Rep.*, 2002, **19**, 312-331.
54. H. C. Hemker and S. Béguin, *Thromb. Haemost.*, 1993, **70**, 724-728.
55. C. J. Pallister and M. S. Watson, *Haematology*, Scion Publishing, United Kingdom, 2010.
56. E. W. Davie, K. Fujikawa and W. Kisiel, *Biochemistry*, 1991, **30**, 10363-10370.
57. J. Hirsh, T. E. Warkentin, S. G. Shaughnessy, S. S. Anand, J. L. Halperin, R. Raschke, C. Granger, E. M. Ohman and J. E. Dalen, *Chest*, 2001, **119**, 64S-94S.
58. R. Balhorn, *Genome Biol.*, 2007, **8**, 8.
59. F. P. Ottensmeyer, R. F. Whiting and A. P. Korn, *Proc. Natl. Acad. Sci. U. S. A.*, 1975, **72**, 4953-4955.
60. L. C. Chang, J. F. Liang, H.-F. Lee, L. M. Lee and V. C. Yang, *Aaps Pharmsci.*, 2001, **3**, art. no.-18.
61. R. Porsche and Z. R. Brenner, *Heart Lung*, **28**, 418-428.
62. C. H. Lee, H. C. Cheng and L. W. Ko, *Emergency Med.*, 2013, **3**, 157.
63. B. Girolami and A. Girolami, *Semin. Thromb. Hemost.*, 2006, **32**, 803-809.
64. T. E. Warkentin, M. N. Levine, J. Hirsh, P. Horsewood, R. S. Roberts, M. Gent and J. G. Kelton, *New. Eegl. J. Med.*, 1995, **332**, 1330-1336.

65. R. J. Simko, F. F. W. Tsung and E. J. Stanek, *Ann. Pharmacother.*, 1995, **29**, 1015-1021.
66. J. L. Francis, J. B. Groce and G. Heparin Consensus, *Pharmacotherapy*, 2004, **24**, 108S-119S.
67. S. Horton and S. Augustin, in *Haemostasis*, ed. P. Monagle, Humana Press, 2013, vol. 992, pp. 155-167.
68. S. C. Ma, V. C. Yang, B. Fu and M. E. Meyerhoff, *Anal. Chem.*, 1993, **65**, 2078-2084.
69. Y. Chen, R. N. Liang and W. Qin, *Chinese Chem. Lett.*, 2012, **23**, 233-236.
70. H. Qi, L. Zhang, L. Yang, P. Yu and L. Mao, *Anal. Chem.*, 2013, **85**, 3439-3445.
71. S. Amemiya, Y. Kim, R. Ishimatsu and B. Kabagambe, *Anal. Bioanal. Chem.*, 2010, **399**, 571-579.
72. P. N. Marshall, *Histochem. J.*, **11**, 489-493.
73. P. N. Marshall and S. M. Lewis, *Stain Technol.*, 1975, **50**, 375-381.
74. E. Tuite and J. M. Kelly, *Biopolymers*, 1995, **35**, 419-433.
75. M. D. Klein, R. A. Drongowski, R. J. Linhardt and R. S. Langer, *Anal. Biochem.*, 1982, **124**, 59-64.
76. Q. Jiao and Q. Liu, *Anal. Lett.*, 1998, **31**, 1311-1323.
77. Z. Zhong and E. V. Anslyn, *J. Am. Chem. Soc.*, 2002, **124**, 9014-9015.
78. A. T. Wright, Z. L. Zhong and E. V. Anslyn, *Angew. Chem. Int. Ed.*, 2005, **44**, 5679-5682.
79. S. Wang and Y.-T. Chang, *Chem. Commun.*, 2008, 1173-1175.
80. S. M. Bromfield, A. Barnard, P. Posocco, M. Fermeiglia, S. Pricl and D. K. Smith, *J. Am. Chem. Soc.*, 2013, **135**, 2911-2914.
81. R. Cao and B. Li, *Chem. Commun.*, 2011, **47**, 2865-2867.
82. N. Vasimalai and S. A. John, *J. Mater. Chem. B*, 2013, **1**, 5620-5627.
83. X. Fu, L. Chen and J. Li, *Analyst*, 2012, **137**, 3653-3658.
84. K. Pu, R. Zhan, J. Liang and B. Liu, *Sci. China Chem.*, 2011, **54**, 567-574.
85. H. Shi, H. Sun, H. Yang, S. Liu, G. Jenkins, W. Feng, F. Li, Q. Zhao, B. Liu and W. Huang, *Adv. Funct. Mater.*, 2013, **23**, 3268-3276.
86. F. M. Winnik, *Chem. Rev.*, 1993, **93**, 587-614.

87. S. Karuppannan and J.-C. Chambron, *Chem. Asian J.*, 2011, **6**, 964-984.
88. X. Zhang, S. Rehm, M. M. Safont-Sempere and F. Würthner, *Nat. Chem.*, 2009, **1**, 623-629.
89. L. Zeng, P. Wang, H. Zhang, X. Zhuang, Q. Dai and W. Liu, *Org. Lett.*, 2009, **11**, 4294-4297.
90. Q. Dai, W. Liu, X. Zhuang, J. Wu, H. Zhang and P. Wang, *Anal. Chem.*, 2011, **83**, 6559-6564.
91. D.-H. Kim, Y. J. Park, K. H. Jung and K.-H. Lee, *Anal. Chem.*, 2014, **86**, 6580-6586.
92. R. C. Pasquali, M. P. Taurozzi and C. Bregni, *Int. J. Pharm.*, 2008, **356**, 44-51.
93. A. C. Rodrigo, A. Barnard, J. Cooper and D. K. Smith, *Angew. Chem. Int. Ed.*, 2011, **50**, 4675-4679.
94. H. Ihre, A. Hult and E. Söderlind, *J. Am. Chem. Soc.*, 1996, **118**, 6388-6395.
95. H. Ihre, A. Hult, J. M. J. Fréchet and I. Gitsov, *Macromolecules*, 1998, **31**, 4061-4068.
96. H. Ihre, O. L. Padilla De Jesús and J. M. J. Fréchet, *J. Am. Chem. Soc.*, 2001, **123**, 5908-5917.
97. E. R. Gillies and J. M. J. Fréchet, *J. Am. Chem. Soc.*, 2002, **124**, 14137-14146.
98. C. C. Lee, E. R. Gillies, M. E. Fox, S. J. Guillaudeu, J. M. J. Fréchet, E. E. Dy and F. C. Szoka, *Proc. Natl. Acad. Sci. U. S. A.*, 2006, **103**, 16649-16654.
99. P. Wu, M. Malkoch, J. N. Hunt, R. Vestberg, E. Kaltgrad, M. G. Finn, V. V. Fokin, K. B. Sharpless and C. J. Hawker, *Chem. Commun.*, 2005, 5775-5777.
100. A. Saha and S. Ramakrishnan, *Macromolecules*, 2009, **42**, 4028-4037.
101. M. Cavazzana-Calvo, S. Hacein-Bey, G. d. S. Basile, F. Gross, E. Yvon, P. Nusbaum, F. Selz, C. Hue, S. Certain, J.-L. Casanova, P. Bousso, F. L. Deist and A. Fischer, *Science*, 2000, **288**, 669-672.
102. C. W. Tornøe, C. Christensen and M. Meldal, *J. Org. Chem.*, 2002, **67**, 3057-3064.
103. P. Appukkuttan, W. Dehaen, V. V. Fokin and E. Van der Eycken, *Org. Lett.*, 2004, **6**, 4223-4225.
104. F. Himo, T. Lovell, R. Hilgraf, V. V. Rostovtsev, L. Noodleman, K. B. Sharpless and V. V. Fokin, *J. Am. Chem. Soc.*, 2005, **127**, 210-216.
105. V. D. Bock, H. Hiemstra and J. H. van Maarseveen, *Eur. J. Org. Chem.*, 2006,

- 51-68.
106. P. Wu, A. K. Feldman, A. K. Nugent, C. J. Hawker, A. Scheel, B. Voit, J. Pyun, J. M. J. Fréchet, K. B. Sharpless and V. V. Fokin, *Angew. Chem. Int. Ed.*, 2004, **43**, 3928-3932.
 107. J. W. Lee, J. H. Kim, H. J. Kim, S. C. Han, J. H. Kim, W. S. Shin and S.-H. Jin, *Bioconjugate Chem.*, 2007, **18**, 579-584.
 108. G. Franc and A. Kakkar, *Chem. Commun.*, 2008, 5267-5276.
 109. M. Meldal and C. W. Tornøe, *Chem. Rev.*, 2008, **108**, 2952-3015.
 110. H. Jang, A. Fafarman, J. M. Holub and K. Kirshenbaum, *Org. Lett.*, 2005, **7**, 1951-1954.
 111. M. C. A. Stuart, J. C. van de Pas and J. B. F. N. Engberts, *J. Phys. Org. Chem.*, 2005, **18**, 929-934.
 112. J. Hirsh and R. Raschke, *Chest*, 2004, **126**, 188S-203S.
 113. S. V. Nalage, S. V. Bhosale, S. K. Bhargava and S. V. Bhosale, *Tetrahedron Lett.*, 2012, **53**, 2864-2867.
 114. P. Thirupathi, J.-Y. Park, L. N. Neupane, M. Y. L. N. Kishore and K.-H. Lee, *ACS Appl. Mater. Interfaces*, 2015, **7**, 14243-14253.
 115. M. Schuksz, M. M. Fuster, J. R. Brown, B. E. Crawford, D. P. Ditto, R. Lawrence, C. A. Glass, L. Wang, Y. Tor and J. D. Esko, *Proc. Natl. Acad. Sci. U. S. A.*, 2008, **105**, 13075-13080.
 116. S. Choi, D. J. Clements, V. Pophristic, I. Ivanov, S. Vemparala, J. S. Bennett, M. L. Klein, J. D. Winkler and W. E. DeGrado, *Angew. Chem. Int. Ed.*, 2005, **44**, 6685-6689.
 117. A. Verrecchio, M. W. Germann, B. P. Schick, B. Kung, T. Twardowski and J. D. San Antonio, *J. Biol. Chem.*, 2000, **275**, 7701-7707.
 118. B. P. Schick, D. Maslow, A. Moshinski and J. D. San Antonio, *Blood*, 2004, **103**, 1356-1363.
 119. E. M. A. van de Westerlo, T. Smetsers, M. Dennissen, R. J. Linhardt, J. H. Veerkamp, G. N. P. van Muijen and T. H. van Kuppevelt, *Blood*, 2002, **99**, 2427-2433.
 120. H.-F. Wu, R. L. Lundblad and F. C. Church, *Blood*, 1995, **85**, 421-428.

121. T. Mecca, G. M. L. Consoli, C. Geraci, R. La Spina and F. Cunsolo, *Org. Biomol. Chem.*, 2006, **4**, 3763-3768.
122. T. Mecca and F. Cunsolo, *Polym. Adv. Technol.*, 2010, **21**, 752-757.
123. E. Buhleier, W. Wehner and F. Vogtle, *Synthesis*, 1978, 155-158.
124. P. Y. Hayes, B. P. Ross, B. G. Thomas and I. Toth, *Bioorg. Med. Chem.*, 2006, **14**, 143-152.
125. K. Rajangam, H. A. Behanna, M. J. Hui, X. Han, J. F. Hulvat, J. W. Lomasney and S. I. Stupp, *Nano Lett.*, 2006, **6**, 2086-2090.
126. T. Friedmann and R. Roblin, *Science*, 1972, **175**, 949-955.
127. T. Friedmann, *Nat. Genet.*, 1992, **2**, 93-98.
128. J. Kaiser, *Science*, 2003, **299**, 495-495.
129. E. Marshall, *Science*, 1999, **286**, 2244-2245.
130. S. Y. Wong, J. M. Pelet and D. Putnam, *Progr. Polym. Sci.*, 2007, **32**, 799-837.
131. W. Zauner, M. Ogris and E. Wagner, *Adv. Drug Deliv. Rev.*, 1998, **30**, 97-113.
132. J. Suh, H. J. Paik and B. K. Hwang, *Bioorganic Chem.*, 1994, **22**, 318-327.
133. M. X. Tang, C. T. Redemann and F. C. Szoka, *Bioconjugate Chem.*, 1996, **7**, 703-714.
134. D. K. Smith, *Curr. Top. Med. Chem.*, 2008, **8**, 1187-1203.
135. D. Y. Kwoh, C. C. Coffin, C. P. Lollo, J. Jovenal, M. G. Banaszczyk, P. Mullen, A. Phillips, A. Amini, J. Fabrycki, R. M. Bartholomew, S. W. Brostoff and D. J. Carlo, *Biochim. Biophys. Acta, Gene Struct. Expression*, 1999, **1444**, 171-190.
136. Y. H. Choi, F. Liu, J.-S. Kim, Y. K. Choi, J. S. Park and S. W. Kim, *J. of Controlled Release*, 1998, **54**, 39-48.
137. P. P. Karmali and A. Chaudhuri, *Med. Res. Rev.*, 2007, **27**, 696-722.
138. P. L. Felgner, T. R. Gadek, M. Holm, R. Roman, H. W. Chan, M. Wenz, J. P. Northrop, G. M. Ringold and M. Danielsen, *Proc. Natl. Acad. Sci. U. S. A.*, 1987, **84**, 7413-7417.
139. R. W. Malone, P. L. Felgner and I. M. Verma, *Proc. Natl. Acad. Sci. U. S. A.*, 1989, **86**, 6077-6081.
140. P. L. Felgner and G. M. Ringold, *Nature*, 1989, **337**, 387-388.
141. J. H. Felgner, R. Kumar, C. N. Sridhar, C. J. Wheeler, Y. J. Tsai, R. Border, P. Ramsey,

- M. Martin and P. L. Felgner, *J. Biol. Chem.*, 1994, **269**, 2550-2561.
142. G. Gebeyehu, J. A. Jessee, V. C. Ciccarone, P. Hawley-Nelson and A. Chytil, *U.S. Patent 5334761*, 1994.
143. L. Stamatatos, R. Leventis, M. J. Zuckermann and J. R. Silviu, *Biochemistry*, 1988, **27**, 3917-3925.
144. J. P. Behr, B. Demeneix, J. P. Loeffler and J. Perez-Mutul, *Proc. Natl. Acad. Sci. U. S. A.*, 1989, **86**, 6982-6986.
145. P. Belguise-Valladier and J.-P. Behr, *Cytotechnology*, 2001, **35**, 197-201.
146. D. Joester, M. Losson, R. Pugin, H. Heinzelmann, E. Walter, H. P. Merkle and F. Diederich, *Angew. Chem. Int. Ed.*, 2003, **42**, 1486-1490.
147. M. A. Kostianen, J. G. Hardy and D. K. Smith, *Angew. Chem. Int. Ed.*, 2005, **44**, 2556-2559.
148. S. P. Jones, N. P. Gabrielson, D. W. Pack and D. K. Smith, *Chem. Commun.*, 2008, 4700-4702.
149. P. Posocco, S. Pricl, S. Jones, A. Barnard and D. K. Smith, *Chem. Sci.*, 2010, **1**, 393-404.
150. X. Qu, J. O. Trent, I. Fokt, W. Priebe and J. B. Chaires, *Proc. Natl. Acad. Sci. U S A*, 2000, **97**, 12032-12037.
151. M. Michaud, E. Jourdan, A. Villet, A. Ravel, C. Grosset and E. Peyrin, *J. Am. Chem. Soc.*, 2003, **125**, 8672-8679.
152. G. Roelfes, *Mol. Biosyst.*, 2007, **3**, 126-135.
153. V. Menchise, G. De Simone, T. Tedeschi, R. Corradini, S. Sforza, R. Marchelli, D. Capasso, M. Saviano and C. Pedone, *Proc. Natl. Acad. Sci. U. S. A.*, 2003, **100**, 12021-12026.
154. S. Sforza, G. Haaima, R. Marchelli and P. E. Nielsen, *Eur. J. Org. Chem.*, 1999, 197-204.
155. J. O. Smith, D. A. Olson and B. A. Armitage, *J. Am. Chem. Soc.*, 1999, **121**, 2686-2695.
156. R. M. C. Sutton, K. L. Sutton and A. M. Stalcup, *Electrophoresis*, 1997, **18**, 2297-2304.
157. H. Nishi and Y. Kuwahara, *J. Biochem. Bioph. Meth.*, 2001, **48**, 89-102.

158. A. M. Stalcup and N. M. Agyei, *Anal. Chem.*, 1994, **66**, 3054-3059.
159. J. Wang and D. L. Rabenstein, *Biochemistry*, 2006, **45**, 15740-15747.
160. S. M. Bromfield and D. K. Smith, *J. Am. Chem. Soc.*, 2015, **137**, 10056-10059.
161. M. C. A. Stuart, J. C. van de Pas and J. B. F. N. Engberts, *J. Phys. Org. Chem.*, 2005, **18**, 929-934.
162. N. S. Burren, A. Frigo, R. R. Rasmussen and J. B. McAlpine, *J. Nat. Prod.*, 1992, **55**, 1582-1587.
163. W. C. Tse and D. L. Boger, *Acc. Chem. Res.*, 2004, **37**, 61-69.
164. S. M. Bromfield, P. Posocco, M. Fermeglia, S. Prich, J. Rodriguez-Lopez and D. K. Smith, *Chem. Commun.*, 2013, **49**, 4830-4832.
165. L. B. Jaques, L. W. Kavanagh, M. Mazurek and A. S. Perlin, *Biochem. Biophys. Res. Commun.*, 1966, **24**, 447-451.
166. G. Gatti, B. Casu and A. S. Perlin, *Biochem. Biophys. Res. Commun.*, 1978, **85**, 14-20.
167. E. A. Yates, F. Santini, M. Guerrini, A. Naggi, G. Torri and B. Casu, *Carbohydr. Res.*, 1996, **294**, 15-27.
168. B. Casu, M. Guerrini, A. Naggi, G. Torri, L. De-Ambrosi, G. Boveri, S. Gonella, A. Cedro, L. Ferró, E. Lanzarotti, M. Paterno, M. Attolini and M. Valle, *Arz. Forsch.*, 1996, **46**, 472-477.
169. M. Guerrini, A. Bisio and G. Torri, *Semin. Thromb. Hemost.*, 2001, **27**, 473-482.
170. Q. Zang, D. A. Keire, R. D. Wood, L. F. Buhse, C. M. V. Moore, M. Nasr, A. Al-Hakim, M. L. Trehy and W. J. Welsh, *J. Pharm. Biomed. Anal.*, 2011, **54**, 1020-1029.
171. S. Beni, J. F. K. Limtiaco and C. K. Larive, *Anal. Bioanal. Chem.*, 2011, **399**, 527-539.
172. D. A. Keire, L. F. Buhse and A. al-Hakim, *Anal. Methods*, 2013, **5**, 2984-2994.
173. H. Liu, Z. Zhang and R. J. Linhardt, *Nat. Prod. Rep.*, 2009, **26**, 313-321.
174. S. Bhattacharya, D. Roxbury, X. Gong, D. Mukhopadhyay and A. Jagota, *Nano Lett.*, 2012, **12**, 1826-1830.
175. T. Brand, E. J. Cabrita and S. Berger, *Prog. Nucl. Magn. Reson. Spectrosc.*, 2005, **46**, 159-196.

176. P. S. Pregosin, P. G. A. Kumar and I. Fernández, *Chemical Reviews*, 2005, **105**, 2977-2998.
177. J. Hu, Y. Cheng, Y. Ma, Q. Wu and T. Xu, *J. Phys. Chem. B*, 2009, **113**, 64-74.
178. J. Hu, Y. Cheng, Q. Wu, L. Zhao and T. Xu, *J. Phys. Chem. B*, 2009, **113**, 10650-10659.
179. X. Feng, Y. Cheng, K. Yang, J. Zhang, Q. Wu and T. Xu, *J. Phys. Chem. B*, 2010, **114**, 11017-11026.
180. M. Sokolowska, K. Pawlas and W. Bal, *Bioinorg. Chem. Appl.*, 2010, **2010**.
181. S. P. Jones, G. M. Pavan, A. Danani, S. Pricl and D. K. Smith, *Chem. Eur. J.*, 2010, **16**, 4519-4532.
182. L. E. Fechner, B. Albanyan, V. M. P. Vieira, E. Laurini, P. Posocco, S. Pricl and D. K. Smith, *Chem. Sci.*, 2016, **7**, 4653-4659.
183. A. Oberlin, M. Endo and T. Koyama, *J. Cryst. Growth*, 1976, **32**, 335-349.
184. S. Iijima, *Nature*, 1991, **354**, 56-58.
185. N. Saito, Y. Usui, K. Aoki, N. Narita, M. Shimizu, K. Hara, N. Ogiwara, K. Nakamura, N. Ishigaki, H. Kato, S. Taruta and M. Endo, *Chem. Soc. Rev.*, 2009, **38**, 1897-1903.
186. P.-X. Hou, C. Liu and H.-M. Cheng, *Carbon*, 2008, **46**, 2003-2025.
187. A. P. Graham, G. S. Duesberg, R. V. Seidel, M. Liebau, E. Unger, W. Pamler, F. Kreupl and W. Hoenlein, *Small*, 2005, **1**, 382-390.
188. A. S. Arico, P. Bruce, B. Scrosati, J.-M. Tarascon and W. van Schalkwijk, *Nat. Mater.*, 2005, **4**, 366-377.
189. M. Moniruzzaman and K. I. Winey, *Macromolecules*, 2006, **39**, 5194-5205.
190. M. Terrones, *Int. Mater. Rev.*, 2004, **49**, 325-377.
191. J.-T. Sun, C.-Y. Hong and C.-Y. Pan, *Polym. Chem.*, 2011, **2**, 998-1007.
192. C. Klumpp, K. Kostarelos, M. Prato and A. Bianco, *BBA - Biomembranes*, 2006, **1758**, 404-412.
193. R. J. Chen, Y. G. Zhang, D. W. Wang and H. J. Dai, *J. Am. Chem. Soc.*, 2001, **123**, 3838-3839.
194. F. Wurm, A. M. Hofmann, A. Thomas, C. Dingels and H. Frey, *Macromol. Chem. Physic*, 2010, **211**, 932-939.

195. G. J. Bahun and A. Adronov, *J. Polym. Sci. A*, 2010, **48**, 1016-1028.
196. S. Vardharajula, S. Z. Ali, P. M. T. Tiwari, E. Eroğlu, K. Vig, V. A. Dennis and S. R. Singh, *Int. J. Nanomedicine.*, 2012, **7**, 5361-5374.
197. V. Rastogi, P. Yadav, S. S. Bhattacharya, A. K. Mishra, N. Verma, A. Verma and J. K. Pandit, *J. Drug. Deliv.* 2014, **2014**, 23.
198. L. Lacerda, J. Russier, G. Pastorin, M. A. Herrero, E. Venturelli, H. Dumortier, K. T. Al-Jamal, M. Prato, K. Kostarelos and A. Bianco, *Biomaterials*, 2012, **33**, 3334-3343.
199. D. Pantarotto, R. Singh, D. McCarthy, M. Erhardt, J.-P. Briand, M. Prato, K. Kostarelos and A. Bianco, *Angew. Chem. Int. Ed.*, 2004, **116**, 5354-5358.
200. R. Singh, D. Pantarotto, D. McCarthy, O. Chaloin, J. Hoebeke, C. D. Partidos, J.-P. Briand, M. Prato, A. Bianco and K. Kostarelos, *J. Am. Chem. Soc.*, 2005, **127**, 4388-4396.
201. Z. Liu, S. Tabakman, K. Welsher and H. Dai, *Nano Res.*, 2009, **2**, 85-120.
202. J. Yu, N. Grossiord, C. E. Koning and J. Loos, *Carbon*, 2007, **45**, 618-623.
203. E. A. Whitsitt and A. R. Barron, *Nano Lett.*, 2003, **3**, 775-778.
204. A. G. Ryabenko, T. V. Dorofeeva and G. I. Zvereva, *Carbon*, 2004, **42**, 1523-1535.
205. Y. Bai, D. Lin, F. Wu, Z. Wang and B. Xing, *Chemosphere*, 2010, **79**, 362-367.
206. L. Yan, F. Zhao, S. Li, Z. Hu and Y. Zhao, *Nanoscale*, 2011, **3**, 362-382.
207. P. Wick, P. Manser, L. K. Limbach, U. Dettlaff-Weglikowska, F. Krumeich, S. Roth, W. J. Stark and A. Bruinink, *Toxicol Lett.*, 2007, **168**, 121-131.
208. A. Barnard, P. Posocco, S. Pricl, M. Calderon, R. Haag, M. E. Hwang, V. W. T. Shum, D. W. Pack and D. K. Smith, *J. Am. Chem. Soc.*, 2011, **133**, 20288-20300.
209. S. Javadian, H. Aghdastinat, A. Tehrani-Bagha and H. Gharibi, *J. Chem. Thermodyn.*, 2013, **62**, 201-210.
210. K. Esumi and U. Minoru, *Structure-performance Relationships in Surfactants.* , 2nd edn., Marcel Dekker, New York, 2003.
211. B. F. Cain, B. C. Baguley and W. A. Denny, *J. Med. Chem.*, 1978, **21**, 658-668.
212. H. Gershon, R. Ghirlando, S. B. Guttman and A. Minsky, *Biochemistry*, 1993, **32**, 7143-7151.
213. S. M. Bromfield, P. Posocco, M. Fermeglia, J. Tolosa, A. Herreros-López, S. Pricl, J.

Rodríguez-López and D. K. Smith, *Chem. Eur. J.*, 2014, **20**, 9666-9674.

214. M. Pittelkow, R. Lewinsky and J. B. Christensen, *Synthesis*, 2002, 2195-2202.